R&D

MECHANICAL ENGINEERING LETTERS

2009

Research & Development

2009

Mechanical Engineering Letters, Szent István University

Annual Technical-Scientific Journal of the Mechanical Engineering Faculty,
Szent István University, Gödöllő, Hungary

**Selected Collection from the Research
Results of Year 2009**

Contents

Institute for Mathematics and Informatics

Professor Dr. Zoltán VARGA
Director of the Institute

Dear Reader,

Below we give a short summary of the research activity of our institute. The Institute for Mathematics and Informatics consists of two departments**:** Department of Mathematics and Department of Informatics. In year 2009, our main research areas and results, by departments, have been the following:

Department of Mathematics

Mathematical modelling in a variety of applied fields has been going on in international collaboration, including

- observer design for ecological systems, monitoring and control of a cell population exposed to radiation to be applied in radiotherapy;
- population harvesting, analysis of the demographic background of a pension system, dynamic analysis of stage-structured populations with applications in biological pest control, methodological development of statistical detection of plant patches etc.
- The paper included in the present issue is an overview of recent results concerning a research line we initiated five years ago, and intensively developed over the last year: game-theoretical and dynamic modelling of economic behaviour.

Department of Informatics

- On climate change mitigation a significant step forward was the preparation of the 5th National Communication and the EU Biannual Report. These reporting obligations stem from the UNFCCC Kyoto Protocol and the EU membership (the 280/2004/EC and 166/2005/EC guidelines). Both reports are peer reviewed, and the NC receives an In-depth Review from an international expert team delegated by the UNFCCC.
- In the field of image processing a new method was developed in the Department for detection of amorphously shaped images in a noisy environment.
- Concerning reachability and observability of discrete time dynamic systems, we proved that controllability to origin of time varying discrete-time linear systems, under a difference-algebraic condition, is equivalent to a generalized Fuhrmann's rank condition. It was also shown that reachability and observability for time varying discrete-time linear systems are equivalent to a structured Kalman's rank condition, under the difference algebraic independence of the structure matrices.

www.it.gek.szie.hu

Detecting Amourphously Shaped Objects in a Noisy Imaging Environment

Sándor MOLNÁR*, Péter KLINKÓ*, István SZABÓ**

*Department of Informatics, Institute for Mathematics and Informatics
**Department of Machine Construction, Institute for Mechanics and Machinery

Abstract

In the present paper, we propose a method of detecting amorphously shaped objects in real-time ultrasonic images when high level of noise is present. In general, noisy imaging environment can lead to faulty object segmentation. Shape recognition algorithms can give ambiguous results even for detecting objects with permanent shapes. From prior knowledge, indexed object templates are introduced that are aimed to incorporate the most relevant object.

Keywords

shape detection, pattern recognition, segmentation

1. Introduction

Object recognition in image analysis is the most challenging task and still heavily studied especially in the computer vision discipline. The key to the successful object recognition is to detect certain features pertinent to the given object such as shape contour, texture or color that uniquely determine the presence and the location of the object. If no additional information is available about the detectable object other than its pure shape contour, edge detection analysis is widely used as the first step in extracting valuable shape information from the raw image. At first look, shape information is embodied in those regions where sudden changes can be observed in the image's intensity function. Wherever a sudden change is observed in the intensity profile, an edge is detected. The most common approach in edge detection algorithms is to convolve the raw image with some small-sized approximation of the derivative operator kernels followed by a threshold filtering. Depending on the approach the algorithms fall into two main groups. The most commonly used methods are based on either inspecting the first derivatives of the image intensity function (e.g. Sobel) or seeking the zero crossings in the second derivatives (Laplacian of Gaussian) [1]. Although both approaches are equivalent, but methods based on inspecting the first derivatives are less sensitive to noise. One of the most preferred version of the first derivative approaches is developed by Canny [2], where some level of noise reduction and connectivity of neighboring pixels by

threshold hysteresis are also taken into account. Another preferred convolution type of approach is the recently developed SUSAN algorithm [3] which does not require any type of inclusion of a derivative kernel, therefore the algorithm's sensitivity to noise is greatly reduced. In the presence of high background noise, only regions with high contrast can be successfully recovered while some parts are occluded or suppressed in the background. In noisy imaging environment, only by the means of edge filtering operators, we cannot successfully reconstruct the complete shape contour. The recovered shape has missing segments, and unnecessary artifacts can appear. In this case some interpolation is necessary for the missing line segments from the prior knowledge of the full shape in order to reconstruct the complete contour. Another disturbing issue is when the object lies in a more complex pattern structure, and only a fraction of the recovered edge pattern carries useful information about the single shape's contour to be extracted. Some of these issues were already addressed in early studies of pattern recognition by Hough [4]0 and others [5], [6], and a Hough transformation method was developed for detecting simple analytic curves (e.g. lines, circle, ellipse). In a later work by Ballard [7], the Hough transform was generalized for any non-analytic curves and composite shapes. Based on the object's contour, an R-table is constructed that contains information about the object's central position with respect to the image gradient direction at the boundary points. Each raw of the table corresponds to one gradient angle and consist of the object's center positions relative to the boundary point coordinates where the local gradient directions lie in the same interval. In contrast to the original approach of the Hough transform for simple shapes like circle or ellipse, the generalized R-table algorithm does not hold one to one correspondence between the object's center and the local gradient angle relative to the boundary points. In the detection process for each pixel, the possible object positions are estimated and the corresponding accumulator array at the object position is incremented by the magnitude of the local gradient. The accumulator array can be further extended by considering that the object can be scaled by s and rotated by. The resulted space is termed as Hough space in the literature [7], [8]. The actual object search is taking place in the Hough space by incrementing the accumulator array for all rotated or scaled object instances represented by the set of parameters. As the result of the accumulator approach, the object can be detected with good confidence even when some parts of the border are occulted [7] or the object is partially covered by overlapping [9]. If there is no prior knowledge about the shape to be detected, segmentation methods are widely used to extract the object's area from the actual image. The most often used segmentation methods in medical imaging are the so called level-set methods where the segmentation is based on a dynamical model that an initial curve (initial level-set) evolves in a force field description of the gradient image. To achieve segmentation, the algorithm and its variants require numerical integration of a first order pde $\partial_t \varphi + \mathbf{F} \nabla \varphi + v_N |\nabla \varphi| - v_K |\nabla \varphi|$ that pulls the initial

curve towards the edges. $\mathbf{F}$ denotes the external force field, and $v_N v_K$ are the

normal and curvature based speed functions. Although the method allows the segmentation of irregular shapes, but difficulties arise when the object lies in a complex pattern that cannot be simply excluded from the segmentation process. The object's internal pattern will also be segmented while the main object's outline is only partially recovered. The above mentioned issues clearly show that detecting an object with irregular shapes with no priori knowledge is rather cumbersome task especially when the object is considerably occluded. For processing large set of noisy images, we propose employing object templates as the first approximation to the irregular shape to be recovered. In the following sections, we first discuss the employed shape model followed by the shape detection algorithm, and then we present our results and future improvements of the method.

2. Formulation of the model

In the previous section, we covered the main objectives of the shape recognition process.
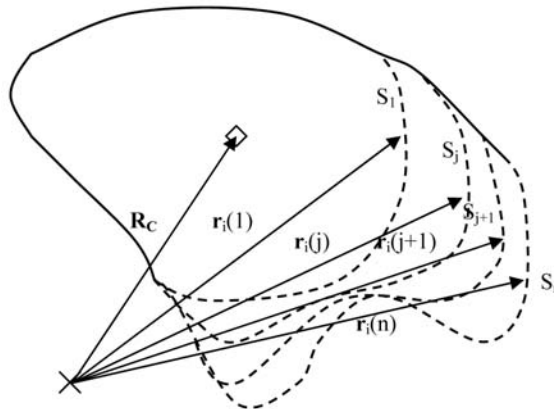
Figure 1. Formulation of the object templates used for modelling amorphous shapes. The set of single instances S_i are indexed allowing some parts of the shape to be continously deformed throughout the reference points $r_i(j)$.of the single shapes. R_C denotes the shape's central position.

In the present study the shapes are irregular and cannot be simply reproduced by a similarity transformation of the single shape. In Fig., we illustrate the underlying concept of our approach for modeling amorphous shapes. Each instance of the shape is recovered from manual segmentation. The results of the subsequent segmentations are then collected into one group to form a set of object templates $S_j = \{\mathbf{r}_i(j)\}$. The templates and the reference points $\mathbf{r_i}(j)$ which compose the outline of the given shape S_j are both indexed. If necessary,

the uniquely shaped regions of the shape sequence can be further deformed via the reference points or new shapes can be added to the existing template set later. The image pattern (e.g. outline of the shape) is represented by a collection of image points where the image intensity changes most rapidly (edge image). Therefore in our model instead of using the raw intensity function of the image as the descriptor of the pattern we use the gradient image. The smaller the gradient in magnitude at some edge points of the shape the less visually recoverable that part of the shape outline. When large amount of noise is present, some parts of the shape are barely visible and cannot be recovered by edge detection.

The object templates $S_j = \{\mathbf{r}_i(j)\}$ corresponding to the border of the shape form a closed domain Ω_j in the image domain I. We define the shape's binary masks $B_j(\mathbf{r})$ as follows

$$B_j(\mathbf{r}) = \begin{cases} 1 & \text{if } \mathbf{r} \in \Omega_j \subset I \\ 0 & \text{otherwise} \end{cases} \qquad (2.1)$$

Let us denote the original and preprocessed image intensity functions by $\phi(\mathbf{r})$, $\varphi(\mathbf{r})$ and edge image by $\varphi_E(\mathbf{r})$. One choice of defining the edge image is to threshold the magnitude of the gradient of φ by a control parameter α

$$\varphi_E(\mathbf{r}) = \begin{cases} 1 & |\nabla\varphi(\mathbf{r})| \geq \alpha \max_I |\nabla\varphi(\mathbf{r}_k)|, \quad 0 < \alpha < 1 \\ 0 & \text{otherwise} \end{cases} \qquad (2.2)$$

If high level of noise is present, the image gradient is taken after the noise reduction of the original image by convolving ϕ with a Gaussian kernel:

$$\varphi(\mathbf{r}) = (\phi * g)(\mathbf{r}) \qquad (2.3)$$

$$g(\mathbf{r}) = \frac{1}{2\pi\sigma^2} e^{-r^2/(2\sigma^2)}$$

Note that the original defining space is now extended by setting periodic boundary conditions for $\mathbf{r} \notin I$. The gradient image spectrum is then obtained in the frequency space

$$F_D[\nabla\varphi(\mathbf{r})](\mathbf{k}) = F_D[\phi(\mathbf{r}) * \nabla g(\mathbf{r})](\mathbf{k})$$

11

or using complex notation $\varphi_G(\mathbf{r}) = \partial_x \varphi(\mathbf{r}) + i\partial_y \varphi(\mathbf{r})$

$$F_D[\varphi_G(\mathbf{r})](\mathbf{k}) = -\frac{1}{\sigma^2} F_D[\phi(\mathbf{r})](\mathbf{k}) F_D[(x+iy)g(\mathbf{r})](\mathbf{k}) \qquad (2.4)$$

The final result of the spectrum for the gradient image $\varphi_G(\mathbf{r})$

$$F_D[\varphi_G(\mathbf{r})](\mathbf{k}) = 2\pi \left(i\frac{k_x}{N_x} - \frac{k_y}{N_y} \right) F_D[\phi(\mathbf{r})](\mathbf{k}) F_D[g(\mathbf{r})](\mathbf{k}) \qquad (2.5)$$

where the subscript D corresponds to the DFT, and N_x and N_y are the image dimensions to directions x and y. The main advantage of the approach is that the convolution and the evaluation of the gradient image all together can be carried out in only one step in the frequency space. The complex gradient $b_j(\mathbf{r})$ of the binary mask can be also defined according to Eq. (2.5), but the smoothing function g($\mathbf{r}$) only plays the role of making $B_j(\mathbf{r})$ differentiable.

The object's statistically best fit position is determined by the correlation function of the gradient edge images

$$C(\mathbf{r}) = \left\langle b_j / \|b_j\|, \varphi_G \right\rangle = \frac{1}{\|b_j\|} \sum_k \left(b_j(\mathbf{u_k}) - \bar{b}_j \right)^* \left(\varphi_G(\mathbf{r} + \mathbf{u}_k) - \bar{\varphi}_G(\mathbf{r}) \right) \qquad (2.6)$$

Since only modifications to the original image template B_j make any change in the subsequent evaluation of $C(\mathbf{r})$, it is practical to normalize the correlation function $C(\mathbf{r})$ only for b_j. The image domain I is finite, and the periodic boundary conditions are required to ensure that $\int_0^{N_x} \int_0^{N_y} \partial_y \varphi(x,y) dy dx = 0$ and $\int_0^{N_y} \int_0^{N_x} \partial_x \varphi(x,y) dx dy = 0$. So we can further simplify Eq. (2.6) if the mean values $\bar{b}_j$ and $\bar{\varphi}_G$ are both set equal to zero.

$$C(\mathbf{r}) = \frac{1}{\|b_j\|} \left(\sum_\mathbf{k} b_j^*(\mathbf{u_k}) \varphi_G(\mathbf{r} + \mathbf{u_k}) \right) \qquad (2.7)$$

The real part Re($C(\mathbf{r})$) corresponds to the sum of the scalar products of the gradient vectors while the imaginary part Im($C(\mathbf{r})$) comes from the sum of the vectorial products. From the correlation theorem, the spectrum of $C(\mathbf{r})$ is

$$F_D\big[C(\mathbf{r})\big](\mathbf{k}) = \frac{1}{\|b_j\|} F_D^*\big[b_j(\mathbf{r})\big](\mathbf{k}) F_D\big[\varphi_G(\mathbf{r})\big](\mathbf{k}) \tag{2.8}$$

The similarity between S_j and the image pattern is the measure of $c(\mathbf{r}) = |\text{Re}(C(\mathbf{r}))|$ by our definition, and same shapes with opposite contrast are considered to be the same. The position $r_m = \max[c(\mathbf{r})]$ is the position where the shape template statistically best fits the image pattern. We must point out that a single shape template S_j can also be stretched or shrunk in both dimensions and rotated by θ, and therefore the correlation $C(\mathbf{r}, j, \mathbf{a}, \theta)$ must be recalculated for the transformed object template $S_j(\mathbf{a}, \theta)$. As a result of scaling, the components of the complex gradients will be inversely scaled and the gradient phase will be shifted by θ. The complete object search is taking place in a closed domain of defining space for $C(\mathbf{r}, j, \mathbf{a}, \theta)$ by allocating a finite parameter set $\{\mathbf{a}, \theta\}$ of interest. From the elements of $\{\text{Re}(C(\mathbf{r}, j, \mathbf{a}, \theta))\}$, we can arbitrarily construct a finite series c_K which always contains its maximum and minimum. Therefore $\max|\text{Re}[C(\mathbf{r}, j, \mathbf{a}, \theta)]|$ always exists, and the convergency of the algorithm is garanteed.

3. Results

Pattern or shapes are the indication of sudden changes in the gradient image compared to their surroundings. After calculating the gradient images φ_G and b_j with Eq. (2.5) for ϕ and B_j, then we proceed calculating the correlation function in Eq. (2.7) for a finite set of parameters of interest $\{\mathbf{a}, \theta\}$. The parameter set is allocated by setting up a meshgrid in the domain formed by the maximum and minimum values of scaling and rotation parameters.

After sweeping through the set of parameters and shape templates, the position of the best fit template is found in the image space at $\mathbf{r}_m = \mathbf{R}_C$ where $c(\mathbf{r}_m, j_m, a_m, \theta_m) = \max[c(\mathbf{r}, j, \mathbf{a}, \theta)]$. All calculations for Eq. (2.5) and Eq. (2.8) were carried out in the frequency space with FFT that has significant speed advance over evaluating the above mentioned equations directly. The required computation time can be further reduced if the shape orientations are almost identical.

In Figure 2, we present our result for the object search of *musculus longissimus dorsi* in a real-time ultrasonic image. The object search was performed for the binary edge image $\varphi_G = \varphi_E$ defined in Eq. (2.2) with threshold parameter $\alpha = 0.18$ (Figure 2.b) and for a canny edge image $\alpha = 0.15$ (Figure 2.a). The original image (c) and the edge images (a) and (b) show that there are two huge gaps of the shape outline that cannot be recovered by the edge filtering on the left and on right side of the shape. The outline corresponding to these gaps are very faint and unidentified by edge filtering. These gaps with low

13

contrast to their sorroundings are partially comprised in the background noise and barely noticable. It is also noticable that inside the shape there is a complex pattern of edges that has to be ignored by the object detection. The image also contains letters, notes, and frames that further complicate the situation. It is another and (Figure 2.c). The plot of the correlation $c(\mathbf{r})$ is presented in Figure 2.d. for the best fit template. As a result of having periodic boundary conditions allowed, $c(\mathbf{r})$ is plotted in the full image space. The position that $c(\mathbf{r})$ has its maximum value is marked with a white arrow. In all images (a), (b), and (c) the detected shape is also indicated by overlaying the shape on the image at position $\mathbf{r}_m$. Almost identical results were found for both images (a) and (b), and even the central coordinates for the best fit shape position $\mathbf{R}_C=\mathbf{r}_m$ were identical. The detected shape remarkably fits to the appropriate image area of interest in both cases. In Fig. 3, more examples are presented for detecting the same object in several ultrasonic images. In Fig. 3(d) gives an example when the shape outline cannot be recovered unambiguously, but the best fit shape still fits well.

a

c

b

d
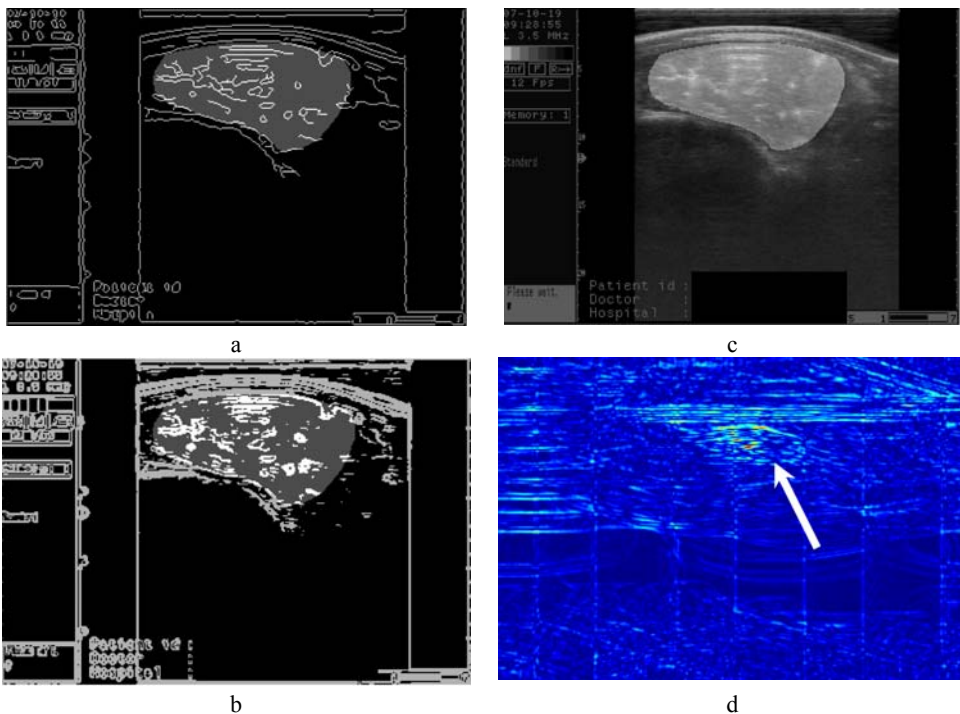
Figure 2. Shape detection of *musculus longissimus dorsi* from a real-time ultrasonic image (256×370, 8bit). The upper and lower left images are edge images. On the upper left, the binary edge image is extracted with using the Canny edge filter. On the lower left (b), the edge image is simply obtained by thresholding the gradient image. The lower right (d) image shows the correlation $c(r)=|\mathrm{Re}(C(r))|$ in the image space. The solution for $c(R_c)=\max|\mathrm{Re}(C(r))|$ yields the position of the statistically best fit shape template (white arrow). The detected shape template is superimposed to the original image (c) and the edge images (a) and (b) at the best fit position.

4. Conclusions

In the present paper we discussed our method for detecting amorphously shaped objects in noisy images. The shapes are irregular and their outline is only partly recoverable from the background noise. For these situations, we proposed employing object templates that are uniquely shaped and can be further deformed via some reference points. As in common with the literature on the subject, we referred to the shape outline as the set of points in the image intensity function having the highest gradient in magnitude (edges). Our further goal is to recover the shape even when its domain is embedded in a complex pattern structure. Therefore the proposed method takes advantage of correlating the gradient edge image with the gradient edge mask obtained from the shape templates. Additional linear transformations are also taken into account (scaling and rotation) for dealing with perspective view. The method works well even with a few templates and were able to recover the shape of interest with good confidence regardless how the preprocessed gradient edge image was obtained. The method can be improved by applying a model of stretching tensor for modeling the applied deformations to the shape templates.

a

c

b

d
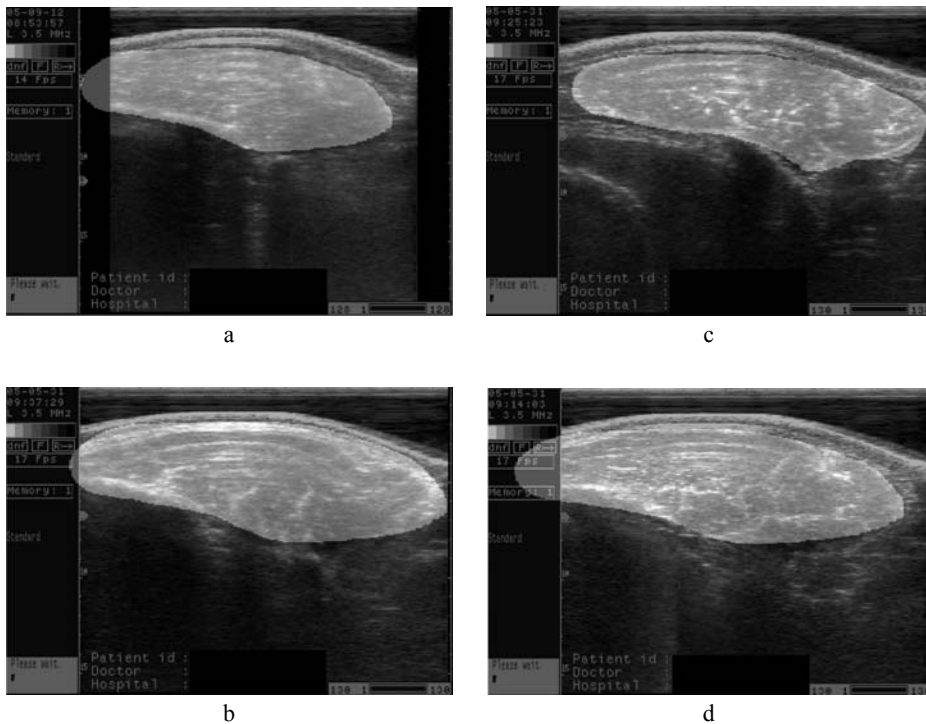
Figure 3. More examples of detecting *musculus longissimus dorsi* from ultrasonic images (256×370, 8bit). In images (a), (b), and (c) the shape is succesfully recovered. In image (d), the shape is also detected, but the result is not as good as in the other examples due to the fact that the shape outline is not well separable.

Acknowledgment

References

[1] D. Marr and E. Hildnth, Proc. Royal Soc. London Bulletin, Vol. B207, (1980) 187.

[2] J. Canny, IEEE Trans. Pattern Anal. Mach. Intell., Vol. 8, No. 6, (1986) 679.

[3] S.M. Smith and J.M. Brady, International Journal of Computer Vision, Vol. 23, No. 1, (1997) 45.

[4] P.V.C. Hough, A method and means for recognizing complex patterns, U.S. Patent 3 069 654 (1962).

[5] C. Kimme, D.H. Ballard, and J. Sklansky, Communications of the ACM, Vol. 18, No. 2, (1975) 120.

[6] S.D. Shapiro, Computer Graphics Image Processing, Vol. 8, No. 2, (1978) 219.

[7] D.H. Ballard, Pattern Recognition, Vol. 13, No. 2, (1981) 111.

[8] A.S. Aguado, E.Montiel, and M. S. Nixon, Pattern Recognition, Vol. 35, No. 5, (2002) 1083.

[9] D.M. Tsai, Image and Vision Computing, Vol. 15, No. 12, (1997) 877.

Game Theory and Evolutionary Dynamics in Economic Behaviour[1]

Zoltán VARGA

Department of Mathematics,
Institute for Mathematics and Informatics

Abstract

The paper is an overview of our recent results with different coauthors concerning a research line we initiated five years ago. If a conflict situation is described in terms of a game-theoretical model, different solution concept of this game provide rational strategy choices for the involved parties, called players. In the case when the conflict is repeated the players can adapt their strategy choice to the observed outcomes of the previous games. Therefore it is also reasonable to set up a dynamic model for the strategy choice of the players that describes the time-dependent behaviour of the players. In the paper different applications of this modelling methodology in economic context are briefly summarized, ranging from the dynamic stability of coalitionist behaviour, to the survival of "competitor" versus "optimizer" behaviour; from the evolutionary game model for a marketing cooperative to the dynamic analysis of the conflict of industrial producers with the environmental policy. A game-theoretic approach to standing timber auction is also shortly presented.

Keywords

game theory, Evolutionary Dynamics, game model

1. Introduction

Game theory, as a mathematical discipline, has been initially developed for the description of conflicts occurring in economic activity (see e.g. von Neumann and Morgenstern, 1944), proposing different solution concepts supporting rational decisions in different conflict situations. In the so-called *strategic* or *normal form games*, a player chooses his *strategy* and expresses his interest in terms of his *payoff function* which, however, may also depend on the strategy choice of the other players. In such games the *equilibrium solution* introduced in Nash (1950) for multiplayer games rapidly gained popularity in economic modelling.

Apart from modelling of economic and social conflicts, normal form games also turned out to be appropriate in the description of animal behaviour at population level, where the evolutionary concept of *fitness* corresponds to the payoff. The concept of *evolutionarily stable strategy* (ESS), a particular version of Nash equilibrium, became a new paradigm in evolutionary biology. Evolutionary theory not only operates with the concept of evolutionarily stable strategy, but also offers appropriate dynamic models for the propagation, elimination or asymptotic coexistence of certain behaviour types. The so-called *replicator dynamics* describes the time variation of certain behaviour types in a population, and in important particular cases the asymptotic behaviour of the replicator dynamics also explains why ESS describes the "final state" of an evolutionary process, see Hofbauer and Sigmund (1998). In biological context, replication means that a behaviour type is passed down from parent to offspring. In the sense of the replicator dynamics a behaviour type will propagate in the population, if it performs better than the population average. Another option for the description of dynamic strategy choice (change of behaviour types) is the so-called *partially adaptive dynamics* introduced in Garay (2002). For some more recent results on dynamic evolutionary models in population biology see e.g. Cressman et al. (2001), Cressman and Garay (2003), (2006), (2009), Garay et al. (2003), Cressman et al. (2004a), Garay (2009).

In our model recalled in Section 2, adapting an idea sketched in Weibull (1995), the replication of carriers of a behaviour type is thought of as resulting from imitation. In this section dynamic stability of coalitionist behaviour will be discussed. In Section 3 both replicator dynamics and partially adaptive dynamics are used to model time-depending economic behaviour and to analyze the problem of survival of "competitor" versus "optimizer" behaviour. In Section 4 a game-theoretical model for the behaviour in a marketing cooperative is presented. Under conditions on the penalty for unfaithfulness of cooperative members, a particular Nash equilibrium, a so-called *attractive solution* of the game is obtained. In this model partially adaptive dynamics also describes the time-dependent strategy choice of the players, and additional conditions also imply that the strategy choices converge to a strict Nash equilibrium. Our results on the attractive solution in case of a probabilistic market situation are also reported. In section 5 a similar game-theoretic model for the conflict of producers with the environmental policy is presented. Finally, in Section 6 a game model is considered to find conservative (or maximin) solution for bidders in a first-price sealed-bid auction of a standing timber.

2. Dynamic stability of coalitionist behaviour for two-strategy bimatrix games

Evolutionary game theory applied to bimatrix games has traditionally been restricted to predicting the players' behaviour in the context of a non-cooperative game. In our paper Cressman et al. (2004b), the purpose was to investigate continuous-time

dynamic models that describe the evolution of the frequency for cooperative coalitionist behaviour relative to that of non-cooperative behaviour in pair-wise conflicts between agents of two populations that are given as a bimatrix game.

The basic idea is to adapt the replicator dynamics recalled in the Introduction. In the biological evolutionary game context, where coalition formation has received little attention, replication means that "like begets like": a behaviour type is passed down from parent to offspring. The replication of carriers of a behaviour type can then be thought of as resulting from imitation. An agent is ready to review his strategy at a certain rate depending on the success of another strategy. In the corresponding replicator dynamics, the time rate of a strategy's relative frequency change is positive if this strategy performs better than the average, and negative in the opposite case. Our model can also be applied to the social evolution of behaviour types (strategies) in a population of pair-wise interacting agents, such as when individuals represent firms or some other social or economic units.

Originally the replicator dynamics was introduced for the study of game-theoretical conflicts in biological evolutionary processes. This is based on the Darwinian theory, where the competitiveness of behaviour types is the key issue since these types will increase in relative frequency if their fitness (payoff) is greater than the mean fitness of the whole population. The aim of the paper was then to study whether replicator dynamics corresponding to the theory of cooperative games can describe the propagation of coalitionist behaviour.

We proposed dynamic models where in each population of agents the basic behaviour types are: coalitionist and non-coalitionist. In the *monomorphic dynamic model*, based on a two-strategy two-person (bimatrix) game, in the pair-wise conflict of coalitionists a two-person coalition is formed, and always the Nash equilibrium strategies are played if at least one of the agents is non-coalitionist. In the *polymorphic dynamic model*, the pair-wise conflict of two coalitionists is again modelled by a two-person coalition game, but if at least one of the agents is non-coalitionist, both use one of the two fixed pure strategies. We also studied the asymptotic behaviour of these models. Applying the technique of *Lyapunov functions*, we have shown that in the monomorphic model the coalitionist players eliminate the non-coalitionists. In the polymorphic model the coalitionists are able to propagate in the population but in general they cannot eliminate the non-coalitionist behaviour. Numerical examples also illustrate the results.

3. Evolutionary dynamics for economic behaviour: competition versus optimization

In classical game theory the action of a player called *optimizer* is to optimize his own payoff. In evolutionary game theory instead, a Darwinian *competitor* always wants to be better than the average. In our paper Garay and Varga (2006), in a dynamic situation the survival of "competitor" versus "optimizer" behaviour was studied. Starting from a classical symmetric two-person normal

form game, the paper was aimed at the development of a dynamic model in which it can be predicted whether in a game-theoretical conflict the competitor or the optimizer behaviour would survive in the long run.

It is known that in a situation of competition not always profit maximizing is the best survival strategy. Hansen and Samuelson (1988) pointed out that if the agent has negligible effect on others' payoff then the payoff maximizer will survive, but when this assumption is not met, survival does not imply optimality. Later Schaffer (1989) demonstrated that if the firms have market power (i.e. the firm's success depends on other players' behaviour) then the profit-maximizers are not the best survivors. The reason is that, although a 'spiteful' firm decreases its payoff as well, it decreases the maximizer's payoff even more. Schaffer's idea is similar to our one, but there is a major difference: he applied the standard biological set up, namely considered a "population" of firms that never change their strategies, and the selection process guarantees the long-term realization of a Nash equilibrium. We, instead, consider rational players, who can change their strategies in a smooth way according to their payoff functions and have complete information about of the current state of the game. Moreover, our approach is dynamical, since in it both the behaviour of the players and the selection process are described by differential equations.

For the strategy choice of the players the partial *adaptive dynamics* of Garay (2002) is applied which means that each player can change his actual strategy in a continuous way, corresponding to the direction of the gradient of his payoff function. We suppose that the change of weight of the players is described by the *replicator dynamics*. This replicator dynamics determines which behaviour type will survive.

The further details are obtained for an illustrative example, where the payoff of the game between competitor and optimizer is quadratic. It is shown that there is no totally mixed equilibrium, which means that the two behaviour types can not coexists. Moreover, applying the technique of *centre manifold theory* (see e.g. Carr, 1981) we obtained that, under simple conditions on the model parameters, the equilibrium state corresponding to the exclusive presence of the competitors is locally asymptotically stable. In other words, an optimizer with sufficiently small weight will be selected out by the competitor.

4. Evolutionary game model for a marketing cooperative with penalty for unfaithfulness

In agriculture we often face the situation that producers of a given product form a marketing cooperative for the commercialization of their product. Such a cooperative in a given region may perform several activities, ranging from product processing to complex marketing. In Varga et al. (2010) we considered a marketing cooperative that negotiates a contracted price with large buyers, sharing risk among members of the cooperative. By the time of the actual commercialization of the product, the market price may be higher than what the cooperative can guarantee for members, negotiated on beforehand. Some

"unfaithful" members may be interested in selling at least a part of their product outside; the cooperative, however, can punish them for it. This conflict situation is described in terms of a game-theoretical model.

In the quoted paper, considering first the case of constant market price, we set up a normal-form game model of a marketing cooperative, where every single member and the cooperative itself are the players. The strategy of a player is the proportion of the total production sold to the cooperative, while the cooperative chooses a penalty as its strategy to punish unfaithfulness. For this game an *attractive solution*, a particular Nash equilibrium is obtained (for a definition see Varga et al., 2010). As an extension of this a game model, we also obtained an attractive solution for the case of a Cournot type oligopoly market with linear inverse demand function.

Considering not only one production and commercialization period (one year), but also the long-term behaviour of the players, we can ask, if for each player there is a reasonable time-dependent strategy choice, and if so, what are the long-term consequences of this choice. Similarly to the dynamic model of Section 3, the proposed strategy dynamics is a variant of the partial adaptive dynamics known in multispecies evolutionary game theory, see Garay (2002). The intuitive background of this dynamics in the present model is the hypothesis that each player will increase (or decrease) his strategy (quantity sold to the cooperative, or penalty rate), if the corresponding strategy change results in the increase (or decrease) of his payoff; provided the rest of the players stick to their actual strategies. This means that the sign of the corresponding partial derivative will determine the process of the strategy choice. Based on the *stability analysis* of the corresponding system of differential equations, it is shown that, if the market price is determined by a Cournot type oligopoly, in the case of an effective penalty, the players are driven towards an attractive solution of the game, according to this evolutionary strategy dynamics. For the members this attractive solution is to sell all their products to the cooperative, which may guarantee the long-term survival of the cooperative.

Finally a model with redistribution of penalty is studied. For the symmetric case, when all members produce the same amount, the stabilization is even stronger, if the collected effective penalty is partly distributed among the faithful members. If the effective penalty is not too high and the oligopoly effect is not too strong, then a unique strict Nash equilibrium exists, and from the stability analysis of the strategy dynamics, in terms of the model parameters, sufficient conditions have been obtained under which this strict Nash equilibrium is asymptotically stable equilibrium for the strategy dynamics; in particular, the strategic choice of the members converges to this equilibrium.

In another paper, Gambarelli (2009), we considered an agricultural cooperative where producers, as part of their strategy in dealing with the cooperative, at the beginning of the yearly production cycle declare a projected quantity to be sold to the cooperative at a contracted price. At the time of the harvest, as a second strategy choice, each producer decides how much of his production he would actually sell to the cooperative. If a producer does not deliver the contracted amount, he will be punished by the cooperative,

proportionally to the undelivered amount and to the extra profit gained from selling on the direct market. It is up to the cooperative to set the penalty rates. If by the time of the harvest, the direct market price turns out to be lower than the contracted price guaranteed by the cooperative, the latter would not buy more than the contracted amount. We found a Nash equilibrium solution for this conflict situation, supposing that the higher direct market price will occur with a given probability. The obtained theorems are illustrated with a marketing cooperative for the commercialization of apples.

5. Dynamic model for the conflict of producers with the environmental policy

In our joint paper Scarelli et al. (2009), a game-theoretic model similar to that of Section 4 was applied in the context of environmental protection. Namely, the following conflict situation is considered: Certain companies produce and sell the same product, both in green and non-green version. The production cost of the non-green version is lower, but the government sets an environmental tax on it. For the description of the situation a multi-person normal form game is defined where the strategy choice of each producer (player) is the proportion at which it produces the green version, while its payoff is the net profit remaining after paying the eventual environmental tax. The government's strategy is setting the tax rate, its payoff is the tax collected from the producers (which is invested then in environmental protection). First, in the simplified case when the market price does not depend on the production of the considered players (i. e. their total market share is sufficiently small), an attractive solution for the game conflict is obtained, provided the government threatens the non-green product with a maximum tax rate, and all producers produce only green products.

   A more realistic situation is when the market price linearly decreases with increasing total output offered by the considered producers. Then an attractive solution similar to the previous case is obtained, in which the government can achieve that all producers offer only green product, by threatening them with punitive taxation higher than the extra profit gained from the production of the non-green product.

   In Garay et al. (2009), we have shown that in this game, in the case of a limited taxing, the above attractive solution is an unstable equilibrium of the strategy dynamics. It is also proved that in case of an appropriate taxing policy of the government, the system displays an asymptotic equilibrium, in particular the producers are driven towards a required equilibrium behaviour.

6. Conservative solution in a first-price sealed-bid auction of a standing timber

The sale by auctions is frequently used for many physical or financial products. One of them is the standing timber of private or public forests in many countries

of the world, see e.g. Li and Perrigne (2003). In particular, if the standing timber belongs to a public owner, the market has to follow a public evidence procedure, including public auctions.

In Carbone et al. (2009), we have proposed a game-theoretic model for the auction of a standing timber. In general terms, the formalization of the conflict situation taking place in an auction between bidders, mainly depends on the information the bidders are supposed to have about the valuation and the possible bidding strategy of the other bidders. For the mathematical description of the conflict we considered a *first-price sealed-bid auction* (FPSB) which means that bidders simultaneously submit sealed bids so that no bidder knows the bid of any other participant. The highest bidder pays the submitted price.

In our model, just for the simplicity of the formalization, we supposed that in the auction there are only two bidders. Each bidder knows only the probability distribution of the bidding of other bidder. Since we will deal with continuous random variables representing the bidding of the partner bidder, ties have zero probability and therefore can be neglected. Our approach is different from the usual one (see e.g. Aliprantis and Chakrabarti, 2000) at several points. First, in the usual approach, a bidding strategy is a function of the valuation of the object given by the bidder, while in our model the strategy itself will be a possible choice of a bid value taken from an interval determined by the would be bidders. Furthermore, the usual approach provides a Nash equilibrium of the corresponding game, based on the uniform distribution of the valuation of the other players, since it looks rather difficult to find a Nash equilibrium if the distribution is not uniform. When the problem is considered from the viewpoint of a given player, say Player 1, his bidding is a deterministic value of the considered interval, while this player only guesses according to a probability distribution, what the bidding of the other player will be. We used non-uniform distributions, which made it possible to include risky and non-risky bidding behaviour in the model. Indeed, choosing an appropriately shaped distribution function, we can describe the behaviour of the bidder either adverse or propense to risk. Finally, instead of an equilibrium solution, which implicitly involves rationality in the behaviour of the players, we dealt with the maximin or conservative solution for a fixed bidder. This solution is based on the idea that a bidder counts on the worst case, supposing the unknown bidding of the other bidders might minimize his expected payoff, and he, by his own strategy choice, tries to maximize this minimum.

The situation when Player 1 plays against several players, can be handled similarly. It is also possible to build into the model that some Players play more risky bidding strategies, while others are averse to risk. If we suppose the parameters of the corresponding families of distributions can be independently attributed to different players, for the conservative solution the minimization should be carried out over all possible parameter vectors, and Player 1 then maximizes this minimum by his appropriate bidding choice. Finally, in our paper Carbone et al. (2009), the theoretical results have been also illustrated with a case study concerning a standing timber auction of a forest located in central Italy.

References

Aliprantis, Charalambos D. and Chakrabarti, Subir K. (2000), Games and Decision Making, Oxford University Press.

Carbone, F., Scarelli, A. and Varga, Z. (2009), Conservative Solution in a First-Price Sealed-bid Auction of a Standing Timber. 1-8. (mimeo)

Carr, J. (1981) *Applications of Centre Manifold Theory.* Springer-Verlag.

Cressman, R., Garay, J. (2003), Stablility *N*-species coevolutionary systems. *Theor. Pop. Biol.* 64: 519-533.

Cressman, R., Garay, J. (2006) A game–theoretical model for punctuated equilibrium: species invasion and stasis through coevolution. *BioSystem* 84: 1-14.

Cressman, R., Garay, J (2009), A Predator-Prey Refuge System: Evolutionary Stability in Ecological Systems *Theor. Pop. Biol*. 76: 248-257.

Cressman, R., Garay, J., Hofbauer, J. (2001), Evolutionary stability concepts for *N*-species frequency-dependent interactions. *J. Theor. Biol*. 211: 1-10.

Cressman, R., Krivan, V., Garay, J. (2004a), Ideal free distributions, evolutionary games, and population dynamics in multiple-species environments. *Am. Nat.* 164 (4): 473-489.

Garay, J. (2002), Many Species Partial Adaptive Dynamics. *BioSystems* 65: 19-23.

Garay, J. (2009) Cooperation in defence against predator *J. Theor. Biol* 257: 45-51

Garay, J., Cressman, R., Varga, Z. (2003), Optimal behaviour of honey bees based on imitation at fixed densities. *Com. Ecol.* 4(2): 219-224.

Cressman, R., Garay, J., Scarelli, A., Varga, Z. (2004b), The dynamic stability of coalitionist behaviour for two-strategy bimatrix games. *Theory and Decision*, 56, No. 1-2, pp. 141-152.

Garay, J. and Varga, Z. (2006), Evolutionary dynamics for economic behaviour: competition versus optimization. *Pure Mathematics and Applications* 16, No. 4, 399–409.

Garay, J., Scarelli, A., and ., Varga, Z. (2009), Dynamic model for the conflict of producers with the environmental policy. AIRO2009, the 40th Annual Conference of the Italian Operational Research Society, September 8-11, Siena, Italy. Abstracts 94-95.

Gambarelli, G., Bertini, C., Scarelli, A., and Varga, Z. (2009), Equilibrium solution in a game between a cooperative and its members. 1-11. (mimeo).

Hansen, R.G., Samuelson, W.F. (1988), Evolution in economic games. *J. Econ. Behav. Org.* 10: 315-338.

Hofbauer, J., Sigmund, K. (1988), The theory of evolution and dynamical systems. Cambridge University Press.

Li T., Perrigne I. (2003), Timber sale auctions with random reserve prices. *Review of Economics and Statistics* 85 (1), 189-200.

Nash, J. (1950), Equilibrium points in n-person games. *Proceedings of the National Academy of Sciences* 36(1):48-49.

von Neumann, J. and Morgenstern, O. (1944), *Theory of Games and Economic Behavior*. Princeton Univ. Press.

Scarelli, A., Garay, J. and Varga, Z. (2009), Game-theoretic model for the conflict of producers with the environmental policy of the government 1-8. (mimeo).

Schaffer, M.E. (1989), Are profit-Maximisers the best survivors? *J. Econ. Behav. Org.* 12: 29-45.

Varga, Z., Scarelli, A., Cressman, R. and Garay, J. (2010), Evolutionary game model for a marketing cooperative with penalty for unfaithfulness. *Nonlinear Analysis: Real World Applications.* 11, Issue 2, April, 742-749.

Weibull, J. W. (1995), *Evolutionary Game Theory*. Cambridge-London: The MIT Press.

A Rank Condition for Controllability and Reachability of Time-Varying Discrete-Time Linear Systems[1]

Sándor MOLNÁR[*], Ferenc SZIGETI[**],
Márk MOLNÁR[***]

[*]Department of Informatics, Institute for Mathematics and Informatics,
[**]Department of Control Engineering, University Los Andes, Merida, Venezuela
[***]Doctoral School of Business Management and Economics,
Szent István University, Gödöllő, Hungary

Abstract

For discrete-time linear systems, controllability and reachability are not equivalent. Instead of the well-known Kalman's rank condition, which characterizes reachability, controllability to origin of the time invariant, discrete-time linear system is equivalent to the Fuhrmann's rank condition. In the first part of this paper we prove that controllability to origin of time varying discrete-time linear systems, under a difference-algebraic condition, is equivalent to a generalized Fuhrmann's rank condition. In the second part we prove that reachability and observability for time varying discrete-time linear systems are equivalent to a structured Kalman's rank condition, under the difference algebraic independence of the structure matrices.

Keywords

discrete-time, reachability, controllability, systems

1. Introduction

It is well-known that the time-invariant discrete-time linear system

$$x(t+1) = Ax(t) + Bu(t) \tag{1.1}$$

is reachable if and only if it verifies the Kalman's rank condition

$$\text{rank}\big(B, AB, \ldots, A^{n-1}B\big) = n \tag{1.2}$$

or, equivalently, if

$$\sum_{i=0}^{n-1} \text{Im}\left(A^i B\right) = R^n. \tag{1.3}$$

The controllability to origin of system (1.1) is equivalent to the Fuhrmann's rank condition

$$\text{Im}\left(A^n\right) \subset \sum_{i=0}^{n-1} \text{Im}\left(A^i B\right) \tag{1.4}$$

see [1.3].

The reachability and controllability for time-varying linear systems

$$\dot{x}(t) = A(t)x(t) + B(t)u(z) \tag{1.5}$$
$$y(t) = C(t)x(t) + D(t)u(t) \tag{1.6}$$

can also be characterized by rank conditions, instead of the controllability Grammian of (1.5). This result was obtained under several analytic or differential-algebraic conditions, both for the finite and infinite dimensional systems (see [1], [2]). For example, if the basis of the Lie algebra is generated by $\{A(t)\}$, is $A_1, \dots, A_I$ then the controllability and the reachability of (1.5) is equivalent to the generalized Kalman's rank condition

$$\sum_{0 \le n_1, \dots, n_I < n} \sum_{j=1}^{J} \text{Im}\left(A_1^{n_1} \dots A_I^{n_I} B_j\right) = R^n$$

if the time varying coefficients in the expansion $A(t) = \sum_{i=1}^{I} a_i(t)A_i$ are differential algebraically independent. A similar result is false for the reachability of a time varying discrete-time system. Reachability of system (1.5) cannot be characterized by this setting; for this, consider the basis $e_1, \dots, e_n \in R^n$, and the sequences $b_1, \dots, b_n$ which are algebraically independent in difference. Then, the system

$$x(t+1) = \left(\sum_{i=1}^{n} b_i(t)e_i\right)u(t)$$

is not reachable from zero, because the reachability subspace of this system at each moment is 1-dimensional. However, it is controllable to zero.
Concerning reachability and observability of system (1.5)-(1.6) the generalized Kalman's rank conditions for reachability for this system is

$$\sum_{j=1}^{J} \sum_{0 \le n_1,\ldots,n_I < n} \mathrm{Im}\!\left(A_1^{n_1}\ldots A_I^{n_I} B_j\right) = R^n \qquad (1.7)$$

and for the observability is

$$\sum_{k=1}^{K} \sum_{0 \le n_1,\ldots,n_I < n} \mathrm{Im}\!\left(A_1^{*n_1}\ldots A_I^{*n_I} C_j^*\right) = R^n. \qquad (1.8)$$

For the continuous time system it was proven that under differential algebraic independence of the time varying coefficients $a_1(t),\ldots,a_I(t),b_1(t),\ldots,b_J(t)$, the generalized Kalman's rank condition (1.7) is equivalent to controllability (reachability) of the system (1.5)-(1.6). Similarly, if the coefficients $a_1(t),\ldots,a_I(t),c_1(t),\ldots,c_K(t)$ are differential-algebraic independent, then the generalized Kalman' rank condition (1.8) is equivalent to observability (reconstructibility) of the system (1.5)-(1.6), (see [1], [2]).

1.1. Definitions

Given the time-varying discrete time system

$$x(t+1) = A(t)x(t) + B(t)u(t) \qquad (1.1.1)$$
$$y(t+1) = C(t)x(t) + D(t)u(t) \qquad (1.1.2)$$

with

$$A(t)^{n \times n}, B(t) \in R^{n \times p}, C(t) \in R^{q \times n}$$
$$D(t) \in R^{q \times p}, t = 0,1,2,\ldots,$$

we consider $u : Z_T \mapsto R^P$, controls and $x : Z_{T+1} \mapsto R^n$, trajectories of system (1.1) where $Z_K = \{0,1,\ldots,k-1\}$. In these conditions, we say the system (1.1) is *controllable to zero* if for all $\xi \in R^n$, there exists a control u, such that the corresponding trajectory, with the initial condition $x(0) = \xi$, satisfies $x(T) = 0$. The system (1.1) is *reachable from zero* if for every $\eta \in R^n$ there exists a control u, such that the corresponding trajectory of (1.1.1) satisfies $x(T) = \eta$. Let

$$
\begin{aligned}
V_A &= \{A(t); t = 0,1,\ldots\} \, V_B = \{B(t); t = 0,1,\ldots\} \\
V_C &= \{C(t); 0,1,\ldots\}
\end{aligned} \qquad (1.1.3)
$$

be the vector spaces generated by the system (1.1.1)-(1.1.2). If $\{A_1,\ldots,A_I\},\{B_1,\ldots,B_J\},\{C_1,\ldots,C_K\}$ are bases of the vector space V_A,V_B,V_C respectively, then we have:

$$A(t) = \sum_{i=1}^{I} a_i(t)A_i, B(t) = \sum_{j=1}^{J} b_j(t)B_j, C(t) = \sum_{k=1}^{K} c_k(t)C_k \qquad (1.1.4)$$

for $t = 0,1,2,\ldots$

Let R be a given ring, we consider a fixed homomorphism $\delta : R \mapsto R$ such that

$$\delta(a+b) = \delta a + \delta b, \delta(ab) = (\delta a)(\delta b).$$

Then we say that (R,δ) is a *difference ring*.

Examples

(i) Let $S(R)$ be the ring formed by the sequences $Z \mapsto R$. If we take δ as the shift operator $(\delta a)(n) = a(n+1)$, we have that $S(R)$ is a difference ring.

(ii) Let $R = Z[x_0, x_1,\ldots]$ be the ring of polynomials over the ring of integers. If $\delta x_i = x_{i+1}$, this operator induces the ring $Z\{x\}$ of difference polynomials of the indeterminate x, that is, $x_0 = \delta^0 x, x_1 = \delta x, x_2 = \delta^2 x,\ldots$ Given $(R,\delta),(R_1\delta_1)$ difference rings and a ring homomorphism $F : R \mapsto R_1$ we say that F is a difference ring homomorphism if $F(\delta a) = \delta_1 F(a)$, for $a \in R$.

Given a difference ring (R,δ) and $a \in R$, we consider the difference ring homomorphism

$$F_a : Z\{x\} \mapsto R, p(x) \mapsto p(a)$$

we say that a is transcendent if the kernel $N(F_a) = 0$, that is, if $p(x) \in Z\{x\}$, is such that $p(a) = 0$, then $p(x) = 0$. Given $a_1,\ldots,a_k \in R$, we consider the difference ring homomorphism

$$F_{a_1,\ldots,a_k} : Z\{x_1,\ldots,x_k\} \mapsto R, p(x_1,\ldots,x_k) \mapsto p(a_1,\ldots,a_k)$$

we say that $a_1, \ldots, a_k$ are difference algebraically independent *if the kernel* $N(F_{a1,\ldots,a_k}) = 0$, *that is, if* $p(x_1, \ldots, x_k) \in Z\{x_1, \ldots, x_k\}$ *is such that* $p(a_1, \ldots, a_k) = 0$, *then* $p(x_1, \ldots, x_k) = 0$.

The *fundamental matrix* of system 1.5. is given by:

$$\Phi(t+T,t) = A(t+T-1)\ldots A(t+1)A(t) =$$
$$= \sum_{\mathbf{i} \in \mathbf{Z}_I^T} \delta^{T-1} a_{i_1}(t)\ldots \delta a_{i_{T-1}}(t) a_{i_T}(t) A_{i_1}\ldots A_{i_{T-1}} A_{i_T}.$$

From this, we obtain the following expression:

$$\Phi(t+T,t) = \sum_{\mathbf{i} \in Z_I^T} m_{\mathbf{i}}(a)(t) A_{\mathbf{i}}, \qquad (1.1.3.1)$$

where

$$i = (i_1, \ldots, i_T) \in Z_k^T, \ A_i = A_{i1} A_{i2iT} (\delta a)(t) = a(t+1),$$

is the translation operator acting over the sequences, and

$$m_{\mathbf{i}}(a) = \left(\delta^{T-1} a_{i_1}\right)\left(\delta^{T-2} a_{i_2}\right)\ldots\left(\delta a_{i_{T-1}}\right) a_{i_T},$$

is a difference monomial. The solution of the difference equation with initial condition $x(\tau) = 0$, is the sequence

$$x(\tau+T) = \sum_{t=1}^{T} \Phi(\tau+T, \tau+t) B(\tau+t-1) u(\tau+t-1)$$

$$\sum_{t=1}^{T}\sum_{j=1}^{J}\sum_{\mathbf{i} \in \mathbf{Z}_I^{T-t}} \delta^{t-1} b_j(\tau) \delta^t m_{\mathbf{i}}(a)(\tau) A_{\mathbf{i}} B_j u(\tau+t-1) \qquad (1.1.3.2)$$

$$\sum_{t=1}^{T}\left(\sum_{\mathbf{i} \in \mathbf{Z}_I^{T-t}} \delta^t m_{\mathbf{i}}(a)(\tau) A_{\mathbf{i}}\right)\left(\sum_{j=1}^{J} \delta^{t-1} b_j(\tau) B_j\right) u(\tau+t-1)$$

We denote by $A = A(A_1, \ldots, A_I)$ the associative algebra generated by the matrices $A_1, \ldots, A_I$, and I as the identity matrix.

The vector spaces

$$V^0 = V(I)$$

$$V^1 = V(A_1, \ldots, A_I)$$

$$V^T = V(A_{i_1} A_{i_2} \ldots A_{i_T}) \, \mathbf{i} = (i_1, \ldots, i_T) \in Z_I^T$$

define a *gradation* in the associative algebra A.

1.2. Controllability

Lemma 1.1 If the coefficients $a_1(t), \ldots, a_I(t)$ in are difference-algebraically independent, then there exists t, such that

$$\mathrm{Im}\,\Phi(t+T,t) = \mathrm{Im}\,V^T = \left\{ A_{\mathbf{i}} x \; : \; \mathbf{i} \in \mathrm{Im}\,Z_I^T, x \in R^n \right\}$$

Proof. It is obvious that $\mathrm{Im}\,\Phi(t+T,t) \subset \mathrm{Im}\,V^T$.

Let $\mathrm{Im}\,\Phi(t+T,t) = \mathrm{Im}\,V^T = \left\{ A_{\mathbf{i}} x \; : \; \mathbf{i} \in \mathbf{z}_I^T, x \in R^n \right\}$ be a base of $\mathrm{Im}\,V^T$. Then, each column $A_{\mathbf{i}} e_j$ can be expressed as

$$A_{\mathbf{i}} e_j = \sum_{l=1}^{L} \Gamma_{\mathbf{i}j}^l A_{\mathbf{i}_l} e_{j_l} \tag{1.2.1}$$

Suppose that the inclusion is proper. Then there exists an element $A_{\mathbf{i}_l} e_{j_l}$ of the base such that $A_{\mathbf{i}_l} e_{j_l} \notin \Phi(t+T,t)$. However, the fundamental matrix can now be expressed in terms of (1.2.1) :

$$\Phi(t+T,t)\xi = \sum_{j=1}^{n} \xi_J \left(\sum_{\mathbf{i} \in Z_I^T} m_{\mathbf{i}}(a)(t) A_{\mathbf{i}} e_j \right) =$$

$$\sum_{j=1}^{n} \xi_j \sum_{l=1}^{L} \left(m_{\mathbf{i}_l}(a)(t) + \sum_{(\mathbf{i},j) \notin I_b} \Gamma_{\mathbf{i}j}^l m_{\mathbf{i}}(a)(t) \right) A_{\mathbf{i}_l} e_{j_l}$$

where the set $I_b = \left\{ (\mathbf{i}_1, j_1), (\mathbf{i}_2, j_2), \ldots, (\mathbf{i}_L), j_L \right\}$, corresponds to the base in V^T. From the fact that the $a_1, a_2, \ldots, a_I$ are difference-algebraically independent, it follows that there exists t such that for at least one this expressions holds

$$m_{\mathbf{i}_j}(a)(t) + \sum_{(\mathbf{i},j) \notin I_b} \Gamma_{\mathbf{i}j}^l m_{\mathbf{i}}(a)(t) \neq 0, \quad j = 1, \ldots, n. \tag{*}$$

Hence, there exists $\xi \in R^n$ such that

$$\sum_{j=1}^{n} \xi_j \left(m_{\mathbf{i}_l}(a)(t) + \sum_{(\mathbf{i},j)\notin I_b} \Gamma_{\mathbf{i}j}^l m_{\mathbf{i}}(a)(t) \right) = 1,$$

that is, $\Phi(t+T,t)\xi = A_{\mathbf{i}_l} e_{j_i}$, which is a contradiction.

We notice that there exists an infinite set of values t which satisfies the (*) expression.

On the other side, the expression

$$\sum_{\tau=1}^{T} \Phi(t+T,t+\tau)B(t+\tau-1)u(t+\tau-1) =$$

$$\sum_{\tau=1}^{T}\sum_{h=1}^{p} u_h(t+\tau-1) \sum_{j=1}^{J} \sum_{\mathbf{i}\in\mathbf{Z}_I^{T-\tau}} \delta^{\tau-1} b_j(t)\delta^{\tau} m_{\mathbf{i}}(a)(t) A_{\mathbf{i}} B_j e_h,$$

belongs to

$$\sum_{j=1}^{J}\sum_{\tau=0}^{T-1} \mathrm{Im}(V^{\tau}B_j) = \left\{ A_{\mathbf{i}} B_j u \; :\in R^p, j\in Z_J, \mathbf{i}\in Z_I^{\tau}, \tau\in Z_T \right\} \qquad +$$

Definition 1.1 We say that the system $(1.1.1)$ is T-horizon controllable to zero if it is controllable to zero in every time interval of length T.

Theorem 1.1 If the system $(1.1.1)$ is T-horizon controllable to zero, then

$$\mathrm{Im}V^T \subset \sum_{\tau=0}^{T-1}\sum_{j=1}^{J} \mathrm{Im}V^{\tau}B_j \qquad\qquad (1.2.2)$$

Proof. We suppose by *reductio ad absurdum* that $(1.2.2)$ is false. It follows from the previous lemma that there exists a t such that the rank of the matrix $\Phi(t+T,t)$ is the same as the dimension $\mathrm{Im}V^T$. This implies the existence of $\xi\in P^n$ such that $\Phi(t+T,t)\xi \notin \sum_{\tau=0}^{T-1}\sum_{j=1}^{J} \mathrm{Im}\left(V^{\tau}B_j\right)$. We have

$$\Phi(t+T,t)\xi = -\sum_{\tau=1}^{T}\Phi(t+T,t+\tau)B(t+\tau-1)u(t+\tau-1)$$

$$\in \sum_{\tau=0}^{T-1}\sum_{j=1}^{J} \mathrm{Im}V^{\tau}B_j$$

which is a contradiction. $+$

Remark 1.1 *We have that*:

a) The subspaces

$$\ldots \supseteq V^T \supseteq V^{T+1} \supseteq \ldots \tag{1.2.3}$$

form a descending chain. So, there exists $T_1 > 0$ such that

$$\ldots \supseteq V^{T_1} = V^{T_1+1} = \ldots$$

b) The subspaces

$$\ldots \subseteq X^t = \sum_{\tau=0}^{t-1} \sum_{j=1}^{J} \mathrm{Im} V^\tau B_j \subseteq \sum_{\tau=0}^{t} \sum_{j=1}^{J} \mathrm{Im} V^\tau B_j = X^{t1} \subseteq \ldots \tag{1.2.4}$$

form an ascending chain and, from this follows the existence of $T_2 > 0$ such that in (1.2.4), for $t \geq T_2$, we have equality.

From the above remark it can be concluded that for $T \geq T_1, T_2$ in (1.2.3) and (1.2.4) we have equalities.

Let $X \subset \mathrm{P}^{\,n}$ be a vector subspace, then,

$$V^t X = \left\{ Ax \,:\, A \in V^t, x \in X \right\}$$

We obviously have $\mathrm{Im} V^t = V^t R^n$.

Remark 1.2 If $T > 0$ is the same integer as above, then

$$\mathrm{Im} V^T = \mathrm{Im} V^{LT+t} \subset \sum_{\tau=0}^{LT+t-1} \sum_{j=1}^{J} \mathrm{Im} V^\tau B_j$$
$$= \sum_{l=0}^{L-t} V^{lT+t} \sum_{\tau=0}^{T-1} \sum_{j=1}^{J} \mathrm{Im} V^\tau B_j. \tag{1.2.5}$$

where this last term does not depend on $t = 0, 1, \ldots$ *and* $L = 1, 2, \ldots$

Suppose that X^T *is an* L*-dimensional subspace of* R^n *and consider this number* L *in the inclusion. Hence, we can choose a basis*

$$\left\{ A_{\mathbf{i}_1} B_{j_1} e_{k_1}, \ldots, A_{\mathbf{i}_L} B_{j_L} e_{k \left\{ A_{\mathbf{i}_1} B_{j1} e_{k_1}, \ldots, B_{j_L} e_k \right\}} \right| L \right\}$$
$$\subset \sum_{l=0}^{L-1} V^{lT} \sum_{j=0}^{m-1} \mathrm{Im} V^\tau B_j,$$

such that the lengths of the products $A_{\mathbf{i}_1}, \ldots, A_{\mathbf{i}_L}$ *denoted by* $\langle \mathbf{i}_1 \rangle, \ldots, \langle \mathbf{i}_L \rangle$, *respectively, satisfy the inequalities*

$$0 \le \langle \mathbf{i}_1 \rangle < T, \ T \le \langle \mathbf{i}_2 \rangle < 2T, \ldots, (L-1)T \le \langle \mathbf{i}_L \rangle < LT.$$

Let $\tau_l = LT + t - \langle \mathbf{i}_l \rangle$, $l = 1, 2, \ldots, L$. Define the control by $u(\tau) = 0$, if $\tau \notin \tau_1, \ldots, \tau_l$, and $u(\tau_{l-1}) = (0, \ldots, u_l, \ldots, 0)$, where (u_l) is embedded into the vector as the k_l-coordinate, and assume that $x(0) = 0$. Let us compute the final state

$$\sum_{\tau=1}^{LT+t} \Phi(LT+t, \tau) B(\tau-1) u(\tau-1) =$$

$$\sum_{l=1}^{L} \Phi\big(LT+t, LT+t-\langle \mathbf{i}_l \rangle\big) B(LT+t-\langle \mathbf{i}_l \rangle - 1) u(\tau-1)$$

$$\sum_{l=1}^{L} \sum_{\langle \mathbf{i} \rangle = \langle \mathbf{i}_l \rangle} \sum_{j=1}^{J} \delta^{LT-\langle \mathbf{i}_l \rangle} m_{\mathbf{i}}(a)(t) \delta^{LT-\langle \mathbf{i}_l \rangle - 1} b_j(t) A_{\mathbf{i}} B_j e_{k_l} u_l$$

Now, let us express $A_{\mathbf{i}} B_j e_{k_l}$ as a linear combination of the basis elements:

$$A_{\mathbf{i}} B_j e_{k_l} = \sum_{r=1}^{L} \mathop{\Gamma}_{\mathbf{i}, j, l}^{r} A_{\mathbf{i}_r} B_{j_r} e_r.$$

Let $I_{bas} = \{(\mathbf{i}_1, j_1, k_1), \ldots, (\mathbf{i}_L, j_L, k_L)\}$.

Then the final state is

$$\sum_{\tau=1}^{LT+1} \Phi(LT+t, \tau) B(\tau-1) u(\tau-1) =$$

$$\sum_{r=1}^{L} u_r \Bigg(\delta^{LT-\langle \mathbf{i}_r \rangle} m_{\mathbf{i}_r}(a)(t) \delta^{LT-\langle \mathbf{i}_r \rangle - 1} b_{j_r}(t) +$$

$$+ \sum_{(\mathbf{i}, j, k_l) \notin I_{bas}} \mathop{\sum_{\langle \mathbf{i} \rangle = \langle \mathbf{i}_l \rangle}}^{} \mathop{\Gamma}_{\mathbf{i}, j, l}^{r} \delta^{LT-\langle \mathbf{i}_l \rangle} m_{\mathbf{i}}(a)(t) \delta^{LT-\langle \mathbf{i}_L \rangle -} b_j(t) \Bigg) A_{\mathbf{i}_r} B_{j_r} e_{l_r}$$

$$= \sum_{r=1}^{L} P_r(a, b) A_{\mathbf{i}_r} B_{j_r} e_{l_r}.$$

The polynomials in difference $P_1(a, b), \ldots, P_L(a, b)$ are non-trivial. Hence their product is a non-zero polynomial in difference. The algebraic independence in difference of the sequences $a_1, \ldots, a_I, b_1, \ldots, b_J$ implies the existence of a

$t > 0$ such that $P_1(a,b)(t),\ldots,P_L(a,b)(t) \neq 0$ simultaneously. Hence the matrix formed from the columns

$$P_1(a,b)(t)A_{i_1}B_{j_1}e_{k_1},\ldots,P_L(a,b)(t)A_{i_L}B_{j_L}e_{k_L}$$

is of full rank. Therefore, the image space of the application

$$u = (u_1,\ldots,u_L) \mapsto (u(0),u(1),\ldots,u(LT+t-1)) \mapsto$$

$$\sum_{\tau=1}^{LT+i} \Phi(LT+t,\tau)B(\tau-1)u(\tau-1) = P_1(a,b)(t)A_{j_1}B_{j_1}e_{k_1}u_1 +$$

$$\ldots + P_L(a,b)(t)A_{i_L}B_{j_1}e_{k_L}u_L$$

is the subspace $\sum_{l=0}^{L-1}V^{lT}\sum_{\tau=0}^{T-1}\sum_{j=1}^{J}\operatorname{Im}V^{\tau}B_j$. *However*

$$\operatorname{Im}\Phi(LT+t,0) \subset \operatorname{Im}V^{LT+t} \subset \sum_{l=0}^{L-1}V^{lT}\sum_{\tau=0}^{T-1}\sum_{j=1}^{J}\operatorname{Im}V^{\tau}B_j$$

$$\sum_{\tau=1}^{LT+t}\Phi(LT+t,\tau)B(\tau-1)u(\tau-1).$$

This means that the system (1.1.1) is controllable to zero in the interval. Therefore we obtained the following theorem.

Theorem 1.2 Let us assume that the coefficients $a_1(t),\ldots,a_I(t),b_1(t),\ldots,b_J(t)$ are difference-algebraically independent. Then, if

$$\operatorname{Im}V^T \subset \sum_{\tau=0}^{T-1}\sum_{j=1}^{J}\operatorname{Im}V^{\tau}B_i,$$

holds then the system (1.1.1) is controllable to zero.

2. Reachability

Given the system (1.1.1)-(1.1.2) we define the *structural rank for reachability* as the value

$$\operatorname{MaxDim}\sum_{t=0}^{T-1}\operatorname{Im}\left(\sum_{\mathbf{i}\in\mathbf{Z}_I^{T-t}}\alpha_{\mathbf{i}}A_{\mathbf{i}}\right)\left(\sum_{j=1}^{J}\beta_jB_j\right), \qquad (2.1)$$

with respect to the parameters $\alpha_{\mathbf{i}}, \beta_j$. It is easy to see that if the structural rank is equal to r, then the rank of the subspace

$$\sum_{t=0}^{T-1} \mathrm{Im}\left(\sum_{\mathbf{i} \in \mathbf{Z}_I^{T-t}} \alpha_{\mathbf{i}} A_{\mathbf{i}} \right)\left(\sum_{j=1}^{J} \beta_j B_j \right) \subseteq R^n$$

is r a.e. in the space of parameters $\alpha_{\mathbf{i}}, \beta_j$.

We can define analogously the structural rank to observability

$$\mathrm{MaxDim}\sum_{t=0}^{T-1} \mathrm{Im}\left(\sum_{\mathbf{i} \in \mathbf{Z}_I^{T-t}} \alpha_{\mathbf{i}} A_{\mathbf{i}} \right)\left(\sum_{k=1}^{K} \gamma_k C_k^* \right) \qquad (2.2)$$

Theorem 2.1 Suppose that the time-varying coefficients $a_1(t), \ldots, a_I(t)$, $b_1(t), \ldots, b_J(t)$ are difference algebraically independent. Then, the system (1.1.1)-(1.1.2) is reachable over the time interval $[\tau, \tau + T] = \{\tau, \tau + 1, \ldots, \tau + T\}$ for infinite values of τ, if and only if the structural rank for reachability is (2.1) n. Similarly, if the time-varying coefficients $a_1(t), \ldots, a_I(t), c_1(t), \ldots, c_K(t)$ are difference algebraically independent, then the system (1.1.1)-(1.1.2) is observable over the time interval $[\tau, \tau + T]$, for infinite values of τ, if and only if the structural rank to observability (2.1), is n.

Proof. If there exist $\alpha_{\mathbf{i}}, \beta_j$ such that

$$\mathrm{MaxDim}\sum_{t=0}^{T-1} \mathrm{Im}\left(\sum_{\mathbf{i} \in \mathbf{Z}_I^{T-t}} \alpha_{\mathbf{i}} A_{\mathbf{i}} \right)\left(\sum_{j=1}^{J} \beta_j B_j \right) = R^n$$

then there exists an invertible $n \times n$-minor $M(\boldsymbol{\alpha}, \boldsymbol{\beta})$ of the reachability matrix, hence

$$Det M(\boldsymbol{\alpha}, \boldsymbol{\beta}) \neq 0.$$

Therefore, the difference polynomial

$$p(\ldots, a_{\mathbf{i}}, \ldots, b) = Det M(\ldots, \delta^t m_{\mathbf{i}}(a), \ldots, \delta^t b_j) \neq 0.$$

Hence, there exist infinitely many $\tau \in Z_+$, such that

$$n = \operatorname{Rank}M\left(\ldots, \delta^t m_{\mathbf{i}}(a(\tau)), \ldots, \delta^t b_j(\tau)\right) \le$$

$$\operatorname{Rank} \sum_{t=1}^{T} \left(\sum_{\mathbf{i} \in \mathbf{Z}_I^{T-t}} \delta^t m_{\mathbf{i}}(a)(\tau) A_{\mathbf{i}} \right) \left(\sum_{j=1}^{J} \delta^{t-1} b_j(\tau) B_j \right) \le n.$$

Thus, for these $\tau \in Z_+$ the system (1.1.1)-(1.1.2) is reachable over the time interval $[\tau, \tau + T]$. The second assertion of the theorem concerning observability follows from the duality between reachability and observability.

For the structural properties see [1], [3].

As a consequence of the above theorem we have the following application to bilinear systems.   +

Theorem 2.2 If the coefficients $c_1(t), \ldots, c_K(t)$ are difference algebraically independent, then the observability of the bilinear system

$$x(t+1) = \sum_{i=1}^{I} v_1(t) A_i x(t) + B(t)u(t),$$
$$y(t) = C(t)x(t) + D(t)u(t)$$

is also equivalent to the structural rank condition for the observability.

Proof. It suffices to choose the controls $v_1(t), \ldots, v_I(t)$ such that the family $v_1(t), \ldots, v_I(t), c_1(t), \ldots, c_K(t)$ is difference algebraically independent. +

Example 2.1 *The system*

$$x(t+1) = \begin{pmatrix} 0 & a_1(t) & 0 \\ -a_1(t) & 0 & a_2(t) \\ 0 & -a_2(t) & 0 \end{pmatrix} x(t) + Bu(t)$$

where

$$a_1(t) = 1, a_{1,}(2t) = 1, a_2(2t) = 0, a_2(2t+1) = 1.$$

We have for the products $A_1 A_2 A_1 = 0, A_2 A_1 A_2 = 0$, hence

$$x(2t+1) \quad = Bu(2t) + A_1 Bu(2t-1) + A_1 A_2 Bu(2t-2)$$
$$x(2t) \quad = Bu(2t-1) + A_2 Bu(2t-2) + A_2 A_1 Bu(2t-3).$$

This system has the memory of length 3. In order to have the reachability of the system we need the fulfillment of the rank conditions:

$$\text{MaxDim}(\operatorname{Im}\beta_1\beta + \operatorname{Im}\alpha_2\beta_2 A_2 B + \operatorname{Im}\alpha_{21}\beta_3 A_2 A_1 B)$$

$$= \text{Rank}\begin{pmatrix} b_1 & 0 & 0 \\ b_2 & b_3 & 0 \\ b_3 & -b_2 & b_1 \end{pmatrix} = 3, b_1 b_3 \neq 0$$

if $\beta_1, \beta_2, \beta_3, \alpha_2, \alpha_{21} \neq 0$, *the final time is* $2t$, *and*

$$\text{MaxRank}(\operatorname{Im}\beta_1\beta + \operatorname{Im}\alpha_2\beta_2 A_2 B + \operatorname{Im}\alpha_{21}\beta_3)$$

$$= \text{Rank}\begin{pmatrix} b_1 & 0 & 0 \\ b_2 & b_3 & 0 \\ b_3 & -b_2 & b_1 \end{pmatrix} = 2, b_1 b_3 = 0$$

if $\beta_1, \beta_2, \beta_3, \alpha_2, \alpha_{21} \neq 0$ the final time is $2t+1$. For example, if $b_1 b_3 = 0$, then the system is not reachable over any interval, due to the difference algebraic dependence of $a_1(t), a_2(t)$. The (non-difference) algebraic polynomial which vanishes at $a_1(t), a_2(t)$ is

$$a_1(t)a_2(t) = 0.$$

It is easy to show that if $a_1(t)a_2(t)$ are difference algebraically independent, then the maximal rank is 3 for all $B \neq 0$.

These results can be applied to observers design for time varying linear and bilinear systems with time dependent observer gain.

References

[1] F. Szigeti. *A differential-algebraic condition for controllability and observability of time-varying linear systems*, in Proc. 31st CDC of IEEE, Tucson, Arizona, 1992, 3088-3090.

[2] F. Szigeti. *Kalmas's rank conditions for infinite-dimensional time-dependent*, in Proc. EQUADIFF'91, Barcelona, Spain, 1992, 927-931.

[3] P. Fuhrmann. *On weak and strong reachability and controllability of infinite dimensional systems*, I. Opt. Theory and Appl. 9. 77-87, 1972

[4] F. Szigeti, F.J. Bokor and A. Edelmayer. *On the reachability subspaces of time varying linear systems*, in Proc. ECC'95, 2980-2985.

[5] Reinschke, K.J. *Multivariable Control - A Graph-theoretic approach*, Berlin, Springer-Verlag, 1988

Institute for Process Engineering

Professor Dr. János BEKE
Director of the Institute

Dear Reader,

On behalf of my colleagues in Institute for Process Engineering I would like to introduce the highlights of research activity from the year of 2009. The Institute for Process Engineering consists of three professional working areas as follows: Department of Automotive Technology, Department of Energetics, Department of Measurement Technology

Selected articles from the research activities represent the importance of energy-saving technologies, the relation between artificial technics and environment.

- Department of Energetics
  In the field of intensification of grain drying technologies: the efficiency of a drying technology depends on the technological and material properties. The microwave energy transfer theoretically is possible. But, by applying the experience coming from the industrial practice in the crop drying without a scrupulous investigation it may cause serious problem, because, the more complicated biological materials placed into microwave field behave differently compared to the industrial "dead" mass.
- Department of Automotive Technology
  Concerning the rolling resistance on terrain: one of the major sources of loss when a vehicle is traversing terrain – especially on soft soil – is rolling resistance. Researchers have usually examined the magnitude of the deformation of tire and soil during rolling under steady-state conditions. The unevenness of the terrain and the inhomogeneity of the soil give rise to substantial vertical vibrations, which change the magnitude of deformations, and thus rolling resistance. The effect of these vibrations must therefore be taken into account.
- Department of Measurement Technology
  Energetic aspects of hammer mill: comminution and grinding of cereals during animal feed processing needs a valuable energy consumption and therefore it has an important role in agriculture. The task of the process is to make the animal food with the proper size distribution at an optimal energy consumption. The performance of the conventional hammer mill equipped with frequency inverter was investigated with a complex and novel measuring system.

<div align="center">www.fomi.gek.szie.hu</div>

Limits and Possibilities for Intensification of Grain Drying Technologies

János BEKE

Department of Energetics,
Institute for Process Engineering

Abstract

The efficiency of a drying technology depends on the technological and material properties. However, the further development of conventional drying technologies in regards to economical and grain quality, is limited. By eliminating some typical problems of the usual convective drying method, the microwave energy transfer theoretically is possible. But, by applying the experience coming from the industrial practice in the crop drying without a scrupulous investigation it may cause serious problem, because, the more complicated biological materials placed into microwave field behave differently compared to the industrial "dead" mass. It seems that the internal temperature map of the drying material depends on the type of applied energy transfer, but the inner moisture distribution is the function of a morphological composition.

   In this study the above problems have been analyzed experimentally and some principles of convective and microwave drying have been derived.

Keywords

1. Introduction

The agricultural application of convective drying is under investigation worldwide, and it seems that we already know its most important influencing factors. In practice, a specific energy demand of convective drying in regards to acceptable costs cannot be decreased less than *3000 kJ/kg* of water. It seems there are several theoretical ways of reducing the drying energy consumption. One of the possibilities could be changing the method of energy transfer. A material-centric drying demands extra energy, and the improvement of the energetic parameters often raises questions about profitability. The problems of process analysis, of bringing these demands of opposite signs into accordance are caused by the fact that grains do not always behave according to the basic laws of heat and mass transfer. Theoretical process simulations, therefore, do not always converge to the practical tests.

2. Specifications of energy transfer methods

By analysing the applicability of the different energy transfer forms in grain drying, the following theoretical notes should be taken.

The conductive method looks disadvantageous for grain drying, because it would mean the use of a huge heating surface, which would result in a tremendous energy loss. The other problem is that the low conductivity factor of grains could make a heat transfer of very low efficiency possible.

As it is known that theoretically during *drying by radiation* the amount of transferred heat is directly proportional to the biquadratic of the applied temperature, and the energy transfer can be automated during the whole water removal process.

The possibility of drying grains by radiation is determined by the spectral optical features of the crop. This parameter of the kernel is also a function of its internal structure, its water control system and colour. The main feature of the grain is that – as a colloid capillary porous material – it responds differently to different wavelengths (Beke and Vas, 1994).

Microwave water removal can be realised principally by the fact that the object to be dried – due to its material properties – is an excellent dielectric material. The polarisation of the electrons – dipole as well as ionic – can be recorded in the crop bed placed into microwave field. One part of the electric power transforms into heat, which is appropriate for removing the superfluous water content of crops. In the case of an accurately controlled process, the two components of the water conductivity gradient (the diffusion as well as the thermo diffusion component) can be directed to be parallel with each other. This phenomenon helps to decrease the time of heating. Also, the advantage of the method is that it can be easily automated. However, it must be noted that the microwave drying of biological materials has a relatively short history, therefore it raises questions unanswered yet.

3. Modelling problems

The standard model of drying process
During the course of analysing the drying process, the basic question is whether the theoretical or the experimental description is the appropriate method to be followed. In the case of convective thick layer drying– as a typical diffusion type simultaneous energy and mass transport process – Fick's II. law should be used. But to solve it as a complicated problem, a number of initial and boundary conditions need to be prescribed; thus, theoretical formulas can be used in very simple cases only. Additionally, the properties of single kernels are quite different compared to those of grains stored in bulk.

The whole practical description of the drying process is quite popular and can provide information that serves well in practice, but – as a black box solution – it does not give any information in regards to the inner heat and mass transport.

In agricultural conditions, an intermediate solution, the so-called semi-empirical method, seems, perhaps, a usable tool.

If by any chance a uniform convective drying model is created, which should be pertinent for describing the dehydration process of several types of biological materials, it is quite evident that, by using the temperature (t) and the moisture ratio (Y) of drying medium as well as the temperature (Θ) and the moisture content (X) of drying material as dominant independent variables, the drying process of grains could be described mathematically.

This function is useful to characterize the microwave drying as well if the temperature of the drying medium is substituted with the special microwave performance (p).

To establish a basic model, it is useful to create an elementary volume inside the bulk, which – by its multiplication – is an adequate tool for simulating the whole drying zone. To derive the right formulas, the following parameters should be determined experimentally:

For the analysis of the convective drying process:

- The input properties of the drying medium (v_1–air velocity, ρ_1–density, t_1–temperature, h_1–enthalpy, Y_1–moisture ratio).
- The input properties of the drying material (m_1–mass, ρ_{m1}–density, X_1–moisture content, Θ_1–temperature).
- The output properties of the drying medium (v_2–air velocity, ρ_{12}–density, t_2–temperature, h_2–enthalpy, Y_2–moisture ratio)
- The output properties of the drying material (m_2–mass, ρ_{m2}–density, X_2–moisture content, Θ_2–temperature)
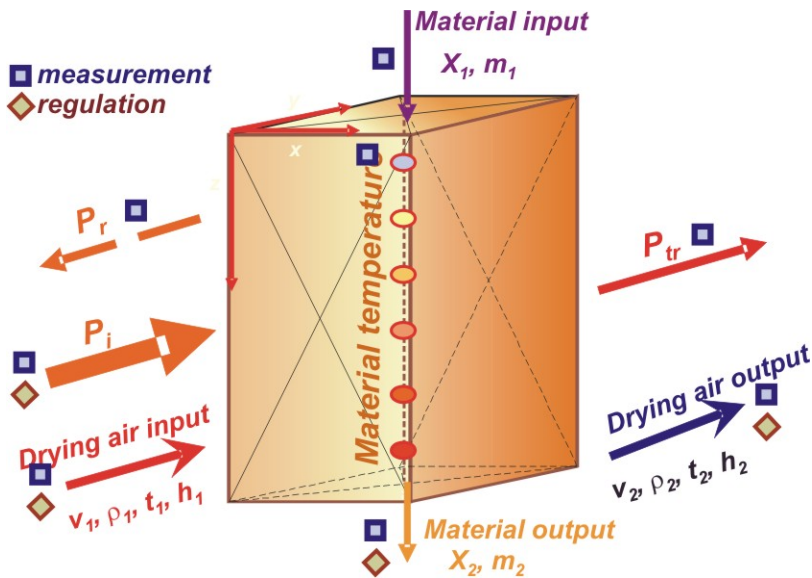- The values of the material temperature inside the elementary volume

Figure 1. A classical model of grain drying

The additional parameters for microwave drying experiments are:
– Incident microwave performance (P_i)
– Reflected microwave performance (P_r)
– Transmitted microwave performance (P_t) (depending on the setup construction).

In order to solve the basic equations, first the functions of density, the specific heat and the drying rate should be derived, for which the measure and/or regulation of parameters schemed in Figure 1. are needed.

In that case when the equality of the input and output enthalpy of drying air during microwave drying experiments is ensured, the microwave energy is used for drying only.

In order to solve the basic equations of the model for the whole drying zone, the block diagram showed in Figure 2 should be computerized.
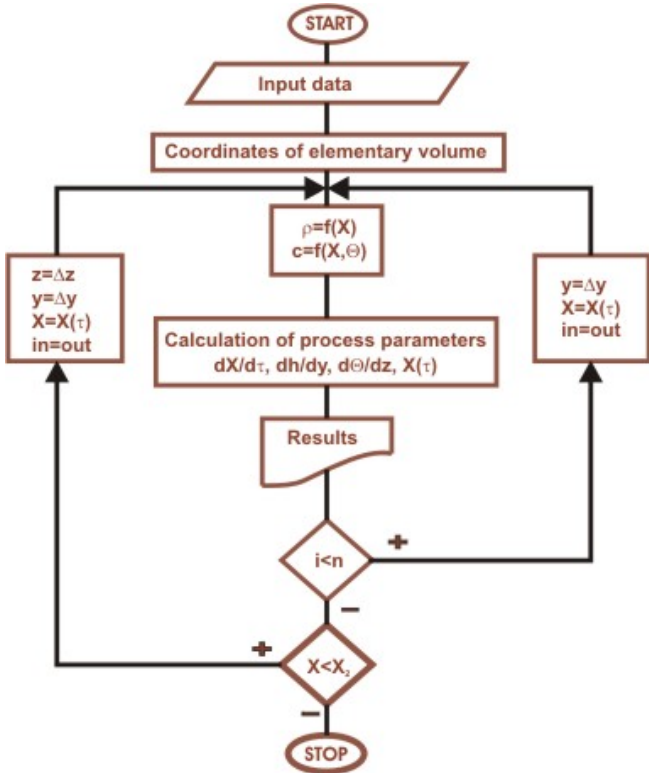
Figure 2. Block diagram for process simulation

The main considerations of convective grain drying

The simulation of the convective grain drying process depends – among others – on the relationship between the flow directions of the air and the material, but

from the aspect of the theoretical approach, there is a slight difference only between modelling the cross-flow, the counter-flow and the concurrent flow drying. Hence, the global modelling method will be introduced in the next few paragraphs through an empirical cross-flow model.

By applying the global type description, the drying rate is determined on the basis of the measured technological parameters. Using the temperature (t) and the humidity ratio (Y) of the drying air, as well as the temperature (Θ) and the water-content (X) of the drying material, the dewatering process can also be determined mathematically.

By analysing the process in the coordinate system in Figure 1, the heat balance of the drying medium can be described by the following equation.

$$\frac{dt}{dy}\left(c_{pa} + Yc_{pv}\right) \ 1 - \alpha(t - \Theta) = 0 \tag{1}$$

A rather rough description of the convective heat-transfer is possible by using the similarity theory or dimension analysis. For practical purposes, the Barker formula (1965) is appropriate to calculate the convective heat transfer coefficient (α) in the grain bed:

$$\alpha = Ac_{pa}l\left(\frac{2r_p l}{C + Dt}\right)^B \tag{2}$$

The values of the constants in S.I. units respectively are: A=0.2755; B=-0.34; C=0.06175; D=1.65·10^{-4}/.

To set up the heat balance of the drying mass, the temperature of the crop should be presumed to change during drying. Heat energy got into the crop-layer on the one hand increases the temperature of grains; on the other hand, it causes moisture motion as well as evaporation

$$\frac{d\Theta}{dz}\rho(X)V_m c(X,\Theta) + l\left[r_o + c_{pv}(t - \Theta)\right]\frac{dY}{dy} - \alpha \ (t - \Theta) = 0 \tag{3}$$

In order to solve the $\rho(X)$ function detailed, the standard investigation of grains in bulk has proved that change in bulk density during drying is the exponential function of the moisture content (Beke, 1992).

$$\rho = \rho_{(X=0)} \cdot K^X \qquad [\text{kgs/m}^3] \tag{4}$$

The exact value of K is given respectively by the quotient of the bulk densities at *X=1* and *X=0* of the moisture content.

$$K = \frac{\rho_{(X=1)}}{\rho_{(X=0)}} \tag{5}$$

For example, for shelled corn K=0,8.

It is known that the specific heat of materials with water content has an additive character. It is, therefore, possible to consider the specific heat as a function $c=f(\Theta,X)$, which gives a more precise solution. It has been proved by the use of detailed calorimetric methods that within the range of convective drying ($X=0.1$ to 0.6; $\Theta=0$ to $90\ ^{\circ}C$) the specific heat can be written in the form of the following equation (Beke, 1991.).

$$c = c_s + A \cdot X^a + B \cdot \Theta^b \tag{6}$$

For example, for shelled corn a=0,98, B=0,01, b=0,80.

The mass balance equation of the drying process can be derived by analysing the process of the water transport take place between the drying material and the air. Presuming a loss-free condition, the mass balance equation can be written as follows:

$$\frac{dY}{dy}1 - \frac{dX}{d\tau}V_m\rho(X)\tau = 0 \tag{7}$$

To solve Equation (7), the actual drying rate ($dX/d\tau$) must be known. While applying the empirical method, the drying rate is determined by the measurable parameters of the drying technology. The global function that describes convective drying more precisely is as follows (Beke and Vas, 1994) .

$$\frac{\partial X}{d\tau} = f(X_1, v, t, h_1) \tag{8}$$

The solution for the above function can be found by employing the so-called fixed parametric method, which means that, to guarantee the appropriate experimental conditions, only one parameter is allowed to change. By summarizing the partial results, the final drying rate equation is as follows (Beke 1992):

$$\frac{\partial X}{\partial \tau} = X^\alpha v^\beta \exp(vt - \mu Y_1 - \Gamma) \tag{9}$$

where $\alpha, \beta, \nu, \mu, \Gamma$ are constant for shelled corn 1.06, 0.50, 0.028, 3.0, 8.21 respectively.

Characteristic properties of microwave grain drying process

Depending on the moisture content of the material and the technological parameters, the drying rate is assumed to vary from zero to the vaporization rate of the free water surface rate determined by the energy input. For example, under microwave conditions, the vaporization rate of a free water surface-as a mass transport of global description- can be derived as follows by the means of the specific microwave performance (p), the specific heat (c_w), the temperature change ($\Delta\Theta$) of the water, as well as the latent heat (q_o):

$$\left(\frac{dX}{d\tau}\right)_o = \frac{p \cdot 60}{q_o + \Delta\Theta \cdot c_w} \quad \text{(kg/kg min)} \tag{10}$$

The well-known Gibbs–Helmholtz type enthalpy formula proves a direct relationship between the vapour pressure in the capillary and the absorption binding force. Furthermore, the relative partial vapour pressure ($\Phi = p_g/p_s$), as an independent variable, can be used for calculating the energy consumption of the water loss.

To calculate the relative vapour pressure as a function of the moisture content of the drying material, the following Clapeyron formula is useful to start with:

$$\frac{dp_g}{dT} = \frac{q_o}{(v_g - v_w)T} \tag{11}$$

From Equation (11) the following formula can be derived:

$$\ln p_g = \frac{q_c}{q_o} \ln p_s + C \tag{12}$$

In Equation (12), which is valid for isothermal conditions, q_c is the evaporation heat in the capillary and p_s marks the partial vapour pressure on the free water surface. In pursuance of Equation (12) in a logarithmic coordinate system, the p_g–p_s relation can be plotted as a straight line. Thus, the integer C can be eliminated because the two optional points of the line can be described by the following equation:

$$\frac{q_k}{q_o} = \frac{\ln p_{c2} - \ln p_{c1}}{\ln p_2 - \ln p_1} \tag{13}$$

By measuring the energy input as well as by drawing the drying kinetic curves, the vapour pressure on the material surface can be determined. The obtained specific partial vapour pressure helps to calculate the moisture content

value where the energy consumption of the drying process is equal to the evaporation heat of the free water surface ($\Phi=1$).

Equation (14) describes well the formation of the partial vapour pressure on the grain surface (Figure 3).

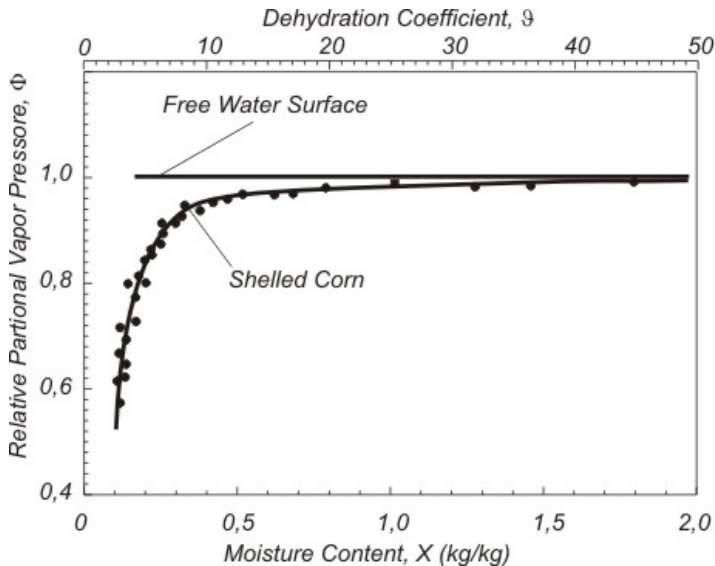$$\Phi = \frac{\delta X}{\delta X + e^{-\delta X}} \tag{14}$$

Figure 3. Change in relative vapour pressure on the surface of the drying material as a function of the moisture content

The course of the water loss procedure is frequently described by plotting the change in moisture ratio during drying. The moisture ratio – as it is known – does not allow comparing the dewatering process of the materials with the different initial moisture content. This problem can be eliminated by introducing the dehydration coefficient (ϑ) in the following relation (which can be considered as the analogy of the so-called Guhman's Criterion of heat transport):

$$\vartheta = \frac{X - X_e}{X_e} \tag{15}$$

We can see that, the dehydration coefficient (ϑ) is a considerably independent variable in the solution of the drying rate function. Because the drying rate as a function of the dehydration coefficient shows an exponential trend (Beke 1999), the drying rate can be calculated by Equation (10) with the following correction:

$$\frac{dX}{d\tau} = \frac{p \cdot 60}{q_o + \Delta\Theta \cdot c_w} \exp\left(-\frac{m}{\vartheta}\right) \tag{16}$$

In theory the value of energy factor (m) varies between zero and plus endless (Figure 4). When the value of specific energy consumption that is needed for drying is about the latent heat of water, *m* is nearly equal to zero. But coming to the end of drying process the value of m becomes extremely high indicating the exponentially increasing energy consumption. It has, therefore, a sort-property that depends on the morphological composition of the material to be dried.
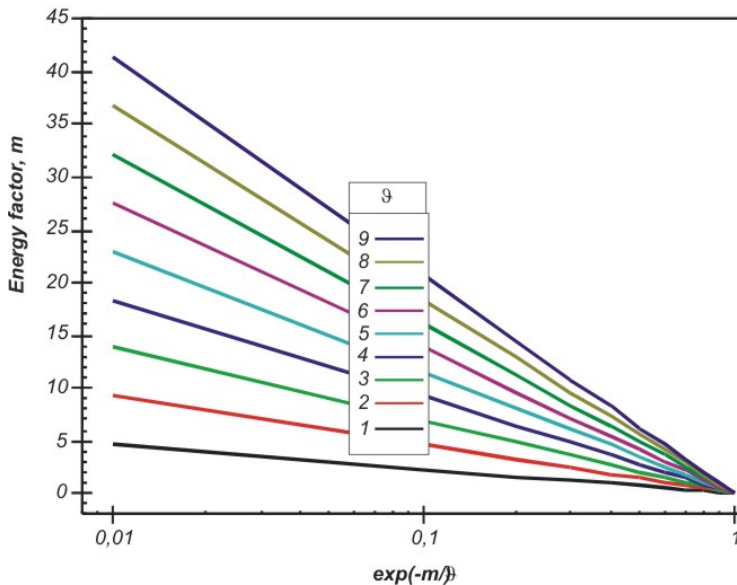
Figure 4. The m=f(ϑ) relation for shelled corn in the microwave field

It is evident that in the numerator of Equation (10) the input energy can also be calculated by different energy transport methods thus, the drying rate function can be made formally more uniform.

4. The roll of temperature and moisture content in drying process

Under convective conditions there is a quite close connection between the water loss procedure and the morphological composition of the drying material (Beke and Vas 1994). The intensity of the water loss is the highest near the germ. Coming to the end of the drying process and moving away from the embryo, the surface evaporation velocity tends to be zero in consequence of getting the effect of the confining layer of the kernel peel stronger (Figure 5).
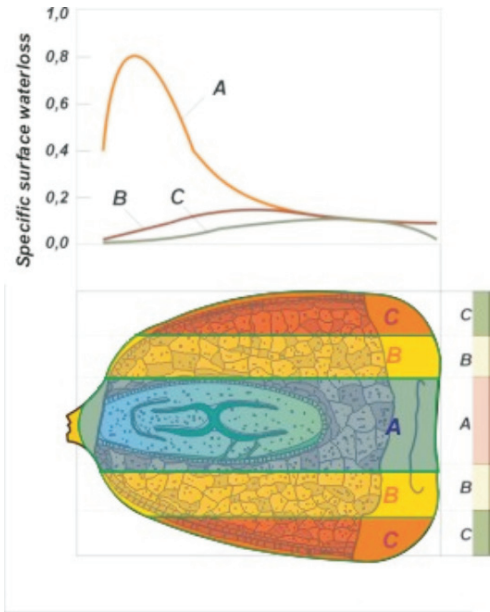
Figure 5. Surface water-loss distribution in shelled corn in the
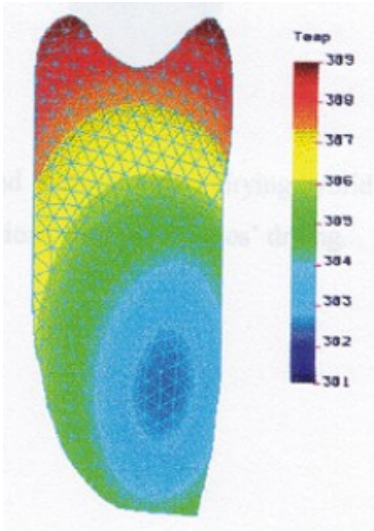case of convective heat transportation

*Figure 6.* The inner temperature map of the convectively dried maize kernel

The temperature values show a reverse distribution (Nemenyi et al. 2000) as compared to the moisture map (Figure. 6, 7). Since the evaporation has a significant cooling influence, the moister parts of the drying material remain at low temperature. Consequently, during the falling drying rate period - as the result of the relatively dried surface - local overheating and some mechanical

stress can occur. This phenomenon can be observed in the course of convective drying of any biological material.
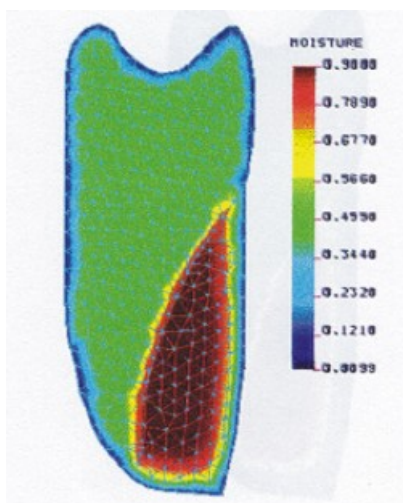
Figure 7. Moisture distribution in the convectively dried maize kernel

During microwave drying also, meaningful information can be obtained by testing the inner moisture content and temperature relations of the samples. As the experiments show, the initial uniform moisture distribution in the corn changes during drying, but the embryo remains the wettest part of the kernel all the time. (Figure 8). This phenomenon results from the internal structure and the basic function of the kernel. Since the biggest part of the seed, the endosperm, is for feeding the embryo, the main direction of the water flow points towards the embryo.
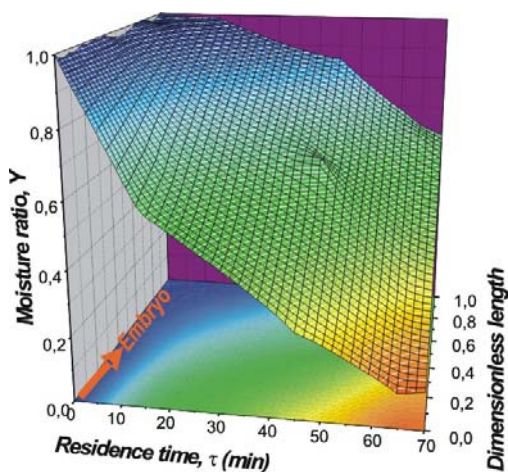
Figure 8. The internal moisture distribution of corn kernels in microwave field

The internal temperature distribution of shelled corn appears to show some anomaly at first sight, because, as in convective conditions, a temperature map of contrary character in relation to the moisture distribution would be expected. But in this case, the warmest point of the kernel is situated very close to the wettest area at the inner top of the embryo and its surroundings (Figure 9). This occurs, because the greatest intensity of the polarisation is established at the spot of the highest density of ions and polar molecules. Moreover, the low thermal conductivity of corn prevents fast heat propagation. Since the scale of polarisation remains at a low level in the dried components and the surface cooling effect is perceptible at the place of the highest moisture content, there is an almost homogenous inner temperature map. The biggest deviation of temperature is only a few °C.
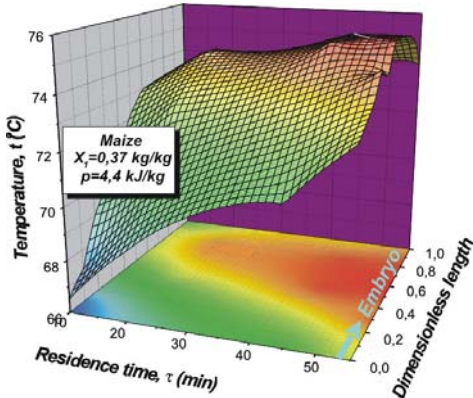
Figure 9. The inner temperature distribution of corn kernels in microwave field

By taking the phenomena mentioned above into consideration, furthermore, by regarding the costs of the two investigated energy resources, in theory, an efficient and economical drying process could be established as the Figure 10 shows.
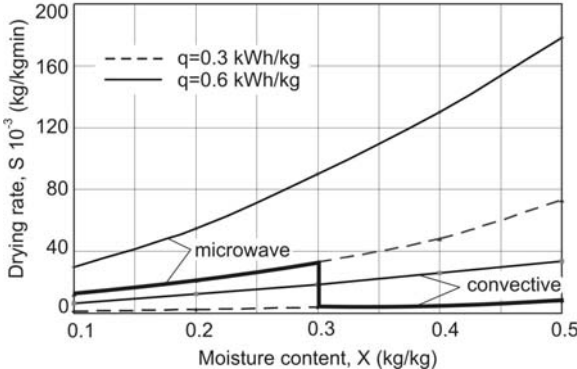

Figure 10. Theoretical drying process by combining the convective and microwave energy transfer

5. Closing remarks

To obtain an acceptable result, materials of biological origin need special drying technologies because not even a single kernel can be considered as an isotropic material of homogenous internal structure, which makes these organic materials more complicated due to the fact that the internal structure of bulks is a function of the factors affecting at the exact moment as the result of random events.

The specific microwave power is the driving force of the internal moisture movement, playing the same role in microwave conditions as what the air temperature does in the convective water removal process.

Inner moisture distribution is the feature of the material determined by the nature of the material to be dried and the internal temperature map of the drying material is a process parameter depending on the type of the energy transfer applied.

An appropriate combination of the convective and microwave energy transfer an economical and efficient grain drying technology could be developed.

Symbols

A, B, C: constants
T: absolute temperature (K)
X: the moisture content of the material (kg/kg)
$dX/d\tau$: Drying rate (kg/kg min)
V_m: the specific volume flow of the drying material (m^3/sm^2}
a,b: constants depending on the type of material
$c(X, \Theta)$: the specific heat of the grain (kJ/kgK)
c_s: the specific heat of the material with X=0 kg/kg and t=0 ^{o}C,
c_{pv}: the isobar specific heat of vapour (kJ/kgK}
c_{pa}: the isobar specific heat of air (kJ/kgK or Btu/IbF)
l: specific air flow rate (kg/sm^2, kg/m^{2}hr or Ib/ft^{2}hr)
n: number
p: specific microwave performance (W/g water)
p_g: partial vapour pressure in the capillary
p_s: partial vapour pressure on the free surface
q_o : water latent heat (kJ/kg)
r_p: equivalent particle radius (m or ft)
t: air temperature (^{o}C or ^{o}F).
x,y,z: coordinate axis
v_g, v_w : the specific volumes of vapour and water
t: the temperature of the drying air (^{o}C)
Φ: relative partial vapour pressure
ϑ: dehydration coefficient
Θ material temperature (^{o}C)

α: convective heat-transfer coefficient (W/m^{2}K).

α, β, ν, μ, Γ :constants

δ : constant, depending on the features of the material

$\rho(X)$: bulk density (kg/m^3}.

τ: Residence time (min)

Acknowledgement

References

Beke, J.: Testing the Specific Heat of Pioneer-type Maize Hybrids. Hungarian Agricultural Engineering. Gödöllö, Hungary. 1991. 4. 46-47. p.

Beke, J.: Some aspects of modelling convective corn drying. Drying Technology, New York, 1992. 5. 1317-1321.

Beke, J.: A szemes kukorica szárítási folyamatának elemzése. (Analysing the drying process of shelled corn) Bp., Akadémiai Kiadó, 1999. 113 p.

Beke, J.-Vas, A.: Testing the Drying Process of Shelled Corn on Aspects of Nutritional Quality and Thermal Efficiency. Drying Technology, New York, 1994. 5. 1007-1027. p.

Beke, J - Vas, A: Corn Drying as a Modelling Problem. Contemporary Agricultural Engineering. Novi Sad, Yugoslavia. 1996. 5. 7-10. p.

Beke, J. - Mujumdar, A.S. - Giroux, M.: Some Fundamental Attributes of Corn and Potato Drying in Microwave Fields. Drying Technology. New York, 1997. 15. 2. 241-252. p.

Neményi, M., Czaba, I., Kovács, A., Jáni, T. (2000) Investigation of simultaneous heat and mass transfer within the individual maize kernels during drying. Computers and Electronics in Agriculture. Vol. 26. pp. 123-135.

Components of Rolling Resistance on Terrain

Péter KISS

Department of Automotive Technology, Institute for Process Engineering

Abstract

One of the major sources of loss when a vehicle is traversing terrain – especially on soft soil – is rolling resistance. Many workers have attempted theoretical and practical definitions of this. They have usually examined the magnitude of the deformation of tire and soil during rolling under steady-state conditions. However, the magnitude of rolling resistance continually varies during motion. The unevenness of the terrain and the inhomogeneity of the soil give rise to substantial vertical vibrations which change the magnitude of deformations, and thus rolling resistance. The effect of these vibrations must therefore be taken into account.

   This paper reports a determination of rolling resistance components through field experiments designed to distinguish rolling resistance losses from other tire-soil interaction losses (slip). Soil and tire deformation losses were determined separately. The experiment involved measurement of vertical acceleration at the wheel center. The acceleration and mass data yielded the dynamic load $\Delta Q = m \cdot a$ which is superposed on the static weight of the vehicle and continually alters the magnitude of the soil and tire deformation and thus the rolling resistance. The test results permitted four components of rolling resistance to be determined. These are (1) soil deformation, (2) tire deformation, (3) the additional soil deformation caused by the dynamic load and (4) the additional tire deformation from the same cause. Tire deformation was responsible for 39% and soil deformation for 37% of rolling resistance in the experimental vehicle and soil conditions. The additional tire losses accounted for 5% of rolling resistance and the additional soil losses 8%. The remaining 11% of rolling resistance consisted of other – individually negligible – losses such as air resistance, which were not separately distinguished. The measurements were checked against energy (power) measurements from torque and speed sensors, and these confirmed the rolling resistance calculations.

Keywords

rolling resistance, rolling and deformation energy

1. Introduction

As a vehicle moves across terrain its wheels deform the soil and the tires themselves undergo deformation. The soil and tire deformations give rise to

energy losses which contribute to the as rolling resistance. Unevennesses in the terrain surface generate vertical vibrations, resulting in additional energy loss through the further soil and tire deformation caused by the vibration forces. The accepted view is that rolling resistance consists of two components: soil and tire deformation. This neglects the effects of vibrations, which are particularly prominent on terrain, where the resulting extra soil and tire deformation substantially increase rolling resistance. The objectives of the research reported here were to determine (1) the work expended on vertical soil deformation, (2) the tire deformation energy and (3) the additional soil and tire deformations caused by vertical vibrational acceleration, and to (4) break down the rolling resistance into components using the energy losses thus obtained.

Scientific investigation into wheel rolling resistance can be traced to Coulomb in the 19th century, and it has drawn the attention of many workers since then (important early studies: Bernstein 1913; Goryatchkin 1936; Bekker 1956) and continues to be of interest today. Rolling resistance may be understood as the torque of force N pushing the wheel by arm f running through the center line of the wheel. In field tests, to simplify measurement, the traction force required to draw the vehicle is given instead of the rolling resistance. The formulas usually applied to rolling resistance do not take account of vibration, and are thus true only for a completely smooth, homogeneous soil surface where vibrations are absent or negligible. If, however, the soil surface is inhomogeneous and/or not completely smooth, the rolling wheel must follow the surface variations, and this generates vertical vibrations. These vibrations are transmitted to the whole body of the vehicle, changing its potential and kinetic energy. The vibrations frequently cause considerable losses, forming part of the rolling resistance.

The motion of a vehicle over terrain is therefore basically a non-stationary process. The dynamic effects arise from the unevenness of the terrain profile, the inhomogeneity of the soil and – if the vehicle exerts a useful traction force – the dynamic changes of the traction force. Slip also produces a dynamic effect. All of these effects are of a stochastic nature, and the resulting vibrations are also random.

The vibrations also affect the tire-soil interaction, generating additional, non-static loads and therefore causing additional tire and soil deformation. The rolling resistance when moving across terrain is therefore the result of a dynamic process and constantly varies. The standard approach involves breaking down rolling resistance into the two components of tire and soil deformation. This breakdown may be retained, but further components are required to incorporate the tire and soil deformation caused by the dynamic change of load. It is possible to determined these components of rolling resistance.

2. Test equipment and procedures

Field traction tests with a tractor were carried out to determine the components of rolling resistance experimentally. The inflation pressure of the tire was varied

between 0.6 and 1.4 bar in steps of 0.2 bar. The soil type on the test plot was sandy loam, of density 2.7 g/cm³ (without air and water), 8% moisture content (on dry base) and 46.1% pore volume. The tractor had Michelin 540/65 R 26 X M 108 tires on the front wheels and 650/65 R 38 X M 108 on the rear. The gross vehicle weight was 6040 kg, with 2715 kg on the front axle and 3325 kg on the rear (as determined by weighbridge measurement).

2.1. Soil energy absorption

To independently determine the energy absorbed by the soil, it was necessary to measure the deformation of the soil. This was done using a terrain profilometer operating on the principle of communicating vessels. Each measurement section was profiled in the virgin and deformed condition. Profiles were relative to the same base surface, the difference giving the magnitude of the vertical soil deformation.

The soil in principle absorbs energy in the infinite half-space, but in practice this space must be restricted to finite dimensions. The deformation energy was therefore calculated from the measurable surface deformation, disregarding the compaction of the deeper levels of the soil Kiss, Laib (2005). The following relation gives the soil deformation energy:

$$W_s = A \cdot \int_0^z p(z)dz \qquad (1)$$

where A is the contact surface of the tire and soil, p the soil pressure, z the measured soil deformation.

2.2. Tire deformation energy

The tire deformation work was calculated using the formula:

$$W_a = \psi \cdot Q \cdot l \qquad (2)$$

where ψ is the rolling resistance factor for the tire (from the tire catalogue), $\psi = 0.04$; Q the wheel load and l the length of the contact surface.

2.3. Additional inertial force caused by vibration

The vertical accelerations set up inertial forces which cause additional tire and soil deformation. The work done in effecting these deformations shows up in the form of energy loss as the wheel turns. The additional dynamic force is superposed on the static wheel load $\Delta Q = m \cdot a$, where m is the mass acting on the wheel and a is the reference vertical vibrational acceleration measured at the center of the wheel, measured by an acceleration sensor. This dynamic increment causes additional energy losses in the soil and the tire.

2.4. Additional soil and tire deformation caused by vibration

The equivalent spring constant of the tire-soil interaction consists of the series-connected spring constants of the tire and the soil. The soil spring constant is determined from the pressure-sinkage relation. The force acting on the soil on the contact surface is:

$$F = \frac{k \cdot A}{D^n} z^n = c_{zs} \cdot z^n \tag{3}$$

where k is the coefficient of shape change of the soil; D the equivalent diameter of the soil-tire connection surface; c_{zs} the soil spring constant and n the soil dependent constant n=0.85.

   The work done on the soil by the dynamic force component is:

$$W_{ds} = c_{zs} \int_z^{z^*} z^n dz = \frac{c_{zs}}{n+1} \left(z^{*n+1} - z^{n+1} \right) \tag{4}$$

where z^* is the instantaneous sinkage caused by the wheel load plus the dynamic force component. The following formula was used to determine z*:

$$z^* = D \cdot \sqrt[n]{\frac{Q + \Delta Q}{A \cdot k}} \tag{5}$$

   A similar calculation may be performed for the work done in the tire by the load force plus the dynamic force component. The general relation between tire load Q and compression h is:

$$Q = c_{za} \cdot h^{1,2} \tag{6}$$

where c_{za} is the tire spring constant and h the static deflection (deformation) of the tire.

   The work done by the dynamic component may be calculated by the formula:

$$W_{da} = c_{za} \int_h^{h^*} h^{1.2} dh = \frac{c_{za}}{2.2} \left(h^{*2.2} - h^{2.2} \right) \tag{7}$$

where h^* is the instantaneous tire deflection caused by the wheel load plus the dynamic force component, and is given by:

$$h^* = \left(\frac{Q + \Delta Q}{c_{za}} \right)^{0,833} \tag{8}$$

2.5. Work done by the rolling resistance

The sum of the components of rolling resistance defined above (W_s; W_a; W_{ds}; W_{da}) was compared with the work done by the rolling resistance calculated from the experimental energy data obtained by continuous measurement in the tractor field test. The power component due to the rolling resistance, taken from the drawbar experiment data, yields the work done by the rolling resistance. The tractor's instantaneous speed of travel gives the time required to traverse the contact length, and the angular speed of the wheel gives the angular rotation of the wheel $\hat{\varphi}$ required to travel this distance. The rolling resistance work is:

$$W_r = \frac{P_r}{2\pi \cdot n_v} \cdot \hat{\varphi} \tag{9}$$

where P_r is the power dissipated by the rolling resistance (determined from the drawbar energy balance Kiss (2004)); and n_v is the rotational speed of the tractor drive wheel.

3. Results

Table 1 shows the initial data for calculating the rolling resistance components. These are: the tire pressure, the acceleration at the wheel center during the measurement, the coefficient of shape change of the soil, the tire spring constant, the tire deflection, the contact surface area and length, the wheel load and the soil sinkage. The data were determined by measurement or calculation from measurement.

Table 2 shows the tire and soil deformation work and the deformation caused by the increased load owing to vibration. This table also shows the deformation work increment owing to the additional load ΔQ.

The tire deformation work during the test varied between 126.1 and 188 J on the front wheel and between 362.1-448.4 J on the rear wheel. The tire deformation h^* resulting from the wheel load increased by the vibrations ($Q + \Delta Q$) was between 2.4 and 3.3 cm on both the front and rear wheels. The deformation work in the tire from the dynamic load component was 21.2-34.8 J at the front and 38.9-73.1 J at the rear wheel.

The soil deformation work varied over the ranges 86.5-303.2 J under the front wheel and 233.4-724 J under the rear wheel. The increased soil deformation z^* due to vibration varied between 1.9 and 5.6 cm at the front wheel and between

1.8 and 4.6 cm at the rear wheel. The work of the dynamic load increment ΔQ in the soil was 32.8-68.2 J at the front wheel and 49.3-124.4 J at the rear wheel.

Column 2 of Table 3 shows the rolling resistance work W_r calculated using the energetic data from the drawbar test, by formula 9. The third and fifth columns show the total deformation work ΣW_s ; ΣW_a under the front and rear wheels under wheel load Q. Columns 4 and 6 show the total deformation work on the soil ΣW_{ds} and the tire ΣW_{da} caused by the dynamic load increment ΔQ on the front and rear wheels. These four work components are summed in the seventh column, and the "remainder work" is given in the eighth column. This "remainder energy" is:

$$W_k = W_r - \left(\Sigma W_s + \Sigma W_{ds} + \Sigma W_a + \Sigma W_{da} \right) \qquad (10)$$

The "remainder work" (W_k) comprises additional losses not otherwise taken into account, such as the relative slip at the contact surface and the compaction work in lower strata of the soil. It also includes losses which are present but were omitted from the power balance, such as the inertial loss caused by instantaneous accelerations and decelerations in the direction of travel or the air/wind resistance, which was not measured but may have an effect.

The single-hatched area on Figure 1 represents the soil deformation work (including the work done by the dynamic force component) and the plain area the tire deformation work, also including the dynamic component. The cross-hatched area shows the other losses. Soil deformation thus accounted for a total of 45% of the rolling resistance, and tire deformation 44%. In this measurement, the remaining incidental energy was 11% of the total.

As a check, the rolling resistance was also broken down into components in terms of power loss. These are shown on Table 4.

The rolling resistance power P_g given in the table is derived from the power balance of the drawbar test. The power values for soil deformation and tire deformation P_s; P_a were obtained by applying the formula $P = \dfrac{W}{t}$ (where t is the time to traverse the contact length) to the work values for soil and tire deformation given in Table 2. The power dissipated by the vibrations in the soil (P_{ds}) and the tire (P_{da}) was obtained from the relation $P = W \cdot \omega$, where ω is the vertical vibration frequency. The sum of the power components is also less than the total power take-up by the rolling resistance. The explanation of the remainder power P_k is the same as that for the rolling loss work.

Table 1. Initial data for calculation of rolling resistance components
(indexes: 1. front wheel; 2. rear wheel)

Number of test	Tire inflation pressure [bar]	Vibration acceleration [m/s^2]	Coefficient of shape change of the soil [bar]	Tire spring constant [N/cm]		Tire deformation [cm]		Length of the contact surface [m]		Contact surface [cm^2]		Wheel load [kN]		Soil deformation [cm]	
	p	a	k	c_{za1}	c_{za2}	h_1	h_2	l_1	l_2	A_1	A_2	Q_1	Q_2	z_1	z_2
1.	1.4	1.05	5.355	3800	7600	2.3	2.2	0.329	0.470	1175	1764	10.37	19.26	4.6	2.7
2.	1.4	1.10	5.383	3800	7600	2.2	2.2	0.329	0.470	1175	1764	9.82	19.81	4.3	3.2
3.	1.4	1.80	12.91	3800	7600	2.2	2.2	0.329	0.470	1175	1764	9.70	19.93	1.5	1.2
4.	1.4	1.20	5.241	3800	7600	2.2	2.2	0.329	0.470	1175	1764	9.58	20.05	4.4	3.5
5.	1.0	1.05	7.870	3100	6100	2.7	2.6	0.389	0.512	1396	2034	10.21	19.42	2.6	1.7
6.	0.8	1.05	6.142	2800	5400	3.0	2.9	0.426	0.538	1535	2221	10.43	19.20	3.3	2.0
7.	1.2	1.15	5.700	3450	6850	2.4	2.4	0.357	0.490	1278	1885	9.83	19.80	3.8	2.9
8.	0.6	0.85	3.840	2600	5000	3.1	3.1	0.470	0.571	1701	2465	10.00	19.63	5.1	3.7

Table 2. Deformation and deformation work caused by additional load (indexes: 1. front wheel; 2. rear wheel)

Number of test	Tire deformation work [J]		Tire deformation increased by additional load [cm]		Work in tire from dynamic load component [J]		Soil deformation work [J]		Soil compaction increased by additional load [cm]		Work of dynamic load component in soil [J]	
	W_{a1}	W_{a2}	h^*_1	h^*_2	W_{da1}	W_{da2}	W_{s1}	W_{s2}	z^*_1	z^*_2	W_{ds1}	W_{ds2}
1.	136.5	362.1	2.5	2.4	22.3	38.9	283.6	552.4	5.2	3.6	68.2	87.7
2.	129.2	372.4	2.4	2.4	21.2	43.0	251.1	632.3	4.9	4.2	61.9	108.4
3.	127.7	374.8	2.5	2.6	34.8	73.1	86.5	233.4	1.9	1.8	37.5	71.1
4.	126.1	376.9	2.4	2.5	22.1	48.1	250.6	691.2	5.0	4.6	57.6	124.4
5.	158.9	397.7	2.9	2.9	25.6	47.4	157.8	338.7	2.9	2.2	32.8	49.3
6.	177.7	413.2	3.3	3.1	29.0	51.4	204.7	400.4	3.7	2.7	48.1	64.0
7.	140.4	388.1	2.6	2.7	24.1	49.1	222.1	566.7	4.4	3.8	57.7	102.8
8.	188.0	448.4	3.3	3.3	23.0	45.8	303.2	724.0	5.6	4.6	56.5	94.1

Table 3. Summary of components of rolling resistance work, also given (in brackets) as a percentage of rolling resistance work

Number of test	Rolling resistance work [J]	Rolling resistance components [J]				Sum of components]J]	Remainder energy [J]
		Soil deformation	Dynamic load work in soil	Tire deformation	Dynamic load work in tire		
	W_r	$\sum W_s$	$\sum W_{ds}$	$\sum W_a$	$\sum W_{da}$		W_k
1.	2270.0 (100%)	836.0 (36.8%)	185.2 (8.2%)	557.0 (24.5%)	70.7 (3.1%)	1648.9 (72.6%)	621.1 (27.4%)
2.	2675.0 (100%)	883.4 (33.0%)	196.8 (7.4%)	557.0 (20.8%)	73.2 (2.7%)	1710.5 (63.9%)	964.5 (36.1%)
3.	2703.5 (100%)	319.9 (11.8%)	124.7 (4.6%)	557.0 (20.6%)	122.8 (4.5%)	1124.5 (41.6%)	1579.0 (58.4%)
4.	2850.2 (100%)	941.8 (33.0%)	206.7 (7.3%)	557.0 (19.5%)	79.8 (2.8%)	1785.3 (62.6%)	1064.9 (37.4%)
5.	1699.6 (100%)	496.5 (29.2%)	92.5 (5.4%)	606.8 (35.7%)	81.2 (4.8%)	1277.0 (75.1%)	422.6 (24.9%)
6.	1630.3 (100%)	605.1 (37.1%)	124.7 (7.7%)	637.6 (39.1%)	88.1 (5.4%)	1455.5 (89.3%)	174.8 (10.7%)
7.	2282.3 (100%)	788.8 (34.6%)	182.1 (8.0%)	580.7 (25.4%)	82.1 (3.6%)	1633.7 (71.6%)	648.6 (28.4%)
8.	2094.5 (100%)	1027.1 (49.0%)	162.8 (7.8%)	676.7 (32.3%)	73.7 (3.5%)	1940.4 (92.6%)	154.1 (7.4%)

5. Conclusion

– The motion of a vehicle moving across terrain, owing to vibrations caused by the unevenness of the terrain profile and the inhomogeneity of the soil, is a dynamic process.
– The vibrations give rise to inertial forces which increase the extent of tire deformation and soil compaction, and thus the rolling resistance.
– The additional soil and tire deformations are proportional to the extra inertial forces caused by the vibrations.
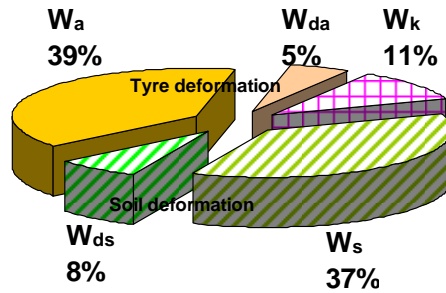
Figure 1. Components of rolling resistance (W_a tire deformation work, W_{da} work done on tire by dynamic load component, W_s soil deformation work, W_{ds} work done on soil by dynamic load component, W_k other additional losses)

Table 4. Rolling resistance components in power terms
$$(\Sigma P = P_s + P_{ds} + P_a + P_{da})$$

Number of test	P_r [kW]	t [s]	ω [s^{-1}]	Components				ΣP [kW]	P_k [kW]
				P_s [kW]	P_{ds} [kW]	P_a [kW]	P_{da} [kW]		
1.	5.85	0.387	8.0	2.16	1.48	1.44	0.57	5.65	0.20
2.	6.10	0.437	8.9	2.02	1.75	1.27	0.65	5.70	0.40
3.	7.00	0.385	15.4	0.83	1.92	1.45	1.89	6.09	0.91
4.	7.81	0.364	8.9	2.59	1.84	1.53	0.71	6.67	1.14
5.	3.73	0.454	7.3	1.09	0.68	1.34	0.59	3.70	0.03
6.	3.80	0.428	4.1	1.41	0.51	1.49	0.36	3.78	0.02
7.	4.85	0.469	7.0	1.68	1.27	1.24	0.57	4.77	0.08
8.	4.64	0.450	3.5	2.28	0.57	1.50	0.26	4.61	0.03

– Tire deformation was responsible for 39% and soil deformation for 37% of rolling resistance in the experimental vehicle and soil conditions. The additional tire losses accounted for 5% of rolling resistance and the additional soil losses 8%. The remaining 11% of rolling resistance consisted of other – individually negligible – losses such as air resistance, which were not separately distinguished.

– The measurements were checked against energy (power) measurements from torque and speed sensors, and these confirmed the rolling resistance calculations.

References

Bekker, M. G. 1956. *Theory of land locomotion. The mechanics of vehicle mobility*. Ann Arbour, The University of Michigan Press

Bernstein, R. 1913. *Probleme zur experimentellen Motorpflugmechanik.* [Experimental test of the mechanics of motor plough] Der Motorwagen Vol. 16

Goryatchkin, V. P. 1936. *Theory of Agricultural Machines* (in Russian) Moscow

Kiss, P. Laib, L. 2005. Energy Determination of Vertical Soil Deformation in Case of Tractor Wheels and Soft Soil. In: *Proceedings of the 15th International Conference of the ISTVS* p. 3B03/8, Hayama, Japan

Kiss, P. 2004. The tractor's performance balance under non-stationary conditions. In: *Book of Abstracts AgEng 2004 Conference Engineering the Future*, p. 352-353. ISBN 90-76019-258, D 2004/0277/4, Leuven, Belgium

Energy and Quality Performance Investigation of Hammer Mill

Péter KORZENSZKY, Károly PETRÓCZKI

Department of Measurement Technology,
Institute for Process Engineering

Abstract

Comminution and grinding of cereals during animal feed processing needs a valuable energy consumption and therefore it has an important role in agriculture. The proper quality of the animal food has an optimal grain size distribution. The task of the process is to make the animal food with the proper size distribution at an optimal energy consumption. The performance of the conventional hammer mill equipped with frequency inverter was investigated with a complex and novel measuring system.

Keywords

comminution of cereal, grinding, frequency inverter, measuring system [1, 2, 3, 4]

1. Introduction

The hammer mill is a conventional and widely used machine in animal feed processing. The theory and the practice of the energy consumption of comminution of the material – here generally cereal – has an important role on the one part of cost and the other part of the quality of the animal food. This paper deals with only a few technical and energetic aspects of the topic and the influence of the grain distribution to the animal organism doesn't belong to it.

2. Methods and materials

During early investigations the hammer mill could work at given and constant speed values. The aim of our research work were to analyse the performance of the hammer mill with continuous speed control. The main points of our investigations were the following:
- Investigation of grinding process in model experiments with using electric motor with frequency inverter and high-speed measuring system,
- investigation of the mechanical and electrical power requirement in different stages of grinding.

Test conditions
Experiments were carried out with a Zenit Junior hammer mill which is similar to widely used machines. Because of the perspicuity of the investigations and

measuring setups the measuring parameters i.e. the date, the parameter settings, the actual options of data recorders were coded in file names. The project contains the temperature of the laboratory, too. Certificated seed from the same supplier was used with constant parameters: species, grain size and moisture content. In addition to it, examination of the purity of the material was carried out by organoleptic inspection. Sample quantity was determined in 10 kilograms.

The experiments were carried out in laboratories of Process Engineering Institute, Faculty of Mechanical Engineering, Szent István University.

Measuring set-up
During the investigations the modified Zenit Junior hammer mill assembly was elaborated with a new high speed measuring system. There were two important examination fields in connection with our investigations. The first was tests with constant mill speed in steady state in according to the previous ordinary research works. The second was the investigation of the machine in unsteady state, which wasn't investigated before. In the unsteady grinding phase dynamic changes happen in relatively short time periods. In fast transient processes – which are transitions between two stationary states –, some measured variables may multiply their initial value and the measurement system should be able to make high resolution and precise measurements.
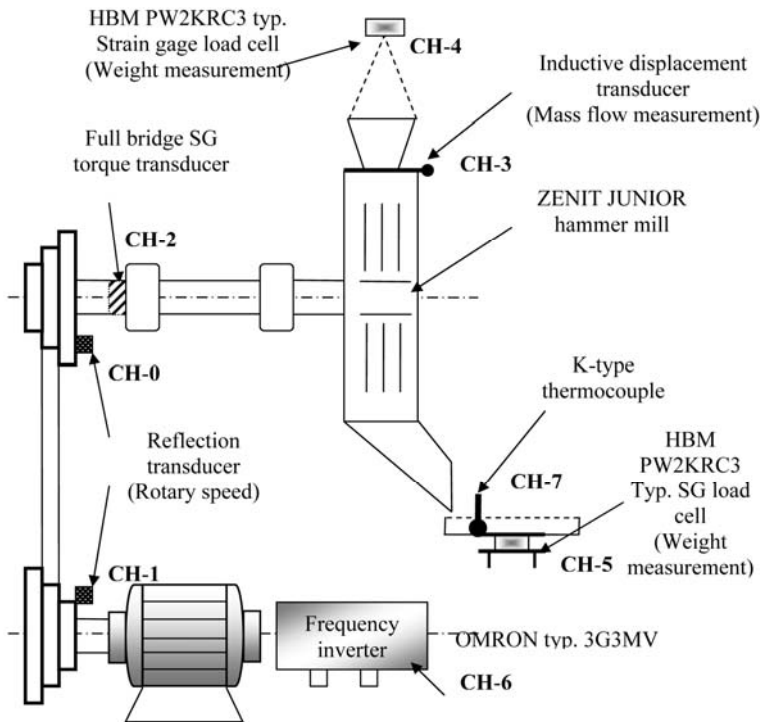
Figure 1. Block diagram of test bench mounted with frequency inverter and measuring sensors

A comparison of the unsteady state functions and the derived kinetic functions with steady state were the important aims of the research. This method is the basis of producing general and generalized characteristics. The diagram of the new experimental apparatus (Figure 1.) shows the new measurement system with indication of input and output parameters.

A frequency inverter which is fitted in performance and loading to the Leroy Somer (LS132ST) type asynchronous motor was chosen 5.5kW, 2900 RPM. With the help of the frequency inverter the speed can be controlled continuously. Due to the engine construction and some rational parameters, we limited the rotary speed value to a certain extent larger value than the nominal rotary speed (*3600* rpm at *60Hz*). The engine drives the shaft of the grinding machine through the V-belt transmission so 6500 rpm (99 m/s) can be reached in the grinding space.

The data gained from the sensors and transmitters were recorded with a SPIDER 8 data logger. The data logger's basic construction is applicable for simultaneous sampling of 8 separated channels. The first two channels (0 and 1) are applicable for receiving impulse-like quantities, the 6th and 7th channels are applicable for receiving transmitter universal output signals (*0-10 V, 4-20 mA)*. Bridges, half bridges and quarter bridges can be attached to the other channels. Fig. 2. shows the equipped grinding machine with frequency inverter, 8-channel data logger and a data recorder computer.

Figure 2. Zenit Junior hammer mill and the measuring system SPIDER 8 data recorder, Measurement Computer, Frequency inverter

Application of frequency inverter

For producing different hammer peripheral speed, an electric motor equipped with a frequency inverter was used. One of the analog output of the inverter was programmed to give the signal which is proportional with the power. This power signal was measured and recorded by Spiser8 PC measurement electronics. I In according to the instruction manual, the inverter's output frequency was limited the interval to *0-60 Hz.*, The electric motor cannot be driven at higher frequency without any damage. The maximal speed was limited to *3600 rpm* (*60Hz*).

With the application of frequency inverter, rotary speed changes could be made without stopping the equipment and mounting pulleys.

The picture of OMRON 3G3MV-A4055 typ. frequency inverter can be seen in Figure 3.

Figure 3. OMRON frequency inverter

During the investigation the following important parameters were measured: rotary speed of the hammer mill (n), torque (M), temperature of the material at the input and at the output of the hammer mill, input-output quantity of the material (m), throat size, input electric current (I), electric and mechanical power (P).

A HBM made SPIDER 8 data logger and the Catman v4.5 measurement software were used during the investigation. Table 1. contains the specification of data recorder channels and measured parameters.

Table 1. Specification of applied 8 channels

Channel number	CH 4	CH 5	CH 6	CH 7
Specification	Load cell (input material container)	load cell (output material container)	Frequency inverter	Thermometer
Channel number	CH 0	CH 1	CH 2	CH 3
Specification	Rotary speed (electric motor)	Rotary speed (mill shaft)	SG Torque transducer	Inductive displacement transducer (throat hole)

During data recording 50 Hz sampling frequency was used. One measurement contained approximately 5000 recorded data per channels. 40.000 data are altogether recorded and evaluated in one measurement repetition. Each measurement was repeated at least three times.

3. Results

Stationary operation

The mechanical power (P_{mech}) and the peripheral speed (v_{per}) shows a linear relation. Theoretically this means that, with increasing rotary speed, the power increases linearly. On the basis of measurement data, the conclusion is that there is a second degree connection between the hammer peripheral speed (v_{per}) and the power on the shaft of the grinding machine (P_{2mech}). X_{mean} particle size decreases proportionally with the rotary speed growth. In Figure 4., the specific energy requirement (E_f), power (P_{2mech}) and mean particle size (X_{mean}) can be seen as the function of hammer peripheral speed.
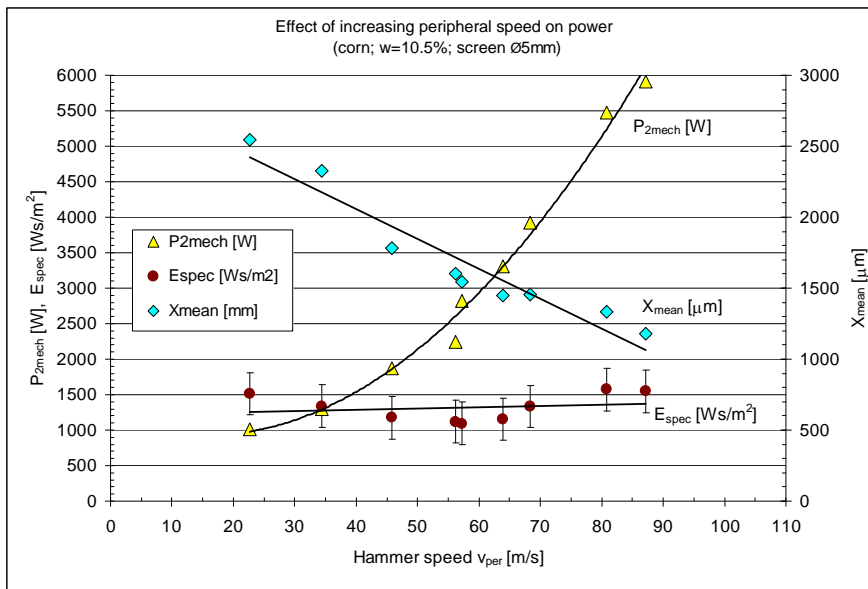
Figure 4. Mechanical power (P_{2mech}), specific energy requirement (E_f) and mean particle size ($X_{áltag}$) as a function of hammer peripheral speed

Non-stationary operation

The previous traditional examinations were dealing with the stationary steady state of grinding, because the important phases of grinding happen in these stages. The unsteady state is the phase of filling-up and discharge of the grinder happens. This transient phenomenon did not take part before in traditional grinding practice, because constant hammer peripheral state was assumed.

Unsteady state was avoided intentionally. In today's practice, we can define the adequate state of grits after finishing the grinding process, sampling and screen analysis for agro-technical requirements. If they are not adequate, they get back to the grinding process. This means that we work is repeated for our aim. Extension of constant interval with hammer peripheral speed changes and the examination of unsteady phase give us an opportunity to predict what will happen. With the usage of frequency inverter the transient phase can be lengthened if the technology needs so.

Relation of power and charge in non-stationary operation
In the unsteady phase at the beginning of charge formation, the speed of changes is the machine's own feature. The amount of charge depends on the hammer peripheral speed because a part of the grinding energy is produced by the hammer's beating. Increasing hammer peripheral speed needs more electric energy so higher power can be gained on the grinding machine's shaft. Different mechanical powers are connected to different hammer peripheral speeds. With changing peripheral speed, the charge and the mechanical power show a linear connection. The lines start from the origin, because the known no-load power levels were subtracted – offset compensation – from the measured performance values. On the basis of the graph, it can be seen that the slope of the lines varies as a function of peripheral speed. Figure 5. shows the change of mechanical power in function of charge growth in the case of different hammer peripheral speeds.
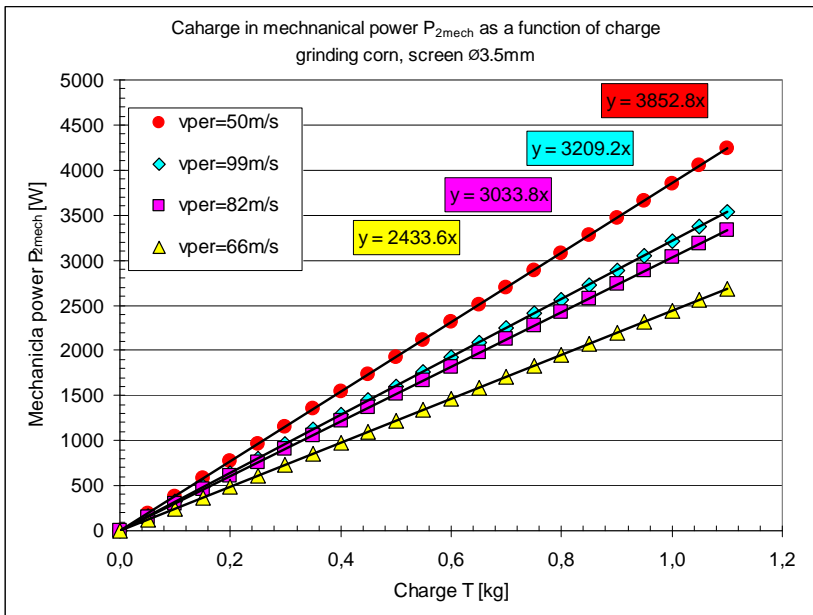
Figure 5. Mechanical power as a function of charge in the
unsteady phase of grinding

In the figure, the angular co-efficient of the line connected to hammer peripheral speed $v_{per}=50$ *m/s* is the greatest. Although one may predict that this should be the least. The grinding process finished safely at this rotary speed, but operating with this rotary speed is not economical. On lower rotary speed in the transient phase operating the grinding machine is not worth.

It can be stated that, in the transient phase of grinding in cases of different hammer peripheral speeds, there is a linear connection – starting from the origin – between the charge (T) and the mechanical power need (P_{2mech}).

4. Conclusions and suggestions

The new measuring set-up is not only applicable for reproducing traditional testing, but it is capable for the complex measurement of fast changing grinding processes.

This assembly can be adapted to all those systems where monitoring and controlling of hammer mills or similar machines are needed. The modular system structure is an advantage of the system.

The described system is capable to work in feed back control. In the future the analysis of dynamic relations with the application of the constructed measurement assembly – especially for avoiding working irregularities are recommended.

The electric motors completed with frequency inverters are applicable for the direct drive. With this, the transmission is simpler. Some machine parts such as V-belts, V-belt sheaves, tension roller can be left out of the traditional system. This may result in significant weight reduction in connection with actual machines.

It is a further advantage that the motor of the hammer mill is capable of starting at a load deviating from the nominal value so the particle size to be produced can be pre-defined. With usage of frequency inverter, the current peaks can be avoided which occur because of the traditional star-delta starting processes.

Acknowledgements

References

[1] Fogarasi L., Petrócki K., Judák E., Korzenszky P. (2008): (Comminution-kinetic and energetic foundation of automatic control of grinders), XXXII. Kutatási és fejlesztési tanácskozás az agrárgazdaság gépesítéséről (2008. január) SZIE Gödöllő ISBN 963-611-438-2, ISBN 963-611-439-0

[2] Korzenszky P. (2007): Effect of Hammer Speed on Particle Size Distribution in Hammer Mills, Hungarian Agricultural Engineering 20/2007, HU ISSN 0864-7410, 76. p., 51-52.p.

[3] Korzenszky P., Fogarasi L. (2009): Comminution of cereal feed components – new technological facilities, International Conferences in Agricultural Engineering, Synergy and Technical development is the Agricultural Engineering, Gödöllő, ISBN 978-963-269-111-4, 135.p.

[4] Korzenszky P., Judák E. (2005): Measurement Assembly for Energetic Analysis of Comminuters, Hungarian Agricultural Engineering, 18/2005, HU ISSN 0864-7410, 72-74.p.

Institute for Environmental Engineering Systems

Professor Dr. István FARKAS
Director of the Institute

Dear Reader,

The Institute for Environmental Engineering Systems consists of three departments as Department of Environmental and Building Engineering, Department of Physics and Process Control, Department of Logistics. There are several research activities going on falling into the interest of the departments. At the same time, they have interrelations in order to find new technical solutions which are appropriate to fulfil the environmental engineering requirements. That gives a strong opportunity for sustainable development and allowing the common way of approach in the solution of different nature of problems. That gives a basis to the research activities of the Institute.

Form the results of the research activity carried out in the framework of the Institute and its partner organizations in 2009 the following main topics are selected out to publish in the recent issues of the Journal of Mechanical Engineering Letters:

Solar energy applications:
  – Comparison of PV modules under different spectral conditions. From the spectral measurement a relation was determined between the higher red and infrared rate of the solar radiation versus the rate of the normalized energy production of the polycrystalline and amorphous silicon photovoltaic modules.

Heat and mass transfer:
  – Experimental and modelling poplar wood chip drying. The developed thermodynamic model of the drying process simulates the development of temperature and moisture content in bulks of the wood chips at different height in the dryer. This work was conducted by the honorary professor of the Institute.

Conveyor design:
  – Computing design parameters of vertical screw conveyors. It includes the interpretation and calculation of two important parameters of their design, namely the critical angular velocity and the conveying speed.

Spreading of grains and fertilizer:
  – The analysis of ballistic diagrams by throwing seed-corn and fertilizer grains horizontally. Using dimensionless variables a new relation was developed which enables the calculation of the throwing distance.

www.gek.szie.hu

Computing Design Parameters of Vertical Screw Conveyors

János BENKŐ

Department of Logistics, Institute for Environmental Engineering Systems

Abstract

Vertical screw conveyors are hardly mentioned in the home technical literature. They are very rarely applied in practice in spite of their many advantages. This presentation deals with the explanation and calculation of two important parameters of their design, namely the critical angular velocity and the conveying speed.

Keywords

1. Introduction

The home literature deals with the vertical screw conveyors unduly little and they are rarely used materials conveying equipments in spite of their several advantages. Their application advantages are the economy, small space need horizontally and vertically, flexible unloading possibility (the chute can be connected at any height and angle to the housing wall circumference) as well as the light structure. A drawback can be mention that the operation of the equipment needs the presence of friction. Therefore it is not recommended for conveying highly abrasive materials.

This study deals with two important operation parameters of vertical screw conveyors: the critical angular velocity (rpm) and the convey rate including their determination. In the theoretical investigations the motion of a single grain is analysed. It can be made because different experiments proved that the application of particle model results in negligible inaccuracies and the results can be generalised. It is especially worth to mention that the theoretical research verified the phenomenon that after a short acceleration period a steady-state material flow is evolved in the screw conveyor.

2. Methods

The equilibrium equations of the vertical screw conveyor for steady-state motion can be derived from the differential equation describing the actions in an arbitrary alignment screw conveyor of δ angle to the horizontal [1] by substituting $\delta = \pi/2$:

$$- g \sin \alpha - \mu_1 \frac{|\mathbf{B}|}{m} + \mu_2 \frac{|\mathbf{N}|}{m} \sin \beta = 0 \,, \tag{1/a}$$

$$\frac{|\mathbf{N}|}{m} = r\omega_0^2 - 2r\omega_0 \dot{\varphi}_r + r\dot{\varphi}_r^2 \,, \tag{1/b}$$

$$\frac{|\mathbf{B}|}{m} = g \cos \alpha + \mu_2 \frac{|\mathbf{N}|}{m} \cos \beta \,, \tag{1/c}$$

$$\sin \beta = \frac{\omega_0 \cos^2 \alpha - \dot{\varphi}_r}{\sqrt{\omega_0^2 \cos^2 \alpha - 2\omega_0 \dot{\varphi}_r \cos^2 \alpha + \dot{\varphi}_r^2}} \,, \tag{1/d}$$

$$\cos \beta = \frac{\omega_0 \cos \alpha \sin \alpha}{\sqrt{\omega_0^2 \cos^2 \alpha - 2\omega_0 \dot{\varphi}_r \cos^2 \alpha + \dot{\varphi}_r^2}} \,, \tag{1/e}$$

where
- r convolution radius,
- m mass,
- β angle between the vector of absolute velocity and the binormal unit vector,
- $\dot{\varphi}_r$ angular velocity of relative motion,
- μ_1 friction coefficient between the mass point and the convolution surface,
- μ_2 friction coefficient between the mass point and the housing,
- $\mathbf{B}$ constraint force on the spiral curve,
- $\mathbf{N}$ constraint force on the housing wall,
- ω_0 angular velocity of the screw conveyor axis,
- g acceleration of gravity.

It is noteworthy that the above system of equations is only formally different form those results published in papers [2], [3], [4], about conveying screw conveyors theory. In addition equations (1/c) and (1/e) are alternates rather than independent expressions.

Notations can be understood from the Fig. 1, where the line in angle α is the image of the evolved α angle helix in plane. In the figure $\mathbf{v}_k$ is the circumferential velocity ($|\mathbf{v}_k| = r\omega_0$) of the helix and $\dot{s}$ is the speed of the mass point relative to the helix ($\dot{s} = r\dot{\varphi}_r / \cos \alpha$), v is the absolute velocity of the mass point. $\mathbf{S}_1$, and $\mathbf{S}_2$ are the friction forces on the convolution surface and on the housing wall. The $\mathbf{t}$ and $\mathbf{b}$ vectors are unit vectors of trihedral coordinate system of surface. In this coordinate system unit vectors $\mathbf{t}, \mathbf{n}$ and $\mathbf{b}$ are pair-wise orthogonal.
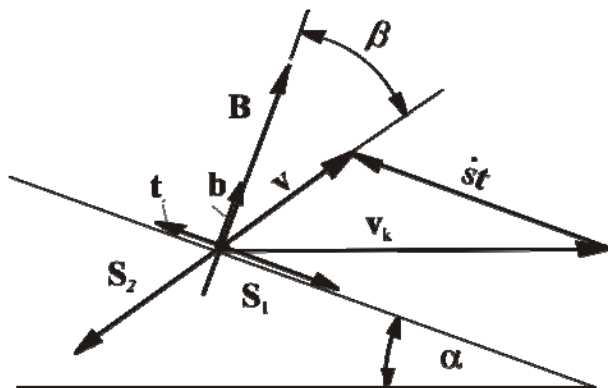
Figure 1. Velocity components of a mass point and the system of forces while the mass point is moving on the convolution surface

3. Result, discussion

Critical value of angular velocity

The conditions of the relative motion formation are a fundamental question of design. For the investigation the initial values $\dot{\varphi}_r(0) = 0$, $\mathbf{v}=\mathbf{v}_k$ and $\beta = \pi/2-\alpha$ belonging to the start time (t=0) are substituted into equation system (1). Then $\sin\beta=\cos\alpha$ and $\cos\beta=\sin\alpha$ hold. Therefore the equilibrium equations − after substitution − are

$$-g\sin\alpha - \mu_1 \frac{|\mathbf{B}|}{m} + \mu_2 \frac{|\mathbf{N}|}{m}\cos\alpha = 0 ,$$

$$\frac{|\mathbf{N}|}{m} = r\omega_0^2 ,$$

$$\frac{|\mathbf{B}|}{m} = g\cos\alpha + \mu_2 \frac{|\mathbf{N}|}{m}\sin\alpha .$$

It can be concluded from the first row that the mass point moves in the direction **t** only if value of the positive sign term which is proportional to the square of angular velocity ω_0 is higher than the sum of the absolute value of negative sign terms.

After arranging and substituting we will obtain:

$$-\frac{\sin\alpha + \mu_1\cos\alpha}{\cos\alpha - \mu_1\sin\alpha} + \frac{\mu_2 r\omega_0^2}{g} = 0 ,$$

and utilising the $\mu_1=tg\rho$ identity, we have:

$$\omega_0 \geq \omega_{0krit} = \sqrt{\frac{g}{\mu_2 r}\,tg(\alpha+\rho)}\;.\qquad(2)$$

Hence the critical angular velocity of screw conveyor axis can be computed if the geometry and friction coefficient data are available. Determination of the critical value is essentially important for the construction and design practice because it produces the minimal angular velocity below which value the conditions for the relative motion do not exist and the screw conveying is impossible. Consequently the initial data of ω_0 must be higher than the critical value. (It is mentioned that the developed formula expresses the same as the well known critical revolution speed relationship in the literature.)

Conveying capacity of vertical screw conveyor
For the determination of the capacity it is assumed that the material flows in concentric layers along helixes which have the same coil pitch and different radii. Utilisation of this means that one can determine the velocity of all grains if the magnitude and the direction of the velocity of a single particle is known. Moreover, since the axial displacement of the layers are the same in accordance with the assumption all the particles moves with the same speed axially (i.e. in direction z). In short, it is enough to determine the v_z velocity of a single particle to compute the z directional conveying capacity.

The conveying capacity:

$$Q = 3.6 A v_z \rho_h \phi \qquad [t/h],\qquad(3)$$

where
  – A conveying cross section [m^2],
  – v_z conveying velocity of material in the axial direction of screw conveyor (m/s),
  – ρ_h bulk mass density of conveyed material [kg/m^3],
  – ϕ loading (filling) coefficient.
The cross section of screw conveyor housing is $A = D^2\pi/4$, where D is the nominal diameter of the screw conveyor.

The conveying velocity
One can recognize in Fig. 1 that the axis of screw conveyor is perpendicular to the base of slope of angle α, so that the conveying velocity(v_z) is the vertical component of absolute velocity (**v**) which makes β angle to the binormal vector. As a result of the horizontal velocity component the path of the material is a helix of $\pi/2-(\alpha+\beta)$ coil pitch [1], [3].

The conveying velocity which decisively influences the conveying rate is interpreted as the axial component (v_z) of the absolute velocity (**v**). This is

$$v_z = \dot{s}\sin\alpha = \frac{r}{\cos\alpha}\dot{\varphi}_r\sin\alpha = r\dot{\varphi}_r \operatorname{tg}\alpha \text{, or} \tag{4}$$

$$v_z = \dot{s}\sin\alpha = r\omega_0\frac{\cos(\alpha+\beta)}{\cos\beta}\sin\alpha. \tag{5}$$

on the basis of Fig. 1.

According to the expressions (4) and (5) the determination of conveying velocity needs the knowledge of relative motion angular velocity ($\dot{\varphi}_r$) or the β conveying angle which characterise the direction of absolute velocity (**v**). They are computed from the algebraic equation system (1) by using a numerical procedure. On the basis of (1), (4) and (5) $v_z = v_z(\alpha,\mu_1,\mu_2,\omega_0)$, thus the conveying velocity is function of coil pitch angle, the friction coefficients and the angular velocity of screw conveyor. Due to the sophisticated implicit relationships, the computations need computer implementation.

The application software developed in our institute was elaborated primarily in order to compute conveying velocity. The program uses the revolution speed (n), nominal diameter (D), friction coefficients (μ_1, μ_2) and the s/D rate as input data from which the conveying angle (β) the angular velocity of relative motion ($\dot{\varphi}_r$) and the conveying velocity (v_z) are computed. In addition the software is applicable to make different analyses and to construct diagrams that assist the design.
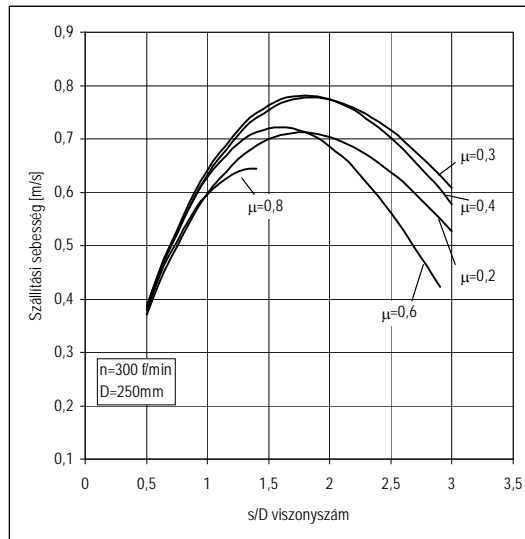
Figure 2. The conveying speed as function of *s/D* rate at different friction coefficients

As example Figs 2 and 3 are shown, where the conveying velocity curves are depicted as functions of *s/D* rate. In Fig. 2 the effect of friction coefficient can be analysed. The place of maximum of curves can be considered as optimal *s/D* rates, since the highest conveying velocities and rates belong to them which can be reached in the given conditions. The curves in Fig. 3 exhibit velocity functions for fixed friction coefficient (μ=0,6) and different revolution per minute values. Obviously, the character of curves is the same as those previously (Fig. 2) and as it was expected, the curves move upward with increasing revolution speed i.e. there are higher conveying velocities at higher rpm values.
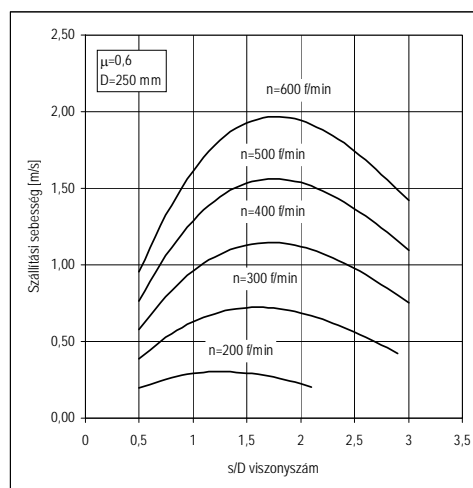
Figure 3. The conveying speed as function of *s/D* rate at different revolution per minute values

The design cannot change usually the friction coefficient, therefore the selection of the coil pitch angle and the proportional (*coil pitch/diameter*) rate, the angular velocity and the proportional revolution speed may result in the desired conveying velocity and the conveying rate. The diagrams similar to Fig. 2 and 3 can support this difficult course of decision-making.

It is noteworthy, that the results do not give a good account of the current design practice. It is well known that the design engineers choose the *s/D* rate around 1, which corresponds near computed optimum values at quite low rotation speed values (100... 200 rpm).

References

[1] BENKŐ J.: Particle model for description of operation of screw conveyors. Bulletin of the University of Agricultural Sciences, Volume 1, Gödöllő, 1995-1996.

[2] BÉLAFALI J.: Függőleges szállítócsigák. A+CS, 27. évf. 6. sz. 1982.

[3] BÖ'TTCHER, S - GABLER, H.: Untersuchungen zur Antriebsleistung - berechnung senkrechter Schneckenförderer Fördern und Heben 32. 1982. (6).

[4] RADEMACHER, F. J. On the Characteristics of vertical screw conveyors for free flowing bulk material. VDI-Forschungsheft 592, VDI-Verlag, Düsseldorf, 1979.

[5] THÜSING, H. - FINK, M.: Die Förderschnecke als stetiger Senkrechtförderer für Schütt- und Stückgut. Fördern und Heben, 1958. (5).

[6] VIERLING, A - EPHREMIDIS, CH.: Untersuchungen zum Fördervorgang bei waagerechten Senkrechtförderer. Fördern und Heben, 7. k., 1957. (9).

Comparison of PV Modules Under Different Spectral Conditions

István SERES[*], István FARKAS[*], Ivett KOCSÁNY[*],
Philipp WEIHS[**]

[*]Department of Physics and Process Control, Institute for Environmental Engineering Systems
[**]Institute for Meteorology, University of Natural Resources and
Applied Life Sciences

Abstract

During the more than 4 years of operation of the 10 kWp PV system installed at the Szent István University, sufficient amount of data were collected to start analysis of the system operation. There are two types of photovoltaic modules installed in the system: amorphous (DS – Dunasolar) and polycrystalline (ASE – RWE Schott) silicon ones. As the energy production of the different technologies is measured separately, such data give the basis to the analysis.

From the long time analysis of the power distribution a seasonal change can be recognized in the rate of the energy production of the ASE and DS modules. The rate of the normalized energy production was used for the analysis. As the effect is partly considered to the spectral dependence of the PV modules spectral measurements were carried out for a period in the autumn of 2009. In this paper the results of the spectral measurements were compared for the power of the same period in order to get relationship between them. From the spectral measurement a relation was determined between the higher red and infrared rate of the solar radiation versus the rate of the normalized energy production of the polycrystalline and amorphous silicon photovoltaic modules.

Keywords

PV system, energy production, spectral measurement, spectral dependence

1. Introduction

Among the solar energy application possibilities the solar PV systems can be a great help in reducing the consumption of traditional energy resources.

By implementing PV modules, the most important is to reach the best efficiency under different circumstances.

The performance of a photovoltaic unit depends on yield of energy production. In view of this, it is now becoming essential to look into various aspects of the PV energy conversion into electric energy form that is suitable to drive the electric loads. When sun shines on the PV array produced DC

electricity, without any emissions, and environmental impact or contamination. The DC power is converted to AC power with an inverter and can be used to power local loads or fed back to the utility. The PV application can be grouped in three types it is depends on the scheme of interaction with utility grid: stand alone, grid connected and hybrid (Stuart et al, 2007). The main PV installation in Szent István University, Gödöllő, Hungary is a grid connectied system.

2. System description

On the campus of the Szent István University, Gödöllő, Hungary a 10 kWp photovoltaic system was constructed. The system was installed (on 8th October, 2005) on the flat roof of a student hostel building of the campus. The azimuth angle is 5° to East and the tilt angle is 30°, which is a good yearly average value for the site. The system has three different subsystems, two identical parts of 3,1 kWp from amorphous silicon DS40 modules (Dunasolar Ltd.), and a 3,5 kW part of ASE100 modules from polycrystalline (RWE Solar Gmbh) technology. Every subsystem uses a separate inverter (Sunpower SP3100/600 and SP2800/550), through which the produced energy is converted to the 230 V, 50 Hz electrical grid.
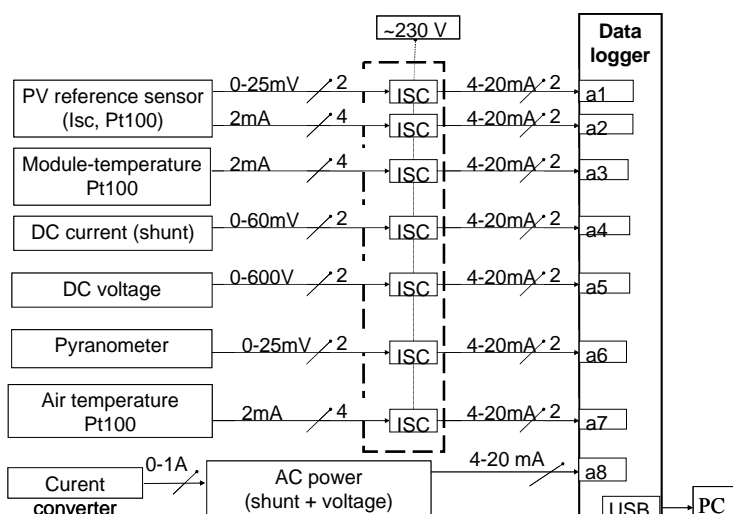
Figure 1. The input quantities of the data logger system

This set up was the largest PV installation (the total power is 9,6 kW) in the country untill the last year. It was designed for at least 25-30 year life time (for example the solar panels have 20-year power warranty). The estimated annual amount of energy produced is about 10 000 kWh, depending on the weather. During first four year of operation this value was 40 119 kWh. As the system has three (but two identical) subsystems, an important question was how the

system energy production is shared among the different subsystems (Seres and Farkas, 2007).

The four year of operation produced fairly enough data for the comparison of the subsystems. From the literature it can be known, that the modules with different technologies are working in different way under various meteorological (mainly on radiation and temperature) conditions. The quantities measured are *the irradiation* (in the panel plane by a silicon reference sensor, and the total radiation by a pyranometer), *the temperature* (environmental and module temperatures, for each type, by Pt100 sensors), *PV array* (DC) voltage, current and *power* and the *AC* voltage, current, *power* and energy supplied to the *electrical grid*. The measurement of the key quantities was carried out by a PC based data logging system. The connection of the analog input channels with the description of the measured quantities are shown in Fig. 1 (Seres and Farkas, 2009).

Besauce of the big distance between the data logger computer, and the measurement points (inverter room and sensor connection boxes), signal converters were installed to the system in order to serve as an amplifier. The signal converters (ISC – isolated signal converter) transform all different output signals of the sensors (e.g. different voltage levels) to 4-20 mA signal, what is sent to the AD converter unit of the data logger PC.

3. Analysis of the energy production

Beside the energy production of the total system the production of the subsystems were also measured continuously and separately.
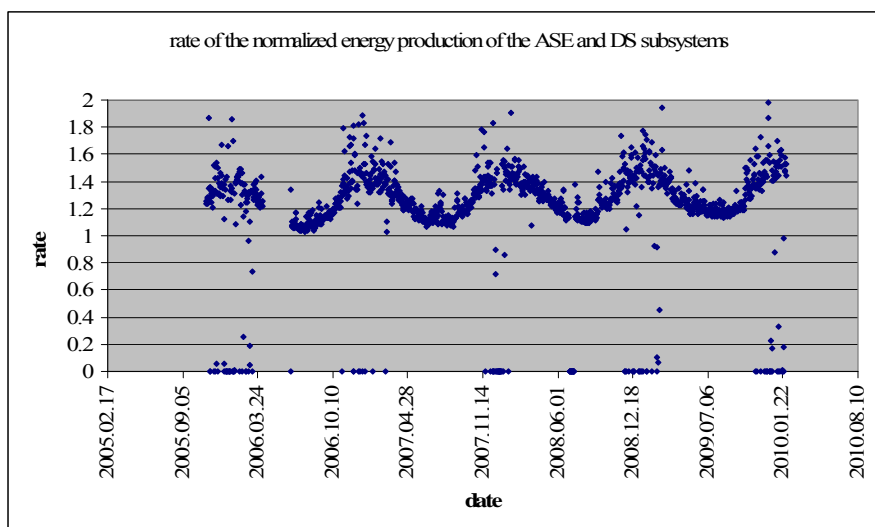
Figure 2. Rate of energy production of polycrystalline
vs amorphous

From the daily power distribution of the different subsystems it can be seen, that DS subsystems are working almost exactly the same way, and the power of the ASE subsystem is higher. From these data the comparison of the energy production of the different module technologies under different meteorological conditions were investigated. During the analysis the normalized energy production (the energy production divided by the nominal power – so the energy production of a 1 kWp unit) was used because of the different nominal power of the subsystems.

The measurements show a seasonal effect in the rate of the polycrystalline versus the amorphous subsystems normalized energy production. During winter period is about 20% higher than in summer period (Fig. 2).

4. Spectral measurements

In the framework of a common project between the Vienna University of Natural Resources and Applied Life Sciences (BOKU) and the Szent István University, Gödöllő (SZIUG) an MS-170 type of spectrometer of the BOKU was installed in Gödöllő for a period of two months.

Figure 3. The used spectroradiometer
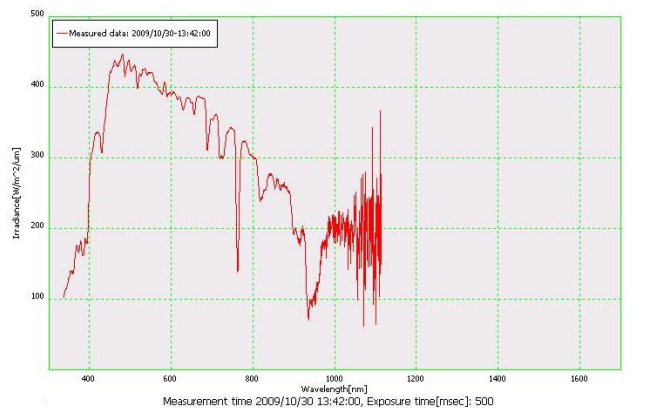
Figure 4. Spectral measurement on 30. 10. 2009

The used spectrometer (Fig. 3) can measure the power distribution of the solar spectra by nanometer resolution, in the range of 360-1100 nanometers. The sensitivity is 1 W/m^2/nm. As the measured values were uselessly noisy above the 930 nm range, they were omitted during the analysis.

The spectral data of the incoming radiation was saved in every minute from the middle of September to the beginning of November. For example, a measured spectra is shown in Fig. 4.

5. The analysis of the spectral data

To separate the useful range of the spectra of the incoming radiation classification was used based on the traditional physical wavelength ranges. The used classification can be seen in Table 1 as follows.

Table 1. The used spectral ranges

Range	Wavelength
Infrared	above 780 nm
Red	640 - 780 nm
Orange	600 - 640 nm
Yellow	570 - 600 nm
Green	490 - 570 nm
Blue	430 - 490 nm
Violet	380 - 430 nm
Ultraviolet	below 380 nm

As an example for the classification for a given day is shown in Fig. 5.
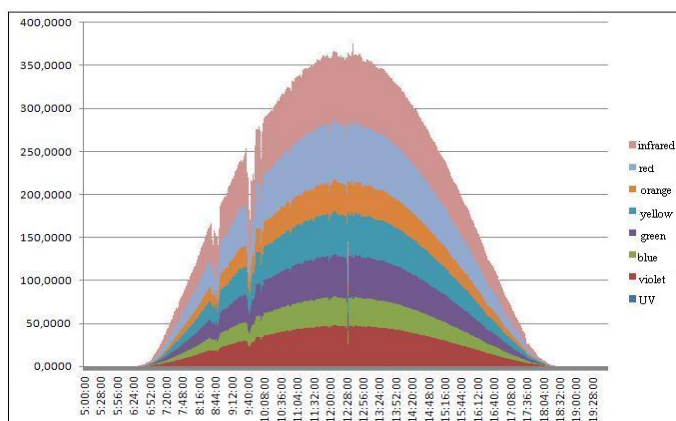
Figure 5. Classification of the incoming solar radiation
on a sunny day (21. 09. 2009)

Based on such observation data analysis was elaborated for understanding the behavior of different technologies. From the measured data the energy production data under low radiation (morning and evening hours, cloudy days - it can be seen on Fig. 6) were analyzed separately from the data under high radiation conditions.
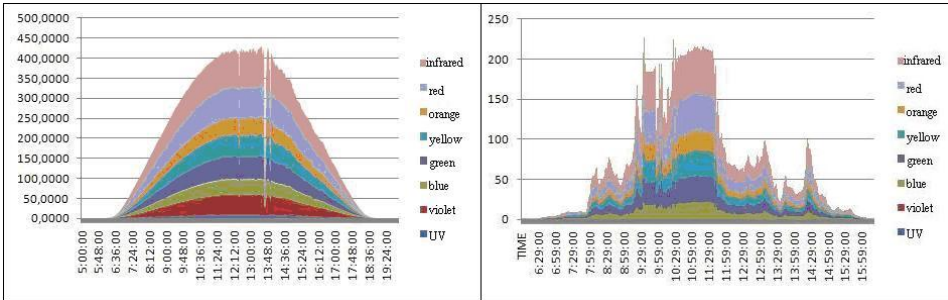
Figure 6. Spectra of a cloudy and a sunny day

From the spectrometer data of the days indicated in Fig. 7 were used for the further analysis.
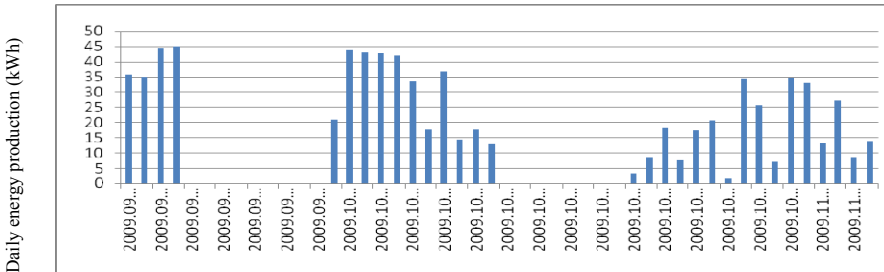
Figure 7. Energy production of the PV system during the days of analysis
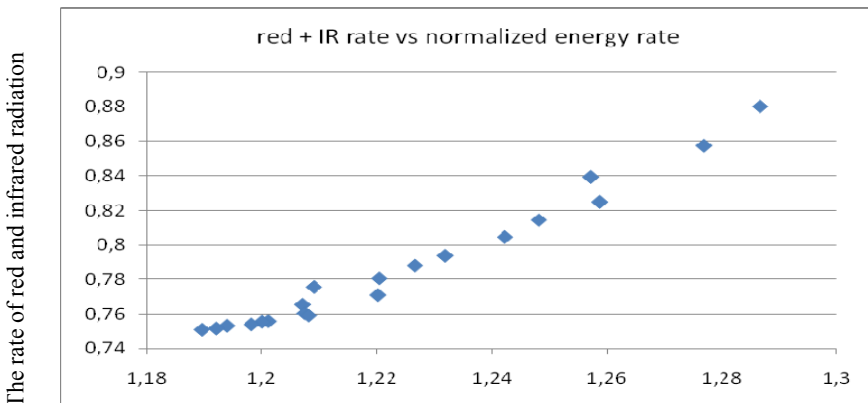
Figure 8. Comparison of red and infrared radiation rate to ASE/DS normalized energy production rate for 04. 10. 2009

During the analysis it was presumed, that the red and infrared range of the solar radiation is more important than the rest. To check this the rate of the power of the red and infrared radiation compared to the other ranges was determined for every minutes, and it was averaged to 10 minutes time intervals (as the energy data are available for 10 minutes averages as well). For sunny days the rate of the red and infrared radiation was compared to the rate of the ASE/DS normalized energy production for what an observable relation was determined, as it can be seen in Fig. 8.

From the graph it can be seen that higher ASE/DS rate occurs for higher red and infrared rate in the solar radiation. To check the stability of the effect more days were analyzed the same way (Fig. 9).
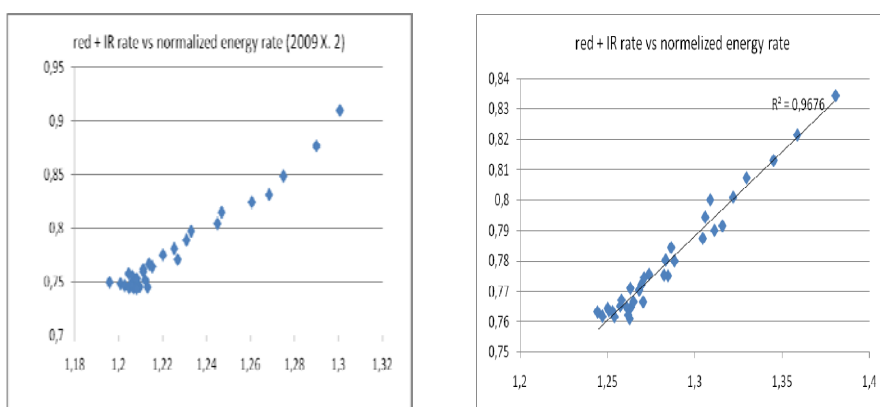
Figure 9. Comparison of red and infrared radiation rate to ASE/DS normalized energy production rate for different days
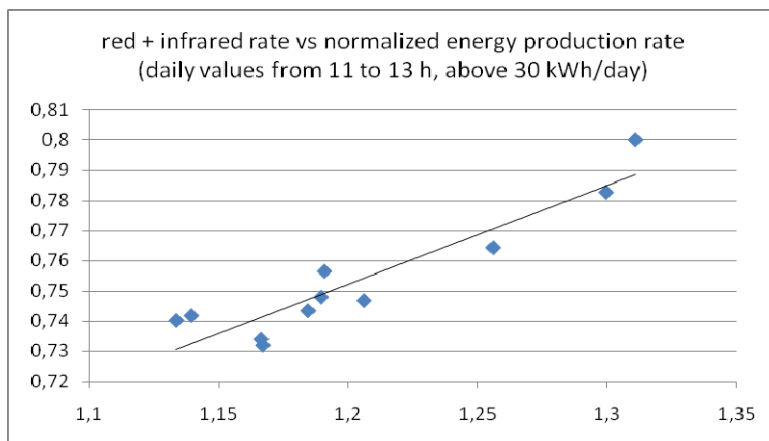
Figure 10. Comparison of red and infrared radiation rate to ASE/DS normalized energy production rate for sunny days (daily average data from the period of 11 to 13 hours, when the total energy production is above 30 kWh/day)

The analysis was performed separately for the sunny, partly sunny and cloudy days. From the graphs in Fig. 8 and Fig. 9, the data of the sunny and partly sunny days can be seen.

Each dot represents a daily average data for the period of 11 – 13 hours (earlier and later – mainly in November – the radiation data were quite low to cause higher measurement errors). For the dark cloudy and for the morning – evening periods the data did not show reliable relation.
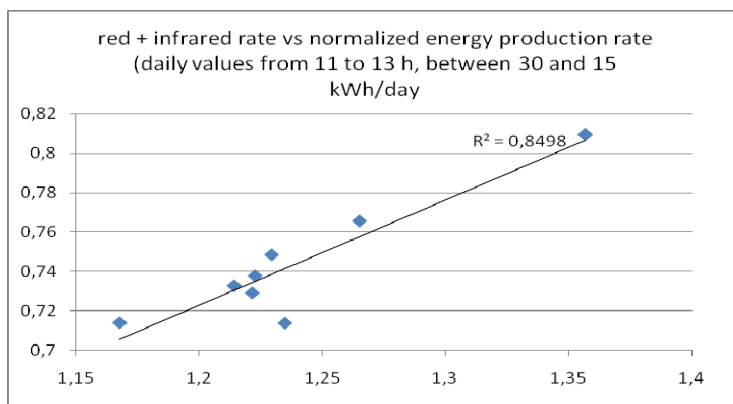
Figure 11. Comparison of red and infrared radiation rate to the ASE/DS normalized energy production rate for sunny days (daily average data from 11 to 13h, when the total energy production is between 5 and 30 kWh/day)

6. Conclusion

From the spectral measurement a relation was determined between the higher red and infrared rate of the solar radiation versus the rate of the normalized energy production of the polycrystalline and amorphous silicon photovoltaic modules. The normalized energy produced by is such solar modules proportional to the red and infrared rate of solar radiation. Consequently, in case of low module temperature and high irradiation an optional amount energy production could be reached.

Acknowledgement

References

Stuart R. W., Martin A. G., Muriel E. W., Richard C.: Applied photovoltaics, Printed and bounded by TJ International Ltd., Padstow, Cornwall, 2007.

Seres, I. and Farkas, I.: Development of a 10 kWp photovoltaic system – efficiency analysis, Proceedings of ISES Solar World Congress 2007, Beijing, China, September 18-21, 2007, pp. 1652-1656.

Seres I. and Farkas I.: Energy production issues of a 10 kWp photovoltaic system, CD-ROM Proceedings of the Conference Synergy and Technical Development (Synergy2009), Gödöllő, Hungary, 30. August - 02. September 2009, p. 6

The Analysis of Ballistic Diagrams by Throwing Seed-Corns and Fertilizer Grains Horizontally

Zita NAGY[*], Pál SOÓS[**]

[*]Department of Logistics, Institute for Environmental Engineering Systems,
[**]Institute for Mechanics and Machinery

Abstract

It is a well known fact that the integrals in the basic equations of ballistics can not be solved exactly, therefore mathematicians and experts of strategical ballistics worked out different methods in order to determine the trajectory /1/,/2/, /3/, /6/. For the purpose of developing the spreader used in the agriculture we made experiments by throwing seed-corns and fertilizer grains horizontally in order to determine the throwing distance. Using the dimensionless variables x/x_0 and v_0/v_t, which were composed of the parameters of the theoretical and the real throwing trajectory, we worked out a new relation, which enables the calculation of the throwing distance.

Keywords

experimental throwing facility, new exponential relation, terminal velocity, throwing distance

1. Introduction

The *purpose* of the research is to develop the centrifugal spreaders used in the agriculture, as well as to make horizontal throwing experiments at a given falling height. Further, on the basis of the experiments carried out with seed-corns and fertilizer grains, we aim to work out a *new relation* which may simplify calculating the throwing distance of the grains. The new relation may be the basis of developing simulation programs, which would make redundant lots of expensive experiments made in huge halls and would result in significant savings.

2. Experiment's description

In our experiments we have used agricultural grains (seed-corns, fertilizer, etc.). In the used strewing technologies the throwing velocity of these grains was 10-30 m/s, the terminal velocity was between 5-15 m/s, which is significantly different compared to the data of military ballistics.

In case of classical military ballistics there are generally high velocity factors, e.g. more hundreds m/s throwing velocity, as well as the drag factor of the bullets. In this case the alteration of the Reynolds number and the gyration of the Earth must be considered, as well.

The measurements were carried out within the framework of a research project /4/, /5/. We used 18 sorts of grains for the throwing experiment. The horizontal throwing was carried out with 3 different throwing velocities: v_{01}=10 m/s, v_{02}=18.83 m/s, v_{03}=25.13 m/s; the falling height was y_M=0.56 m.

For the throwing of the grains we have developed a rotation dial ejection facility.

The tangential velocity of the strewing dial of fertilizer spreader is between 15-25 m/s. The thrown grains were caught in a riffle on the surface of sandy soil, where the *"impacts"* could be seen clearly. The outline of the strewing mechanism is described in *Figure 1* below.
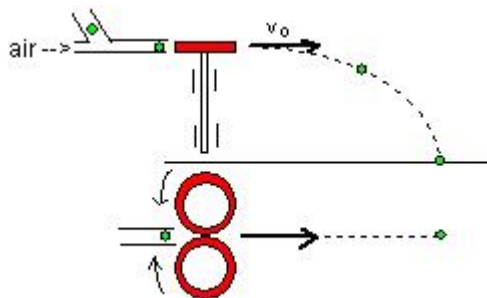
Figure 1. The outline of the experimental throwing facility

3. Description of our numeric calculation program

In the professional literature /3/ the basic relations of ballistics (Kármán equations) are as follows:

$$x = \int_0^t v_x dt = \frac{v_0^2}{g} \int_0^{\vartheta} \frac{[f(\vartheta)]^2}{\cos^2 \vartheta} d\vartheta$$

$$y = \int_0^t v_y dt = \frac{v_0^2}{g} \int_0^{\vartheta} \frac{[f(\vartheta)]^2 \sin \vartheta d\vartheta}{\cos^3 \vartheta}$$

In the course of the deduction the term of time can be determined:

$$t = \frac{v_0}{g} \int_0^{\vartheta} \frac{f(\vartheta) d\vartheta}{\cos^2 \vartheta}$$

where

$$f(\vartheta) = \cfrac{1}{\sqrt{1 + \cfrac{kv_0{}^2}{mg}(\ln\cfrac{1+\sin\vartheta}{\cos\vartheta} + \cfrac{\sin\vartheta}{\cos^2\vartheta})}} = \cfrac{1}{\sqrt{1 + \left[\cfrac{v_0}{v_t}\right]^2(\ln\cfrac{1+\sin\vartheta}{\cos\vartheta} + \cfrac{\sin\vartheta}{\cos^2\vartheta})}}$$

because when the grain is flapping

$$mg = k.v_t{}^2$$

Beforehand we notice that in this equation there is the v_0/v_t *dimensionless variable.*

Considering that it cannot be calculated with the Kármán equations, we have created a numeric program in order to calculate the integrals in it.

The "running variable" of the equations is the angle of the tangent of the trajectory and the +x axle (ϑ), therefore there is an angular step in the program. The angular step can be varied at one's discretion in our program and can also be 1/1000 degree. We do not describe in depth the program on horizontal throwing; we only indicate the parameters shown by the new program adapted to the new calculations:

- f(teta, degree) the angle of the tangent of the trajectory and the +x axle,
- y_M (m) the falling height,
- x (m) calculated throwing distance,
- y (m) momentary calculated falling height,
- v_0 (m/s) throwing velocity,
- v_t (m/s) (terminal) flap velocity,
- x_0 (m) theoretical throwing distance at y_M,
- t (s) falling time (related to x-y),
- x/x_0 values,
- v_0/v_t values,
- v_x (m/s) horizontal velocity component at y_M,
- v_y (m/s) vertical velocity component at y_M
- v_r (m/s) resultant velocity at y_M,

The values calculated with the program can be treated like they were calculated with the Kármán equations.

The integration borders can be varied in the program. It can be adjusted so that in case of each spacing, e.g. each 1/100 degree, the above values are shown.

Introduction of the dimensionless variables

In the above specification with the parameters of an angle ϑ more relations can be demonstrated. To each angle ϑ a value of x/x_0 and v_0/v_t is assigned. These

shall be treated like the variables of an x-y frame of reference. If we succeed to find relation between these two dimensionless variables, which can be *described with an equation*, then we have achieved our goal. In the two variables there are 4 values. When throwing from a certain falling height we know 3 of these values (x_0, v_0, v_t). If we know the values of x/x_0 and v_0/v_t in the *relation described with an equation*, then the throwing distance x can be calculated.

We have examined the trajectory diagrams in order to find relation between the two dimensionless variables.

4. Results and discussion

4.1. Analysis of trajectory diagrams

We have examined the *realistic* (with drag) and the *theoretical trajectory diagrams* (without drag) of the grains. For example we show trajectory diagrams of BEAN and MILO *(Figures 2 and 3)*. We have measured their characteristics when making throwing experiments.

The falling height is signed with y_M. The related values of the trajectory diagrams were calculated with the program.
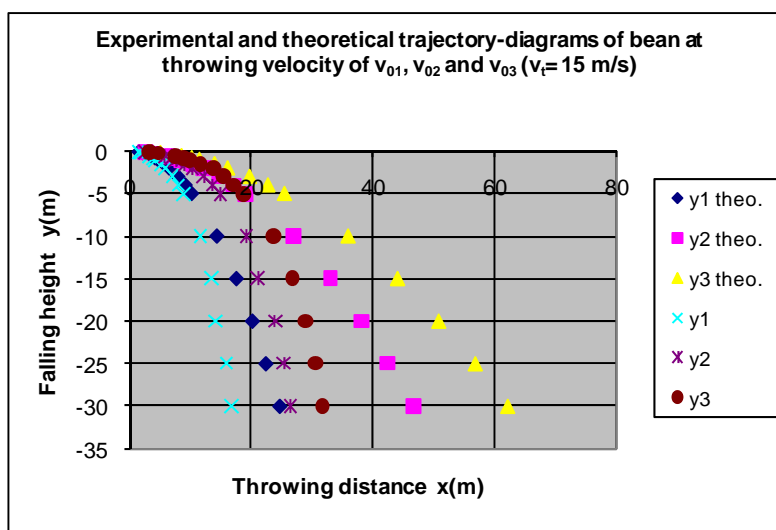
Figure 2. The experimental and the theoretical trajectory diagrams of bean at three different throwing velocity
(v_{01}=10 m/s, v_{02}=18,83 m/s, v_{03}=25,13 m/s, v_t=15 m/s)

It can be seen from the diagrams that the shape of the falling diagrams depends on the *starting throwing velocity* (v_0) and the *terminal velocity* of the grain (v_t).
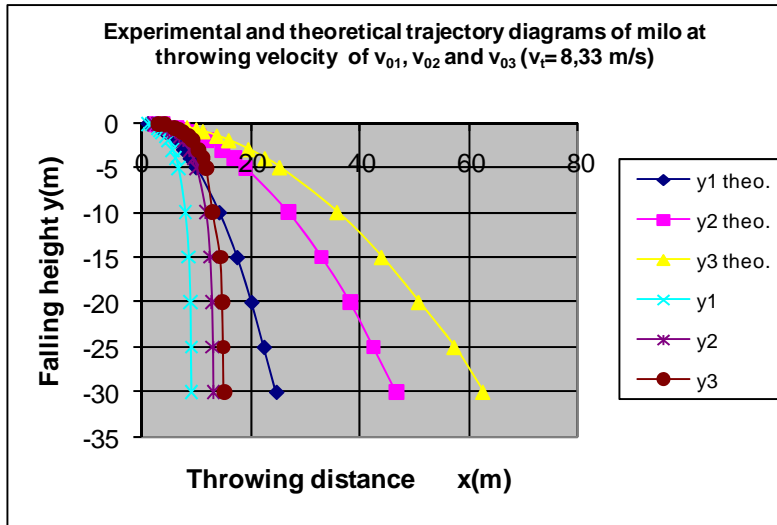
Figure 3. The experimental and the theoretical trajectory diagrams of MILO at three different throwing velocity (v_{01}=10 m/s, v_{02}=18,83 m/s, v_{03}=25,13 m/s, v_t=8,33 m/s)

4.2. The variation of values x/x_0 depending on the y_M falling height

The variation of values x/x_0 depending on the falling height is demonstrated on *Figure 4* below. It can be seen that the diagrams demonstrated with the calculated points are decreasing. v_0 and v_t values belong to each diagram.
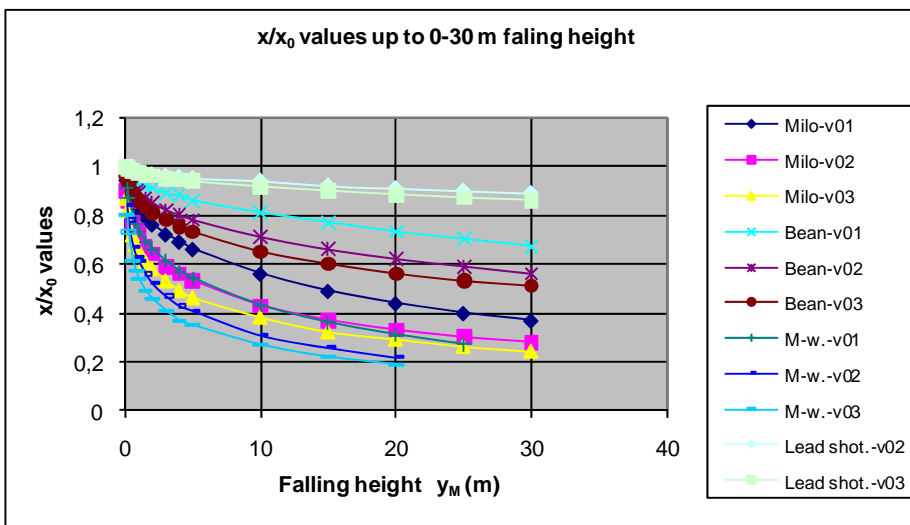
Figure 4. The variation of values x/x_0 depending on y_M falling height (0-30m)

The diagrams of the lighter grains (mangel-wurzel, milo) are lower, while the diagrams of the more heavy grains are higher.

We have prepared a diagram on the points using DATAFIT program. A well suited relation is:

$$y = x^a . e^{(b-cx)} \tag{1}$$

where in our case: $y = x/x_0$, $x = y_M$

All together the equation of the diagrams:

$$x/x_0 = y_M e^{(b-c.y_M)} \tag{2}$$

The equation of each diagram is the same, only the exponents are changing.

For example we demonstrate the exponents related to three different throwing velocities in case of MILO ($v_t = 8,33$ m/s):

MILO	$v_{01} = 10$ m/s	$v_{02} = 18,83$ m/s	$v_{03} = 25,13$ m/s
a	-0,0637	-0,1259	-0,1600
b	-0,1852	-0,3302	-0,4099
c	0,0225	0,0192	0,0182
v_0/v_t	1,2	2,26	3,01

In case of MILO for example the equation related to throwing velocity $v_{03} = 25,13$ m/s (yellow trajectory on Figure 4)

$$x/x_0 = y_M^{-0,160} . e^{(-0,409-0,018.y_M)}$$

Using this relation the location of the points of the diagram can be calculated. For example $y_M = 10$ m with replacement $x/x_0 = 0,383$.

4.3. The variation of values x/x_0 depending ont he values v_0/v_t
We demonstrated the values x/x_0 depending on the values v_0/v_t in case of four grains using our program (Figure 5).
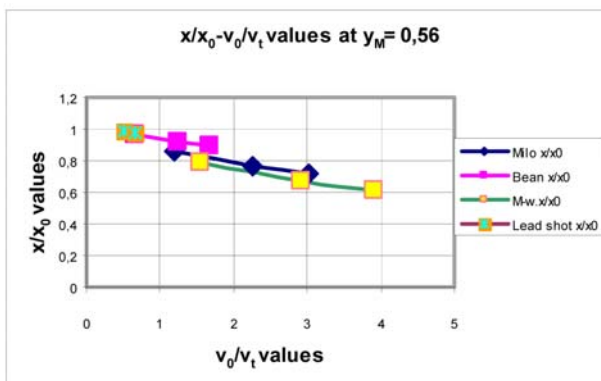
Figure 5. The variation of the values x/x_0 depending on v_0/v_t at $y_M = 0,56$ m falling height

Taking a look on the points, the variation can be demonstrated with a diagram like $\mathbf{y}=e^{-bx}$, where $y=x/x_0$, $x=v_0/v_t$. at zero on axis of abscissa ($x=v_0/v_t=0$), the offset $y=x/x_0=1$.

The point of grains at different flap (terminal) velocity are demonstrated quite "congested", therefore it makes sense to close up the x/x_0 values of more grains in order to get a relation *which is valid for more grains (in this case for four grains).* That's why we do not mark the grains (*Figure 6*).
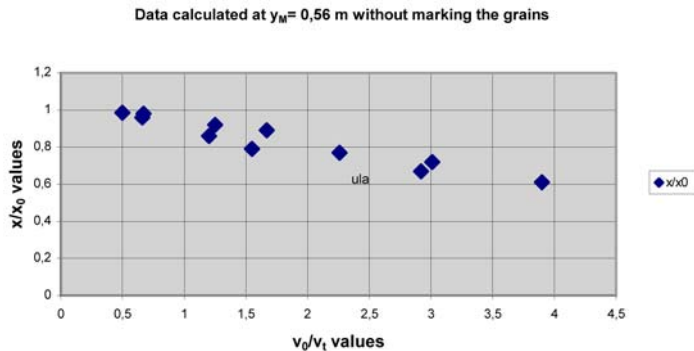
Figure 6. The variation of values x/x_0 depending on v_0/vt at $y_M=0,56$ m falling height, without marking the grains

For the x/x_0 values of the four different grains we have adopted with Datafit the function below:

$$y = e^{-b.x} \tag{3}$$

In our case (Figure 6) $y=x/x0$ és $x=v0/v_t$.

Each examined y_M falling height resulted in an exponent b. The values of exponent b are demonstrated by *Figure 7* depending on the falling height.
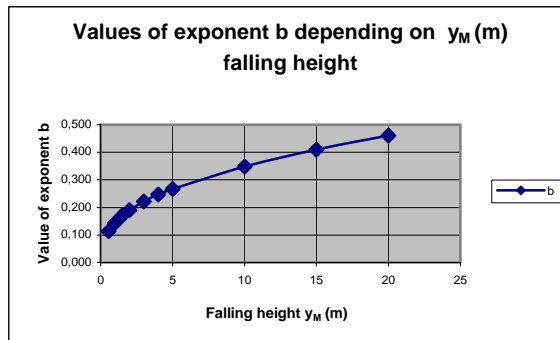
Figure 7. The values of exponent b depending on the falling height

The general shape of the power diagram adapted to the exponent b using Datafit:

$$y = a.x^k, \text{ where } a = 0,144, k = 0,382$$

So the equation of the power diagrams demonstrating the variation of exponent b:

$$y = a.x^k = 0,144.x^{0,382} \tag{4}$$

In our case (Figure 7) y=b and $x=y_M$
So the relation /4/ is the following:

$$b = 0,144.y_M^{\,0,382}$$

This shall be replaced into the relation /3/ instead of exponent b:

$$x/x_0 = e^{-b.v_0/v_t} = e^{-0,144.y_M^{0,382}v_0/v_t}$$

So the throwing distance is:

$$x = x_0.e^{-b.v_0/v_t} = x_0.e^{-0,144.y_M^{0,382}v_0/v_t} \tag{5}$$

Here the value of 0,144 is exponent b related to $y_M=1$ m falling height.

If we know exponent b at a certain falling height, another exponent b can be calculated using the two offsets of the power diagram and the related axis of abscissa:

$$\frac{b_x}{b_1} = \left[\frac{y_{Mx}}{y_{M1}}\right]^{0,382} \tag{6}$$

In the relation /5/ there are 5 parameters, only one may be unknown out of these, but it can be either of them.

The exponential relation /5/ has a big advantage, that the throwing distance may also be calculated with a simple calculator, so the Kármán equations can be used in practice, as well.

It would be practical to work out an exponential relation for not more, but only one type of grain. In this case the exponential relation would be adapted for points located on one trajectory instead spread points, which would result in a more precise calculation.

4.4. Further tests to demonstrate the effect of the throwing velocity and the terminal velocity

We were throwing virtually 16 different types of grains of terminal velocity horizontally at a falling height of y_M=0,56 m, at four different throwing velocity: v_{01}=10 m/s, v_{02}=18,83 m/s, v_{03}=25,13 m/s, v_{04}=35 m/s. The values of x/x_0 and v_0/v_t calculated with our program are demonstrated in *Figure 8 sorted by throwing velocity (v_0).*

The same points are demonstrated in Figure 9 *sorted by the same terminal velocity (v_t).*
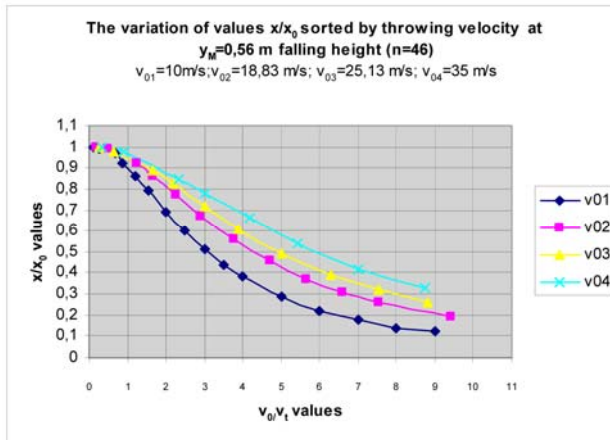
Figure 8. The variation of values x/x_0 sorted by throwing velocity (v_0) at y_M=0,56 m falling height (n=46) /v_{01}=10 m/s, v_{02}=18,83 m/s, v_{03}=25,13 m/s, v_{04}=35 m/s/
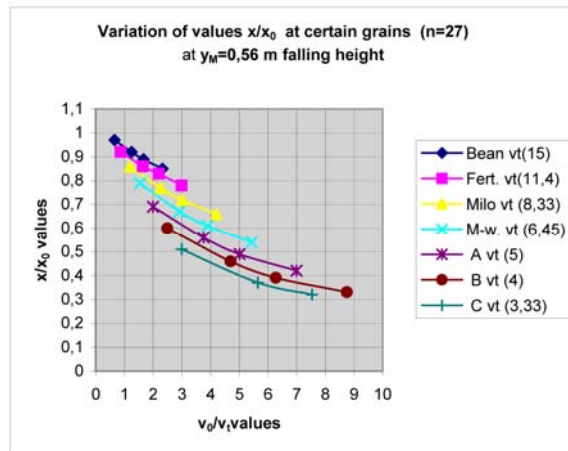
Figure 9. Variation of values x/x_0 sorted by *terminal velocity* (v_t) at y_M=0,56 m falling height (n=27) /v_{01}=10 m/s, v_{02}=18,83 m/s, v_{03}=25,13 m/s, v_{04}=35 m/s/

When sorting by the same terminal velocity, in order to avoid huge size of this paper, we only considered 7 types of grains: BEAN, FERTILIZER, MILO, MANGEL-WURZEL, A-B-C grains (n=27)

From Figures 8 and 9 the conclusion can be drawn that the cohesive values of x/x_0 - v_0/v_t dimensionless variables created by us and sorted by the throwing velocity (v_0) and the terminal velocity (v_t) demonstrate a distinct character and can be mathematically described. We made this, but we will not go in detail in this paper.

The precision of the values calculated with relation /5/

The precision of the calculation in case of certain v_0 and v_t depends on y_M falling height. If the falling height is higher, the bigger the error may be.

Checking calculation: (random)

For example in case of MILO $v_{03} = 25,13$ m/s, $v_t = 8,33$ m/s, $v_0/v_t = 3,01$

x/x_0 values			
Falling height	x/x_0 value calculated with the program	x/x_0 value calculated with relation /5/	Error [%]
$y_M = 0,56$ m	0,72	0,706	-1,94
$y_M = 2$ m	0,58	0,566	-2,41
$y_M = 5$ m	0,46	0,446	-3,04

Similar to the values of the 3rd column of the above table the calculation can also be made in other cases easily with a calculator using relation /5/.

5. Summary

We made experiments by throwing 18 different types of grains, mainly seed-corns and chemical fertilizers horizontally. We measured the throwing distances at certain falling height. The database which we created this way was used to check the correctness of our theoretical tests.

In order to use the ballistic basic equations, we examined in detail the theoretical and the experimental (realistic) trajectories.

We introduced the x/x_0 and v_0/vt dimensionless variables.

First we examined the variation of values x/x_0 depending on y_M falling height.

Finally we worked out a relation which enables the calculation of the x/x_0 value and so the throwing distance can be calculated easily.

$$x = x_0 . e^{-0,144. y_M^{0,385} . v0 / vkr}$$

In case of the models we have examined this relation can be regarded as a *general relation*. The three parameters defining the throwing distance:

- Throwing velocity (v_0),
- Flap (terminal) velocity (v_t),
- Falling height (y_M)

can be selected arbitrarily.

The precision of the relation depends on the falling height. In case of the most of the 18 different types of grains, which all have different aerodynamic characteristics, the error may be under 5 % in case of a falling height of 0-4 m.

References

[1] Bánházi J.-Koltay J.-Soós P.: Theoretical principals of the function of field machines(in Hungarian), Mezőgazdasági Kiadó, Budapest, 1984.

[2] Bohl W.:Technische Ströhmungslehre, Vogel Buchverlag, Würzburg, 1989.

[3] Kármán Tódor- Maurice A. Biot: Mathematical methods (in Hungarian), Műszaki Kiadó,Budapest 1967

[4] Soós Pál, Definition of the flow parameters of granular materials (in Hungarian) OTKA, Gödöllő 2001

[5] Soós P. (1998) Mathematical and mechanical methods for the solution of specific agricultural machinery problems (in Hungarian) Gödöllő, GATE University notes.

[6] Villette S; Cointault F; Piron E; Chopinet B (2005). Centrifugal spreading: an analytical model for the motion of fertiliser particles on a spinning disc. Biosystems Engineering, 92(2),157–164

Institute for Mechanical Engineering Technology

Professor Dr. Gábor KALÁCSKA
Director of the Institute

Dear Reader,

The Institute for Mechanical Engineering Technology (consists of three departments: Department of Material and Engineering Technology, Department of Maintenance of Machinery, Department of Mechatronics) had the following main research area during 2009.

Concerning the materials science:

- Optimisation of the milling process in order to prepare powders having grains in the order of the nanoscale magnitude
- Symmetry properties and shape factors of two-dimensional figures: the symmetry-diagram was defined which is able to determine the exact and the approximate symmetry axes.
- Theoretical studies of carbon nanostructures: algorithms for the loading simulation and for the determination of the tensile properties were designed.

Manufacturing technologies and Maintenance

- In place of brittle ceramics used so far have appeared up-to-date so called tough ceramic materials resisting better against mechanical effects. Such material is the zirconium-dioxide, too. Extensive experiments were carried out to clarify the machining features of zirconium-dioxide.
- Different type semi-finished engineering polymers were studied from the point of machining. The main- and feeding-directional cutting forces were measured and analyzed in the function of feed and cutting depth, while the chip removal was also investigated.
- Development of nano- and micro composite materials on the bases of magnesium catalyzed cast Polyamide 6 matrix. The composites are expected to use in the field of reconstruction engineering of farm-machines.

Mechatronics:

- To establish further research, significant development in the field of PLC laboratory facilities was carried out.
- The activity using the electro-rheology phenomena has grown an efficient research area.
- New research area has been established on the application of electro-pneumatic systems and also research has been started on the field of *X-by-wire* systems.

www.geti.gek.szie.hu

Short Response Time Fluid Flow Control by New Development ER Valve

László FÖLDI, László JÁNOSI

Department of Mechatronics, Institute for Mechanical Engineering Technology

Abstract

Use of intelligent materials has been a more widespread technology in the last ten years in the area of research and development of mechatronic equipments. It's main reason is that some problems of the utilization needed such a solution, which couldn't be solved only with new materials produced by material texture modification.

A claim has come up in the research of the mechatronical systems to develop materials that can get and understand an information from a computer and change their attribution accordingly. The connection, what we can establish between the computer and material, sets a limit to the quality characteristics that can be operated by the computer. This transposal can be ensured by an effect that's induction and abolition rate can be compared or the control is bigger just as the velocity of the change of a material characteristic. From a control technology point of view using electric or magnetic field is the most obvious.

One group of these materials is electro-rheologic (ER) liquids that change their shear strength according to the electric field. The flow qualities of the ER liquids can be continually changed inside certain borders, with orders of magnitude shorter interval from the previous hydraulic solutions. Making an opportunity by creating faster controlling and regulating systems from the present ones this is one of our goal.

The main aim of this work is the modification of basic properties of this kind of liquids and specification of its utilization possibilities in mechatronic systems such as hydraulic control equipments. Mathematical model as well as its numerical solution of a flow control valve (ER valve) as an appropriate element of hydraulic systems has been prepared during this work. Function tests of this unit have been carried out by computer aided simulation of the above mentioned mathematical model.

Keywords

Electro-rheological effect, Flow control, Hydraulics, modeling

1. Introduction

The ER phenomenon as a material model is described by the Bingham model related to ER liquids, which is based on the mathematical model describing the

non-newton liquids [3]. The Bingham model is a complex viscoplastic rheological model [1]. As a material model it can be divided into an ideally ductile an ideally viscous member [7]. (Fig. 1)
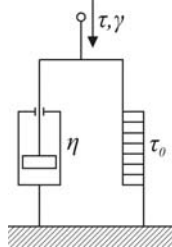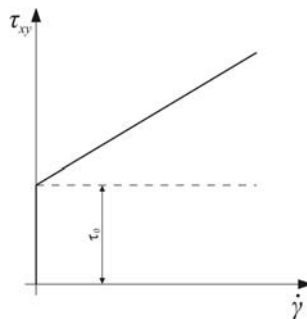

Figure 1. The Bingham model

Figure 2. The shearing tension in the function
of shearing gradient

1.1 Research objectives

The aim of testing of the flow properties of the ER liquids is to establish a model, which can be generally applied of testing the behaviours of ER liquids made of different materials considering the physical data of the applied materials. By computer simulation the parameters of this mathematical model can be determined, which can be generated by minimum search. As the first step of the model identification the approximate search of the minimum of the established target function is accomplished by genetic algorithm, then the refinement of the result with the known numerical methods.

2. The application of the flow regulator

During the further material and application tests it is practical to use a device which has application possibilities too. In this consideration for further investigations we need the design of a hydraulic ER valve, which can be operated built in hydraulic circuits [8].
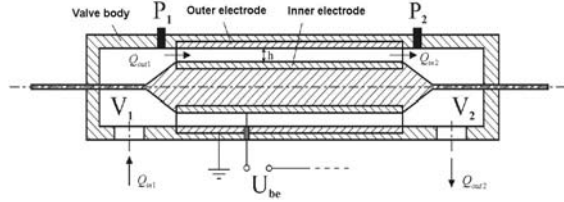
Figure 3. The ER valve
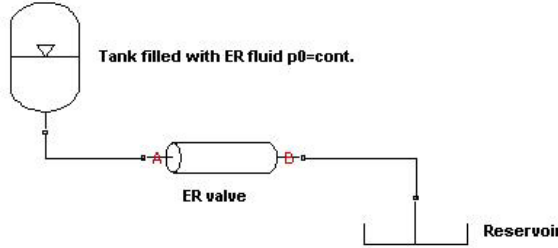
Figure 4. The conceptual diagram of simulation

2.1 Applied Mathematical Model

The flow rates which go in and out the valve can be determined by the following equations:

$$Q_{in1} = \mu \cdot A_1 \cdot \sqrt{\frac{2 \cdot (p_0 - p_1)}{\rho_f}} \tag{1}$$

$$Q_{out2} = \mu \cdot A_2 \cdot \sqrt{\frac{2 \cdot (p_2 - p_3)}{\rho_f}} \tag{2}$$

Where μ is the coefficient of flow loss, p is the pressure and ρf is the density of the liquid. On the basis of the incoming and leaving flow rates the balance (differential) equations are the followings [9]:

$$Q_{in1} = \frac{V_1}{E_f} \cdot \frac{dp_1}{dt} + Q_{out1} \tag{3}$$

$$Q_{in2} = \frac{V_2}{E_f} \cdot \frac{dp_2}{dt} + Q_{out2} \tag{4}$$

In equations (3) and (4) the Ef is the bulk modulus of the liquid. The flow rate between the electrodes is:

$$Q_{out1} = Q_{in2} = \frac{L \cdot \Delta p_N}{12 \cdot \eta \cdot b \cdot h^3} \qquad (5)$$

In equation (5) L means the length of the electrodes, η is the ER liquid's dynamic viscosity, b is the inside circumference of the electrode, h is the size of the gap between the electrodes. The pressure drop of the liquid flowing through the ER valve is composed of two parts: the first part is resulted by the liquid's ideal viscid behavior (Δp_N); the second part comes from the electric field (Δp_{ER}). Hence by the right of Bingham-model the pressure drop is [5] [6]:

$$\Delta p_{12} = \frac{12 \cdot \eta \cdot L \cdot Q_{out1}}{b \cdot h^3} + \frac{2 \cdot L \cdot \tau_{ER}}{h} \qquad (6)$$

The size of τ_{ER} depends on the ER liquid's physical parameters and the electric field:

$$\tau_{ER}(t) = \alpha \cdot E^\beta \cdot \left(1 - e^{-\frac{t}{T}}\right) \qquad (7)$$

In the equation (6) the α and the β are parameters, the T is the time constant. The value of the time constant depends on the applied electric field too. With the above equations the behavior of the ER valve can be described .

2.2 The Numerical Solution of the Applied Mathematical Model
The solution of the mathematical model of the ER valve was accomplished by MATLAB with block–oriented method, using Kelvin-Thompson return-circuit principle [2] .
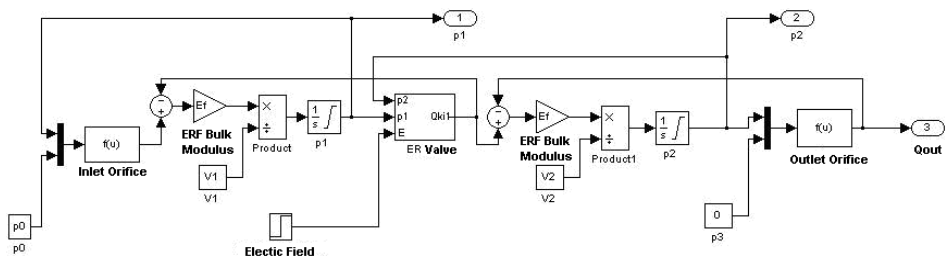
Figure 5. The block diagram of simulation

With this method the volume, which was evolved by the constant pressure difference, put on the ER valve can be measured. In this layout the liquid volume can be controlled by electric field strength. With this we can create a

hydraulic valve, which without moving parts, can be controlled by the application of electric field. It can be seen from the measurement data of the professional literature [4], that for the evolution of the effect it is enough (2-10) ms, which is a much smaller value that the indication time of the proportional valves applied nowadays.

3. The results of operation of the model

In Fig 6 at making the simulation results we applied 6 bar inlet pressure.
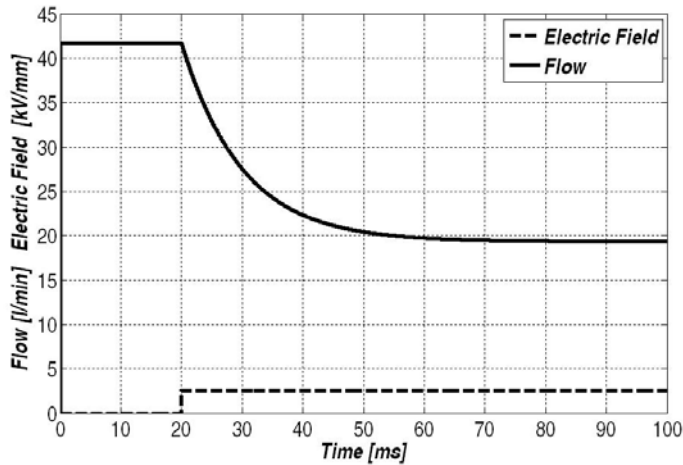
Figure 6.

As it seems on the figure 6 the flow is 42 l/min up to 20 ms, then by switching 2 kV/mm electric field the streaming flow decreases to 18 l/min in 40 ms.
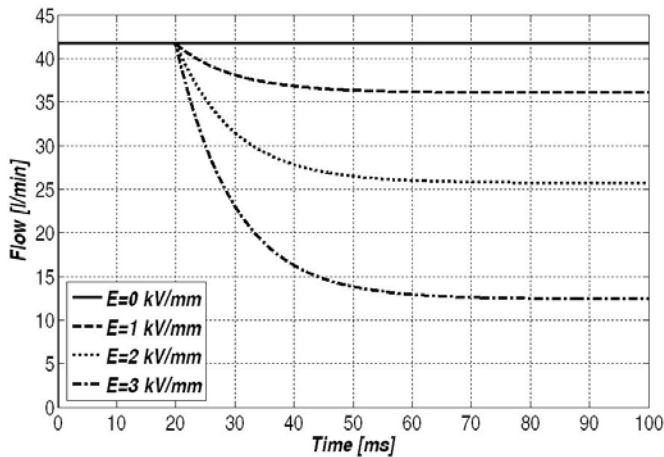
Figure 7.

At the simulation in the figure 7 constant 6 bar inlet pressure (p0) was used. It is shown that how the flow changes at various size electric fields.

4. Experimental system and results

The system consists of three main parts, like: the hydraulic power unit, ER circuit, data acquisition and control system. The hydraulic unit ensures the flow of ER fluid by a driving servo cylinder. The ER valve with flow meter and the pressure difference meter are fitted into the ER circuit [10].
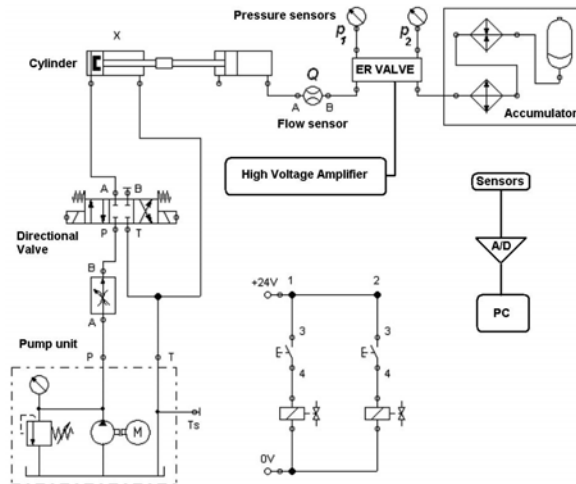
Figre 8. Experimental setup

Figure 9. Experimental setup (picture)

4.1 Results

The pressure difference required by the ER fluid to flow was ensured by a bladder-type accumulator had been pre-charged up to 6 bar before the experiment. The change of shearing stress of the fluid was determined by the equation of 6 from the pressure difference and the fluid flow rate after the electric field was switched on.
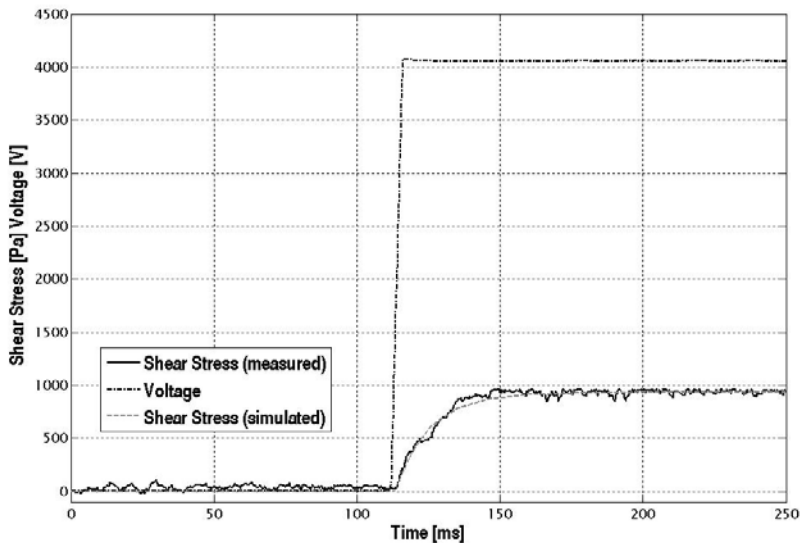
Figure 10. The results of simulation and measurement
(Experimental setup No 1)

The Fig 10 shows the change of shearing stress of the ER fluid (line) influenced by the change of electric field of 8.2 kV/mm. The measure of orifice of applied ER valve is h = 0.5 mm, the length is l = 200 mm, the potential is U = 4.1 kV. The broken line shows the result of simulation made by the mathematic model introduced before.

The changing of shear stress is shown on Fig 11 as well in the function of time. 3 kV electric power and h=0,5 mm gap was used and this setup effected E=6 kV/mm gradient. It can be noticed on the figure that smaller the gradient used means the higher response time coming from the effect and the changing is significant.

The time variable of the exponential function used in the case of simulation at the first experimental set up was (E=8.2 kV/mm) $T_1 = 12$ ms while at the second experiment was (E=6 kV/mm) $T_2 = 32$ ms respectively.

It can be seen from the experimental results that the electric gradient used has a significant influence on the response time of the ER effect. To open up these details requires further experiments. This is the target of the further research work.
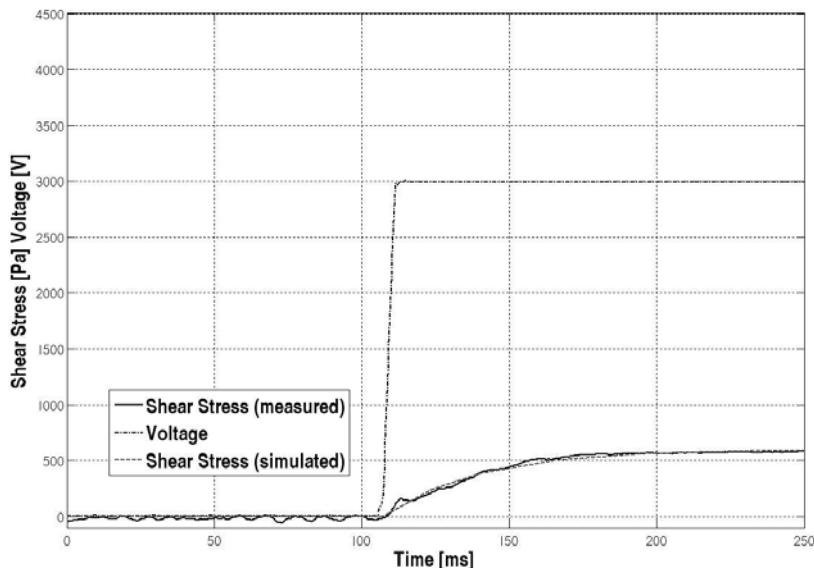
Figure 11. The results of simulation and measurement (Experimental setup No2)

5. Conclusions

On the basis of simulation experiments we can assume that the above introduced ER valve can be applied in hydraulic systems. Certainly this concept has to be further tested in term of application technique, such as the wear-effect of the particles of the used ER fluid and the temperature dependency of the ER effect. Since the developed flow control valve doesn't contain moving parts and it can be controlled by external electrical field, thus, in theory, the probability of mechanical failures can also be decreased.

References

[1] Csizmadia B. – Nándori E. (szerk.): Modellalkotás, Nemzeti Tankönyvkiadó, Budapest, 2003.

[2] Dr. Farkas I.: Számítógépes szimuláció. Gödöllő, 1999.

[3] H.-G. Lee – S.-B. Choi: Dynamic properties of an ER fluid shear and flow modes, In: Materials and Design, 2002., XXIII. évf.

[4] Valasek I. – Auer J. (szerk.): Kenőanyagok és vizsgálataik, Tribotechnik Kft., Budapest, 2003

[5] Seung-Bok Choi, Dong-Won Park, Myoung-Soo Cho : Position control of a parallel link manipulator using electro-rheological valve actuators. Mechatronics, Volume 11, Issue 2, 1 March 2001, Pages 157-181

[6] S. B. Choi, Y. T. Choi, E. G. Chang, S. J. Han, C. S. Kim: Control characteristics of a continuously variable ER damper. Mechatronics, Volume 8, Issue 2, March 1998, Pages 143-161

[7] Zrínyi M.: Intelligens anyagok, Magyar Tudomány, 1999., 6. sz., 682.

[8] L. Földi, L. Jánosi: Design of electro-rheological flow control valve. 7th Youth Symposium on Experimental Solid Mechanics, May, 14-17 2008, Wojcieszyce, Poland

[9] L. Földi, E. Sárközi, L. Jánosi: Mathematical Analysis of Electro-Rheological Flow Control Valve. Mechanical Engineering Letters, 2008. Pages 107-112

[10] L. Földi, L. Jánosi: Analysis of electro-rheological fluid in hydraulic systems. Sustainable Construction & Design, 2010, Submitted and accepted

Machining Characteristics of Some Engineering Polymers

Róbert KERESZTES, Gábor KALÁCSKA

Department of Maintenance of Machinery,
Institute for Mechanical Engineering Technology,

Abstract

Nowadays parts made of up-to-date engineering plastics are used more and more in mechanical engineering practice. These machine-elements are produced most frequently by injection molding or by one cutting process. The injection molding technology are used generally for great number of pieces, in case of serial production while cutting processes are preferred to piece (unit) or smaller number production.

We used lathe and measured the main- and feeding-directional cutting force at different engineering polymers (cast PA6, POM C and UHMW PE HD 1000). The analysis made can be well used in practice.

Keywords

1. Introduction

Among cutting processes the turning takes place often. During turning engineering plastics many problems can arise. Among these one is the splint (continuous chip) forming which can cause accident and can cause failure maybe the total ruin, fracture of the cutting tool. Because of this it is important to set the proper cutting parameters by which it is possible forming elemental or transitional (easily fracture) chip, too.

It is also important to know during cutting the amount of the main cutting force. Knowing this the load of cutting tool can be made more constant as well as the remnant stress in the material chipped can be reduced to minimum in case of proper cutting parameters.

2. Testing methods, instruments

The cutting is a machining method during which the required shape of the workpiece is formed by removing the surplus material layer in smaller – bigger particles (chip) with a suitable tool. Relative displacement is needed between the

tool and workpiece for chip removal, for cutting movement. The following (Fig. 1) figure shows the relations of arising forces during turning.
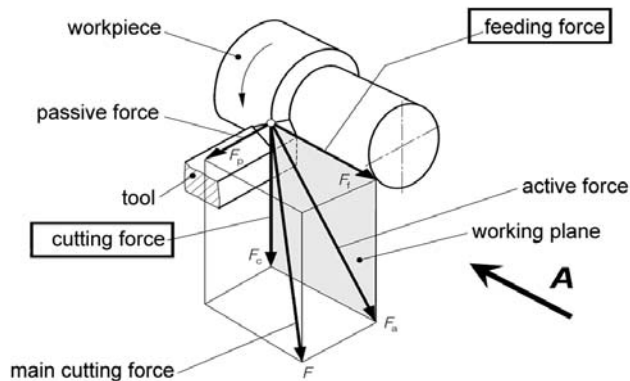

Figure 1. Turning force components (ISO 3002/4, DIN 6584)

Equipment used for tests.
The CNC-lathe, type EMCO COMPACT 5, was used for tests. The equipment can be found in the laboratory of Institute for Mechanical Engineering Technology its programming takes place of G-codes. The photograph of the workpiece clamped as well as the shank with strain-gauges clamped into tool-box and the turning tool can be seen in Figure 2.

Figure 2. The lathe and the workpiece clamped

The tool clamping structure used for measuring the forces can be seen in Figure 3. The first section of the Figure shows the 3D-model.
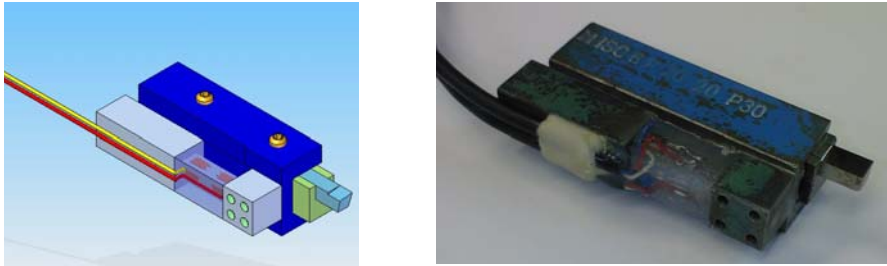
Figure 3. The force measuring shank model and its real picture

2-2 pcs. strain gauges are fixed at every side. Coupling the strain gauges into total (full) – bridge those is a possibility measuring the forces arising in two directions. To measure the main cutting force F_v (tangential) arising from the movement in vertical plane of the tool and F_f feeding (axial) force arising from the movement in horizontal plane. A second tool-box is fixed to 4 pcs. threaded holes on the measuring-shank into which the real cutting tool is fixed. The strain gauges measure the tangential (lower – upper) and the feeding (right side – left side) forces connect to a Spider-8 type measuring amplifier though wires, which amplifier convert the analogous signals into digital than transmits to the computer. With the help of Catman 3.1 program data measured can be seen. The frequency of measuring and data collecting is 25 Hz.

Materials tested.
The materials tested are those polymer basic types that are often used in engineering practice to manufacture machine-elements. Table 1 shows the name of product, the whole name and the marks accruing on lather diagrams. The specimens prepared for cutting are shown in Figure 4.

Table 1. Name and mark of plastics

Serial number	Product name [6]	Whole name	Own mark
1.	DOCAMID 6G H	Cast polyamide 6, (Magnesium)	PA 6G Mg
2.	DOCAMID 6G	Cast polyamide 6, (Natrium)	PA 6G Na
3.	DOCACETAL C	Polyoximethylene / Polyacetal	POM C
4.	DOCALENE	UHMW – Polyethylene	HD 1000

Figure 4. Specimens prepared for cutting

In the Table 2. the more important properties of polymers tested can be seen summarized.

Table 2. More important properties of plastics

Polymer	Strength [MPa]	Toughness (Charpy) [kJ/m^2]	Sliding characteristic (μ)	Thermo-duricity [°C]	Hardness	Density [kg/dm^3]
PA 6G Na	77 - 110	112	0,15 - 0,5	-40 - 140	Rockwell 85 – 98 HRC	1,15 – 1,6
PA 6G Mg	77 - 110	112	0,15 - 0,5	-40 - 140	Rockwell 85 – 98 HRC	1,15 – 1,6
POM C	70 – 80	8	0,25 – 0,45	5 – 120	Rockwell 86 – 90 HRC	1,4
HD 1000	20 – 24	no fracture	0,2 – 0,3	-80 – 110	Shore 60 – 65 D	0,96

Cutting parameters
Feeding/rev.:   f = 0.025, 0.05, 0.1, 0.2   mm/rev.
Depth of cut: a = 0.1, 0.25, 0.5, 1, 2   mm
Cutting speed: v = 50, 100, 200   m/min

Table 3. contains the parameters summarized used at tets. Each cutting speed data registered means test carried out by one-one material to which belong one feeding and one depth of cut. This gives 60 measuring by each material.

Table 3. Cutting speeds in the function of feeding and depth of cut

f / a	0,025 mm/rev.			0,05 mm/rev.			0,1 mm/rev.			0,2 mm/rev.		
0,1 mm	50 m/min	100 m/min	200 m/min	50 m/min	100 m/min	200 m/min	50 m/min	100 m/min	200 m/min	50 m/min	100 m/min	200 m/min
0,25 mm	50 m/min	100 m/min	200 m/min	50 m/min	100 m/min	200 m/min	50 m/min	100 m/min	200 m/min	50 m/min	100 m/min	200 m/min
0,5 mm	50 m/min	100 m/min	200 m/min	50 m/min	100 m/min	200 m/min	50 m/min	100 m/min	200 m/min	50 m/min	100 m/min	200 m/min
1 mm	50 m/min	100 m/min	200 m/min	50 m/min	100 m/min	200 m/min	50 m/min	100 m/min	200 m/min	50 m/min	100 m/min	200 m/min
2 mm	50 m/min	100 m/min	200 m/min	50 m/min	100 m/min	200 m/min	50 m/min	100 m/min	200 m/min	50 m/min	100 m/min	200 m/min

Forming of the cutting tool.
The cutting angles of high-speed steel (HSS Co5) turning tool have been determined on the basis of technical tables. The relief angle: $\alpha_0 = 10°$, the rake

angle: $\gamma_0 = 5°$. The grinding of turning tool was carried out on profile-grinding machine using diamond grinding wheel. The ready made turning tool can be seen in Figure 5.
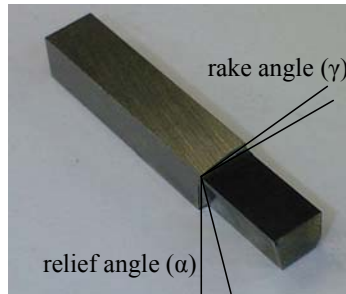

Figure 5. The bit of turning tool used.

3. Test results and their evaluations

We have measured two-way forces during tests. The tangential-directional main cutting force and the axial feeding-directional force. We have grouped the materials by depth of cut, by feeding within on these by cutting speed. Unite these in one file we have got four series main cutting force and the same series feeding-directional cutting force diagrams. We have made one-one diagram by parameter from these.
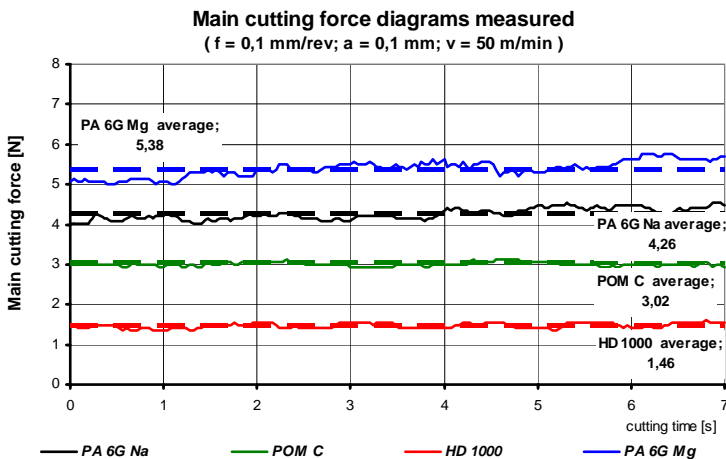
Figure 6. Main cutting force value at materials tested at cutting parameters given.

Figure 6. and 7. show one-one sample diagram. The cutting force given (main or feeding directional) as well as the feeding (f[mm/rev.]), depth of cut (a[mm]) and the cutting speed (v[m/min.]) appear in the diagram title. The force values

[N] given appear on the vertical axis, the cutting time [s] appears on the horizontal axis. We have presented all four materials in one diagram, so it can be well comparing that at same cutting parameters how great force befalls onto the cutting tool at various materials. Each colour marks one material according to mark explanation under the diagram. Continuous line shows the test results. The dotted line shows the average during measuring time given. Its value can be seen beside the line.
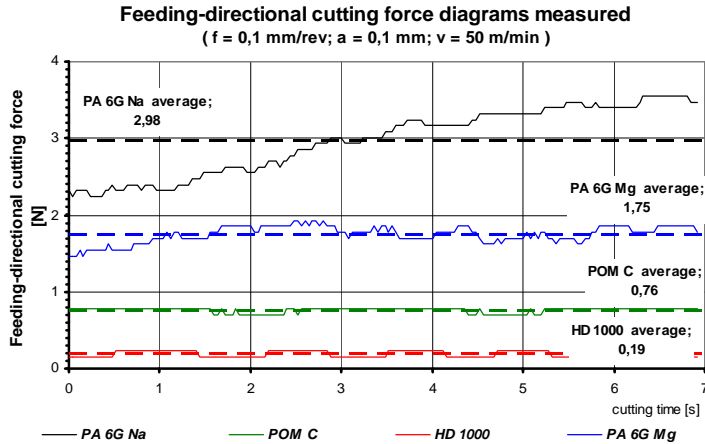
Figure 7. Feeding-directional cutting force at materials tested at parameters given.

As each workpiece tested had the same directions the measuring time period was continuously changing because of various feeding and cutting speed values. Therefore we have 7 s –time taken into account at most measuring. In case of certain cutting parameters this value could not be reached, therefore at these parameters the cutting time was reduced to 4 at one case 2 s respectively. After putting down into each diagram we have presented the main –and feeding-directional cutting forces in the function of depth of cut and of feeding from average values belonging to parameters given according to the following samples (Figure 8 – 11).
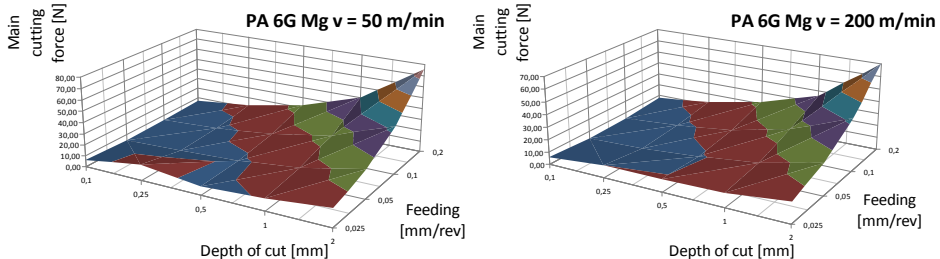
Figure 8. The value of main cutting force in the function of depth of cut and of feeding, PA 6G Mg
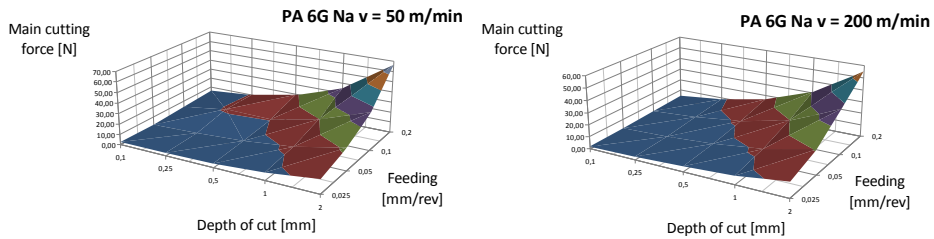
Figure 9. The value of main cutting force in the function of depth of cut and of feeding, PA 6G Na
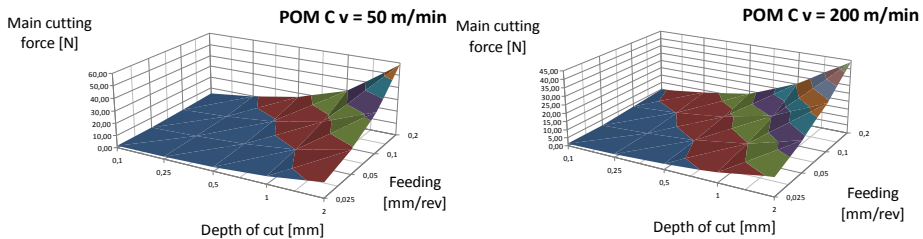
Figure 10. The value of main cutting force in the function of depth of cut and of feeding, POM C
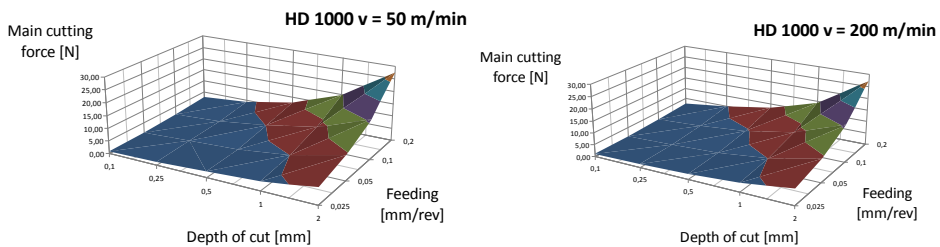

Figure 11. The value of main cutting force in the function of depth of cut and of feeding, HD 1000

Specific cutting resistance.
Cutting materials the specific cutting resistance (k_s) is an important factor. The following sample shows its change in the function of depth of cut and of feeding (Figure 12).
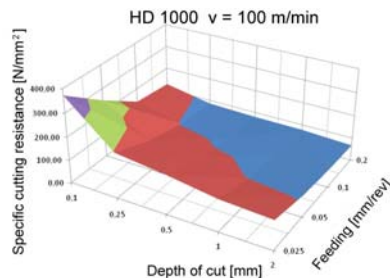
Figure 12. The value of specific cutting resistance in
the function of depth of cut and of feeding, HD PE 1000

117

According to the relation to be found in the literature the main cutting force is the function of the specific cutting force (or resistance) and of the chip area. As during measuring we have also measured the main cutting force, the chip area was given because of parameters set, so the value of the specific cutting force can be got by transposing the original relation.

$$F_v = k_s \cdot A = k_s \cdot a \cdot s \Rightarrow k_s = \frac{F_v}{a \cdot s} \rightarrow \left[\frac{N}{mm^2} \right]$$

The material tested and the cutting speed used occur in the title of sample diagram. Beside the depth of cut and feeding the specific cutting resistance (y-axis) in N/mm^2 unit can be found on the datum lines.

Chip pictures (photographs)
The chip removed during machining have been collected and photographs have been made. Based on these the types of chips formed can be examined. Figure 13. shows the chip pictures (splint, continuous chip, transitional platelike, elemental) in the function of feeding and depth of cut at 50 m/min cutting speed at POM C material. It can be established those parameters at materials in case of which chip type meets well the practical requirements.
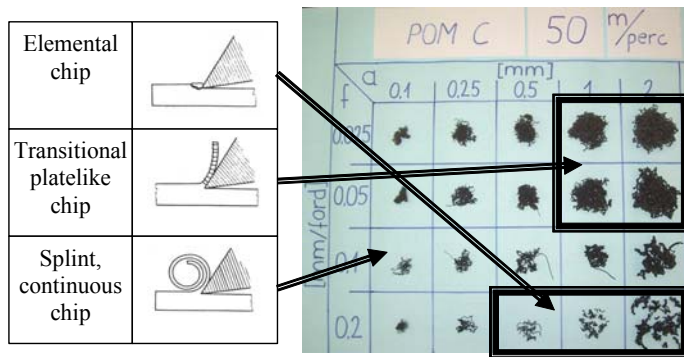

Figure 13. The forming of chip picture in the function of depth of cut and of feeding, POM C

4. Summary

It can be established from the test results that PA 6G Mg –material proved to be the toughest from both the cutting force and the specific cutting resistance point of view. The specific cutting force decreases substantially by increasing the cutting parameters (feeding, depth of cut). Taking into account the chip type formed it can be said that it is a hardly machineable material. Using the lower feeding (0.025 mm/rev) is suggested.

The PA 6G Na polymer shows a little lower toughness from the cutting force point of view, on the other hand in case of the specific cutting force it shows already more important change, approximately it reduces into third. Its value with the increasing of feed and depth of cut does not decrease such amount as in case of Mg-containing material. At cutting the small feeding (0.025 mm/rev) and the greater depth of cut (1-2 mm) is suggested.

At POM C –material could be observed the further decrease of cutting – and specific cutting force. Both decreased into half approximately, but in case of latter, similarly finding PA 6G Na –material, neither here decreased such amount with increasing the feeding and depth of cut as at Mg –containing material. From the standpoint POM C had got the most favourable chip picture among the engineering plastics taking part in tests. Comparing to PA 6G –materials here is suggested the use of greater feeding with increasing depth of cut which results more favourable chip type forming, too.

The smallest cutting forces can be measured at HD 1000 –polymer. It can be well observed at the value of the specific cutting resistance that this material has got the lowest toughness. From the standpoint of turning this is not a favourable material as regarding the chip type formed is split (continuous chip) in great part of cases tested. The analysis made can be well used in practice. The favourable values of feeding, of depth of cut and of cutting speed, within the ranges tested, can be set for cutting materials tested and for the favourable chip picture.

References

[1] Antal – Fledrich – Kalácska – Kozma: Műszaki műanyagok gépészeti alapjai, Műszaki műanyagok gépészeti alapjai, Minerva-Sop Bt. Sopron, 1997

[2] Angyal B., Dobor Lné., Palásti K. B., Sipos S. – A Forgácsolás és Szerszámai – Műszaki Könyvkiadó, Budapest, 1988

[3] Frischerz, Dax, Gundelfinger, Häffher, Itschner, Kotsch, Staniczek – Fémtechnológiai Táblázatok – B+V Lap- és Könyvkiadó Kft., 1997

[4] Dr. Kalácska Gábor - Műszaki Műanyag Féltermékek Forgácsolása - Quattroplast Kft., Gödöllő, 2005.

[5] Nagy P. S. – Szerszámgépek, gyártórendszerek – BDMF jegyzet, Budapest, 1997

[6] www.quattroplast.hu

Theoretical Models for Some Possible Elements of Carbon Nanotubes Networks

Ibolya ZSOLDOS, Gyula KAKUK, Tamás PATAKI

Department of Material and Engineering Technology,
Institute for Mechanical Engineering Technology

Abstract

A family of connected Y-junctions is defined and models of the new nanostructures are shown. Two-, three- or more branched nanorings are constructed from two, three or more Y-junctions so that two tubes of every Y-junction are joined to the neighbouring tubes with the third tube being free. The set of the two-branched nanorings is shown in detail, while three- and more branched rings are illustrated by characteristic examples. The stability was calculated for every modelled structure.

Keywords

carbon, nanotubes, mathematical modelling

1. Introduction

Today the straight carbon nanotubes are the strongest materials, nevertheless they show this property only in one direction. Their extremely high strength can be led by nanotube junctions into different directions of the three-dimensional space. The significance was discovered in their electric properties, as well.

Considering the structure it was early shown that different nanotube junctions can be built if pentagons and heptagons are also built into the hexagonal graphite structure: various symmetrical and asymmetrical Y-junctions [1-5], bends [6], T-junctions [7]. It was proved theoretically that any number of tubes having an optional type and diameter can be connected in a junction [8, 9]. Nanotube junctions consisting of more than 3 tubes were observed in various experiments [10-15]. It was presented that nanotubes of any chirality can be connected in a Y-junction [16, 17]. From different nanotube junctions different nanotube networks can be built. The basic types of regular networks are named as supersquare (the network constructed from X-junctions), supergraphene (the honeycomblike network constructed from Y-junctions), supercubic (the network constructed from junctions having 6 perpendicular tubes) and superdiamond (the network constructed from tetrahedral junctions) [11]. Several mechanical properties (Young's modulus, bulk modulus and deformation mechanisms) were determined for supersquares and supergraphenes [18, 19]. Special fractal networks, so-called super-carbon nanotubes based on the nanotube structures

were defined [20]. Others prognosticate a successful future for the random nanotube networks, although these networks have not contained junctions so far, only disordered tubes as dropping pickup sticks. They could be the most stable and the strongest electric conductors having almost zero failure probability. Researchers hope a new and cheap technology for their manufacturing will be found shortly. Several research institutes in the world prepare them today in plastic impregnated technology [12].

The electric properties of the nanotube junctions have excited a large interest in the nanotechnology. It was not by chance because for example a heterogeneous junction built from a zig-zag and an armchair tube behaves like a rectifying diode with nonlinear transport characteristics [21]. The transport properties, the current-voltage characteristics of different Y-junctions are measured [22, 23] and calculated by different simulations [24-26]. A lot of researchers work on the problem how can the Y-junctions behave as nanotransistors or how they can be assembled in such transistors [27-33]. Intense effort can be noticed for the preparation [34-39] which are motivated by different molecular dynamic simulations [40, 41]. Today Y-junctions already are applied not only in electronic fields but e.g. in the strengthening of composites [42].

The transport properties are studied in the case of other junctions [43, 44] e.g. X, T junctions [29], the tetrapod shape junctions [45] and the double toroids [46], as well.

In this paper the family of different connections of Y-junctions is shown by molecular models. The base cases for the connections of two and three Y-junctions are described in details.

2. Two-branched nanorings

In this section the set of the two-branched nanorings is shown. A two-branched nanoring consists of two Y-junctions so that two tubes of both junctions are connected opposite to each other and the third tubes of the Y-junctions are free. In order to aim for the simplicity the models are constructed from tubes having small diameters ((6,0) and (3,3) tubes). The first example can be seen in Figure 1 where two symmetric (120^0) Y-junctions having zigzag type tubes create the model, Fig. 1.a. The connected zigzag type branches formed straight tubes originally. During the relaxation procedure they have bent and the centres of the Y-junctions have become deformed too. The problem can be solved if asymmetric Y-junctions are used and the connected tubes form nanotube bends having pentagons and heptagons at the knees, Fig. 1.b. It has to be mentioned that there is other solution to avoid the deformations: if we use asymmetric Y-junctions so that the diameter of the free tubes are larger than the others [26].

A number of the two-branched nanorings can be defined according to the variation of the following parameters:
- type of the tubes (zigzag or armchair),
- diameter of the tubes,
- length of the tubes.

It is obvious that the number of the different two-branched nanorings is infinite if the diameter and the length are varied. In this section only the differences according to the type of the tubes are shown. The possible variations are summarised in Table 1.
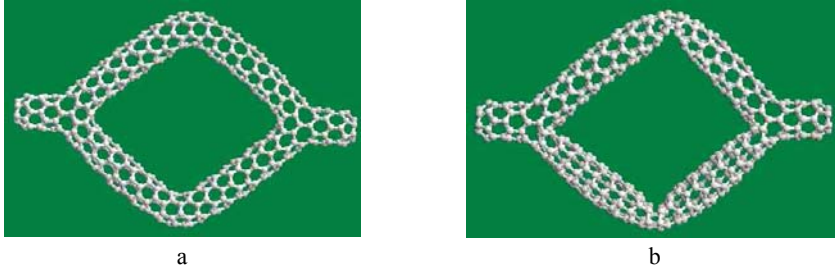

a	b

Figure 1. Two-branched nanoring a: two symmetric Y-junctions connected opposite to each other b: two asymmetric Y-junctions connected opposite to each other, bends are formed at the knees. Every tube is zigzag type tube

The notations below the sketches are introduced for the distinction of the different nanoring types. The following definition is formulated for the general case when not only two but 'N' Y-junctions are connected to form an N-branched nanotube ring (with two connected and one free branches):

$$YN\text{-}x_1 x_2 \ldots x_N\text{-}l_1 r_1\text{-} l_2 r_2 \ldots - l_N r_N$$

where:

- N is the number of the connected Y-junctions, e.g. N=2 for the two-branched nanorings,
- $x_1, x_2, \ldots x_N$ sign the type of the free tubes, their values can be 'A' if the tube type is armchair and 'Z' if the tube type is zigzag,
- l_i and r_i sign the types of the i. connected tube pairs, their values can be 'A' if the tube type is armchair and 'Z' if the tube type is zigzag.

Table 1. The possible variations of the two-branched nanorings according to the type of the tubes

Type of every tube is the same		Types of 5 tubes are the same			
Y2-AA-AA-AA	Y2-ZZ-ZZ-ZZ	Y2-AZ-AA-AA	Y2-AA-ZA-AA	Y2-ZA-ZZ-ZZ	Y2-ZZ-AZ-ZZ
Types of 4 tubes are the same					
Y2-ZZ-AA-AA	Y2-AZ-ZA-AA	Y2-AZ-AZ-AA	Y2-AZ-AZ-ZZ	Y2-AA-AZ-AZ	Y2-AA-AZ-ZA
Y2-AA-ZZ-ZZ	Y2-AZ-ZA-ZZ	Y2-AZ-AZ-ZZ	Y2-ZZ-ZZ-AA	Y2-ZZ-ZA-ZA	Y2-ZZ-ZA-AZ
Types of 3 tubes are the same					
Y2-AA-AZ-ZZ	Y2-ZZ-ZA-AA	Y2-AZ-AA-ZZ	Y2-AZ-AZ-AZ	Y2-AZ-AZ-ZA	Y2-AZ-ZA-ZA

The most characteristic examples are shown in Figure 2-6. The models are optimised namely the asymmetric Y-junctions and the bends are formed so that the sum of the angles of the connected tubes in the ring (in the square) is close to 360^0 as much as possible to avoid the deformations. The pair of the first model shown in Figure 1, the other special case when tubes of the same type are connected (every tube is an armchair type tube) can be seen in Figure 2.
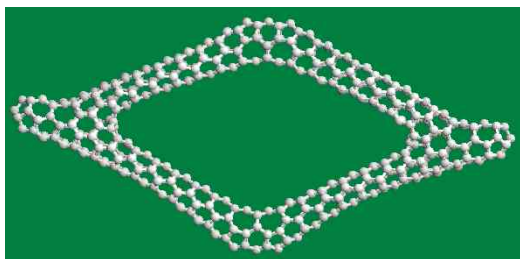

Figure 2. Y2-AA-AA-AA nanoring, every tube is an armchair type tube
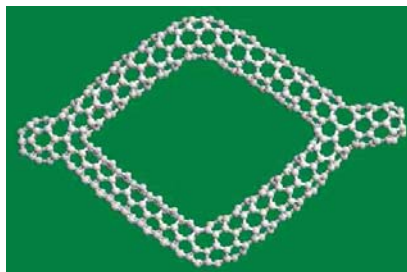
Figure 3. Y2-ZZ-ZZ-AZ nanoring, there is only one armchair type tube

Figure 3 shows the example where the types of 5 tubes are the same: one armchair type tube is joined between five zigzag type tubes.

Figure 4 shows examples where the types of 4 tubes are the same: two armchair type tubes are joined between four zigzag type tubes. The armchair type tubes tend to flattening which is most remarkable for this case.
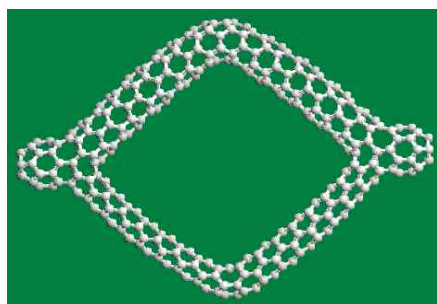
a: Y2-ZZ-ZZ-AA
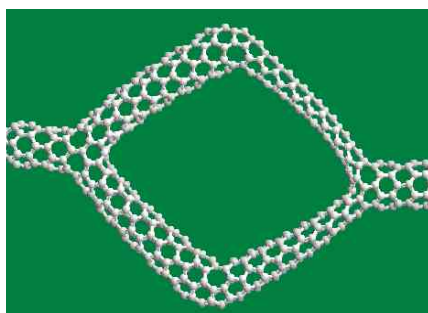
b: Y2-ZZ-ZA-ZA

Figure 4. The contrary type (armchair type) tubes are joined
a: next to each other (below),
b: below each other (on the right side)

Figure 5 shows examples where the types of 3 tubes are the same: on the link side 3 same type tubes are joined in the ring (square), on the right side only 2 same type tubes are joined in the ring (square).
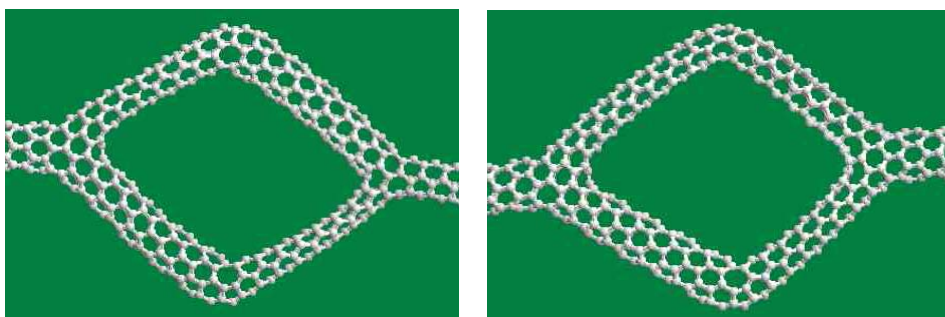
a: Y2-ZZ-AA-ZA   b: Y2-ZA-AZ-ZA

Figure 5. a: 3 armchair type tubes are joined in the ring (square), b: 2 armchair type tubes are joined in the ring (square), the third armchair type tube is free.

In the end of this section I show an example for a special case of the nanotube rings in Figure 6. A seventh tube is joined between the bends of the two-branched ring and so we get a form which is similar to the Wheatstone bridge. The structure can be regarded as four connected Y-junctions where the free tubes of two opposite Y-junctions are turned to each other (to the centre of the structure). Considering the variations of the types of the seven connected tubes the set of the Wheatstone bridge-like structures is large, as well.
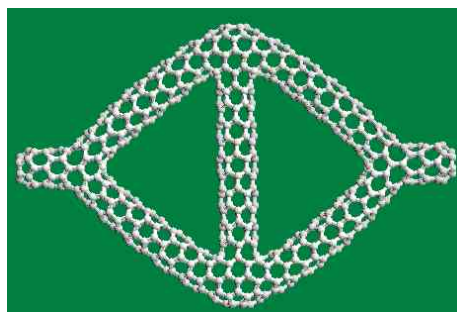
Figure 6. Example for the Wheatstone bridge-like structures

3. Three- and more branched nanorings

Similarly to the two-branched nanorings three or more Y-junctions can be connected to each other so that two tubes of every Y-junction are joined to the tubes of the neighbour Y-junctions, the third tube of every Y-junction is free.

Of course the set is larger than the set of the two-branched nanorings. Several characteristic examples of this set are shown in Figure 7-10

The first models is constructed only from tubes of same type: the Y3-ZZZ-ZZ-ZZ-ZZ nanoring is created (6,0) type tubes, Figure 7a, and the Y3-AAA-AA-AA-AA is created (3,3) type tubes, Figure 7b. It was not needed to build in

bends on the straight tubes because the deformation is much smaller than in the similar case of the two-branched nanorings, Figure 1. However bends can be constructed in place of any straight tubes, of course. The model shown in Figure 8.a has a zigzag-armchair bend and the model shown in Figure 8.b has two unique bends turned opposite to each other. On this model I show the example how can the same model be constructed from tubes having larger diameter. The tubes of the nanoring model shown in Figure 9.a are (8,0) zigzag and (4,4) armchair type tubes. Here it already was considered that every nanotube having chiral vector (n,m) such as n-m divisible by three behaves metallic and the others behave non-metallic. In our case the two upper branches of the Y3-AAA-AZ-ZA-AA nanoring are two heterojunctions turned opposite to each other. This connection can be interesting because we know that a heterojunction built from a zig-zag and an armchair tube behaves like a rectifying diode [20]. The free tubes of the nanoring are armchair tubes and the lower straight tube is zigzag tube. As it is a non-metallic branch it can be omitted from the structure, Figure 9.b.

In the end an example is shown from the set of the four-branched nanorings in Figure 10. Thus in this manner models of optional nanorings consisting of optional number of Y-junctions can be constructed.
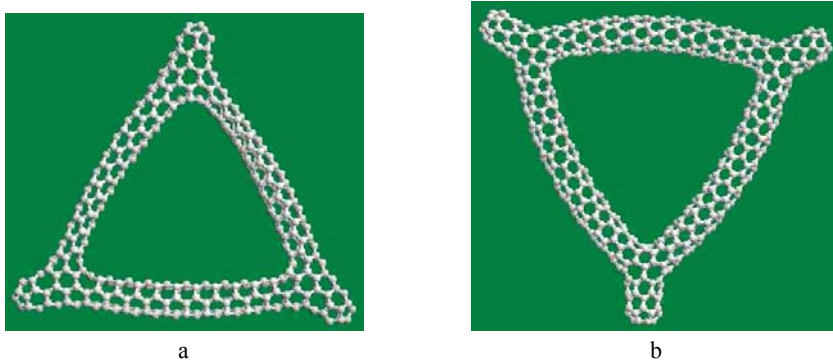

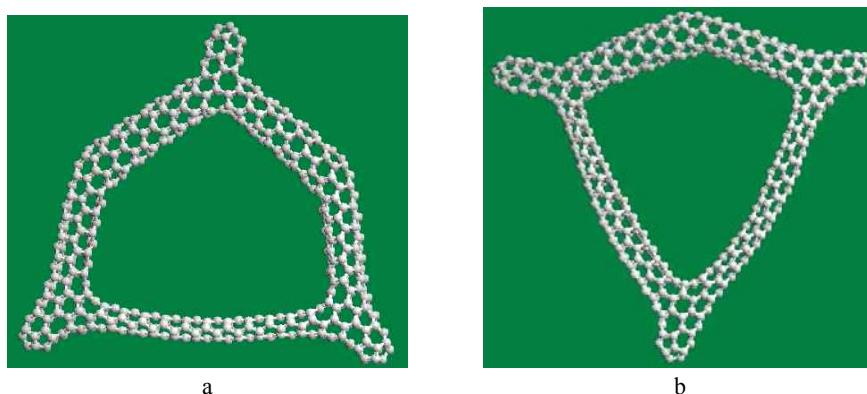*Figure 7.* a: Y3-ZZZ-ZZ-ZZ-ZZ and b: Y3-AAA-AA-AA-AA three-branched nanorings

Figure 7. a: Y3-AAA-AZ-ZA-AA and b: Y3-AAA-AA-ZA-AA three-branched nanorings
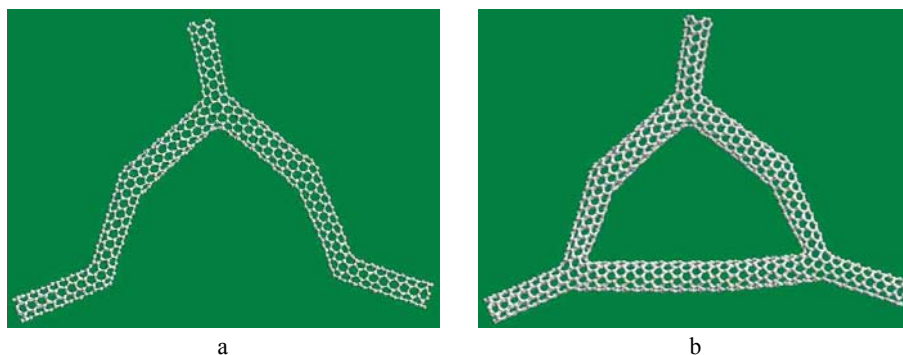
a   b

Figure 9. a: Y3-AAA-AZ-ZA-AA constructed from (4,4) and (8,0) tubes b: the same model omitting the lower straight zigzag type tube
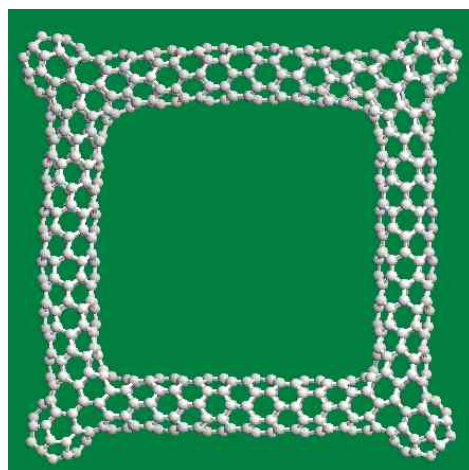

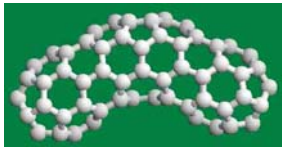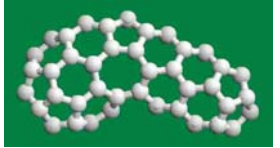*Figure 10.* Y4-ZZZZ-ZZ-ZZ-ZZ-ZZ
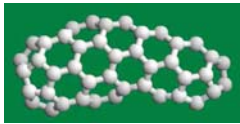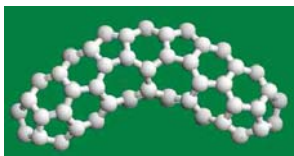
4. Stability of the nanorings

Every model of this work was constructed first in the DTMM system. As in this system the relaxation procedure considers only the nearest neighbour atoms, after the DTMM relaxation a newer relaxation procedure was run applying Brenner's interatomic potential [46] which considers the first and the second co-ordination spheres of every atoms and so it can be avoided that the atoms slide in each other in case of the deformations shown e.g. Figure 1. All figures of this work show models after the second relaxation procedure.

The cohesive energy (the bond energy per atoms, E_c) was calculated by the Brenner potential again. The values of E_c for the models shown in Figure 1-10 are summarised in Table 2. All values are between the cohesive energy of the C60 molecule (-7.29eV) and the graphene (-7.44eV), accordingly all models shown in section 2 and 3 are stable.

Table 2. Values of the cohesive energy of the modelled nanorings

Type	E_c (eV)
Y2-AA-AA-AA	-7.335
Y2-AA-AA-ZZ	-7.318
Y2-AA-AZ-AZ	-7,319
Y2-AA-AZ-ZZ	-7.325
Y2-AA-ZA-AA	-7.329
Y2-ZZ-ZA-AZ	-7.318
Y2-ZZ-ZZ-ZZ	-7.311
Wheatstone bridge-like ring	-7.341
Y3-AAA-AA-AA-AA	-7.335
Y3-ZZZ-AZ-AZ-ZZ	-7.312
Y3-ZZZ-AZ-ZZ-ZZ	-7.308
Y3-ZZZ-ZZ-ZZ-ZZ	-7.304
Y3-ZZZ-AZ-AZ-ZZ-large	-7.373
Y3-ZZZ-AZ-AZ-large	-7.370
Y4-ZZZZ-ZZ-ZZ-ZZ-ZZ	-7.352

I have studied the Y-junctions and the bends used in the upper models one by one, as well. It is reasonable because the rate of the pentagons and heptagons is much larger in them than in the full nanoring structures. The applied bends and Y-junctions are summarised in Figure 11 where the values of the cohesive energy are recorded below the pictures. The values are either between the cohesive energy of the C60 molecule (-7.29eV) and the graphene (-7.44eV) or they are close to the value of the C60. The smallest value can be found in the case of the Y-AAZ-1 junction having two armchair and one zigzag tubes, here E_c= -7.251 eV which is close to the value of the C60. The structures are stable.

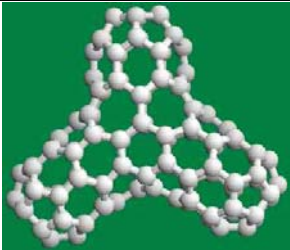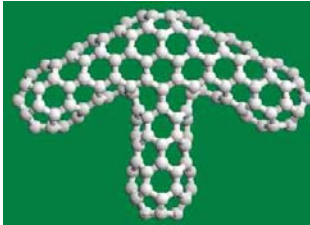|		
Bend-ZZ E_c= -7.292 eV	Bend-AZ-1 E_c= -7.260 eV	Bend-AZ-2 E_c= -7.269 eV
Bend-AA-1 E_c= -7.255 eV	Bend-AA-2 E_c= -7.284 eV	Y-ZZZ-1 E_c= -7.297 eV
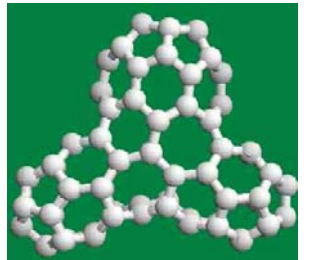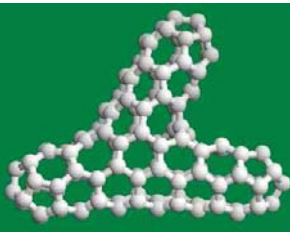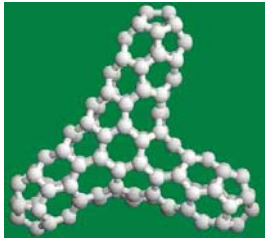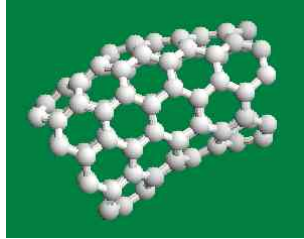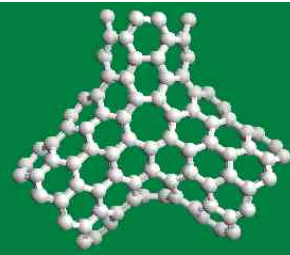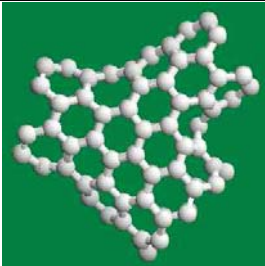
Y-ZZZ-2 E_c= -7.298 eV	Y-ZZZ-3 E_c= -7.313 eV	Y-ZZA-1 E_c= -7.254 eV
Y-ZZA-2 E_c= -7.289 eV	Y-AAZ-1 E_c= -7.251 eV	Y-AAZ-2 E_c= -7.276 eV
Y-AAA-1 E_c= -7.270 eV	Y-AAA-2 E_c= -7.265 eV	Bend-AZ-large E_c= -7.371 eV
Y-AZZ-large E_c= -7.380 eV	Y-AAZ-large E_c= -7.374 eV	

Figure 11. The bends and the Y-junctions used in the nanoring models.

5. Conclusions

A new family of connected Y-junctions are defined. The two-, three- or more branched nanorings are constructed from two, three or more Y-junctions so that

two tubes of every Y-junction are joined to the tubes of the neighbour Y-junctions, the third tube of every Y-junction is free. The nanorings are stable. They can be considered as new basic elements of the nanocircuits.

Acknowledgement

References

[1] Scuseria G E. Negative curvature and hyperfullerenes. Chem. Phys. Letter 1992;195:534–6.

[2] Chernozatonskii L A. Carbon nanotube elbow connections and tori. Phys. Rev. Letters A 1992;170:34-40.

[3] Andriotis A N, Menon M, Srivastava D, Chernozatonskii L A. Rectification properties of carbon nanotube "Y-junction". Phys. Rev. Letters. 2001; 87**:**066802.

[4] Biro L P, Ehlich R, Osvath Z, Koos A A, Horvath Z E, Gyulai J, et. al. From straight carbon nanotubes to Y-branched and coiled carbon nanotubes. Diamond Relat. Mater. 2002;11:1081–5.

[5] Osvath Z, Koos A A, Horvath Z E, Gyulai J, Benito A M, Martınez M T, Maser W K, et. al. Arc-grown Y-branched carbon nanotubes observed by scanning tunneling microscopy (STM). Chem. Phys. Lett. 2002;365:338–42.

[6] Dunlap B I. Connecting Carbon tubules. Phys. Rev. B 1992;46:1933–6.

[7] Menon M, Srivastava D. Carbon nanotube "T junctions": Nanoscale metal-semiconductor-metal contact devices. Phys. Rev. Lett. 1997;79**:**4453–6.

[8] Zsoldos I, Kakuk G, Reti T, Szasz A. Geometric construction of carbon nanotube junctions. Modelling Simul. Mater. Sci. Eng. 2004;12:1-16.

[9] Tasci E,Erkoc S. An algorithm for constructing various kinds of nanojunctions using zig-zag and armchair nanotubes. J. of Nanoscience and Nanotechnology 2007;7:1653-1661.

[10] Ting JM, Li TP, Chang CC. Carbon nanotubes with 2D and 3D multiple junctions. Carbon 2004;42:2997-3002.

[11] Romo-Herrera JM, Terrones M, Terrones H, Dag S, Meunier V. Covalent 2D and 3D networks from 1D nanostructures: Designing new materials. Nanoletters 2007;7:570-576.

[12] Graner G. Carbon nanonets spark new electronics. Scientific American 2007;5:58-65.

[13] Ting JM, Li TP, Chang CC. Carbon nanotubes with 2D and 3D multiple junctions. Carbon 2004;42:2997-3002.

[14] Liu Q, Liu W, Cui ZM, et al. Synthesis and characterization of 3D double branched K junction carbon nanotubes and nanorods. Carbon 2007;45:268-273.

[15] Devaux X, Yu S, Tsareva AN, Zharikov EV, McRae E. Formation mechanism and morphologie of large branched carbon nano-structures. Carbon 2009;47:1244-1250

[16] Laszlo I. Construction of atomic arrangement for carbon nanotube junctions. Phys. Stat. Sol. 2007;244:4265–4268.

[17] Graovac A, Laszlo I, Pisanski T. Shape analysis of carbon nanotube junctions. Match-Communications in Mathematical and in Computer Chemistry 2008;60:917-926.

[18] Coluci VR, Dantas SO, Jorio A, Galvao DS. Mechanical properties of carbon nanotube networks by molecular mechanics and impact molecular dynamics calculation. Phys. Rev. B 2007;75:075417-1-7.

[19] Li Y, Qiu XM, Yang F, Yin Y, Fan Q. Stretching-dominated deformation mechanism in a super square carbon nanotube network. Carbon 2009;47:812-819.

[20] Coluci VR, Galvao DS, Jorio A. Geometric and electronic structure of carbon nanotube networks: 'super'-carbon nanotubes. Nanotechnology 2006;17:617–621.

[21] Yao Z, Postma HWCh, Balents L, Dekker C. Carbon nanotube intramolecular junctions. Nature 1999;402:273-276.

[22] Papadopoulos C, Rakitin A, Li J, Vedeneev A.S, Xu J.M. Electronic transport in Y-junction carbon nanotubes. Phys. Rev. Letters 2000;85:3476.

[23] Bandaru PR, Daraio C, Jin S, Rao AM. Novel electrical switching behaviour and logic in carbon nanotube Y junctions. Nature Materials 2005;4:663-666.

[24] Andriotis A.N, Menon M, Srivastava D, Chernozatonskii L. Transport properties of single-wall carbon nanotube Y junctions. Phys. Rev. B 2002;65:165416.

[25] Andriotis A.N, Menon M, Srivastava D, Chernozatonskii L. Rectification properties of carbon nanotube Y junctions. Phys. Rev. Letters 2001;87:066802-1.

[26] Latgé A, Grimm D, Venezuela P. Y-shaped carbon nanotubes: structural stability and transport properties. J. of Molecular Catalysis 2005;228:125-130.

[27] Park J, Daraio C, Jin S, Bandaru PR, Gaillard J, Rao AM. Three-way electrical gating characteristics of metallic Y-junction carbon nanotubes. Applied Physics Letters 2006; 88:243113.

[28] Kim DH, Huang J, Rao BK, et al. Nonlinear characteristics of pseudo-Y-junction single-walled carbon nanotubes. J. of Applied Physics 2006; 99:056106.

[29] Chernozatonskii LA, Artyukhov VI, Sorokin PB. Silica nanotube multi-terminal junctions as a coating for carbon nanotube junctions. Phys. Rev. B 2006;74:045402.

[30] Kim DH, Huang J, Rao BKChoi WB. Pseudo Y-junction single-walled carbon nanotube based ambipolar transistor operating at room temperature. IEEE Transactions on Nanotechnology 2006;5:731-736.

[31] Kim DH, Huang J, Shin HK, Roy S, Choi W. Transport phenomena and conduction mechanism of single-walled carbon nanotubes (SWNTs) at Y- and crossed-junctions. Nanoletters 2006;6: 2821-2825.

[32] Andriotis AN, Menon M. Are electrical switching and rectification inherent properties of carbon nanotube Y junctions? Applied Physics Letters 2006;89: 132116

[33] Choi WB, Kim DH, Choi YC, Huang J. Y-junction single-wall carbon nanotube electronics JOM 2007;59:44-49.

[34] Heyning OT, Bernier P, Glerup M. A low cost method for the direct synthesis of highly Y-branched nanotubes. Chemical Physics Letters 2005;409:43-47.

[35] Choi YC, Choi WB. Synthesis of Y-junction single-wall carbon nanotubes. Carbon 2005;43:2737-2741

[36] AuBuchon JF, Chen LH, Daraio C, Jin SH. Multibranching carbon nanotubes via self-seeded catalysts. Nanoletters 2006; 6: 324-328.

[37] Yao ZY, Zhu X, Li XX, et al. Synthesis of novel Y-junction hollow carbon nanotrees. Carbon 2007;45: 1566-1570.

[38] Xue BC, Cai WS, Shao XG. Multi-Terminal Carbon Nanotube Junctions. Progress in Chemistry 2008;20:1501-1508.

[39] Fu D, Zeng X, Zou J, Quian H, Li X, Xiong X. Direct synthesis of Y-junction carbon nanotubes by microwave-assisted pyrolysis of methane. Materials Chemistry and Physics 2009;118:501-505.

[40] Terrones M, Banhart F, Grobert N, Charlier J-C, Terrones H, Ajayan PM. Molecular junctions by joining single-walled carbon nanotubes. Phys. Rev. Letters 2002;89:075505-1.

[41] Ponomareva I, Chernozatonskii LA, Andriotis AN, Menon M. Formation pathways for single-wall carbon nanotube multiterminal junctions. New Journal of Physics 2003;5:119.1-119.12.

[42] Gutkin MY, Ovid'ko IA. Effect of Y-junction nanotubes on strengthening of nanocomposites. Scripta Materialia 2009;61:1149-1152.

[43] Wei DC, Liu YQ. The intramolecular junctions of carbon nanotubes. Advanced materials 2009;20: 2815-2841.

[44] Sukirno, Satria, Zulkarnaen, Bisri, Irmelia. Electronic Transport Parameter of Carbon Nanotube Metal-Semiconductor OnTube Heterojunction. ITB J. Sci. 2009;41: 15-37.

[45] Nakada K, Maeda K, Daigoku K. Topology and electronic structure of nanotube junctions of tetrapod shape. J. of Mathematical Chemistry 2009;45:460-470.

[46] Lijnen E, Ceulemans A, Diudea MV, Nagy CSL. Double toroids as model systems for carbon nanotube junctions: through-bond currents. J. of Mathematical Chemistry 2009;45:417–430.

[47] Brenner DW. Empirical potential for hydrocarbons for use in simulating the chemical vapor deposition of diamond films. Phys. Rev. B 1990;42:9458-9471.

Institute for Systems Engineering and Management

Professor Dr. István HUSTI
Director of the Institute

Dear Reader,

On behalf of the workers of the Institute for System Engineering and Engineering Management (consists of three professional working areas called departments: Department of Engineering Economics and Management, Department of Machinery Management and Systems Engineering, Department of Communication Techniques) I'd like to give you a brief summary about our activity in the year 2009.

Department of Engineering Economics and Management

– Adoption of product and technology transfer. We analysed the diffusion of the innovation in the farm machinery sector. We researched the influencing factors of the innovation.

– Developing of the system of agricultural machinery management. We analysed how to facilitate the operative management tasks based an integrated enterprise management system.

Department of Machinery Management and Systems Engineering

– Use of reds of wireless measuring instruments. These reds allow of collecting data about our ambient with a wide range of time and area. They give us a great flexibility for the outplacement of sensors, and are able to alarm us per e-mail or sms.

– Application of cluster of mobile robots on the basis of agent. The mobile robots are able to complete tasks on special terrains. We supposed that more robots are able to do the additional tasks with a good communication and control system.

Department of Communication Techniques

– Developing e-learning materials. We developed more than 10 e-learning materials last year. The e-learning is spreading quickly and every year are more demand for this way of learning

Last year's most successful educational project was the accreditation of our Engineering Manager degree on MSc level. We reviewed our books and notes for students and our list of the taught subjects was expanded by the Business Communication and the Advertisement and PR subjects.

www.remi.gek.szie.hu

Analysis of Market Diffusion of New Agricultural Machinery with Mathematical Methods

Árpád BAK, Viktor MEDINA

Department of Engineering Economics and Management,
Institute for Systems Engineering and Management

Abstract

The sensitivity for new products of different national markets is analysed by comparing the parameters of diffusion models. The present paper provides an overview of the (mathematical) diffusion models for quantitative characterizing of the spread of innovation and shows an adaptation of the Bass-model based on innovation and imitation effects for national and international data. In a former study we examined the possibility of using the model for agricultural machinery in Hungarian circumstances. We calculated the coefficient of innovation and imitation, but we didn't find any publicized data for other countries to be able to compare our results on an international level.

In this paper we tried to stop the gap and we examined the diffusion parameters of Hungarian and German agricultural machinery. From the comparison of the two markets we can state Hungary has a worse coefficient of innovation and imitation because of the lack of capital and the low flow of information. We proposed to build up a well functioning information system, which can help to promote the farmers' flair for innovation and imitation, as they can apply and fill successfully the EU-tenders and get support to buy the new technologies.

Keywords

innovation, mathematical model, diffusion model, model adaptation

1. Introduction

Since 1930 the innovation research has been developing diffusion models to describe the spread of new products or technologies with mathematical functions depending of time and acceptance of people. Lóránd Eötvös and Béla Bucsy were one of the first researchers of this field (Eötvös-Bucsy, 1917). They approached the question from the view of natural science and wrote about the practical use of scientific methods in their paper titled "Theory of evolution". Unfortunately their work was interrupted by the First World War and left without followers.

Later the researches were continued in the USA and in West Europe in the 50's and 60's. The most well know research was made in the health sector, and

examined the diffusion of the new medicine, the tetracycline (Coleman-Katz-Menzel, 1966). During the 18 months of the examination the news about the tetracycline arrived to all doctors, but it was sated that the doctors who were members of any integration or association received earlier the news than their "isolated" individual colleagues.

In the agricultural sector it was analysed the spread of hybrid seeds and pesticides among farmers (Ryan - Gross, 1943). According to the study the spread of the new hybrid maize variety among the farmers from two villages shows a normal S-curve (*Figure 1*). It was observed, that the early adopters had typically more land, higher incomes, more relations out of the village and higher educational qualifications, than those who changed later. The early users got the information first of all from the distributors and retailers, the later users listened to their friends.
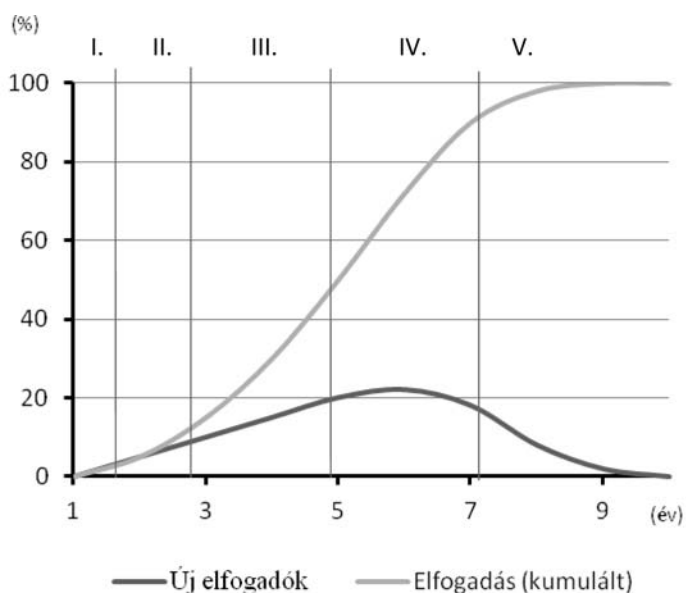
Figure 1: The general empirical curve of the spread of innovation
(Source: Made by own based on Rogers, 1983)
I. Innovators, II. Early Adopters, III. Early Majorit, IV. Late Majority, V. Laggards.

2. Methods

On the basis of Schumpeter's approach the first element of the innovation research is the invention (the birth of a new technology), followed by the innovation (the economic use). The third element of the cycle is the diffusion, the spread of the new technology and the wide public use. The diffusion of the innovation is defined by Rogers (1983) as a process, when the innovation becomes known in the population through certain communication channels. The

diffusion process has four basic components: the new product, the time, the communication channel and the social system.

The spread of a new product can be divided into stages by time according to the observations. Initially the number of the adopters increases slowly, then quickly. After then the number of the adopters increases again slowly, finally stops increasing. This temporal evolution of the spreading has a pattern so called normal *S-curve* (*Figure 1*). The adoption of innovation at individual level has also various stages: recognition, interest, evaluation, testing and acceptance. The individuals can be grouped depending how quick they adopt the innovation (*Figure 1*):

    I.   Innovators (3%),
    II.   Early Adopters (13%),
    III. Early Majority (34%),
    IV. Late Majority (34%),
    V.   Laggards (16%).

The modelling gives the possibility to characterize the diffusion process on a basis of objective factors. The different models describe the experimental curve with different structures and mathematical functions. The adopters are defined by the simplest models as the buyers who first buy the new product. These models examine closed and constant sized markets (e.g. within a country). The first-buyer diffusion models can be divided into three groups:

    – innovation models,
    – imitation models,
    – combined models.

* *Fourt-Woodlock model:* the product life-curve is described by an exponential function on a basis of clean innovation effects:

$$\frac{dN(t)}{d(t)} = p \cdot (m - N(t)) \tag{1}$$

where N(t) is the current market, where the adopters has already bought the new product until the given time, p is the coefficient of innovation and m is the potential market size.

* *Mansfield-model* takes into the consideration the effect of imitation. It is successfully applied at the examination of the spread of industrial products (e.g. locomotives):

$$(dN(t))/(d(t)) = q \cdot (dN(t))/m(m - N(t) \tag{2}$$

where q is the coefficient of innovation. The model approximates the product life-curve with logarithmic function.

* The *Bass-model* (1969) is a combined model on the basis of innovation and imitation effects. This method assumes that the innovators buy on the basis of general communication, and the imitators on the basis of information

exchange among buyers. The newly entered consumers still haven't bought, so the probability of a new purchase is a conditional probability, which can be determined by applying the Bayes-thesis.

The hypothesis of the model says, that the probability of a new buyer's buying at a given time is the linear function of the previous purchases:

$$P(t) = \frac{f(t)}{1 - F(t)} = p + qF(t) \tag{3}$$

where $f(t)$ is the probability of action without conditions at time t, $F(t)$ is the probability of all actions until time t, p is the coefficient of innovation (the probability of the first action at time t=0) q is the coefficient of imitation and

$$F(0) = 0, \text{ and } F(t) = \int_0^T f(t)d(t).$$

The probability of action at given time:

$$f(t) = (1 - F(t)) \cdot (p + qF(t)) \tag{4}$$

All actions until time t, where m is the potential market during the whole life of the product.

Number of new buyers at time t:

$$n(t) = \frac{dN(t)}{d(t)} = (m - N(t)) \cdot \left[p + q\frac{N(t)}{m} \right] \tag{5}$$

$$= p \cdot (m - N(t)) + q(N(t))/m[(m - N(t)] \tag{6}$$

This is the common use of *Fourt-Woodlock and Mansfield-models*. The solution of the differential equation is the cumulative actions and the new action at given time:

$$N(t) = mF(t) = m \left[\frac{1 - e^{-(p+q)t}}{1 + e^{-(p+q)t}} \right] \tag{7}$$

$$n(t) = mf(t) = m \left[\frac{p(p+q)^2 e^{-(p+q)t}}{(p + qe^{-(p+q)t})^2} \right] \tag{8}$$

The pitch of sales can be determined by knowing the parameters:

$$t_{max} = \frac{\dfrac{1}{p+q} \ln q}{p} \qquad (9)$$

The annual sales values can be used to determine the parameters of the model. Bass proposed to use the following method for the calculation: the new actions at given time can be expressed by the quadratic functions of all actions until that time from the continuously figure of the model:

$$n(t) = mp + (q - p)N(t) - \frac{q}{m}N(t)^2 \qquad (10)$$

The continuously model can be replaced in the praxis with the following discrete model:

$$Y(t) = mp + (q - p)N(T-1) - \frac{q}{m}N(T-1)^2 + \varepsilon T = \qquad (11)$$

$$= a + bN(T-1) + cN(t-1)^2 + \varepsilon_T \qquad (12)$$

where Y(T) is the number of new adoptions at time interval t, N(T-1) is the cumulative adoptions at t<T-1 time interval, ε_T is the error grows, which means is supposed to be 0.

The parameters *p*, *q* and *m* characterizing the diffusion can be determined by the quadratic polynomial fitted to the value pairs of Y(T) and N(T-1) with the method of least squares:

$$q = -m \cdot c, \; p = \frac{a}{m} \; \textit{és} \; m = \frac{-b \pm \sqrt{b^2 - 4ac}}{2a} \qquad (13)$$

The following conditions must fulfil: $b \rangle 0, m \rangle 0, c \rangle 0$

3. Results

A conclusion of our previous paper (Husti-Bak, 2009) was that it would be useful to examine and compare the Hungarian values with other countries. Unfortunately we couldn't find data for similar sized countries (e.g. Austria,

Portugal), so in the present paper we compared German (p_1, q_1 and m_1) and Hungarian (p_2, q_2 and m_2) parameters.

We used two data sources for the calculations. One data source was a Hungarian company producing and selling agricultural machinery only for the German market, so we could examine the diffusion of new agricultural machinery on the German market (*Figure 2*). We also made calculations (*Figure 3*) about Hungarian sales of new tractors from Béla Nagy's data collection.

To ensure the model conditions we assumed that the devices are used for at least 9 years, so in our calculations for the period 2001-2009 there was no re-buy. The model was fitted to the cumulative values of annual sales with the least squares method, as Bass proposed. In the present paper we didn't used control data, as in our previous study it was declared that we can predict the sales volumes with good accuracy also in domestic circumstances.
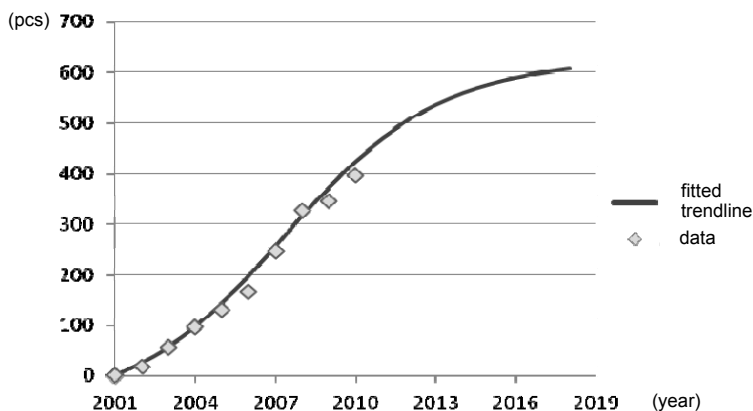

Figure 2: Diffusion of given brand agricultural machinery in Germany
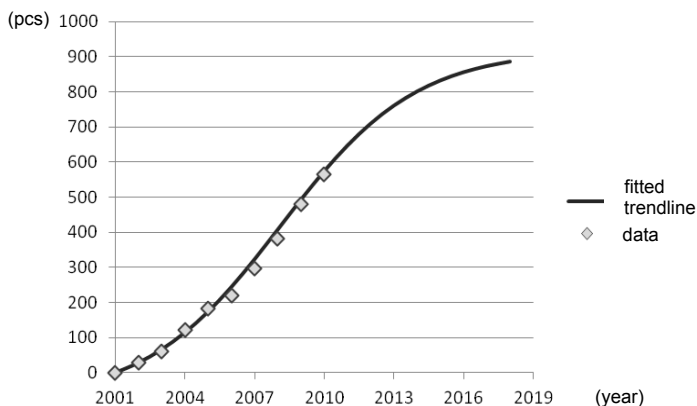(Source: made by own)

Figure 3: Diffusion of given brand new tractors in Hungary
(Source: made by own)

The prediction - based on the model calculated from 9 years data - for the market size until 2017 says 612 first-buyers in Germany and 912 new customers in Hungary (m_1= 612 and m_2= 912). The market possibilities in our country seem 50% better than in Germany.

The diffusion parameters also show some difference between the two markets, but this time Germany has better position. The coefficient of innovation in Germany is 27% higher than in Hungary (*p_1= 0,0405674, p_2= 0,03184)* The coefficient of imitation gives the similar result. Its value in Germany is 26% higher than in Hungary (*q_1=0, 0,3917 q_2= 0,31147)*.

4. Conclusions

The results of the calculations indicate a better coefficient of innovation and imitation in Germany than in Hungary, in spite of a greater number of Hungarian sales. The results can be explained by the following reasons. The lack of capital on the Hungarian market could render more difficult the innovation effects of the new products. The default of imitation effect can be explained by a traditionally low flow of information in the sector, so the farmers aren't informed about the introduction of new technologies. To eliminate the above mentioned problems we need build up comprehensive information system in the sector to ensure well and quick information for the farmers about the EU-subsidies and the new products and technologies. A well functioning information system can help the farmers to apply and fill successful the EU-tenders and get support to buy the new products.

Proposals for other examinations in the future
 – The examination, the prediction and the conclusions can be refined by observing the differences of diffusion of the agricultural machinery from the view of integration of buyers.
 – The model examinations could be expanded by other fitting methods, and so the q and p parameters could be more precise.

References

[1] Bass F. M.: A New Product Growht Model for Consumer Durables, Managaement Scinece, 1969.

[2] Br. Eötvös L. -Bucsy B.: Fejlődéselmélet. Budapest, József Nádor Tudományegyetem, 1919.

[3] Coleman, J. S.-E. Katz-H. Menzel: Medical innovation: A diffusion study. New York: Bobbs Merrill, 1966.

[4] Hajdú J.: Aratócséplőgép eladások alakulása Magyarországon, 2007.

[5] Husti I.: A mezőgazdasági gépesítés ökonómiája és menedzsmentje, Mezőgazdasági Szaktudás Kiadó, Budapest, 1999.

[6] Husti I. - Bak Á. (2009): Matematikai modellek alkalmazási lehetőségei az agrár-műszaki innovációk terjedésének vizsgálatához, Gép (ISSN 0016-8572)

[7] Orova Lászlóné: Az innováció terjedésének modellezése, Marketing és menedzsment, 2006/2-3p

[8] Mahajan, V. - Peterson R. A.: Models of innovation diffusion. Newbury Park: Sage, 1985.

[9] Rogers, E. :Diffusion of Innovation. (2nd edition) New York: The Free Press. 1983.

[10] Ryan R. - Gross N. 1943. The diffusion of hybrid seed corn in two Iova communities. Rural Sociology 8, 15-24.

Synergic Effects in the Technical Development of the Agricultural Production

Zoltán BÁRTFAI, Zoltán BLAHUNKA, Dezső FAUST, Péter ILOSVAI,
Béla NAGY, Zsolt SZENTPÉTERY, Rajmund LEFÁNTI

Department of Machinery Management and Systems Engineering,
Institute for Systems Engineering and Management

Abstract

In general consideration synergy represents the integrated behaviors and operations instead of all the differentiated behaviors of systems. Agriculture and food production and its technical development have a number of inner and outer synergic potential. Positive synergic effects among the subsystems could highly improve operational and production effectiveness and efficiencies. Those synergies are systemized and analyzed which could steam up the technical development and the agro-ecological industry as a whole.

Keywords

Synergy, technical development, agriculture, food production knowledge based agro-industrial production systems

1. Introduction

There are a lot of synergy definitions mainly depending on the activity field of the authors or experts. Before considering synergy and its effects in agriculture and food production and their technical development we suggest a more general approach. A good managed synergy gives us positive change. Right now it is more and more important at development work to understand how changes happen.
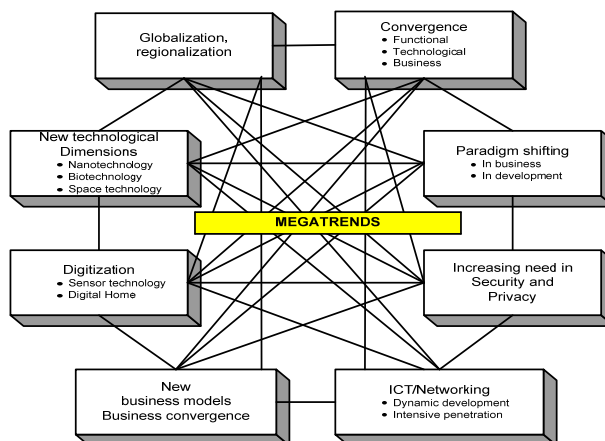

Figure 1. Megatrends and their interconnections

The first statement is very simply; by the system theory states that systems are more than simple summation of parts. Integrating actions and cooperation of parts creates a new entity with new quality and system performance.

The second general statement is that megatrends and their complex interactions and synergic effects have fundamental influences to the whole area of economy and even the everyday life. We summarized the nowadays megatrends in Figure 1. [1].

2. Discussion

Third general statement is that in synergy information and communication and furthermore in man-made systems and organizations the information and communication technology play outstanding roll.

There are approximately forty ways how creators can reach new innovative solutions [2, 3]. From the synergy point of view we highlight two types of them which are shown in Figure2. Rather evidently that the right side processes result synergy and synergic effects. But in the case of segmentation, size reduction and so on it isn't so easy to recognize way they contribute to some kind of synergy. Miniaturization for example opens the way toward functions integration and convergence. You can see this process at mobile phone. It is rational to exploit both methods and approaches in the field of agricultural technical and technological as well as organizational development.

Figure 2. Two important ways to get new innovative solution
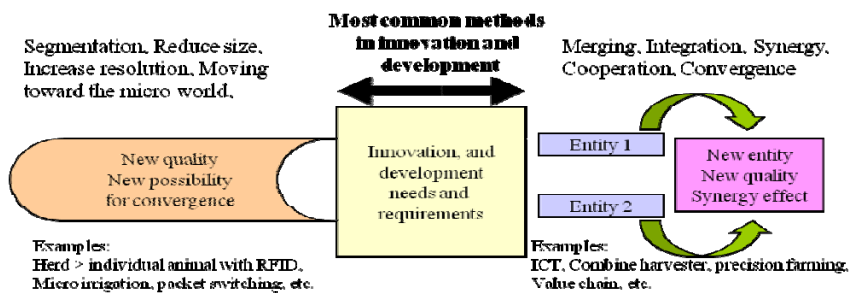
At the abstract level technology always represents how human mind explore the space of possibilities. Technology is the current major vehicle for the evolution. Recently there are a number of important agents and possibilities aid positive synergies. We summarized these aiding factors in Figure 3.
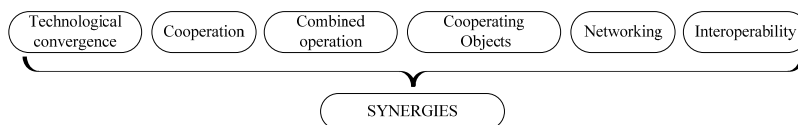
Figure 3. Agents and possibilities helping to evolve synergies

Synergy can appears at different level in economic systems. For the machine level synergy the mechatronics is an excellent example. By The Drebbel Institute for Mechatronics the term has been defined as "Mechatronics is a synergistic approach to the integrated and optimal design of a mechanical system and its embedded control system, where solutions are sought that cross the borders of the different domains." [4]. Mechatronics changed dramatically the operational structures of machines as well as man-machine cooperation. Figure4 shows a general structure of mechatronical system and its cooperation with its operator.

By opinion of some expert synergy can also defined as the combination of human strengths and computer/microcontroller strengths. Computer can process data mach quickly than humans, but does not have the ability to make complex decision.
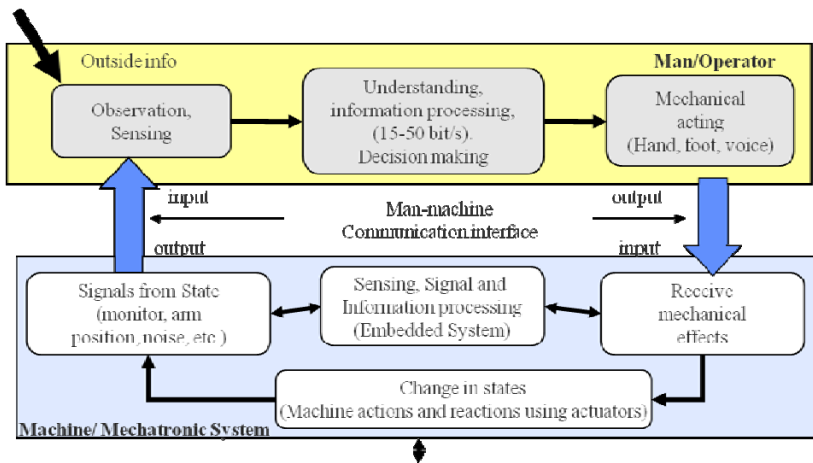
Figure 4. A general structure of mechatronic system and its cooperation with its operator
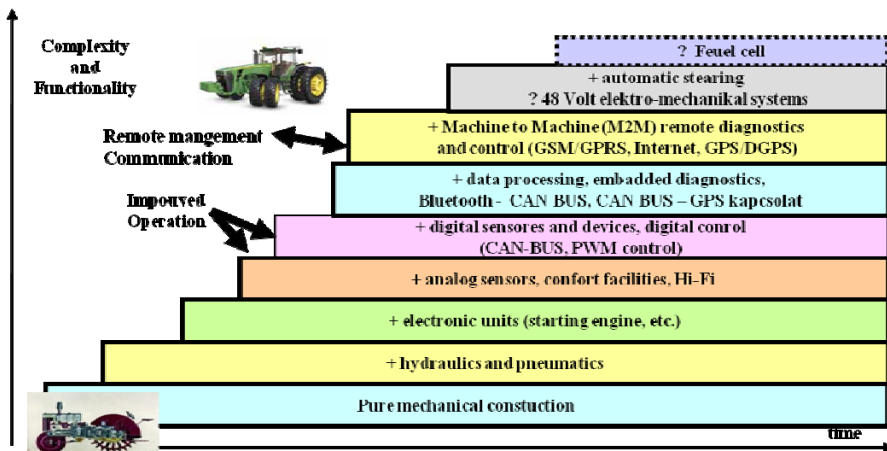
Figure 5. The history of tractor construction development; step by step new synergy

The history of tractor construction development is a good example how technical change happened building in units or modules working by now operational principle. It has always meant new synergy improving functionality of tractors but unfortunately at the same time complexity too. (Figure5).

Embedded systems and controller area networks (CAN BUS) in tractors and combine bring up new possibilities for synergies like remote control and remote diagnostic. At the technical and operational level Precision Agriculture and inside that Precision Crop Production represent very effective synergies. You can see on the general component model of the Precision Crop Production that a lot of technological and operation even scientific area act together to operate this complex system [5]. (Figure6).
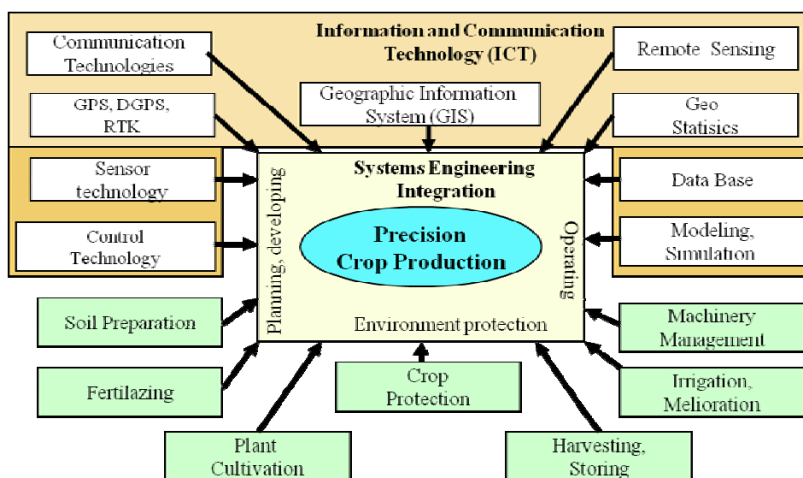
Figure 6. The general component model of the Precision Crop Production System
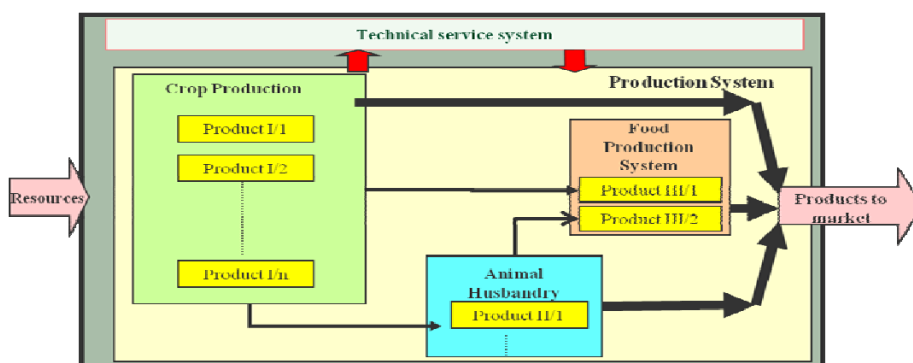
Figure 7. Enterprise subsystem relations

The next level of synergy in agriculture could be integral and well managed cooperation among the different production branch like crop production, animal

husbandry and food production inside an agricultural enterprise. In the practice you can find a lot of good examples where this type of integrated system operation is very successful. As shown in generalized model (Figure7), there is connection and cooperation between production system and technical support and service system. An effective coordination here also produces adventures.

Supply chains represent another level of synergy where enterprises with different function come together to improve effectiveness. The general model of this type of synergy is shown in Figure8. The two sided and effective activity of the integrator determine the success of the integrated cooperation. Of course the quality and timeless of the involved machines and other products as well as services are very important. But you realize that reliable information and knowledge and their effective flows inside the supply chain becoming increasingly important. Research works determined that there is considerable reserve in supply chain type cooperation and common activities.
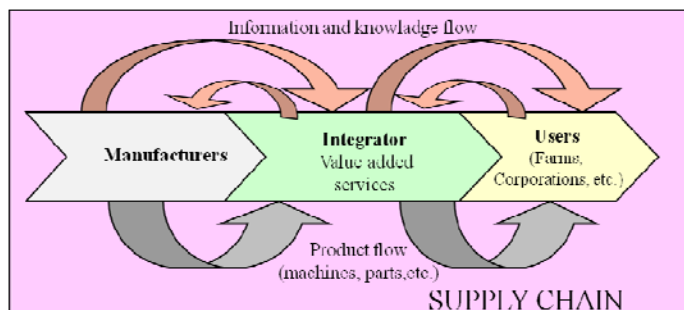
Figure 8. General model of supply chain
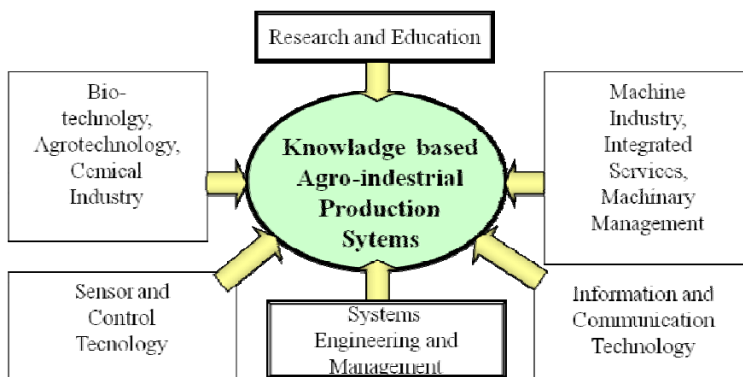
Figure 9. The main cooperating areas aiding Knowledge Based Agro-industrial Production Systems

There are a lot of economical reasons and motivations that press the agricultural commodity producers to form Knowledge Based Agro-industrial

Production Systems. Seemingly it will bring up the surface a new, more complex and effective level of synergy and integrated cooperation. The main cooperating areas are shown in Figure 9.

3. Conclusion

Because research and education become more and more costly these area beadily need cooperation with industries and agriculture with mutual advantages.

Cooperation among agricultural and food production and comers have a long life tradition. (Figure10). Connecting with this synergic level you also can say that there are tremendous unused possibilities.
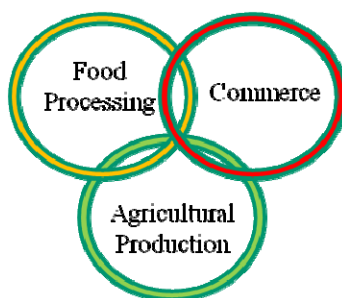
Figure 10. Traditionally cooperating sectors

At the national level there are two very perspective synergic areas namely:
 – Synergy between agriculture and environment protection;
 – Synergy between agricultural renewable energy production and energy industry.

Above a number of levels of synergy where mentioned. Conscious activities in fields of research, education and economic sphere could result better and wider exploitation of open and hidden possibilities

References

[1] D. Faust: Az ingatlangazdálkodás rendszertechnikája. KJK, Budapest, 2004. p 1-3.

[2] Altshuller, Genrich (1984). Creativity as an Exact Science. New York, NY: Gordon & Breach. ISBN 0-677-21230-5.

[3] D. Faust: Systems Engineering. Szent Istvan University, 2009.

[4] The Drebbel Institute for Mechatronics. http://www.drebbel.utwente.nl/; Inroduction, p:1-3

[5] D. Faust: Precision Technologies. Szent István University, 2007.

Application of the Combined Wireless Sensor Network-, and Mobile Robot Technology for Monitoring

Zoltán BÁRTFAI, Zoltán BLAHUNKA, Dezső FAUST, Péter ILOSVAI

Department of Machinery Management and Systems Engineering,
Institute for Systems Engineering and Management

Abstract

Both wireless intelligent sensor network and all terrain mobile robot technologies are relatively new ones. There are a lot of research work in which the two technologies were studied separately. We found that the combination using the wireless sensor network and mobile robots give us much more application opportunities and effectiveness in greenhouse and open air agricultural field monitoring. With the combination the fusion of sensors signals and the mobile router function have especially important adventures.

Keywords

wireless sensor network, mobile robots, monitoring, synergy

1. Introduction

Wireless sensor network and mobile robots are two new technologies in the latest 10-15 years. These are new waves of development. With these technologies we can monitor, measure and control our physical world, connected to the World Wide Web or local area networks. The SmartDust project [1] results – which was supported by Berkeley University DARPA – are appreciates by Business Week [2] to the most effective technology of the 21th century.

Using the wireless sensor network we are able to collect information from big area, for a long time. The installation is easy, the network topology is easily fit for the requirements. With these good attributes there are more and more interesting application. The first applications were ordered by the army. These applications used moving nodes. In the civil applications used mostly not moving nodes.

Publication [2] from 2008 is introduced and analyzed the developing directions and application fields. This book doesn't mention about agricultural applications. One reason can be the high price of the wireless sensor networks. The prices are reduced, there are some example in the precision agriculture. For example the Camalie Vinery project [3], where fixed sensors measure the soil moisture for the optimal watering.

One big constraint is in the agricultural applications the living organizations disturbance of the radio communication. We made measurement of this [4]. We

found the communication range is 70-80% less then open air range. Another problem is to put gateway and laptop in agricultural environment for a long time.

A good solution for these problems is applying wireless sensor network and mobile robots together! The main aim for mobile robots is to discover and monitor. These functions can be extended to be a base station for wireless sensor networks.

2. Discussion

While mobile robots are cruising in outdoor surfaces, we can easy recording the division of the surface. The precision agriculture need to know the exact surface. The seeding technologies also need the detailed surface information [5].

To collect detailed surface information is difficult because of the measuring the stochastic systems. Measuring technology is complex and uncertainty is very high. Five universities [6] made a publication about researching in this topic. The publication said the same, bad uncertainty and complex methods.

The mostly used method to measure the surface is the profilograph with laser or mechanical sensors. Using the profilograph, make an 1-4 m long artificial horizontal line, and measure n pieces of distance. To characterize the surface is used coefficient of variation.

Using profilograph needs very much human resource. One measured data cannot be represented the surface. These values don't have physical signification.

Making measurement with Pioneer P3-AT mobile robots, we can supervise that mobile platform angles are representing the surface. This rule gives us the idea, that using mobile robots and one or more wireless sensor nodes we are able to measure the changing of angles and the dynamic of changing.

Using the MEMS sensors for tilt, accelerate and angle speed measuring. There are many opportunity to place MEMS in mobile robot platform.
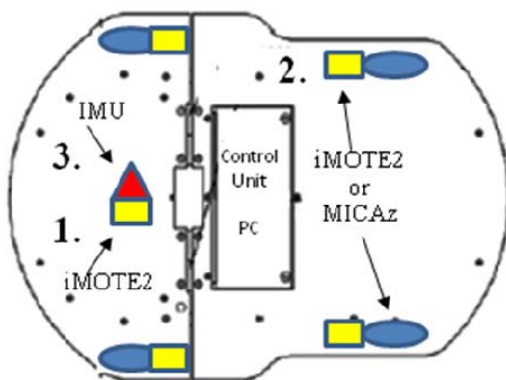

Figure 1. MEMS sensors on mobile robot platform

Using mobile robot or mobile robot swarm we can collect more information from soil, than the earlier measurement systems. This bigger data set makes more accurate and reliable statistical data.

These results are enough to precision agriculture requirements. Also this concept cannot be the only one solution, the robot has construction kinematical properties which are constrains, it limits the accurate and reliability.

3. Wireless sensor network

The intensive technologies in agriculture need high accuracy sensing and automation. The modern environment management using advanced monitoring.

Wireless sensor networks mainly used in industrial environment. Using wireless sensor networks in agriculture is not researched area. In agricultural environment mobile robots and wireless sensor networks must work between plants or animals. The most serious constraint factor is the wireless communication pass loss. To design and operate these systems we must know how the biological environment effects the radio frequency communication.

Using wireless sensor network we are able to collect huge quantity of information for a long time, from the real physical world.
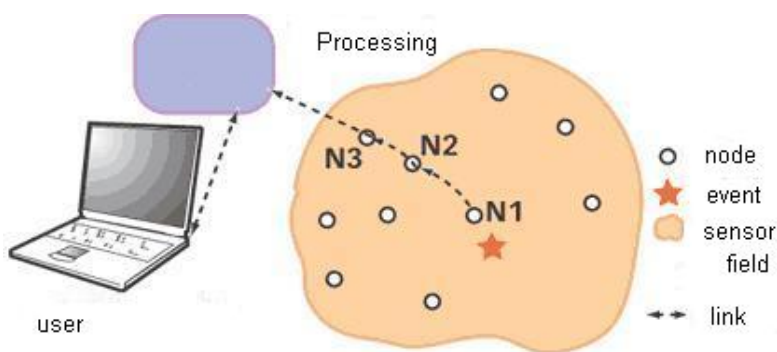
Figure 2. Collecting data from real physical world

Figure 2 is showing how to collect information from agricultural environment. When en event happend the node sends the measured value or information to the proecessing center. Using low power, short range communication, the multi-hop protocol find an optimal route for the information (N1-N2-N3). The processing center is a database for all kind of measured value, from all sensors to the total measuring time. The user can monitoring the whole time, all sensors values.

One of the biggest advantage of the mesuring system: wireless (communication and power). Other hand in this comfortable property, this is serious constraint in communication and battery lifetime.

4. Mobile robots

We use Pioneer P3-AT mobile robots. They designed to use indoor and outdoor environment. These type is the most used robot in own category. With all-time four wheel drive and good design, these robots have good off-road capabilities. The driving motors controlled by PWM controller and encoder. In the top of robot platform we can connect many input device: sonar, laser scanner, normal or stereo camera, GPS, robot arm, etc. For intelligent working, include inner and outer communication, the robots have a PC and a microcontroller. In the platform we can place more MEMS sensors (mote).

Figure 3. Mobile robot on the field

Some parameters of the robots which are important to measure the surface:
- Weight: 11,8 kg (with 3 batteries)
- Axial distance: 275 mm
- Wheel diameter: 225 mm
- Wheel width: 80 mm
- Width (by wheels): 400 mm

MEMS sensors are mass products, so their prices get smaller. This is also a good reason to use them. The stereo camera and laser scanner are good for validate the method. For special requirements more sensors can give good result, but today price level it is too expensive.

5. Synergy of wireless sensor network and mobile robots

Wireless sensor networks are easy to use, flexible measuring systems. There are many type of sensor, for industrial and agricultural measuring. For example: temperature, light, humidity (soil, air, plant), acceleration, inertial sensors, pressure, A/D converter, microphone, etc.

Wireless sensor network has some disadvantages: short range communication, limited battery lifetime. Short range communication is extended by multi-hop

routing protocol. Battery life time can be extended by various technology of energy harvesting (solar, wind power, vibration energy).

Wireless sensor network are very flexible to using them mobile environment, sensors are not able to move.

Mobile robots are a good platform for wireless sensor network. These robots are developed to move indoor and outdoor surfaces. All-time 4 wheel drive and robust design give them very good off-road capabilities. Local WLAN connection makes a high speed flexible data connection. The built-in PC have a big computing capacity including a data base server for wireless sensor network measured values, storing pictures and movies created by remote controlled cameras attached to the robot.

WLAN has a limitation from the access point. This distance is bigger than wireless sensor network range. To extend this constraint GPRS and EDGE technologies give us unlimited communication.

Using mobile robots high tech, high speed devices (PC, motor, GSM) battery lifetime is quit short. Energy harvesting is a good opportunity but not enough for continuous working. External charging, battery changing or pause for energy harvesting can extend the battery lifetime.
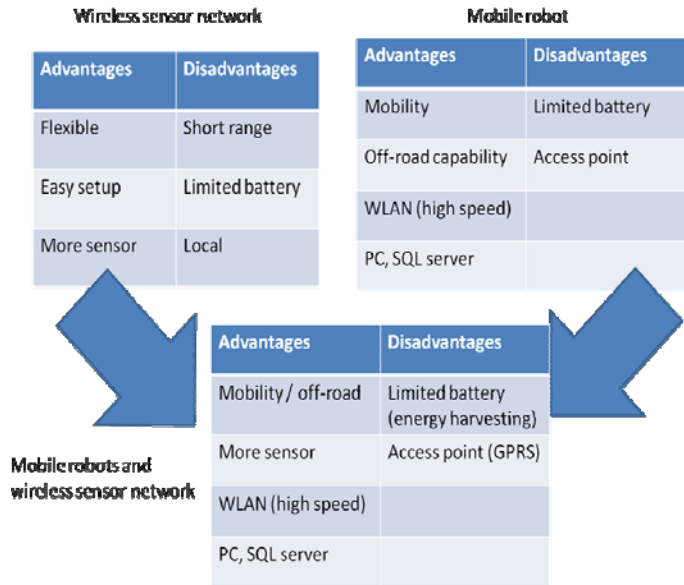
Figure 4. Synergy

Figure 4 shows the advantage of using wireless sensor network with mobile robots. Mobility, flexibility, high capacity communication, computation and monitoring are the common advantages. Limited battery lifetime is the most problem to use this complex system.

In our sample application (monitoring soil surface) the measurement takes just a few minutes, battery lifetime doesn't affect the method.

6. Sample application

Measuring the soil surface is a good combination of mobile robots and wireless sensor network. Mobile robot gives the moving platform and wireless sensor network give the 3 dimensional acceleration sensors.

There are many places to put the sensors (Fig. 1.). The Pioneer P3-AT mobile robot has rigid axes, so the whole chassis moving in the same way. Because these special condition and sensors high price, we choose only one sensor. The sensor is placed to the center of the platform.

The "x" axe shows forward in horizontal plate.

The "y" axe shows left in horizontal plate.

The "z" axe show upward vertical.

When the robot is standing or moving forward in constant speed the sensors measure the 3D position of the platform (pitch, roll). When the robot accelerates or turns the sensor measure the summation of 3D position and current acceleration. That's make difficult the read, explain the result. Because of this problem, we drive the robot in constant speed, straight. The PWM controller keeps the speed constant, but when some obstacle impacts the platform, a short transient acceleration is added to the 3D position. Release these transients we use statistical methods.

Our first idea was, we measure the "z" axe acceleration, integrating twice and we get the soil profile.

$$s_z = \int\int a_z \, dt \, dt \qquad (1)$$

There are many little noises in the process, so integrating these noises make unreadable result. Axe "z" measure both pitch and roll. Measure the pitch in z axe make smaller different than measure in x axe. $(a_z = g \cdot \cos\alpha$ $a_x = g \cdot \sin\alpha)$. For little angles - mostly in soil profile - sin values are bigger than cos values. That's why we use x axe acceleration, a_x to measure pitch, and y axe acceleration, a_y to measure toll.

Figure 5 shows the measured acceleration values when the mobile robot platform goes down in a "strait". In the left graph the strait is 4 cm height, in the right graph the strait is 6 cm height. The graphs show the acceleration values in g/1024 m/s^2. The horizontal axe is the time in 1/100 sec. Because the robot platform goes on constant speed, the time has a linear relation to distance.

In the first part the robot is going in horizontal plate. When the first wheels fall down (second part) the transient holds about half second. This short time the PWM controller restores the original speed for the mobile robot platform.

In the third part the first axe is down and the second axe is in a higher level. That's make a positive a_x acceleration. The fourth part the second axe fall down, make another transient. The fifth part is like the first.

The two axes make always echo. Every axe takes the obstacle. The time of the echo is equal the time to need to go the axial distance. In a constant speed it is a constant echo time. Depends on the size of obstacle, the echoes can overlap. When two obstacles are closer than the axial distance, the second obstacle come earlier than the first echo.
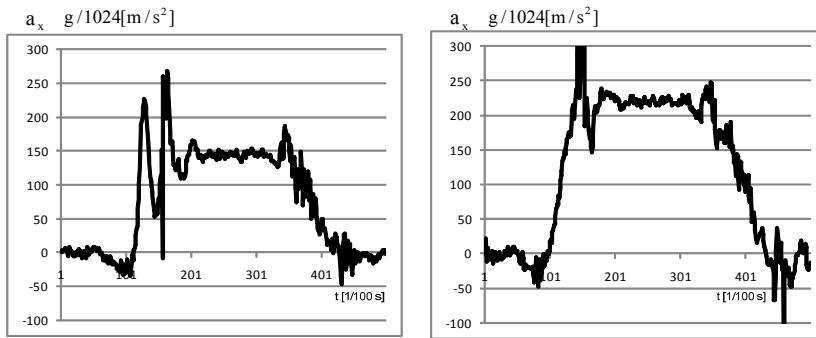
Figure 5. The "x" axe acceleration going down in stairs

Table 1. a_x values in strait

Height [mm]	average of a_x g/1024 [m/s^2]
20	72
40	146
60	221

d: axial distance
h: height
g: gravity
a_x: projetion of gravity
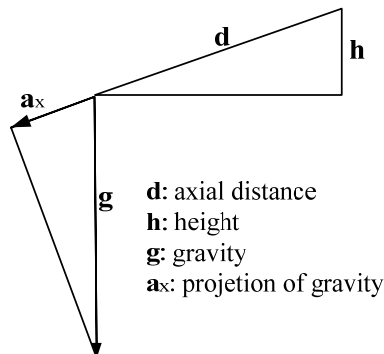
Figure 6. Geometry and force relation

Table 1 shows the average a_x values in 2 cm, 4 cm and 6 cm height strait. These numbers have a quite linear relation. In statically case when the mobile robot platform goes in constant speed the a_x value equals the projection of the gravity. The gravity constant and shows down. These are in the force triangle. in the figure 6 the other triangle shows the geometrically relation. The axial distance is d, and the high level different is h.

The two triangle in figure 6 are similar. It means:

$$\frac{g}{a_x} = \frac{d}{k} \qquad (2)$$

from (2) we can get the h,

$$h = a_x \frac{d}{g} \qquad (3)$$

7. Conclusions

Mobile robot platforms and wireless sensor network is able to measure the soil surface roughness.

Equation (3) says that high level difference between front and rear axes is linear to measured a_x value. Also we can get the high different in left and right site wheels from a_y. From these values we are able to calculate the soil surface, while mobile robot platform goes in straight. Also we know, there are transients when we don't have information about surface. Using mobile robot, or mobile robot swarm, we are able to collect many "line"-s from soil surface.

These values (pitch, roll differences) characterized the surface. Also there are some disturbance (echo, transient) when the values are not accurate and reliable.
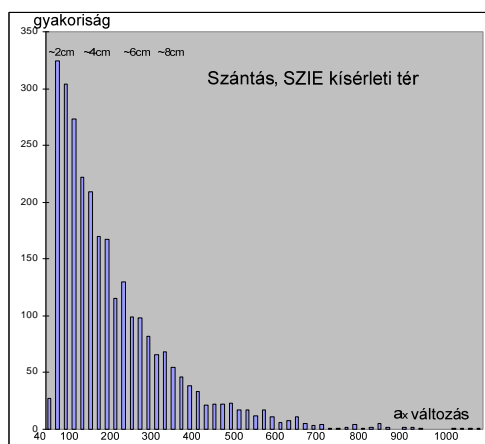
Figure 7. Frequency diagram

Because of these disturbances we made statistically processing too. Figure 7 shows the frequency of a_x differences, while mobile robot platform goes in an experimental field.

References

[1] Banatre, M. et al.: Cooperating Embedded Systems and Wireless Sensor Networks, Wiley, USA, GB, 2008, pp.: 31-51.

[2] 21 ideas for the 21st century. Business Week, pp. 78-167. 1999. Aug.

[3] Mark Holler: High Density, Multiple Depth, Wireless Soil Moisture Tension Measurements for Irrigation Management. White paper: Crossbow Inc. 2008. pp: 1-8.

[4] Blahunka Z., Faust D: Intelligens vezeték nélküli mérőhálózatok rádiófrek-venciás kommunikációja mező-gazdasági környezetben. Gép, LIX évfolyam 2008. pp:7-11.

[5] Faust. D.: Gépek és rendszerek üzemeltetése. SZIE, Gödöllő, 2007. p: 33.

[6] Ont he Soil Roughness Parametrization Problem in Soil Moisture Retrieval of Bare Surfaces from Systematic Aparture Radar. Senssors ISSN 1424-8220, July 2008. pp.4221-4235.

[7] Mobile Ropbots INC. P3 Operations Manual, 2008. pp: 1-63.

Institute for Mechanics and Machinery

Professor Dr. István SZABÓ,
Director of the Institute

Dear Reader,

The Institute for Mechanics and Machinery has been known for integrating fundamental engineering disciplines in the fields of classical mechanics, design, computer aided technologies, and machine constructions since 2005, when the Institute was established by merging two formerly independent departments. Today it consists of three scientific and educational units:

– Department of Mechanics and Technical Drawing
– Department of Machinery
– Department of Agricultural and Food-industrial Machines
– External organization: Department of Biotechnics

Courses provided by our staff covers a wide range from basic engineering areas (e.g. computer aided drawing, statics, strength of materials etc.) to more specialized domains (biomechanics, computer aided analyses, machine design, biosystems engineering, digital image processing, etc.) at all levels of studies (Post secondary, BSc, MSc, PhD).

The Institute for Mechanics and Machinery focuses on several advanced research areas. Running projects financed by the European Union, the Hungarian National Office for Research and Technology and also by industrial partners. Activities are concentrated around the following key topics:

– Biomechanics
– Applied engineering numerical methods
– Computer based modeling and analyses
– Advanced methods in engineering design
– Energy purpose biomass production

Selected papers published in the following section – with some limitations due to the physical boundaries of the Letters given – may give some impression of the scientific activity and interest of the researchers working at the Institute for Mechanics and Machinery.

www.gek.szie.hu

Mechanism Analysis and Synthesis with Computer Aided Methods

István SZABÓ, László KÁTAI

Department of Machine Construction, Institute for Mechanics and Machinery

Abstract

Main objective of this paper is further investigation of complex computer aided engineering tools and systems in defining and experimenting new methods of machine design. A four bar mechanism with pre-defined parameter set was designed using evolutionary algorithms and the result geometry was linked directly to engineering modeling software package. Further investigation has been made for analysing the deformation effects on the pre-defined trajectory.

Keywords

computer aided design, mechanisms synthesis and analysis, genetic algorithm.

1. Introduction

The four-bar mechanism is a simple construction, nevertheless widely used in different machinery due to its versatility and wide spectra of motion. It is a popular mechanism in industrial and farm machinery applications as well as in different manipulators, robots, harvesting machines, etc. The importance can be underpinned with the fact that many complex kinematical structures are derived from this class of mechanism. In case of farm machinery applications these mechanisms are used mainly to provide pre-defined trajectory motion. One of the application examples of the four-bar mechanisms is the straw shaker widely used on different combine harvesters. In this case the basic criteria of the motion is that significant part of the trajectory should coincide with a straight line in order to minimize the damage of the harvested material and maximize efficiency during the working process. Synthesis of a four bar mechanism with given trajectory is rather difficult.

In certain cases the deformation of the mechanisms links can cause problems because of the modification of the pre-defined trajectory. The further aim of this paper is to analyze the mentioned dynamic effect.

2. Analysis of the straw shaker mechanism

The working principle of the straw shaker can be interpreted as a simple four-bar mechanism in which the point P connected to the coupler. The skeleton of the examined construction is shown in Figure 1.
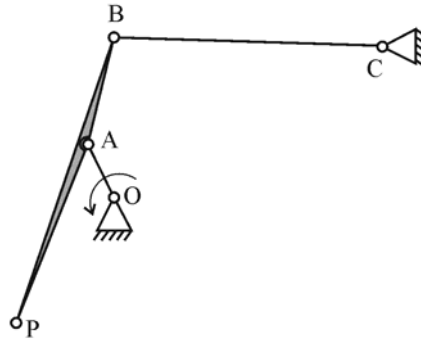
Figure 1. Skeleton of straw shaker construction

At the beginning a mechanical model was created in order to define the kinematical parameters of the mechanism. Although all the geometry (ie. lengths of bars) could have been identified with GA, to restrict the scope of analyses only position of P were set as variables.

Selecting the appropriate coordinate system one can define the P coordinates in the function of crank rotation angle (α_2) according to Figure 2.[2]

The position of certain points of four-bar mechanism can be defined with the length of links (l_1, l_2, l_3, l_4) and their angular position. Concerning the O_2O_1A, and ABO_2 triangles with cosine law the necessary angles can be defined [1].
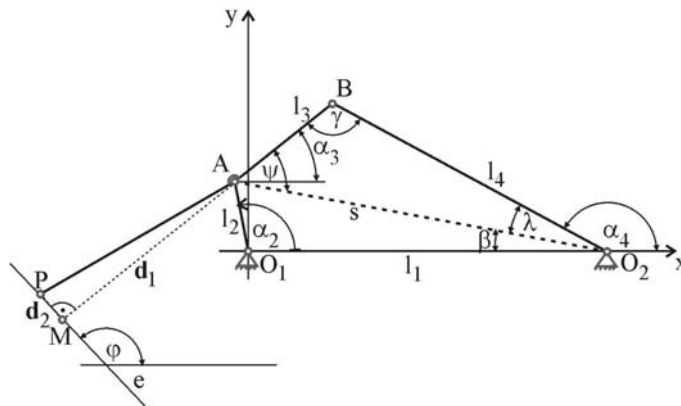
Figure 2. General geometry of a four-bar mechanism

$$s = \sqrt{l_1^2 + l_2^2 - 2l_1 l_2 \cos\alpha_2}$$

(1)

$$\beta = \arccos\frac{l_1^2 + s^2 - l_2^2}{2l_1 s}, \;\; if \; 0 \le \alpha_2 \le \pi$$

(2)

$$\beta = -\arccos\frac{l_1^2 + s^2 - l_2^2}{2l_1 s}, \; if \; \pi \le \alpha_2 \le 2\pi \tag{3}$$

$$\psi = \arccos\frac{l_3^2 + s^2 - l_4^2}{2l_3 s} \tag{4}$$

$$\lambda = \arccos\frac{l_4^2 + s^2 - l_3^2}{2l_4 s} \tag{5}$$

$$\alpha_3 = \psi - \beta \tag{6}$$

$$\alpha_4 = \pi - \lambda - \beta. \tag{7}$$

The searched point P coordinates can be found with the help of point M. further:

$$x_B = l_1 + l_4 \cos\alpha_4; \; y_B = l_4 \sin\alpha_4, \tag{8}$$

$$x_M = x_A - d_1 \cdot \cos\alpha_3, \tag{9}$$

$$y_M = y_A - d_1 \cdot \sin\alpha_3, \tag{10}$$

Therefore point P coordinates are:

$$x_P = x_M - d_2 \sin\alpha_3; \; y_P = y_M + d_2 \cos\alpha_3 \tag{11}$$

The input for the GA was vector $D=[d_1,d_2]$, and the search was limited according to boundary conditions

$$g_j(D) \le 0 \tag{12}$$

for j=1,2….m.
   (Further criteria was that the straight line section of the trajectory should close angle φ with x axis – in general term with line O_1-O_2.)
   In this paper we give a general outline about a research field connected to a perspective new mechanisms design method based on evolution algorithm. A new method is explained where geometry of the model is generated using genetic algorithm (GA).

160

3. Using genetic algorithm for synthesis of mechanisms

The centre element of the examination is a genetic algorithm which can be applied to solve wide spectra of technical and economical problems. With the help of the genetic model solution populations could be generated from which we should choose the most appropriate "individuals" with the help of fitness function. Furthermore information transfer (crossover, recombination) among these "individuals" should be allowed.

The GA followed the procedures given in Figure 3. For the analyses MATLAB 7.0 GA Toolbox was used, with 50 members population, applying Gaussian mutation and ranking based uniform crossover (termination criteria: 200 generations, or 50 generation stagnation).

Figure 3. Schema of the Genetic Algorithm
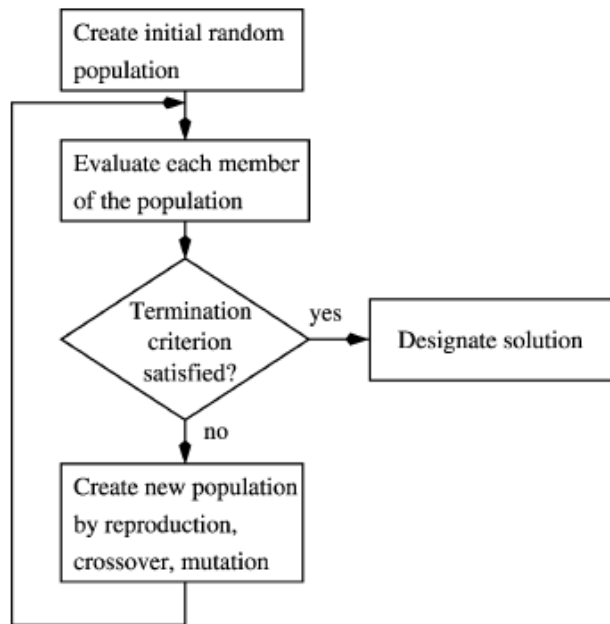
In general case the optimalization means the minimalization of a complex target function according to the followings:

$$\min f\left[p_1(D), p_2(D)...p_n(D)\right] \qquad (13)$$

D is a parameter represents the solution variations, in this concrete problem case, **D**=[d_1,d_2] two dimensional vector;

p_1, p_2…p_n is a function defining the „goodness" quality of solutions **D.**

During the definition of search space the algorithm assumes certain boundary conditions. In general we name it:

$$g_j(D) \leq 0 \tag{14}$$

every j=1, 2, 3...m case.

In this concrete solution the aim was to create a mechanism effects a straight line section of trajectory in the predefined coordinate system (Figure 2.) as describe below:

$$A \cdot x + B \cdot y + C = 0 \tag{15}$$

Connected to each solution it has been examined with defining the $\pm\varepsilon$ interval parallel to the straight line. Furthermore the length of trajectory falling into this interval has been determined.

Considering that the trajectory has parametrically, in the function of rotation of the crank (I_2) been defined, so that during the examination T=360 trajectory points were identified. For determination distance from the straight line Hesse formula was applied:

$$\partial = \left| \frac{A \cdot x_p + B \cdot y_p + C}{\sqrt{A^2 + B^2}} \right| \tag{16}$$

The fitness functions can be described to the followings:

$$\Delta = 1 \text{ ha } \delta \leq \varepsilon$$

$$\Delta = 0 \text{ ha } \delta > \varepsilon \tag{17}$$

In this manner

$$p = \sum_{t=1}^{T} \Delta(D,t) \tag{18}$$

The target function:

$$\min\left[-p(D)\right] - p \tag{19}^*$$

4. Analysis of the deformation

The given straw shaker mechanism analyses was made by Adams software package. During the test procedure the link l_3 (PAB) was substituted by flexible body. This can be made with the help of a so called modal neutral file (mnf).

The model neutral file of the given link can be created in a FEM software package (in our case ANSYS was applied). The main steps of the procedure is shown in figure 4.
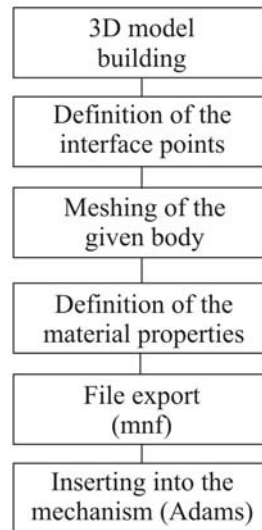
Figure 4. Schema of the flexible body model creation

On the working point (P) of the mechanism we applied external force (250, 500, 750, 1000 N) and analysed the trajectory.

5. Results

In the concrete examined case a mechanism was generated with the following data (length are given in mm):

l_1	l_2	l_3	l_4	T	A	B	C	ε
60	10	20	52	360	1	1	50	2

The applied parameters of the genetic algorithm:
Population: 20 elements, scalar;
Suitability scale:" placing based";
Separation: uniform, stochastic;
Mutation: Gauss-type;
Boundary condition: $0 < D[d_1, d_2] \leq 100$;
Pause conditions: 200 generation, or 50 generation stagnation.
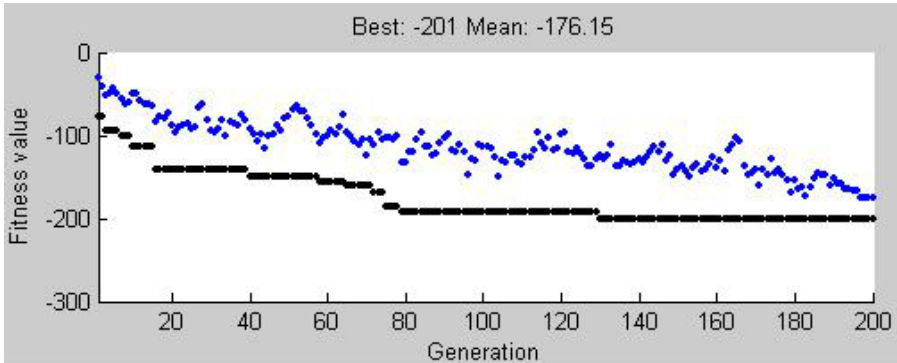
Figure 5. Result of the algorithm

As a result of the model creation the best solution was received around the value **D= [40,356, 16,248].** In this case 201 trajectory point were in the $\pm\varepsilon$ interval defined the straight line section.

Results showed that GA can be used in complex design procedures. It is obvious that GA based optimum seeking can be extended to more complex cases and may be useful in multi-objective optimisation as well.

Concerning the deformation the following figure shows the differences between the original and the deformed trajectories. (In the starting position the l_2 link is in vertical position).
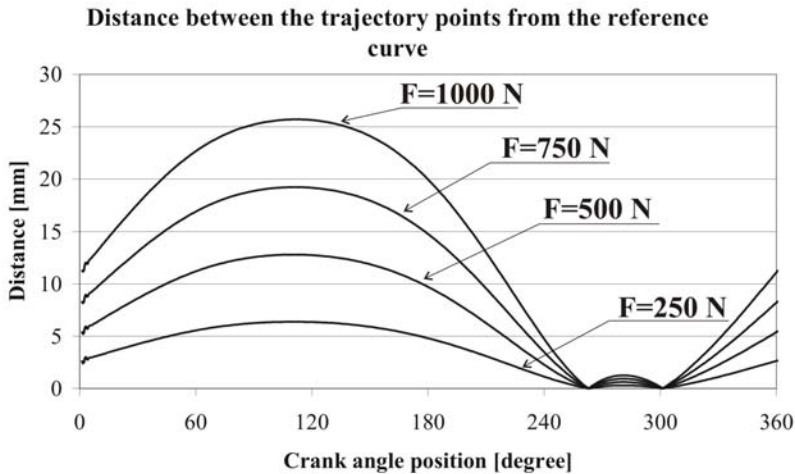
Figure 6. Differences between the trajectory points during one ful rotation

This method gives possibility to examine the borders of maximum load capacity and to assess the working quality of the mechanism.

164

References

[1] Borgulya I. (2004): Evolúciós algoritmusok, Dialóg Campus.

[2] Szabó I. – Kátai L. (2005): Négycsuklós mechanizmus számítógépes analízise Gép, LVI. year, 2005. 11-12. No.

[3] J.E.Shigley – J.J. Uicker (1995): Theory of Machines and Mechanisms. McGraw-Hill

The Effect of Arching on the Outflow Properties of Silos

István OLDAL, István KEPPLER

Department of Mechanics and Technical Drawing,
Institute for Mechanics and Machinery

Abstract

The outflow properties of silo's are the most important parameters of their design. The discharge rate of granular material from silos differs from the discharge rate of containers filled with liquids (it does not depend on the filling height). We demonstrate here, that the constant discharge rate of silos is caused by the formation and collapse of arches in the bin.

Keywords

Outflow, Arching; Granular material; Silo

1. Introduction

The special mechanical behavior of granular assemblies complicates the engineering design process in cases when the interaction with granular materials must be modeled. Granular materials sometimes can be modeled as solid bodies, sometimes as liquids, but there are cases, when none of these two models can be used. One of these cases is the modeling of the outflow of granular material from silos. Unlike in case of fluids, the outflow rate of silos is constant (independent of the height of material above the outlet). Beverloo (1961) and Johannson (1965) evaluated the outflow rate of silos for different cases. We developed a new model for the outflow process, based on the assumption that the constant discharge rate of silos is caused by the formation and collapse of arches in the bin.

2. Silo outflow experiments

To determine the outflow properties of silos, we created two types of model silos (fig. 1.) The bigger silo model was 1250 mm high, its diameter was 440 mm which resulted 0.18 m^3 volume, the silo's hopper was changeable. The outlet diameter changed from 100 mm to 50 mm in case of bin change. The cone half angles were 30°, 45°, 60°. We measured the amount of out flowing material as a function of time.

The smaller silo model was a plastic cylinder having 100 mm in diameter. The hopper was conical and its cone half angle was 45°. We varied the outlet diameter from 25 mm to 100 mm during the experiments. The load was

measured by two load cells. We used grain wheat for the outflow experiments. The aim of the outflow experiment was the determination of the effect of cone angle and outflow aperture size on the outflow rate of the model silo. Our experimental investigation showed that the outflow process is highly affected by the formation and collapse of arches in the bin. To confirm this, we examined the flow of dry sand through a hour-glass aperture. We made high speed photographs of the outflow process.

Figure 1. Model silo measurements
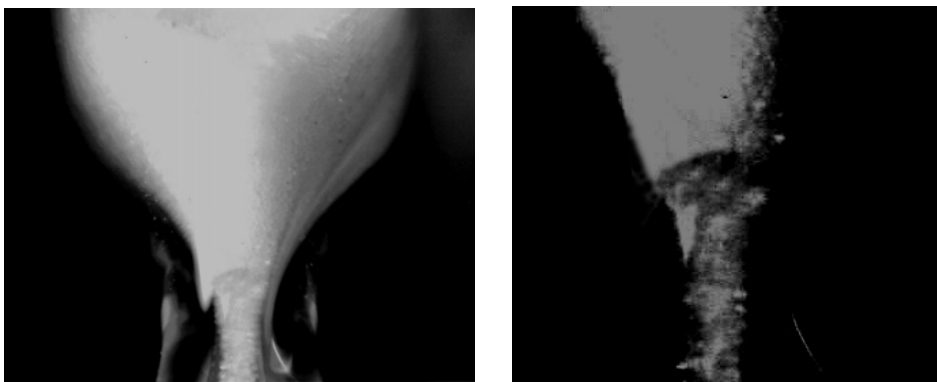
Figure 2. Formation and collapse of arches in the sand-hour

We found that *the formation and collapse of arches gives the special discharge rate of granular materials*. In case of fluids, the flowing velocity and

discharge rate changes with fluid level. In case of granular materials, the velocity is constant (independent of the filling level of silo).

3. Arching phenomenon

Arching phenomenon means the formation and collapse of self supporting arch like "layers" of granular material inside the granular assembly stored in silos. Sometimes these arches are capable to bear the load arising from the weight of the material above them, and block the outflow of granular material. As we will see later, above a critical bin half angle, arching occurs almost every time during the outflow of material from the silo bin, and the most important question in arching theories is the stability of the arches taking form. This stability of arches has great influence on the type of outflow from silo.

Jenike's studies (Jenike 1964) initiated the research activities of analyzing theoretically the arch formation and collapse process in granular assemblies. The first theories were based on the so called *structural mechanics approach* (SM), regarding the granular material as isolated structural members, evaluating the forces acting on separate layers as weight induced stresses. The SM analysis of arching is based on the evaluation of the consolidating stresses, and the stresses acting on the isolated arches. Scientists using SM evaluate the vertex radial stress field causing the consolidation of material in the hopper. They assume, that the material in the arch layers is in *uniaxial* compression. The arching condition is derived from the comparison of the material's uniaxial compressive yield stress and the greatest major principal stress at the abutment of the arch.

The *continuum mechanics approach* (CM) of Enstad (Enstad 1975) is also based on the evaluation of the vertex radial stress field but considers the global equilibrium of the consolidated bulk material in the hopper. In this theory the minor principal stresses are assumed to change from compression to tension at some point at a critical distance from the apex which point defines the *critical outlet width*.

The outlet size of a silo will here be called critical, if the granular material forms arches and because of this, the outflow stops. Drescher et. al. (Drescher 1995) gave a very detailed summary of the arching theories mentioned above, and showed experimentally that the application of current arching models result large differences between the measured and the predicted critical outlet width values. Matchett demonstrated (Matchett 2007), that the critical outlet dimension showed great variation dependent upon assumptions made. Based on these results, we can say, that there is no adequate method for predicting the critical outlet width of silos.

To get closer to this kind of a good arching model, we tried to create a new one, which is a modification of the CM approach, where the modifications are:
  – new measurement methods and tools for the evaluation of material- and yield properties,
  – finite element based technique for the evaluation of stresses arising in the granular assembly

– a new theory of arch formation and collapse based on detailed experimental investigations of the arching procedure.

3.1 Arching experiments

To create a new arching model, we experimentally examined the arch formation and collapse process in granular media, and measured the material- and failure properties of the materials used in arching experiments and theoretical calculations.

The arch examining apparatus developed by us to examine the arch formation and collapse process can be seen on (Fig. 3). It was a flat bottomed container made from thick walled steel on the sides and the bottom, and plexiglass on the front and back. The vertical load acting on the specimen of granular material was made using weights, the lateral load was adjusted with screws to simulate a ratio of vertical and horizontal loads as it is in silos according to Schulze (Schulze 2009).
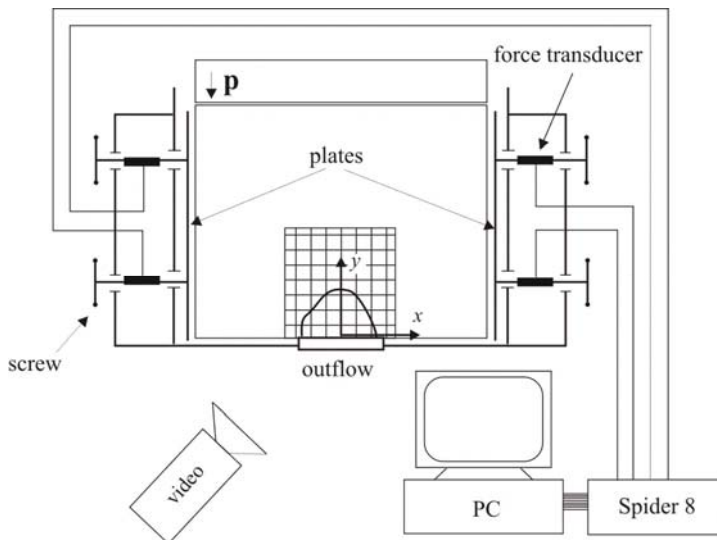
Figure 3. Arch examining apparatus

We used gypsum and cement powders for the arching examinations. After applying the load on the specimen, we started to increase the size of the outflow aperture until the appearance of the first arch. Then we increased the outflow aperture size further, until the collapse of this arch. With the further increase of outflow aperture a number of arches were taking form, until we reached a maximal outlet width, where the collapse of the last arch initiated the outflow of all the material stored in the container. The arch formation and collapse process has been recorded on video camera. Analyzing the videotaped arch formation and collapse processes, we found that

- the arch formation process in most of the cases starts in the middle of the outflow aperture with the fall out of materials, and
- the collapse of an arch starts always somewhere at the foundation of an arch, where "crack lines" penetrate into the granular assembly above the arch.
- During the arch collapse, a number of unstable arches were taking form until the beginning of the outflow of all the material contained within the apparatus.

3.2 Yield in biaxial stress state

In biaxial stress state, the granular assembly is unable to bear compressing load higher than a critical value. This critical value depends on the level of triaxial pre-compression. The granular material is in biaxial stress state if it is placed at the border of an arch (not in uniaxial, as it was supposed in previous models). Knowing the value of this critical value is important for the modeling of arch collapse.

We were able to measure the critical biaxial stress value as a function of the triaxial pre-compression by using our true triaxial apparatus (fig 4.). For this we compressed the specimen in triaxial stress state until a predefined vertical stress, when stresses arising at the horizontal walls prevented the collapse of the granular media.
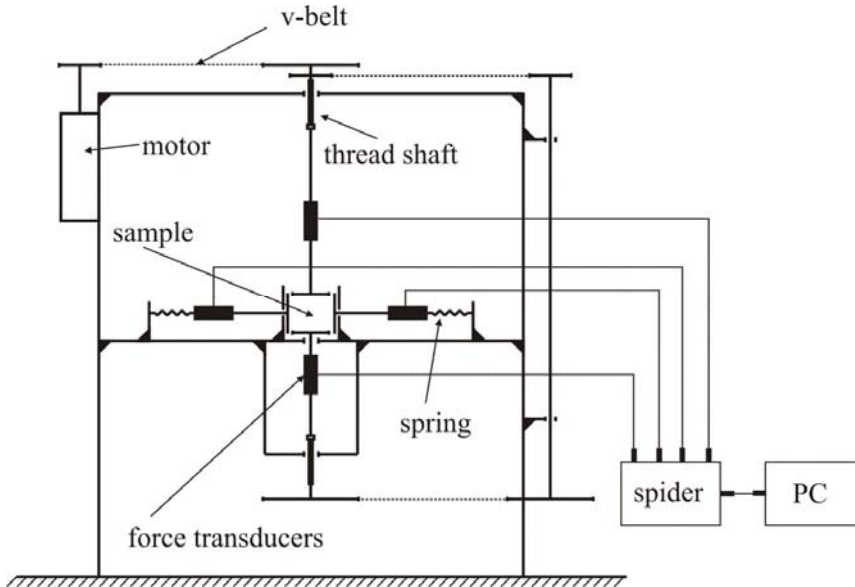
Figure 4. True triaxial apparatus

After the pre-compression phase, we ceased the vertical load to zero, and then removed one of the lateral walls of the specimen's container. After the removal

of the lateral wall, we started to increase the vertical load again (now in biaxial stress state) until the specimen's collapse. On (Fig. 5.) there is a typical vertical loading force characteristics related to one of our critical stress measurements. Knowing the triaxial pre-compressing stresses and the corresponding critical biaxial stress values, the critical biaxial stress function can be evaluated.
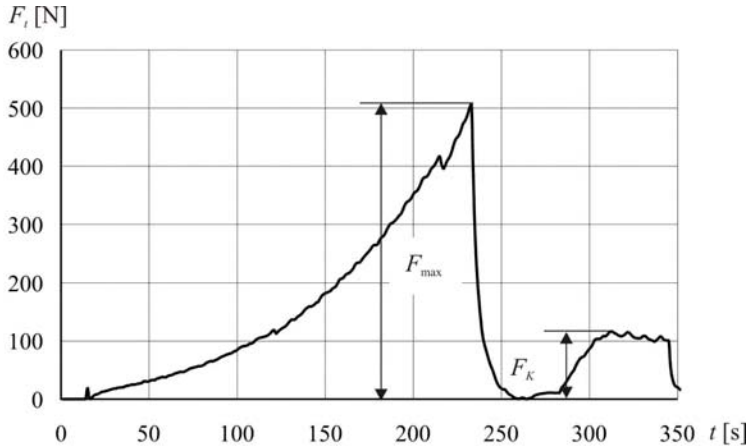
Figure 5. Yield in biaxial stress state

3.3 Stresses in the silo

Knowing the stresses acting on the granular assembly stored in the silo is inevitably important, if we would like to create an adequate arching and outflow model. The scientific investigations made for evaluating the stress distribution in silo's began at 1895, when Janssen (Janssen) evaluated the horizontal pressure acting on silo walls by writing the equilibrium equations of a thin layer of material, using differential slices method (SM method in our terminology). The result of his calculations was an equation analogous to the so called barometric formula used in meteorology, here called Janssen's equation:

$$\sigma_v(h) = \frac{D\rho g}{2K}\left(1 - \exp\left(\frac{2K}{D}h\right)\right).$$

The horizontal silo wall pressure can be evaluated from $\sigma_h = \lambda\sigma_v$ where λ is the ratio of the horizontal and vertical pressure values, which can be evaluated experimentally (Schulze 2009). The EU regulation "EUROCODE 1, Part IV. : Actions in silos and tanks" uses a slight modification of Janssen's method for the determination of silo wall pressure.

The stress distribution in the bin section of the silo is evaluated by using the vertex radial stress field equation

$$\sigma_v(r) = \frac{\rho g r}{1 + N}$$

where N is a constant depending on wall and granular properties.

According to the measurements (Tardos 1999), large stress peaks occur at the joining point between the bin and the hopper. These stress peaks can not be modeled by analytical calculations, and have important effect on the materials arch formation capability.
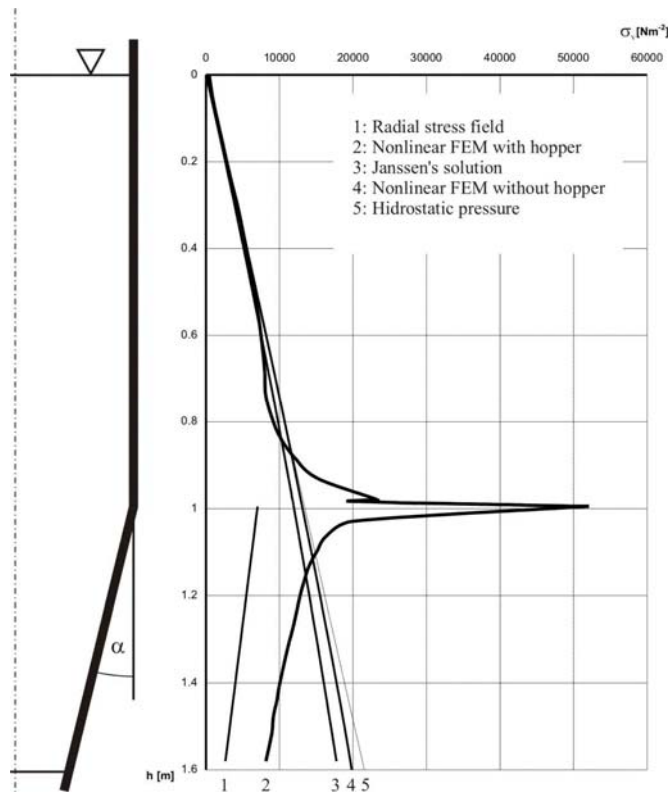
Figure 6. Silo wall pressures determined by different methods

We used ANSYS program for finite element based numerical calculations, with nonlinear stress-strain characteristics from true triaxial measurements as material model, and standard contact pairs with contact detection on Gauss point and Augmented Lagrange method as contact algorithm. PLANE42 2-D structural solid elements were used to model the granular assembly, CONTA172 2-D 3-node surface-to-surface contact and TARGE169 2-D target segment were used for modeling the contact conditions at silo wall. Plane strain stress state was assumed. The symmetry of the silo enabled us to calculate the stresses only

on a half silo, this reduced the time needed for nonlinear calculations. The results of analytical and numerical calculations can be seen on Fig. 6.

There is a good agreement between Janssen's analytical method and the nonlinear finite element model for that part of the silo where the walls are vertical. The radial stress field seems to be underestimate the stresses acting in the hopper. The nonlinear model results a parallel linear stress distribution, but there is a large difference between the two values. The stress peak found in measurements comes out clearly from the nonlinear finite element model also.

3.4 New mechanical model of arching

Our new arching model is based on CM method in the sense that we also define the arching phenomenon as an equilibrium state of the whole material assembly stored in the silo, not as in SM approach, where the stability of individual layers is examined. We started our theoretical investigations using flat bottomed bins. For the determination of stress conditions within the granular assembly, we made a finite element model of the simplest possible flat bottomed container of granular material. The geometrical model is a rectangle shaped domain for the granular assembly placed into the container, with infinite thickness (plain strain condition), and thick walls made of steel. The interaction between the steel wall and the granular material was modeled with contact pairs. The only mechanical assumption, that the granular assembly is unable to bear tension higher than a small minimal value (quite the same condition $\sigma_3 = 0$ is used in CM models) was enough to model the arch formation process.

To analyze the arch formation process we first evaluated the $F(x, y, z)$ stress tensor field within the domain for the case of closed outflow aperture. After this, we opened the aperture for a starting size, and evaluated the stresses again. The opening of the aperture was modeled simply by removing the $u_y = 0$ boundary condition for the finite element nodes at $\dfrac{d}{2}$ distance from the container's centerline. Knowing the stress tensor field according to the opened outlet, we removed from the finite element model the elements loaded with tension, i. e. elements where the first principal stress is positive. We found, that in case of open outlet the first principal stress is changing its sign from tension to compression in a certain height above the outlet.

After the removal of the elements loaded with tension, we evaluated the stress distribution again because of the changes in the boundary conditions caused by the changing of geometry.

Knowing the new stress values, the elements loaded with tension can be removed, and the stresses must be evaluated again. Our calculations showed, that this process stops somewhere because reaching an arch size and shape with these element removals, we will run out of elements loaded with tension. There was always an arch size and shape, which prevents the formation of tension. This means, that after the opening of the container's outlet, there always will

arches taking form within the granular material. These arches are not stable in most of cases, their stability must be examined to find real stable arches.

At the border of the arch taken form because of this transition of first principal stresses from tension to compression, the material elements are in biaxial stress state. In biaxial stress state, the granular assembly is unable to bear compressing load higher than a critical value. Until the third principal stress (which is the higher compressing stress in this case) is higher (compressing stresses are negative) than the critical one evaluated using the yield function, the arch does not collapse. This means that the size of the outflow aperture can be increased without the collapse of the arch until the compressing stresses do go under the critical value evaluated by triaxial measurement.

According to our finite element calculations, the maximal compressing stress value can be found in the vicinity of the bottom of the arch. During our measurements we found, that the "crack lines" started almost in all cases at the bottom of arches, this coincides with the results above.

It is possible now to formulate the necessary condition of arch collapse: the compressing stresses acting on the material in biaxial stress state at the bottom of an arch must be higher than the critical biaxial stress value, which critical value depends on the material properties and the pre-compressing stresses.

3.5 Arching algorithm

Using the previous results, we can define the following procedure called arching algorithm.

1. Designate the range of our interest, define the material- and failure properties:
   - density,
   - Young modulus,
   - Poisson coefficient and the
   - yield function belonging to biaxial stress state.
2. Define the boundary conditions. The opening of the outlet can be modeled here.
3. Solve the equations of elasticity with the previously defined boundary conditions.
4. Evaluate the principal stresses.
5. Remove those material elements, where tension occurs, i.e. where the first principal stress is positive.
6. Evaluate the stresses again, using the new geometry.
7. If somewhere at the newly formed border the compression caused by the third principal stress is higher than the critical compressive stress related to biaxial compression, then this material element also must be removed.
8. After the removal of the broken elements go to step 3.

According to our experiences, the algorithm can stop in three ways.
   - The whole material flows out from the container because of tension.
   - The outflow is caused by the combination of tension and compressive stresses higher than the critical biaxial stress value.

– In some cases, the tension ceases, and in the same time the compressing stress stays smaller then the critical biaxial one, this means the formation of stable arches within the granular assembly.

3.6 Arching in the hopper

Examining the third principal stress distribution in the neighborhood of the silo wall we found, that the third principal stress is significantly higher at the transition zone than anywhere else. We also found, that value of the third principal stress is always smaller in case of closed outlet than in case of open outlet: at the bottom of a silo, the biaxial stress value always will be higher, than the triaxial pre-compressing stress. This means, that after the opening of a silo outlet, the outflow of the granular material theoretically will always begin.

After the removal of the material supposed to flow out of the silo, the third principal (compressing) stress will became higher according to our finite element model. Using this result, we may think, that there inside the silo hopper, there will never be any arching phenomenon, because all the material will flow out of it. However, after the opening of the silo outlet, new material slides down to replace the material fallen out at the beginning. The outflow and the sliding down occur in the same time. Because of this sliding down, the maximal stress value at the transition zone can be regarded as the pre-compressing stress acting on the material sliding to the place, where the material is in biaxial stress state.

Arches are taking form inside the hopper, when the critical biaxial stress value calculated from maximal triaxial pre-compressing stress value at the transition zone is higher, than the minimal third principal stress value taking form at the hopper. The quotient of these two stresses will be called stress ratio.

Evaluating the critical biaxial stress function and the stress ratio (compressive stresses), theoretically we can find three different cases.

– If the stress ratio value is higher than the critical stress, than arches do not occur.
– In the case, when the opposite is true i.e. the stress ratio is smaller than the critical one, than arching is taking form.
– The third case the stress ratio function intersects the critical stress function. In this case we can find the critical outlet size.

On Fig. 7. we can see the critical stress function (calculated from critical biaxial stress values calculated as described before) represented by a line, and stress ratio values according to different outlet half angle. This line divides the plane into an arching and a no arching zone. Square means $\alpha = 10°$ bin half angle, circle means $\alpha = 20°$ and triangle means $\alpha = 40°$ half angle of the bin. The same shapes in different position mean three different outlet sizes for the same half angle of the bin, and the stress ratio represented by them decreases as the outlet size is increasing.

It seems, that for bin half angle $\alpha = 20°$, the stress ratio values are lying on the critical stress line, for $\alpha = 10°$ the stress ratio is always higher than the critical stress, and for $\alpha = 40°$, the stress ratio is always smaller than the critical stress line.
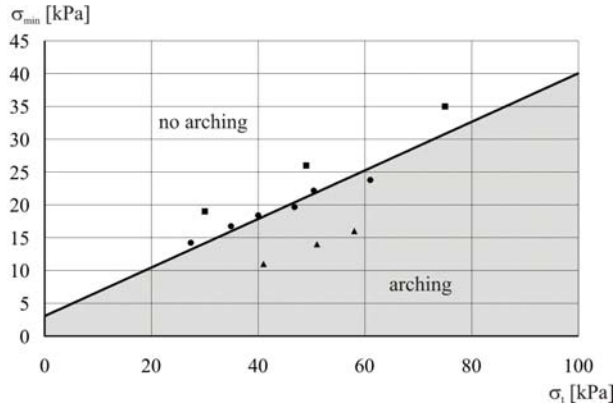
Figure 7. Stress ratio and critical stress function

This means, that for this example, the half bin half angle $\alpha = 20°$, is a critical one according to arching. If the bin half angle is smaller than this critical value, arches do not take form, and when the half angle is higher than this critical one, than arches will take form in all cases. Using Fig. 7. we can say, that there is a critical bin half angle, and in the case of higher half angle than the critical one, arches will always take form during the outflow. If these arches are not stable, they will collapse, and the material will flow out of the bin. But this outflow will be the process of formation and collapse of arches, which differs from the outflow when arches do not take form at all. The difference can be seen by measuring the amount of out flowing material.

4. Predicting the discharge rate

4.1. Theoretical model for funnel flow
In the case when we suppose that the outflow of granular material is a process of formation and collapse of arches in the silo's bin section. The granular material is supposed to be free fall condition below the arch. Flow velocity at the outlet depends on height of falling only. So the first requirement is satisfied by the model namely discharge velocity is constant over height of the bulk material. In order to determine the value of mass flow we have to calculate the velocity.

Because of the assumption of arch formation and collapse during the outflow, the velocity is determined only by height and shape of the arch and the initial velocity. In case of funnel flow, the initial velocity is zero. Falling started from the surface of an arch is described by the function $f(x, \varphi)$. We suppose, that the arch has parabolic shape (Fig. 8.).

$$f(x, \varphi) = h\left(1 - \left(\frac{2x}{d}\right)^2\right)$$
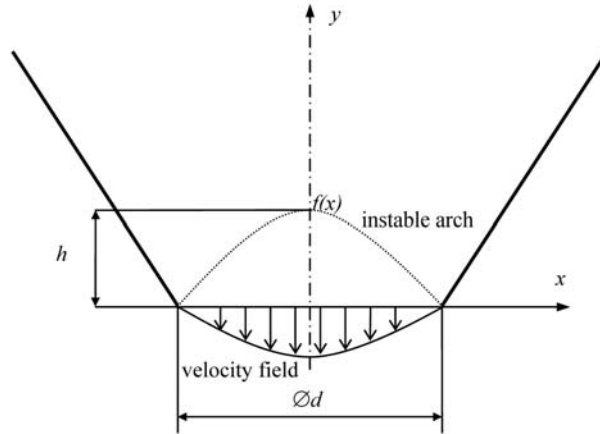
Figure 8. Arch at the outlet of the bin

The velocity in case of free falling is $v = \sqrt{2gh}$.

Using the function of the parabolic surface we get:

$$v(x,\varphi) = \sqrt{2g \cdot h\left(1 - \left(\frac{2x}{d}\right)^2\right)} .$$

The height of an instable arch can not be measured. By introducing $\delta = \dfrac{h}{d}$ shape coefficient of the arch, we get:

$$v(x,\varphi) = \sqrt{2g\delta d} \sqrt{\left(1 - \left(\frac{2x}{d}\right)^2\right)}$$

The average velocity is:

$$v = \frac{4}{d^2\pi} \int\limits_0^{\frac{d}{2}} \int\limits_0^{2\pi} \sqrt{2g\delta d} \sqrt{\left(1 - \left(\frac{2x}{d}\right)^2\right)} x\, d\varphi\, dx = \frac{2}{3}\sqrt{2g\delta d}$$

4.2. Discharge rate

Using average velocity and bulk density discharge rate can be determined. Particles cause declining of outlet size so diameter is reduced with particle size.

$$W = \frac{\pi\sqrt{2g}}{6}\sqrt{\delta}\cdot\rho\cdot(d-d_p)^{\frac{5}{2}}$$

5. Conclusions

To prove our model, we made experiments using model silos with 25, 30, 35, 40, 45, 60, 70, 80, 90, 100 mm outlet diameters. The half cone angle was 45° in all cases. In Fig. 9. we can see the results of measurements made on big and small silos and the computed discharge rates.
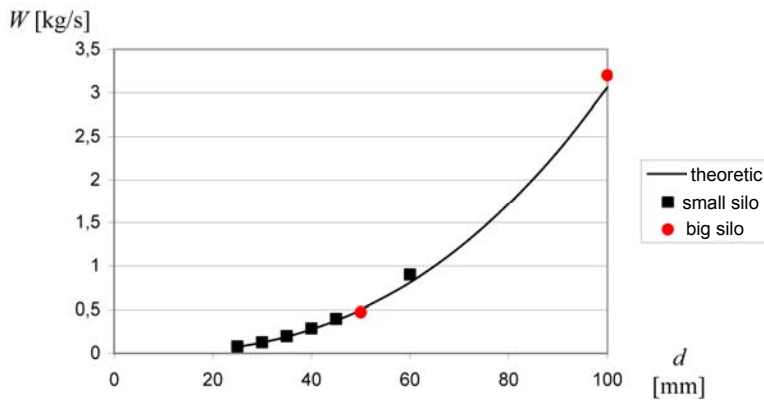
Figure 9. Measured and predicted discharge rates

It can be seen, that our model gives good prediction for the discharge rates in case of small and big silo models also. In the case, when the outlet size is larger than the 60% of silo diameter, the prediction becomes erroneous; our model is capable to model only the case, when the outflow aperture size is below the 60% of the silo diameter.

Acknowledgements

References

Beverloo, R.: The flow of granular solids through orifices, Chem. Eng. Sci. 15, 1961., 262.

Drescher A., Waters A.J., Rhoades C. A.: Arching in Hoppers I-II. Powder Technology Vol: 84 165--183, (1995).

G. Enstad: On the Theory of Arching in Mass Flow Hoppers, Chemical Engineering Science, 30, pp. 1273–1283, (1975).

Janssen H. A. : Getreidedruck in Silozellen, Z. Ver. Dt. Ing., 39, pp. 1045–1049. (1895).

A. W. Jenike: Storage and flow of solids, Utah Univ. Eng. Exp. Stn., Bull. 123 (1964).

J. R. Johansson: Method of calculating rate of discharge from hoppers and bins, Society of Mining Engineers, 1965.

A. J. Matchett: The shape of the cohesive arch in hoppers and silos - Some theoretical considerations. Powder Technology 171 (2007) 133–145.

Dietmar Schulze: Powders and Bulk Solids: Behavior, Characterization, Storage and Flow. Springer, (2007).

Dietmar Schulze: Stresses in silos. http://www.dietmar-schulze.de/spanne.html, (2009).

Gabriel I. Tardos: Stresses in Bins and Hoppers, www.erpt.org/992Q/tard-00.htm (1999).

Pablo Vidal, Manuel Guaita, Francisco Ayuga: Analysis of Dynamic Discharge Pressures in Cylindrical Slender Silos with a Flat Bottom or with a Hopper: Comparison with Eurocode 1. Biosystems Engineering: 91, 335-348, (2005).

A. Couto Yanez, M. Guaita Fernández Et. Al.: Finite element methods for analysis of static pressure distributions in grain silos with eccentric outlets, European

Congress on Computational Methods in Applied Sciences and Engineering ECCOMAS 2000, Barcelona, 11 - 14 September 2000. (2000).

Non-Mechanical Energy Transfer of Electrically Neutral Electrolytes

András SZÁSZ, Olivér SZÁSZ, Gyula VINCZE, Péter SZENDRŐ

Department of Biotechnics,
Institute for Mechanics and Machinery

Abstract

In our present paper we are going to show if electrically neutral electrolyte-flows in a tube, a parallel electric energy-flow can be detected also in the neighborhood of the tube. Also simultaneous appearance of electrical and magnetic fields as well as joint current can be observed. Important consequence of our analysis is that electric energy and electric current occur parallel to the electrolyte-flow taking place in the electrolyte network-system of bio-organism (for example: blood-stream [vascular system], lymphoid-system, urine [urether, urethra] flow, etc.). This effect could have a significant influence on the development of new diagnostic, medical processes as well as on the discovery of water-stream sensitivity, which seems to be a mystical phenomenon for the time being.

Keywords

electrolytes, energy transfer, Poynting-vector, flow

1. Introduction

The electric current density for charge flow is derived usually by the persistent continuous charge-distribution, the discrete behavior of the moving charges generally has not be considered. In this approach the electric displacement-current-density has no role. However, to describe a realistic model for the high-concentration aqueous electrolytes we have to take into account the distribution of the given discrete (anion and cation) charges. The current caused by these charges will have also discrete behavior. Of course, the total current density (as a superposition of the displacement-currents generated of discrete charges) remains continuous: the charge-effective field appears beforehand and afterwards of its passing through a given surface. At this passing procedure the displacement-current density is an odd function of the time, it is automatically eliminated at the averaging. Thus the effects of discrete behavior of the field-carrying charges have no role in a large-time-scale description, but in microscopic studies have to be considered. In this paper we orient our attention to such effects of flowing aqueous electrolytes, which were not in the focus of the description till now.

2. Current conduction in electrolytes

Let us take a single charged particle of electrolyte moving with the speed **v**. Let us suppose that this particle has positive charge (this choice does not influence the final result of calculation). As this particle can be characterized both by its charge and its speed, it carries convective current. In the surroundings of the moving charge a time-varying electric field develops in a form of displacement current. The electric current density carried by the particle is:

$$\underline{\mathbf{j}} = Q\delta(\underline{\mathbf{r}} - \underline{\mathbf{r}}(\mathbf{t}))\underline{\mathbf{v}} + \frac{\partial \underline{\underline{\mathbf{D}}}}{\partial t} \tag{1}$$

Where Q is the electric charge, δ is the Dirac-delta distribution, $\underline{\underline{\mathbf{D}}}$ is the displacement vector and $\underline{\mathbf{r}}(t)$ is the motion function of the particle. If the particle moves along the X-axis according to figure 1, the time function of current density at the position x=0 will correspond to figure 2.a, b and c [Simonyi, 1967].
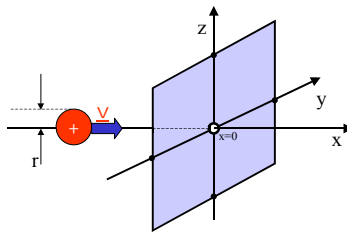

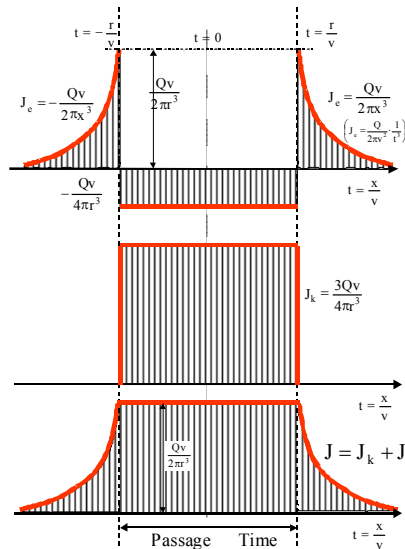*Figure 1.* Passage of charge at the position x=0 on the fixed y-z plane

Figure 2. Displacement (a), convective (b) and summated (c) current density at the passage of a charged particle through a fixed plane

We can see from figure 2 that the displacement current flattens out and pulls out the time function of current. It is clear that this more exact current pattern gives the same result as we may get by applying a simple model without taking into account the displacement current. The proof of this statement is very simple. Take into account that the displacement vector is an even function of the time and take the time average of the displacement current density. Then we get the proof of our statement:

$$\underline{\mathbf{j}}_{ave} = \frac{1}{2T} \int\limits_{-T}^{+T} \frac{\partial \underline{\mathbf{D}}}{\partial t} dt = \frac{1}{2T} \left[\underline{\mathbf{D}}(T) - \underline{\mathbf{D}}(-T) \right] = 0 \tag{2}$$

However by using this more detailed model we may get, later on, more essential consequences.

The flow of negative charged particles is the opposite, as we may see in figure 2, assuming the same charge and speed. As a consequence, the flow of co-directionally moving particles with positive and negative charge in neutral solution will be averaged and the mean value equals to zero. As the passage of particles takes place on the selected plane according to the Poisson statistics, the current fluctuation will be negligibly small in the event of large number of particles as those are inversely proportional to the root of particle numbers.

Let us examine the magnetic field of the particle and the induced energy flow! It is well-know that the magnetic field of a particle moving with the speed $\underline{\mathbf{v}}$ is [Sommerfeld, 1977], [Simonyi, 1967]

$$\underline{\mathbf{H}} = \underline{\mathbf{v}} \times \underline{\mathbf{D}} \tag{3}$$

where $\underline{\mathbf{D}}$ is the displacement vector of the particle which can be expressed as

$$\underline{\mathbf{D}} = \frac{1}{4\pi} \frac{Q}{r^3} \underline{\mathbf{r}} \tag{4}$$

The energy flux density induced by the particle can be calculated by applying the Poynting vector.

$$S = E \times H \tag{5}$$

Supposing that the vector of polarization is proportional to the electric field intensity we get the well-known relationship

$$D = \varepsilon\, E \tag{6}$$

Taking into account the relationships (3), (5) and (6) we have

$$\underline{\mathbf{S}} = \underline{\mathbf{E}} \times \underline{\mathbf{H}} = \varepsilon \underline{\mathbf{E}} \times \left(\underline{\mathbf{v}} \times \underline{\mathbf{E}} \right) = \varepsilon E^2 \underline{\mathbf{v}} - \varepsilon \underline{\mathbf{E}} \left(\underline{\mathbf{v}} \cdot \underline{\mathbf{E}} \right) \tag{7}$$

The result of our calculations shows that the motion of particle is accompanied by electric energy flow. The formula of energy flux density (7) is independent of the sign of the field intensity and accordingly of the sign of the charge. As a consequence, we may establish that the co-directionally moving charged particles induce an electric energy flow of the same direction. According to G. Mie [Mie, 1941], the flow lines of the energy flux density can be seen in figure 3.
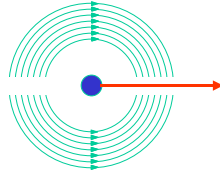
Figure 3. Energy flow lines of a charged particle
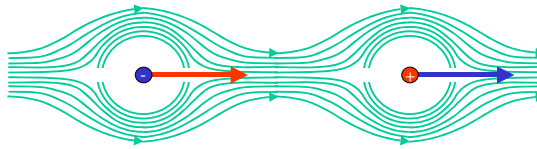
Figure 4. Flow line of several charged particles

It is evident from the above: if a lot of particles move unidirectional in average, this will cause a macroscopic energy flow in the surrounding area in the same direction with the macroscopic flow.

If there is a Poynting vector in the direction of flow, then a photon with the mass per volume unit

$$m = \frac{|\underline{\mathbf{S}}|}{c^2} = \frac{|\underline{\mathbf{E}} \times \underline{\mathbf{H}}|}{c^2}$$

(8)

moves with the speed of light and a

$$|\underline{\mathbf{g}}| = mc = \frac{|\underline{\mathbf{S}}|}{c} = \frac{|\underline{\mathbf{E}} \times \underline{\mathbf{H}}|}{c}$$

(9)

field impulse current density will be generated.

For the appearance of Poynting vector the simultaneous existence of electric and magnetic field strength is necessary, as it can be seen from (4). We can also see from (3) and (4) that the charges of different sign induce electric and magnetic fields of different signs as well. From these two conditions we may

establish that the electric and magnetic field will fluctuate in time under strict phase relationships and in every point of the surrounding field of flow. The time average of this generated electric and magnetic field will be zero. Hence, if the electric and magnetic field fluctuate in time under strict phase relationships the condition

$$\langle \underline{\mathbf{S}} \rangle = \langle \underline{\mathbf{E}} \times \underline{\mathbf{H}} \rangle \neq 0 \tag{10}$$

may be matched up with the conditions

$$\langle \underline{\mathbf{E}} \rangle = 0, \quad \langle \underline{\mathbf{H}} \rangle = 0 \tag{11}$$

By using the same contexture we may see that the fields of charges having different sign do not give any additional effect to the average Poynting-vector as their fluctuation is statistically independent.

Taking into consideration that this process is symmetrical, the field lines of this magnetic field consist of concentric circles surrounding the flux tube. From this fact and on the basis of the excitation law we may conclude that the displacement current is parallel to the direction of macroscopic material stream.

The electric energy current density of an electrolyte-flow

In what follows we give the mathematical formulation of the energy-flow of a moving electrolyte. It is evident, from the physical point of view, that the electric energy flow of the moving electrolyte is resulted by the electric self energy of the moving ions.

Let us give an electrolyte which has n ionic constitutes, then the particle current density resulted by the ions is

$$j_p = \sum_{i=1}^{n} c_i L v \tag{12}$$

where c_i is the concentration i-th ion, L is the Loschmidth number ($L \cong 6 \cdot 10^{23}$) and v is the velocity of bulk electrolyte flow.

If the self-energy of the i-th ion is W_{Bi} then the electric energy current density may be calculated by the equation

$$S = \sum_{i=1}^{n} c_i W_{Bi} L v \tag{13}$$

.

In the case of electrolyte the energy W_{Bi} is called often Born charging energy [Hobbie, 1988]. If the ion has spherical symmetry in electrical point of view then this energy may be evaluated by the integral [Sommerfeld, 1977], [Simonyi, 1967]

$$W_B = \gamma \frac{z^2 Q_e^2}{4\pi} \int_{\infty}^{R_{ion}} \frac{1}{r^2 \varepsilon(r)} dr \qquad (14)$$

,

where z is the valent of ion and γ is an geometric factor which refers to the charge distribution of the ion.

Exact determination of Born charging energy is very difficult, since we don't know the charge distribution of ion and the orientation of the water molecules surrounding an ion. Next problem is that the dielectric permittivity of water close to ion is varied with the distance from the surface of ion. This effect is implied by the saturation of the polarization of the water. In the case of monovalent ion the saturation effect occurs for $r \leq 0.25 nm$ [Hobbie, 1988]. Since in the intra- and extracellular fluid monovalent ions are typical having radius of approx. 0.2 nm the variation of the electric permittivity must be taken into account.

For a monovalent ion the estimated value of the Born charging energy my be found in [Hobbie, 1988] which is $W_B \approx 0.045 eV$.

With this value the equation (13) (in SI units) can be written in the form

$$S = 7.2 \cdot 10^{-21} \cdot \sum_{i=1}^{n} c_i z_i L v \qquad (15)$$

3. Illustrative example

Let us estimate by the equation (15) the energy current density accompanying of a moving electrolyte at different concentrations of NaCl. Let the bulk velocity of the electrolyte be, $v = 2.5 \frac{m}{s}$ which corresponds to the usually flowing speed in the tube of a hydraulic network.

Table 1. Energy Current Density Varies with Concentration NaCl
(estimated values of **S** for the same electrolyte at different
concentrations of NaCl).

Concertration $\left[\frac{mol}{liter}\right]$	$\|S\|\left[\frac{W}{m^2}\right]$
Infinite Dilution	2
0.0005	$1.116 \cdot 10^4$
0.001	$2.232 \cdot 10^4$
0.005	$1.116 \cdot 10^5$
0.01	$2.232 \cdot 10^5$
0.05	$1.116 \cdot 10^6$
0.1	$2.232 \cdot 10^6$

In the case of infinite dilution is distilled water, which contains H_3O^+ and OH^- ions with a concentration. $c_{OH^-} = c_{H_3O^+} = 10^{-7} \frac{mol}{liter}$

In the case of distilled water the Poynting vector is small enough (see Table 1.). If we increase of the NaCl concentration in the water then we get very large values for the Poynting vector.

It is evident that our results can be applied for charged particles of different mobility or even for multi-component electrolytes.

4. Asymmetric role of potentials

If we express the Poynting vector by using the Φ scalar- and $\underline{\mathbf{A}}$ vector-potentials, we get:

$$\underline{\mathbf{S}} = -\left(\underline{\nabla}\Phi + \frac{\partial \underline{\mathbf{A}}}{\partial t} \right) \times \left(\underline{\nabla} \times \underline{\mathbf{A}} \right) \qquad (16)$$

The sign of the scalar potential (Φ) changes, hence, the terms including scalar potential in the expansion of Poynting vector will cancel out after summarizing over the whole system. The Poynting-vector in this approach (at neutral flow conditions) depends on only the $\underline{\mathbf{A}}$ vector-potential (see (17)). Hence, its detection has to build up on the measurements of the vector-potential:

$$\underline{\mathbf{S}} = -\left(\frac{\partial \underline{\mathbf{A}}}{\partial t} \right) \times \left(\underline{\nabla} \times \underline{\mathbf{A}} \right) \qquad (17)$$

Furthermore, the Poynting-vector clearly shows that no energy-flow occurs by static or very low frequency ($\frac{\partial \underline{\mathbf{A}}}{\partial t} \approx 0$) cases.

5. Concluding remarks

The essential consequence of the theory is that in the flowing system of the living organism (for example vascular system, lymph system, urine-flow in urether/urethra, etc.) we may experience also the parallel flow of electric energy.

From the above considerations we may see that only the direction of the motion of particles is important but not the sign of its electric charge.

We may implicate from the Poynting theory that according to the condition $S \neq 0$ also electric and magnetic fields appear in the surroundings of the electrolyte flow. Since the source of magnetic field is the current, we may experience also a current flow parallel to the centre line of tube. This current is the displacement current.

The essential consequence of the theory is that in the flowing system of the living organism (for example vascular system, lymphoid system, urethra etc.) we may experience also the parallel flow of electric energy, impulse and electric current. On this way one may improve the medical diagnostic with a new process. This theory may explain as well why and how some people are able to perceive the swallows.

Reference

Hobbie, R. K. (1988): Intermediate Physics for Medicine and Biology. John Wily & Sons New-York-Chichester-Brisbane-Toronto-Singapore.

Mie, G. (1941): Lehrbuch der Elektrizitat und des Magnetismus. Ferdinand Emke Verlag Stuttgart, (in German).

Simonyi, K. (1967): Electromagnetics. Műszaki Könyvkiadó, Budapest, (in Hungarian).

Sommerfeld, A. (1977): Elektrodynamik. Thun Frankfurt Verlag Harri Deutsh, (in German).

Invited Papers

1. Klaus GOTTSCHALK, Volkhard SCHOLZ
Experimental and Modelling Poplar Wood Chip Drying

The authors' team is research partner of the faculty in the field of energetic research and process modelling.

2. Adriana COTEȚIU, Radu COTEȚIU, Nicolae UNGUREANU
Differential Equations for a Bistable Fluidic Amplifier with Different Phisical Nature Jets

The authors' team is research partner of the faculty in the field of mechanical engineering technologies, mechatronics and process modelling.

3. László KAJTÁR, Miklós KASSAI, István BARÓTFI
Calculation Method for Energy Consumption of Air Handling Units

The authors' team is research partner of the faculty in the field of energetics and environmental engineering.

Experimental and Modelling Poplar Wood Chip Drying

Klaus GOTTSCHALK, Volkhard SCHOLZ

Leibniz-Institut für Agrartechnik Potsdam-Bornim (ATB)

Abstract

Moisture content significantly influences the storability of wood chips. Other factors are mass loss due to microbial metabolic processes and the development of pathogenic moulds causing hygienic problems if the contamination of the bulk exceeds critical quantities. The drying process of the wood chips in the bulk largely depends on particle size and particle size distribution.

Wood chips from poplar were separated to particle sizes of 24 mm, 14 mm and 8,5 mm in average and dried by forced ventilation with heated air. The drying time reached approx. seven days to final moisture content of below 10 % only for large (coarse) sized poplar and willow wood chips. For medium sized particles the drying time was 15 days while on the surface of the bulk of that sample still remained moist. Drying of the small sized chips did not result in satisfying final moisture content within reasonable time. Best results were obtained for large sized wood chips with homogeneous particle size distribution. A thermodynamic model of the drying processes simulates the development of temperature and moisture content in bulks of the wood chips at different heights.

Keywords

wood chip, drying technology, heat transfer

1. Introduction

It becomes important to gain solid bio fuel from arable land as an alternative for farmers to grow woods for combustion. Because renewable energy sources are in competition to fossil fuel it is necessary to develop technologies to process the material for better value return (Scholz et al., 2005). Automatic controlled heating systems can be loaded automatically with wood chips for combustion. Additionally, wood chips can be handled easier during transport and conveying. Wood chips can be stored more compact than wood chunks. Combustion of wood is an alternative to fossil fuel which becomes more important. Finally, wood as fuel material is neutral in CO_2 production. Therefore, it is evident to develop effective processes to produce, handle, and store wood chips for combustion.

Figure 1. Sample of wood chips; medium sized, separated

Figure 2. Sample of wood chips; fine sized, separated

Pre-drying the wood augments the heat value and prolongs the storability. It is therefore usable to dry fresh chopped wood prior combustion or storage. The drying process is strongly dependent on the chip sizes and on the chip size distribution (Scholz, 2004). It was therefore of interest to investigate experimentally the influences of different wood chip size distributions on the drying processes. For this purposes a number of samples with different size distributions were prepared from fresh chopped poplar wood by using a grader to separate samples of different chip sizes (Figures 1 and 2 show examples). Five variants of poplar wood chips of different particle sizes were prepared.

Temperature profiles were measured inside the bulk materials of the samples at different levels. The acquired temperature profiles were used to adapt a thermodynamic model to calculate proceeds of the drying processes. With this model the temperature and moisture content of wood chips in bulk of different particle sizes (coarse - 24 mm, medium - 14 mm, fine - 8.5 mm) can be calculated along the bulk height and time.

2. Experimental investigations

Poplar (var. *Japan 105*) and willow (var. *Salix Viminalix*) were growing on test fields of the institute ATB. Fresh harvested poplar has been cut using a shredder with two different settings to cut the wood into coarse particles of medium sizes (ca. 20 mm) and fine particles of small sizes (ca. 10 mm). A number of samples were separated using a grader to get 3 classes (coarse, medium and fine) of almost homogeneously sized samples. Therefore, samples of poplar with 5 classes of particle sizes (2 non-separated and 3 separated) and 1 sample of willow (non-separated) for comparison have been prepared (Table 1).

Table 1. Physical properties of poplar wood chips

Parameters	poplar non separated		poplar separated		
	coarse g	fine f	coarse fg	medium fm	fine ff
average particle size [mm]	19,5	9,3	23,7	13,6	8,5
bulk height [m]	1,1	1,25	1,05	1,18	1,25
fresh mass FM [kg]	58,05	68,4	56,09	58,37	55,31
bulk density, dry [1] [kg · m^{-3}]	89,04	116,31	89,38	81,16	84,77
dry matter [2] d.m. [%]	48,5	46,7	50,9	51,0	47,8
porosity [-]	0,74	0,66	0,74	0,76	0,75
loss [%]	47.4	33,7	47,8	48,8	40,2
air rate [×10^{-6} m^3 · s^{-1}· kg^{-1}]	115	51,5	650	700	210
air velocity through bulk [m · s^{-1}]	0,01...0,02	0,005..0,010	0,07...0,10	0,09...0,10	0,02...0,03
a [3]	900	1000	300	550	1500
n [3]	1,43	0,87	1,74	1,43	0,75

Rem: [1] after drying experiment; [2] before drying experiment; [3] according to equ. (7)

For the drying tests environment air has been heated to constant temperature of 20 °C and transported to the drying chamber. The airflow was regulated by

using a frequency converter to control continuously the revolution speed of the fan. The drying chamber was divided into 6 compartments with boxes of equal sizes (0.42 m × 0.52 m × 1.4 m) = 0.305 m³, with ground area of 0.22 m² each. All boxes were ventilated with the same air flow regulated to constant temperature (20 °C) and constant air flow rate. Due to different flow resistances for each individual sample of the 6 variants, different air flow rates or flow velocities has been developed in each bulk (box) of the variants.

The drying process for willow and coarse poplar was similar to that of medium sized poplar. But it can be seen from the temperatures for *non*-separated coarse poplar that the top layers of the bulk has not been dried after 18 days and therefore the drying cannot be finished within a reasonable time period for inhomogeneous coarse sized wood chips.

The samples of fine and separated fine poplar had a moisture loss of less than 10 % only after 18 days of continuous ventilation during the drying experiment. Proceed of drying was therefore insufficient for non-separated (inhomogeneous) fine poplar. Additionally, a temperature inversion occurred in the bulk of separated (homogeneous) fine poplar. This phenomenon comes from the development of metabolic heat inside the bulk which cannot be removed.

Comparisons show that separated coarse poplar with homogeneous size distribution had the best drying performance. These positive results came in addition for the reason that relatively high airflow rate through the bulk was developed. The air flow resistances for coarse poplar and willow are almost the same; however, the air flow rates developed differently (Table 1). Willow could be dried quickly within 6 days.
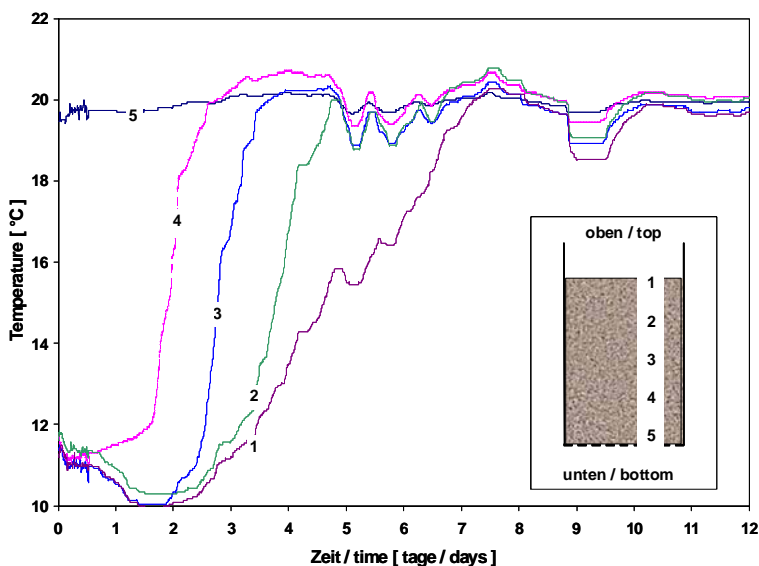

Figure 3. Temperature in wood chips bulk, experiment;
medium sized, separated

The particle size distribution of wood chips influences strongly the drying process of the bulk. The size distribution is also important for handling the chips at the combustion plant. Wood chops with inhomogeneous size distribution and high deviation can cause bridging in the conveyors (Suadicani, 1993). An inhomogeneous size distribution also causes insufficient airflow of the bulk which results in unequal and slow drying. Too fine particles reduce the airflow penetration and the drying process which promotes self heating of the bulk. From the experiments it can be seen that coarse sized wood chips with average size of ca. 25 mm and homogenous size distribution results in the highest drying velocity. Anyway, too big particles may cause problems in the transport systems of the heating plant (Gürtner, 1992; Ebert, 1989).
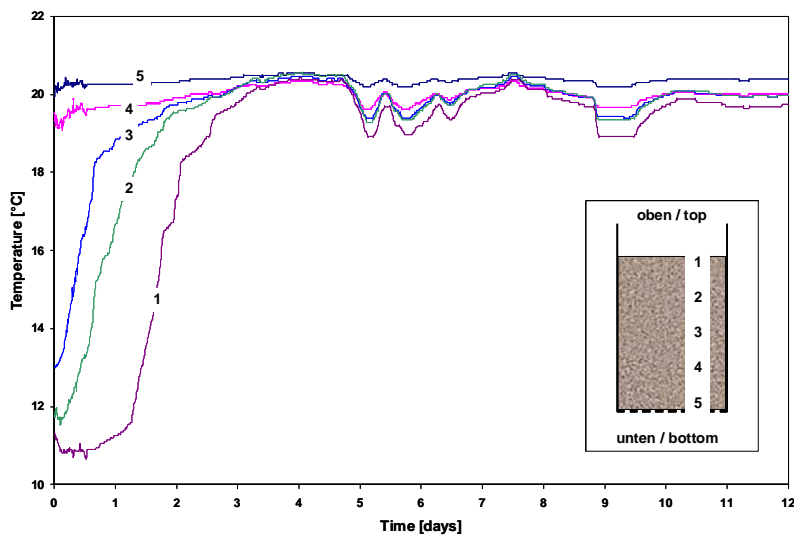

Figure 4. Temperature in wood chips bulk, experiment; coarse sized, separated

3. Model of heat and mass transfer

On homogenous air flow through the bulk of wood chips heat and mass transfer takes place between the particles and the passing air. Heat and mass (water vapour) can transfer in both directions between the particle surface and the air. Particle moisture and air humidity is changing due to mass transfer, while particle temperature and air temperature is changing due to heat transfer. The transfer directions are depending on the 'driving forces'. These 'forces' are water potential differences and temperature differences. While drying, moist is diffusing from inside the particles to the surfaces which is the boundary between particle and air. Therefore, moist on the particle surface can be assumed, since the moisture is diffusing through the material to the surface as long as water potential differences to the humidity of the flowing air exist. The

thermodynamic laws are valid during the interaction of the particle surfaces to the air.

- while a temperature difference between the surface and the air exist, a certain amount of heat is interchanged
- while a partial vapour pressure difference between the moist surface and the humid air exist, water evaporates
- the transfer equations are integrated along the air flow path passing the individual particles

The modelling problem is reduced to a one-dimensional air flow model through a homogeneous bulk. The bulk is divided into a number of layers (discretized spatial differences). The thickness of the layers is chosen as equal to the particles diameter. The heat and mass (water) balance equations are set up in the model. Additionally the heat and mass transfer laws of the boundary layer theory are applied. Finally the state equations for humid air are used. The system of the equations is discretized using the finite difference method (FDM) in time and space. The equations are calculated for each time step along the air flow stream line crossing the layers.

When setting the balance equations the following physical laws are used.

- heat balance, equ. (1)
- heat transfer, equ. (2)
- mass balance, equ. (4)
- mass transfer, equ. (5)
- enthalpy of the evaporation; right hand term of equ. (1)
- pressure head loss within the porous bulk, equ. (7)
- air flow velocity (air flow rate)

By this set the temperature of the air, humidity of the air, temperature of the wood chips and the moisture of the wood chips are calculated transient in the time domain along the height. Some simplifications are taken: (1) the bulk material is homogeneous, i.e. the particle size distribution density is according to a peak function at the particle size; (2) the heat and mass transfer are taken place on discrete layers of the porous bulk material; (3) the boundary conditions at the air inlet and outlet are constant; (4) the bulk height is constant, (5) the physical properties are constant (which means that height and mass loss are neglected).

The system of the model equations is:

$$\frac{dj_Q}{dz} = -c_K \rho_K \frac{dT_K}{dt} + \eta - \frac{dj_m}{dz} \cdot (r_0 + c_{pD} \cdot T_K) \quad \text{(heat conservation)} \tag{1}$$

$$[j_Q]_{Oberfl} = \alpha \ (T_K - T_L) \qquad \text{(heat transfer, surface - air)} \tag{2}$$

$$\frac{dj_Q}{dz} = \frac{\dot{m}_L}{A} \cdot \left[c_L \frac{dT_L}{dz} - r_0 \frac{dx}{dz} \right] \qquad \text{(heat transport, layer - layer)} \tag{3}$$

$$\frac{dj_m}{dz} = -\rho_K \frac{du}{dt} \qquad \text{(mass conservation)} \qquad (4)$$

$$[j_m]_{Oberfl} = k(x_K - x) \qquad \text{(mass transfer, surface - air)} \qquad (5)$$

$$\frac{dj_m}{dz} = \frac{\dot{m}_L}{A} \frac{dx}{dz} \qquad \text{(mass transport, layer - layer)} \qquad (6)$$

The evaporation process is described by the last term in equ. (1). The heat and mass transfer takes place inside the finite boundary layer for the passing heat and vapour between particle surface and air (using the heat transfer coefficient α and the mass transfer coefficient k). Free convective air flow is initiated as long temperature differences inside the bulk (between the layers) and temperature differences bulk to air exist. The air flow is limited by the pressure head loss (equ. 7) of the bulk material.

The air flow resistances of the bulks with the parameters a and n (Table 1, Figure 5) depending on air velocity w passing through the bulk material are calculated with

$$\frac{\Delta p}{h} = a \cdot w^n \quad \text{(pressure head loss } \Delta p \text{ in the bulk divided by height h)} \qquad (7)$$

The parameters were determined by measuring the head losses Δp in the bulk for each sample at different heights h of the box.
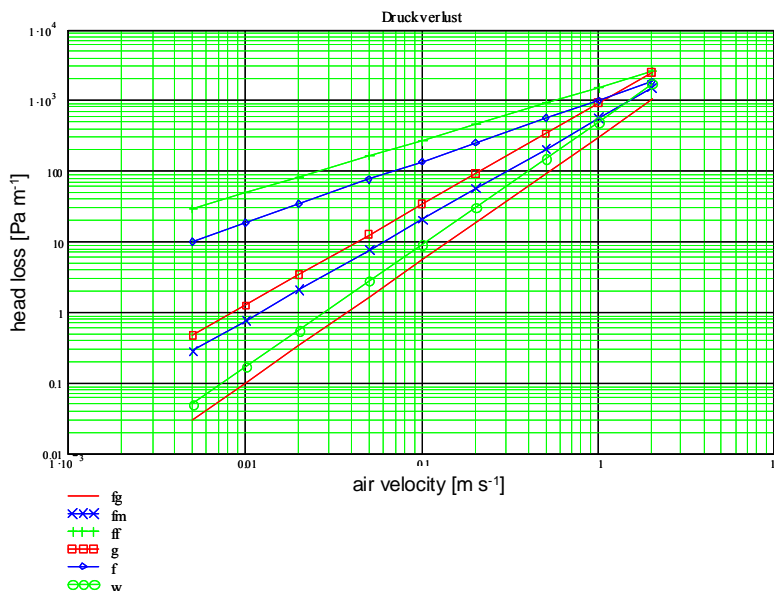

Figure 5. Pressure head loss of air flow through bulks of wood chips at different sizes

4. Results

The results of the experimental tests aimed to investigate the influences of the particle sizes and the particle size distributions and grade of homogeneity on the drying process. Additionally, these results were used to develop and adapt a heat and mass transfer model to simulate the drying process of wood chips.
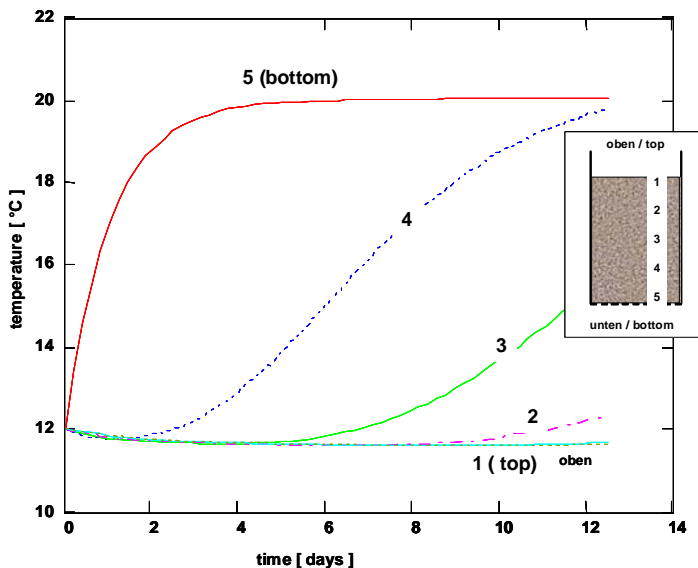

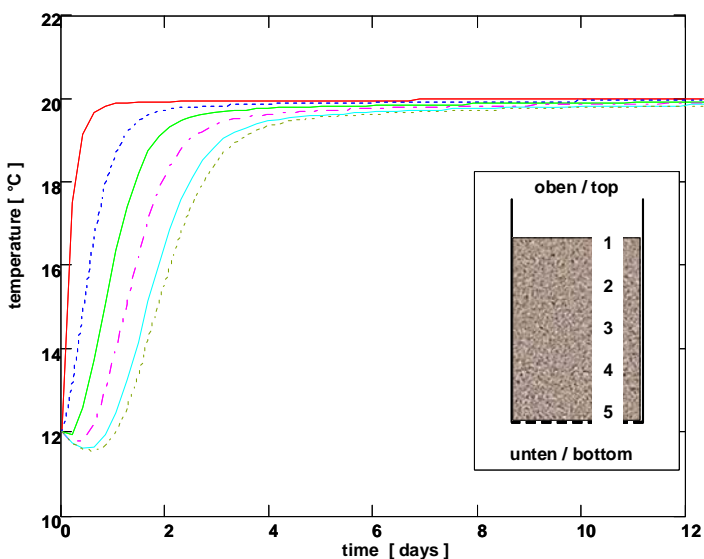*Figure 6.* Temperature in wood chips bulk, model; chip size: coarse, non separated

Figure 7. Temperature in wood chips bulk, model; chip size: coarse, separated

The drying time for separated coarse wood chips was 7 days reaching final moisture content of 10 % (d.b.). For separated medium sized wood chips the drying time was 15 days while the bulk surface of that sample remained moist. Drying of the fine separated chips did not reach the wanted final moist content of 12 % or lower. The best result was obtained for separated coarse (almost homogenously sized) wood chips.

The results of the measurements were used to adapt the model parameters. Acceptable agreements of the measurements and the model calculations could be reached for the different size variants (Figure 6 to Figure 8). The experimental result of the example for medium sized chips is shown in Figure 3. An acceptable agreement model-experiment could not found for separated fine chips. The reason is that the boundary conditions do not yet allow defining time variant conditions in the model for this example.
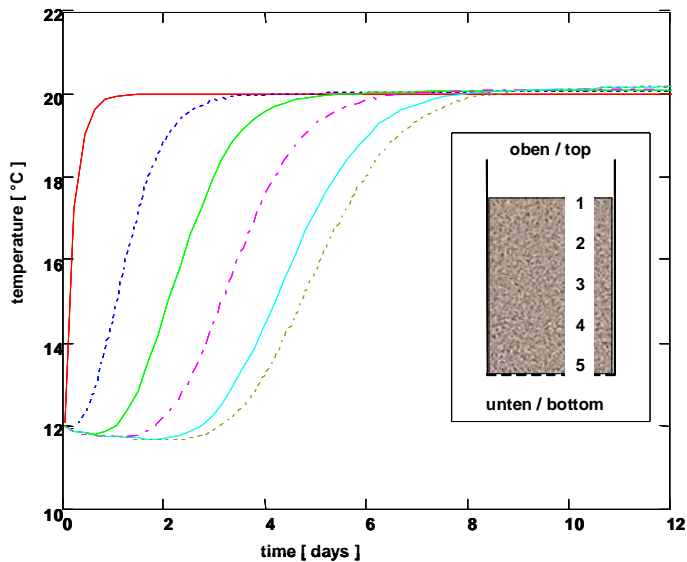

Figure 8. Temperature in wood chips bulk, model; chip size: medium, separated

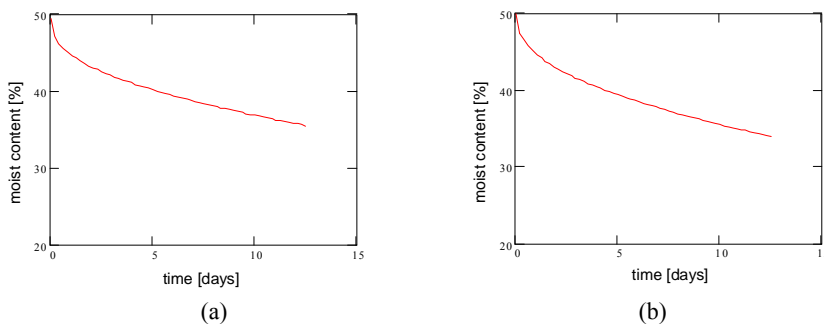(a)   (b)

Figure 9. Model calculations of moisture content in wood chips bulk during drying with cold air at 5 °C, 50 % r.h.; chip size: (a) fine, (b) coarse

Using the model parameters can be varied to predict drying processes. As an example, calculation results are shown in figure 9 for samples of coarse and fine wood chip, drying with air of 5 °C and 50 % rel. humidity.

5. Conclusions

The 'optimal' final moisture content for wood chips to obtain secure storability is recommended to be below 20 % (d.b.), (Gürtner, 1992; Ebert, 1989). This was reached during the experimental drying time for coarse sized (separated) poplar (and non-separated coarse willow wood chips; no more different variants studied here). Almost homogenous coarse sized wood chips with only low additives of fine particles could reach best conditions for air flow through the bulk at highest drying velocity. Calculations with the model allow simulating the drying process for different air conditions. Identifying the parameters from experimental results provided acceptable agreement to the calculated results.

Nomenclature

A	m^2	surface area of particle
c_K	$J \cdot kg^{-1} \cdot K^{-1}$	spec. heat capacity of particle
c_L	$J \cdot kg^{-1} \cdot K^{-1}$	spec. heat capacity of air
c_{pD}	$J \cdot kg^{-1} \cdot K^{-1}$	spec. heat capacity of vapour in air
$\dot{m}$	$kg \cdot s^{-1}$	mass flux
T_K	K	abs. temperature of particle
T_L	K	abs. temperature of air
t	s	time
j_Q	$J \cdot s^{-1} \cdot m^{-2}$	heat flux density
j_m	$kg \cdot s^{-1} \cdot m^{-2}$	mass flux density
k	$kg \cdot s^{-1} \cdot m^{-2}$	mass transfer coefficient
r_0	$J \cdot kg^{-1}$	latent heat of water evapouration
u	$kg \cdot kg^{-1}$	water content of particle
x	$kg \cdot kg^{-1}$	humidity (of air; abs.)
x_K	$kg \cdot kg^{-1}$	humidity (of air; abs.) at surface temperature
z	m	height axis of bulk
α	$J \cdot s^{-1} \cdot m^{-2} \cdot K^{-1}$	heat transfer coefficient
η	$J \cdot s^{-1} \cdot m^{-3}$	heat flux density induced by metabolic heat production
ρ_K	$kg \cdot m^{-3}$	bulk density

References

Gürtner, M, 1992: Energie aus dem Wald. Fachtagung „Energetische Nutzung von Biomasse", Forum für Zukunftsenergien e. V., Landtechnik Weihenstephan, TU München, Band 12 Freising, 27.-28.4.1992, 1992, S. 190–192

Ebert, H.-P., 1989: Heizen mit Holz in allen Ofenarten. Ökobuch Verlag, Staufen i.Br., 1989

Scholz, V. (Ed.), 2004: Energieholzproduktion in der Landwirtschaft. Bornimer Agrartechnische Berichte, Heft 35, 2004

Scholz, V., C. Idler und W. Daries, 2005: Energieverlust und Schimmelpilzentwicklung bei der Lagerung von Feldholz-Hackgut. Bornimer Agrartechnische Berichte, Heft 39, 2005

Suadicani, K., 1993: Verhältnisse bei der Lieferung von Hackschnitzeln. Bericht: „Holz als Energieträger – Technik, Umwelt und Ökonomie". Center für Biomasse-Technologie. Hrsg.: Dänische Energiebehörde, Kopenhagen 1993

Rice, B; O'Donnell, B.; Dodd, V. (1992): Study of Alternative Harvest-Drying-Storage Strategies for Short-Rotation Forest and Forest Residues. Paper AgEng 92, Uppsala, Sweden, 1992

Differential Equations for a Bistable Fluidic Amplifier with Different Phisical Nature Jets

Adriana COTEȚIU, Radu COTEȚIU, Nicolae UNGUREANU

North University of Baia Mare, Faculty of Engineering

Abstract

This paper presents the theoretical researches regarding the differential equations which describe the biphasic mixture motion obtained at the exit of a wall - attachment device. Then, it was verified and augmented with the experimental equations. But this is the subject of other paper. The examined bistable element is a special device with an incompressible fluid as supply jet and air as command jet. In the technical literature no information was given regarding this problem.

Keywords

bistable fluidic element, supply jet, command jet, multi-constituent model, equivalent fluid model

1 Introduction

The theoretical researches regarding the overall equations of the poly-phase fluids motion was made relatively late, in the last decades.

The basis of the mixture fluids theory, as continuous spectrum, was presented by *C. Truesdell.*

In the last time, the scientific researchers' concern about this problem increased thanks to the poly-phase mixture flow applications. These theoretical researches required two mode of action: within the frame work of the multi - constituent model and of the equivalent fluid model [2], [3], [4].

The fluid jet, obtained at the exit of receiving nozzle of the symmetrical bistable amplifier, theoretically and experimentally tested, is a biphasic mixture. It is an oil- gas mixture.

This is the first order nature of poly-phase fluid, because the continuous phase is liquid (oil), while the disperse phase is a gas.

Taking account by the pressure and the temperature values that air dissolves into a liquid (*6-7bar* for water and bigger for oil), that the biggest command pressure value, used in the experimental test, was *3,2 bar,* and that the maximum value of receiving pressure was *4,35 bar,* I adopted, for the differential equations motion establishment, the multi-constituents model.

The model of the bistable fluidic amplifier experimental tested is presented in figure 1.

Figure 1. Distribution plate with bistable fluidic element

2. Continuity equation through viewpoint of the multi-constituents model of poly-phase fluid

In the general case of the poly-phase fluid flow, that a continuous spectrum, it is thought that is form by *N* constituent phase. Each mixture phase is formed by a single material, excepting the interactions and the mass change between them. It is thought that the phases are compressible, that their density are ρ_i *(x, y, z, t),* in a unsteady motion, with the velocity values v_i *(x, y, z, t), i=1, 2...N.*

Through analogy with continuity equation established at a homogeneous fluid, there results the continuity equation for the each phase of the mixture, which not changes substance with other constituent into the control volume [1]:

$$\frac{\partial \rho_i^*}{\partial t} + \nabla \cdot \left(\rho_i^* \vec{v_i} \right) = 0 \ . \tag{1}$$

For a study control volume we make the supposition that the constituents have a mass change - result of the mixture, of the ionization, of the chemical reactions, of the biochemical reactions or of the biological reactions. We note that mass change - h_i and for *i* phase results the general form of the continuity equation:

$$\frac{\partial \rho_i^*}{\partial t} + \nabla \cdot \left(\rho_i^* \vec{v_i} \right) = h_i \quad , i=1,2..N \ . \tag{2}$$

But the partial relative density of *i* constituent [5] is :

$$\rho_i^* = C_i \rho_i , \tag{3}$$

201

where:

ρ_i - is the medium density of the constituent

C_i - is the concentration of the constituent in the poly- phase fluid.

Introucing the relation (3) into (2) there results:

$$\frac{\partial(\rho_i C_i)}{\partial t} + \nabla \cdot \left(\rho_i C_i \vec{v_i}\right) = h_i \;,$$
(4)

where h_i is the local mass change of i phase with others mixture phase, or:

$$\frac{\partial(\rho_i C_i)}{\partial t} + \nabla \cdot \left(\rho_i C_i \vec{v_i}\right) = 0 \;,$$
(5)

without mass change.

For a momentary unsteady regime results the continuity equations equation of the liquid – gas mixture fluid, as biphasic continuous spectrum:

  – for gas:

$$\frac{\partial(\rho_g C)}{\partial t} + \nabla \cdot \left(\rho_g C \vec{v_g}\right) = 0$$
(6)

  – for the carrier liquid:

$$\frac{\partial[\rho_l(1-C)]}{\partial t} + \nabla \cdot \left[\rho_l(1-C)\vec{v_l}\right] = 0 \;,$$
(7)

3. Differential motion equations of the multi-constituent poly - phase fluid.

Generally, for N phases, we obtain the differential motion equations, for each phase, with help of the hydrodynamic's basic principles.

For an elementary volume, delimited all around a point, which belongs to this phase we take account by the momentary cinematic parameters phases', the elementary mass and surface forces, as well as by the local mass changes and quantity of motion changes between all phases.

For i phase, $(i=1, 2...N,)$ quantity of motion equation is:

$$\frac{d\left(\rho_i^{*} \vec{v_i}\right)}{dt} = \nabla \overline{\overline{T_i}} + \rho_i^{*} \vec{f_i} + m_i \;,$$
(8)

where:

  – $\overline{\overline{T_i}}$ - is the symmetric stress tensor;

  – $\vec{f_i}$ - is the unitary mass force;

– m_i - is the part which regards the quantity of motion change between constituents (his transfer from a phase to other).

We noted this change's mass $m_i = \sum_{j=1}^{N} F_{ij}$. It is thought that F_{ij} functions are proportional with relative speed between i and j, phase. That can be expressed that $(v_i - v_j)$.

The proportional control factors are the diffusivities coefficient between gas and liquid phase or other similar coefficients. Taking account by the relation (5) relation (8) becomes:

$$\frac{d\left(\rho_i C_i \vec{v_i}\right)}{dt} = \nabla \overline{\overline{T_i}} + \rho_i C_i \vec{f_i} + m_i,$$ (9)

where $\rho_i C_i = \rho_i^*$ factor is the i phase material density.

The relations:

$$\overline{\overline{T_i}}^s = \overline{\overline{T_i}} + C_i p_i \overline{\overline{I}}$$ (10)

and:

$$n_i = m_i - p_d \nabla C_i$$ (11)

defines the redundant stress tensor $\overline{\overline{T_i}}^s$ and the transfer of the supplementary moment n_i for i phase [5]. In this relation p is the hydrostatic pressure; p_d is the diffusion pressure; $\overline{\overline{I}}$ is the unitary three degree matrix; m_i is the change moment of i phase with others mixture phases

Taking account by the relations (10) and (11) into the relation (8) there results:

$$\frac{d\left(\rho_i C_i \vec{v_i}\right)}{dt} = -C_i \nabla p_i + \nabla \cdot \overline{\overline{T_i}}^s + \rho_i C_i \vec{f_i} + n_i + \left(p_d - p_i\right)\nabla C_i,$$ (12)

where:
– $\frac{d\left(\rho_i C_i \vec{v_i}\right)}{dt}$ is the inertia partial unitary force and unitary elementary convective force;
– $C_i \nabla p_i$ is the unitary elementary pressure force;
– $\nabla \overline{\overline{T_i}}^s$ is the unitary elementary viscosity;
– $\rho_i C_i \vec{f_i}$ is the unitary elementary mass force;
– n_I is the interaction unitary elementary force between phases (advance resistance, portative force);
– $\left(p_d - p_i\right)\nabla C_i$ are the diffusive unitary elementary force;

4. Conservation equations of the internal energy

We add to the continuity equation (5) and to the conservation quantity of motion equation (12) the conservation equation of the internal energy:

$$\frac{d\left(\rho_i^{*}\vec{e}_i\right)}{dt} = \overline{\overline{T}}_i \cdot \overline{\overline{D}}_i - \nabla \cdot \vec{q}_i + \rho_i^{*}\vec{r}_i + \vec{l}_i - m_i\vec{v}_i \ , \tag{13}$$

where:

– $\vec{e}_i$ - is the specific internal energy;

– $\overline{\overline{D}}_i$ - is the symmetric tensor of the rate of strain;

– $\vec{q}_i$ - is the flow density vector of thermal energy;

– $\vec{r}_i$ - is the external heat furnished to the system;

– $\vec{l}_i$ - is the change energy through local transfer of heat with other phases of the poly-phase mixture [2], [3], [5].

5. Jump equations

For the poly-phase fluid we note *[f]* the jump of the *f* field to the interface of constituent phases. For example, the properties jump to the *j* and *k* index phase is:

$$[f] = f^{j} - f^{k} \ , \tag{14}$$

Where f^{j} și f^{k} are the limit values on the interface of the vector / scalar field *f(r, t)* for the *j*, respectively *k* phase, the exterior surface normal $\vec{n}$ of the interface is orients into *k* phase [2], [3], [5].

  Taking account by the integral form of the continuity equation and the conservation quantity of motion equation, given by the relation (15) and (16), it can be expressed the three searched jump equations.
In the relation (15) and (16) which are:

$$\frac{d}{dt}\int_{V}\rho dV = 0 \ , \tag{15}$$

$$\frac{d}{dt}\int_{V}\rho\vec{v}dV = \int_{S}\overline{\overline{T}} \cdot \vec{n} \cdot dS + \int_{V}\rho\vec{f}dV \ . \tag{16}$$

we use the derived formula:

$$\frac{d\rho_i^{*}}{dt} = \frac{\partial\rho_i^{*}}{\partial t} + \left(v_i \cdot \nabla\right)v_i \tag{17}$$

where v_i is the speed to the interface.

Than, we integrate and we obtain the jump equation to the interface. There results:

- the jump equation for the mass, which is:

$$\rho(v - v_i) \cdot \vec{n} = 0 \tag{18}$$

- the jump equation for the quantity of motion, which is:

$$\left[\rho v(v - v_i) \cdot \vec{n} - \overline{\overline{T}} \cdot \vec{n}\right] = 0 \tag{19}$$

and:

- the jump equation for the internal energy:

$$[\rho(e + v^2/2)(v - v_i) \cdot \vec{n} + \left(\overline{\overline{T}} \cdot \vec{n}\right) \cdot v - q \cdot \vec{n}] = 0 \ . \tag{20}$$

In the poly - phase fluid motion equations (5) and (12), because the unknowns' number is bigger than the established equations' number, for the compatibility of the system, we add the joint relations like: $p_i = p_{di}$ *(i=1,2...N)*, when p_i is the hydrostatic pressure of *"I"* phase and p_{di} is the pressure to the interface between fluid phase and *"i" index* dispersion phase. In this case, the last two terms of the relation (12) become zero.

6. Conclusions

- The mathematical model describes the work of the bistable fluidic amplifier both in the stationary regime and in the transitory regime [6], [7]. It was presented in paper [4]. These are:

Goertler ' solutions for the velocity distribution:

$$u = \sqrt{\frac{3J\sigma}{4\rho(x + x_0)}} \sec h^2\left(\frac{\sigma y}{x + x_0}\right) \tag{21}$$

For the attached jet to the wall (stationary regime), we have the following equations:

$$x_1(sau \ x_c) = 2R \sin[(\alpha + \beta + \theta)/2]$$

and:

$$x_2 = 2R \sin[(\alpha + \beta)/2] \tag{22}$$

$$\frac{R}{b_a} = \left(\frac{D}{b_a} + \frac{1}{2}\right)\frac{\cos(\alpha + \beta)}{\cos(\alpha + \beta) - \cos\theta} \tag{23}$$

$$\frac{X_A}{b_a} = \left(\frac{D}{b_a} + \frac{1}{2}\right)\frac{\sin(\alpha + \beta + \theta)}{\cos(\alpha + \beta) - \cos\theta} - \frac{y_a(x_1)}{b_a \sin\theta} \tag{24}$$

$$y_a(x) = \frac{x + x_0}{\sigma}\arg th\left(\sqrt{\frac{x_0}{x + x_0}}\right) \tag{25}$$

$$\cos\theta = \frac{1}{4}[3(t_1 + t_2) - (t_1^3 + t_2^3)] \tag{26}$$

where: $t_1 = th\dfrac{\sigma y_a(x_1)}{x_1 + x_0}$; $t_2 = th\dfrac{\sigma y_a(x_2)}{x_2 + x_0}$

The attachment flow line equation is:

$$\frac{Q_c}{Q_a} = \frac{1}{2}\left[\sqrt{1 + \frac{x}{x_0}} \cdot th\frac{\sigma y(x)}{x_c + x_0} - 1\right] \tag{27}$$

For the S_1, S_2, S_3 subsystems in the transitory regime we have:

$$S_1: \quad T_{d2}'\frac{dp_b}{dt} + p_b = K_{d2}'Q_c,$$

$$S_2: \pm M = p_c \text{ for: } p_b \geq p_{cp1,}$$

$$0 = p_c \qquad\qquad \text{for: } p_b < p_{cp2} \tag{28}$$

$$p_r = p_r(t - t_t)$$

$$S_3: T_a\frac{dp_r}{dt} + p_r = K_a Q_{ac}.$$

or *the transfer functions* corresponding to the attached (*"a"* index), deviation (*"d"* index) and re-attached phase are:

$$H_1(s) = \frac{K_{d2}'}{T_{d2}'s + 1}$$

$$H_2(s) = e^{-\tau_t s} \tag{29}$$

$$H_3(s) = \frac{K_a}{T_a s + 1}$$

The describe function is:

$$N(p_c) = \frac{4}{\pi} \frac{p_{e_{max}}}{p_{cp}} \left[\frac{1}{2} + \frac{1}{2} \sqrt{\left[1 - \left(\frac{p_{c2}}{p_{cp}}\right)^2\right] + \left[1 - \left(\frac{p_{c1}}{p_{cp}}\right)^2\right]} - \frac{p_{c1}p_{c2}}{2p_{cp}^2} \right]^{\frac{1}{2}} \cdot$$

$$\cdot \exp j \cdot \left[arctg \frac{p_{c1} - p_{c2}}{p_{cp}} \cdot \frac{1}{\left[1 - \left(\frac{p_{c2}}{p_{cp}}\right)^2\right]^{\frac{1}{2}} + \left[1 - \left(\frac{p_{c1}}{p_{cp}}\right)^2\right]^{\frac{1}{2}}} \right] \tag{30}$$

And the describe function of the direct way $H_d(s)$ is:

$$H_d(s) = N(p_c) \frac{K'_{d2}K_a}{(T'_{d2}s + 1)(T_a s + 1)} e^{-\tau_t s} . \tag{31}$$

- This model must be supplemented with the relations (4), (12), (13), (18), (19), (20), which was presented in this paper.
- All these equations describe the motion of a poly-phase multi-constituent fluid particle which moves along receiving nozzles, both in the stationary regime and in the transitory regime.
- Finally, the mathematical model was completed with experimental attachment flow line equation. The obtained curves verified jet's progressive attach theory (Coanda Effect).

References

[1] Anton, V., Popoviciu, M., Fitero, I. Hidraulica şi maşini hidraulice, Bucureşti, Editura Didactică şi Pedagogică, 1978.

[2] Coteţiu, A. Studii şi cercetări asupra elementelor fluidice utilizabile în instalaţiile miniere, teză de doctorat, Cluj - Napoca, 1998.

[3] Coteţiu, A. Elemente fluidice de automatizare cu aplicaţii în industrie, Editura Risoprint, Cluj - Napoca, 2004.

[4] Coteţiu, A., Coteţiu, R. Model matematic general pentru descrierea funcţionării unui bistabil fluidic cu jeturi de natură fizică diferită, International Multidisciplinar Conference, University of Baia Mare, 1999.

[5] Florea, J., Robescu, D. ş.a. Dinamica fluidelor polifazice şi aplicaţiile ei tehnice, Editura Tehnică, Bucureşti, 1987.

[6] Florea, S., Dumitrache, I. Elemente şi circuite fluidice, Bucureşti, Editura Academiei Române, 1979.

[7] Florea, S., Dumitrache, I. Cercetarea experimentală a elementelor fluidice, Automatica şi Electronica, nr.5, 1971.

[8] Kirshner, I.M. Fluid amplifiers, McGraw-Hill New-York, 1966.

Calculation Method for Energy Consumption of Air Handling Units

László KAJTÁR* Miklós KASSAI*, István BARÓTFI**

*Department of Building Service Engineering and Process Engineering,
Faculty of Mechanical Engineering, Budapest University of
Technology and Economics,
** Department of Environmental and Building Engineering,
Institute for Environmental Systems, Faculty of Mechanical
Engineering, Szent István University

Research field: energy consumption of HVAC systems, air-conditioning systems, air handling unit, indoor air quality, thermal comfort

Abstract

In accordance with EPBD, energy certification of buildings has been compulsory in Hungary. Additionally energy consumption of heating, air-conditioning, ventilation and lighting shall be calculated separately as well as energy performance of buildings. We worked out new evaluation method of energy consumption air handling units based on probability theory. The new calculation procedure has been developed, in order to determinate energy consumption of air handling units. To achieve this, outdoor climatic parameters (temperature, humidity, enthalpy) have been considered as probability variables. Using this method, comparison between alternative air handling units can be made during the design process.

Keywords

Air handling units, Energy consumption, Probability theory

1 Introduction

From the perspective of air handling technology the key attributes of outdoor air are temperature, humidity and enthalpy. These values randomly vary from minute to minute. The probability theory starts from the bulk of the elementary results of some experiment (e.g.: air temperature measurement). One single real number can be attributed to each elementary event (the measured temperature). The correlation interpreted with this attribution is called the probability variable. There is discrete and continuous distribution probability variable. The air condition values can take any value within a range and may be regarded as a continuous probability variable. A probability variable may have an expected

value, dispersion, distribution and density function. A probability variable with a continuous distribution is characterized by the distribution (F(x)) and density (f(x)) functions. [1]

The probability that the value of probability variable is between „a" and „b":

$$P(a < x < b) = \int_a^b f(x)dx \qquad (1)$$

The distribution function shows the probability of „t" probability variable taking a value less than „x":

$$F(x) = P(t < x) \qquad (2)$$

The distribution functions of outdoor air parameters (temperature, enthalpy) can be applied to determine the actual energy consumption of air handling units [2,3,4]. The temperature, humidity and enthalpy of outdoor air can be accounted continuous distribution probability variable that can be converged as Gauss distribution. [5,6,7].
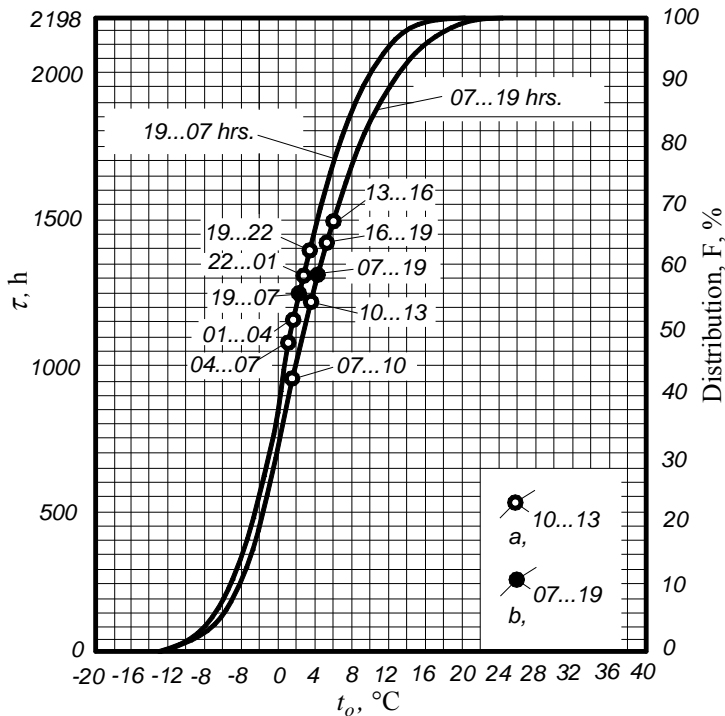

Figure 1. The distribution function of outdoor air temperature from October until March (Budapest, average of measured temperatures between 1964-1972) [9]

Calculation of heating energy consumption it is necessary to take account of variation of outdoor air parameters (temperature, humidity and enthalpy) that vary in daily and season period [12,14]. Making energy calculation of a building, the outdoor air condition values can be regarded as a probability variable that has momentary, maximum, minimum and average values, distribution function which can be defined according daily, weekly, monthly and annual period. We can make more refinements by define a daytime period (07-19 hours) and a continuous operation (0-24 hours) of air handling units. Temperature distribution function is shown on Fig. 1. in that a daytime (07-19 hours) period and nightly period (19-07 hours). Any point of functions show the hours and the percentage of the term when temperature or enthalpy of outdoor air was lower than the examined point. It follows that the τ_{tot} term which concern to the 100% distribution is equal to the reference period. [8]

Integral always can be calculated by the area under the functions during determination of cooling and heating energy consumption. In view of annual energy consumption operational costs can be calculated by knowledge of power and heat cost.

2 The physical and mathematical model

An air handling unit contains two main groups of elements: supply and exhaust units. The main parts of an air handling unit: filter, heat recover unit, pre-heater, re-heater, cooler, by-pass, adiabatic humidifier, fans (Fig. 2.). From these elements have the possibilities to build up different air handling units [10,11]. The main parts of energy consumption are: heat energy, cooling energy, ventilation and pumping power [12,13]. Calculations of these parameters are really complicated by variable efficiency operation of air handling units due to fluctuation of outdoor condition.
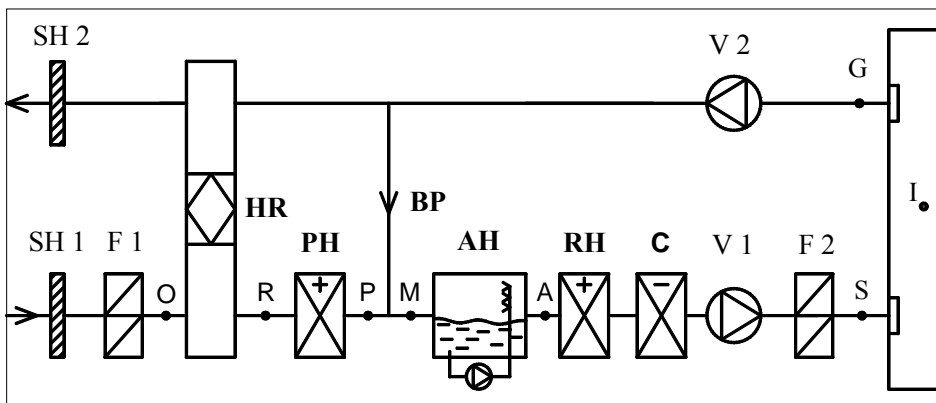

Figure 2. Connection diagram of an Air Handling Unit

The signs of the figure are the followings:
- HR : heat recovery (cross flow heat exchanger)
- PH : pre-heater
- BP : by-pass
- AH : adiabatic humidifier
- RH : re-heater
- C: cooler
- V : ventilator
- F : filter
- SH : shutter against the rain

Determining of energy consumption pumps and fans of AHUs is not complicated whereby they operate by constant efficiency. Heating energy consumption can be calculated by distribution and density functions of outdoor temperature and enthalpy. In this paper air handling process in winter operation is published.

2.1 Energy consumption of heaters:

$$Q_H = \rho \cdot c_{pa} \cdot \dot{V} \int_{-20}^{t_H} F(t_o) dt ; \quad \text{kJ/year} \tag{3}$$

where:
- ρ ; kg/m^3 air density
- c_{pa} ; kJ/kg°C specific heat capacity of air on fixed pressure
- $\dot{V}$; m^3/h air flow rate in heater
- $F(t_0)$; distribution function of outdoor air temperature
- t_H ; °C : air temperature after the heater

2.2 Energy consumption of fan:

$$W_{fan} = \int \frac{\dot{V}_S \cdot \Delta p_{tf}}{\eta_{tf}} d\tau ; \quad \text{kJ/year} \tag{4}$$

where:
- $\dot{V}_S$; m^3/h supply air flow rate delivered by fan
- ΔP_{tf} ; Pa the pressure loss of air handling unit
- η_{tf} ; - the total efficiency of the fan

2.3 Energy consumption of pump:

$$W_{pump} = \int \frac{\dot{V}_{water} \cdot \Delta p_{tp}}{\eta_{tp}} d\tau ; \quad \text{kJ/year} \tag{5}$$

where:

- $\dot{V}_{water}$; m^3/h   supply water flow rate delivered by pump
- ΔP_{tp} ; Pa   lift of the pump
- η_{tp} ; -   the total efficiency of the pump

Integration has to be calculated concerning the annual operation time. Peculiarities of AHUs working are continuous operation (0-24 hours) and intermittent operation (07-19 hours). During the energy consumption calculation of fan and pump integration can be determined easily thereby values of the working point data ($\dot{V}_S , \Delta P_{tf}$; $\dot{V}_{water} , \Delta P_{tp}$) are taken into consideration as constants.

2.4 Fresh air supplied handling unit with pre-heater and re-heater (FAS AHU)
Operation parameters of fresh air supplied AHU with pre-heater and re-heater are shown on the distribution function of outdoor air temperature from October until March in Fig.3.
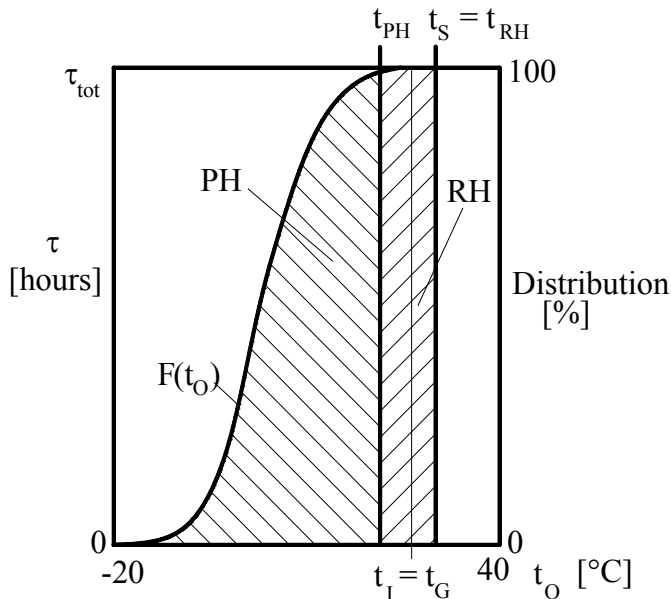

Figure 3. Fresh air supplied by air handling unit in winter time (FAS AHU)

The signs of the figure are the followings:

$F(t_0)$:   temperature distribution function,

t_{PH} ; $^{\circ}$C :   air temperature after the pre-heater,

t_{RH} ; $^{\circ}$C :   air temperature after the re-heater,

t_{S} ; $^{\circ}$C :   temperature of supply air,

t_{I} ; $^{\circ}$C :   temperature of indoor air,

t_{G} ; $^{\circ}$C :   temperature of outgoing air,

t_{O} ; $^{\circ}$C :   temperature of outdoor air.

Energy consumption of pre-heater:

$$Q_{PH} = \rho \cdot c_{pa} \cdot \dot{V} \int_{-20}^{t_{PH}} F(t_o)\,dt\,; \ \ \text{kJ/year} \qquad (6)$$

where:

– ρ ;   kg/m^3 air density

– c_{pa} ; kJ/kg$^{\circ}$C   specific heat capacity of air on fixed pressure

– $\dot{V}$; m^3/h :   air flow rate in heater

Energy consumption of re-heater:

$$Q_{RH} = \rho \cdot c_{pa} \cdot \dot{V} \int_{t_{PH}}^{t_{S}} F(t_o)\,dt\,; \ \ \text{kJ/year} \qquad (7)$$

The areas which shows Fig. 3. are proportional to energy consumption of the elements of air handling unit. In a similar way there is possibility to set up a physical and mathematical model of other air handling unit.

τ_{tot} term which concern to the 100% distribution has to be used for air handling units that are in continuous operation (0-24 hours). Distributions that apply to half day have to be used for air handling units that are in intermittent operation (07-19 hours).

2.5 Fresh air supplied air handling unit with heat recovery, pre-heater and re-heater (FAS-HR AHU)

Operation parameters of AHU with pre-heater and re-heater are shown on the distribution function of outdoor air temperature from October until March in Fig. 4. The signs of the figure are the followings:

– $F(t_{01})$: temperature distribution function after heat recovery,

– t_{R} ; $^{\circ}$C : air temperature after the heat recovery which can be calculated by indoor and outdoor air temperature and technological parameters of heat recover unit.
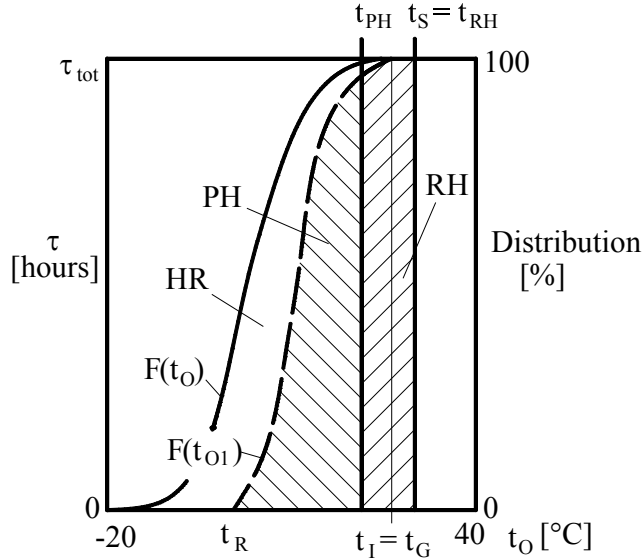
Figure 4. Fresh air supplied air handling unit with heat recovery, pre-heater
and re-heater in winter time (FAS-HR AHU)

Energy consumption of pre-heater:

$$Q_{PH} = \rho \cdot c_{pa} \cdot \dot{V} \int_{t_R}^{t_{PH}} F(t_{o1}) dt \; ; \; \text{kJ/year} \tag{8}$$

Energy consumption of re-heater:

$$Q_{RH} = \rho \cdot c_{pa} \cdot \dot{V} \int_{t_{PH}}^{t_{RH}} F(t_{o1}) dt \; ; \; \text{kJ/year} \tag{9}$$

The areas that are shown on Fig. 4. are proportional to energy consumption of
the elements of air handling unit (PH, RH) and the energy saving of heat
recovery (HR).

*2.6 Air handling unit with pre-heater, air recirculation, adiabatic humidifier and
re-heater (REC-AH AHU)*
The air temperature after the adiabatic humidifier (t_A) can be determined by winter
air handling process on Mollier h-x diagram. Fig. 5. shows the energy
consumption of air handling elements. The areas that are shown on Fig. 5. are
proportional to energy consumption of the elements of air handling unit (PH, RH).
Determining of energy consumption of AHU with by-pass is a similar process
than in the case of fresh air supplied by AHU. The difference between the two

cases is necessary to take account of the effect of the air recirculation during the air handling process. The proportion of air recirculation can be calculated by air volume flows:

$$\frac{\dot{V}_{rec}}{\dot{V}_S} = \frac{a}{a+b} \tag{10}$$

where:

- $\dot{V}_{rec}$; m³/h   re-circulated air volume flow
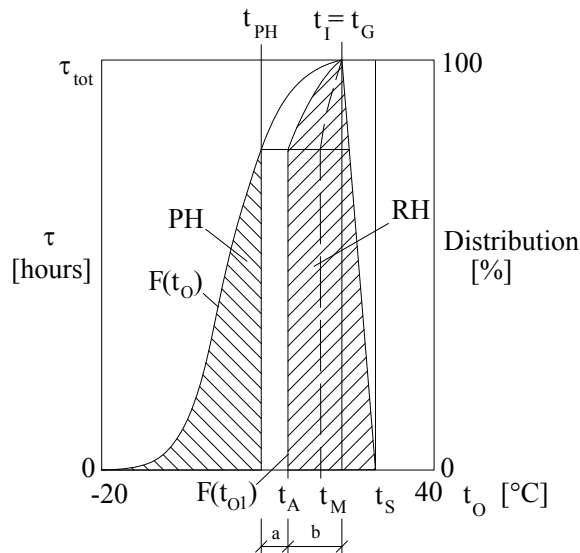- $\dot{V}_S$; m³/h   supply air volume flow.

Figure 5. Air handling unit with pre-heater, by-pass, adiabatic humidifier and re-heater in winter time (REC-AH AHU)

The applied signs on Fig. 5. are the followings:
- t_A ;°C : air temperature after the adiabatic humidifier,
- t_M;°C : air temperature after the air mixing.

Energy consumption of pre-heater:

$$Q_{PH} = \rho \cdot c_{pa} \cdot \dot{V}_{PH} \cdot \int_{-20}^{t_{PH}} F(t_O)\,dt \; ; \;\; \text{kJ/year} \tag{11}$$

where:

- $\dot{V}_{PH}$; m³/h :   air flow rate in pre-heater

Energy consumption of re-heater:

$$Q_{RH} = \rho \cdot c_{pa} \cdot \dot{V}_{RH} \cdot \left[\int\limits_{t_A}^{t_I} F(t_{O1}) dt + \frac{(t_S - t_I)\tau_{tot}}{2} \right]; \; \text{kJ/year} \qquad (12)$$

where:

- $\dot{V}_{RH}$; m³/h :   air flow rate in re-heater,
- $F(t_{01})$:   temperature distribution function after the adiabatic humidifier.

2.7 Air handling unit with heat recovery, air recirculation, pre-heater, re-heater and adiabatic humidifier (REC-AH-HR AHU)
Fig. 6. shows the energy consumption of air handling elements. $F(t_{O2})$ is the temperature distribution function before re-heater.
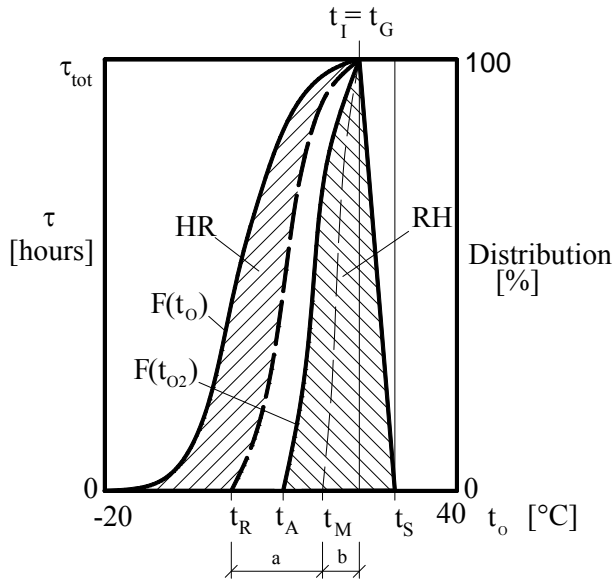

Figure 6. AHU with heat recovery, by-pass, pre-heater, adiabatic humidifier and re-heater in winter time

Energy consumption of re-heater:

$$Q_{RH} = \rho \cdot c_{pa} \cdot \dot{V}_{RH} \cdot \left[\int\limits_{t_A}^{t_I} F(t_{O2}) dt + \frac{(t_S - t_I)\tau_{tot}}{2} \right] \; \text{kJ/year} \qquad (13)$$

The calculation of heating energy consumption can be seen in the above-mentioned air handling units. Energetic analysis can be made in any air handling units in a similar manner with the help of the presented physical and mathematical methods and equations.

3. Results

The energy consumption of four air handling units was analyzed by the developed method. Energetic analysis was made in total heating season which takes from October until March and in the interest of exact energetic calculation was made particularly in a daytime period (07-19 hours) and a nightly period (19-7 hours). The four analyzed air handling units can be seen in under mentioned:
1. Fresh air supplied AHU (FAS AHU)
2. Fresh air supplied AHU with heat recovery (FAS-HR AHU)
3. AHU with air recirculation and adiabatic humidifier (REC-AH AHU)
4. AHU with air recirculation and adiabatic humidifier and heat recovery (REC-AH-HR AHU)

The heating energy consumption of the air handling units from October until March can be seen in the daytime and nightly period in Table 1. and Table 2.

Table 1. Heating energy consumption in the daytime (7:00-19:00)

AHU	PH	RH	Total
	[MJ]	[MJ]	[MJ]
1. FAS AHU	1 158 335	644 640	1 802 975
2. FAS-HR AHU	1 129 161		1 129 161
3. REC-AH AHU	152 868	619 178	772 045
4. REC-AH-HR AHU	-	373 252	373 252

Table 2. Heating energy consumption at night (19:00-7:00)

AHU	PH	RH	Total
	[MJ]	[MJ]	[MJ]
1. FAS AHU	1 235 500	653 488	1 888 988
2. FAS-HR AHU	1 145 563		1 145 563
3. REC-AH AHU	175 977	641 400	817 377
4. REC-AH-HR AHU	-	402 577	402 577

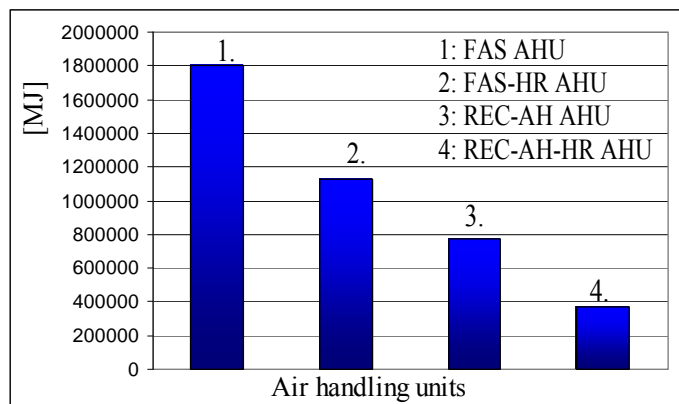Fig. 7. and Fig. 8. show these values in the four air handling cases.

Figure 7. Heating energy consumption
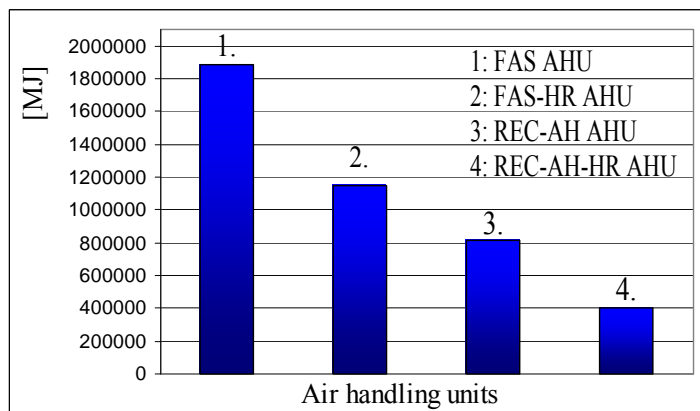in the daytime (7:00-19:00)

Figure 8. Heating energy consumption
at night (19:00-7:00)

Total energy consumption of the four air handling units from October until March can be seen in Table 3. and Fig. 9.

Table 3. Total energy consumption from
October until March (00-24)

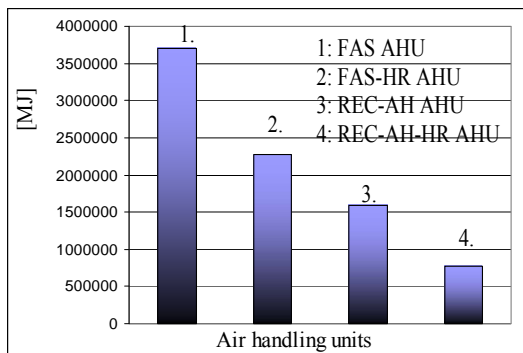| AHU	Heat energy	Pump + Fan en.	Total
	[MJ]	[MJ]	[MJ]
1. FAS AHU	3 691 963	4 806	3 696 769
2. FAS-HR AHU	2 274 724	4 806	2 279 530
3. REC-AH AHU	1 589 423	4 806	1 594 228
4. REC-AH-HR AHU	775 829	4 806	780 634

Figure 9. Total energy consumption from October until March (00-24)

4. Conclusion

Table 4. Rates of energy savings from
October until March (00-24 hours)

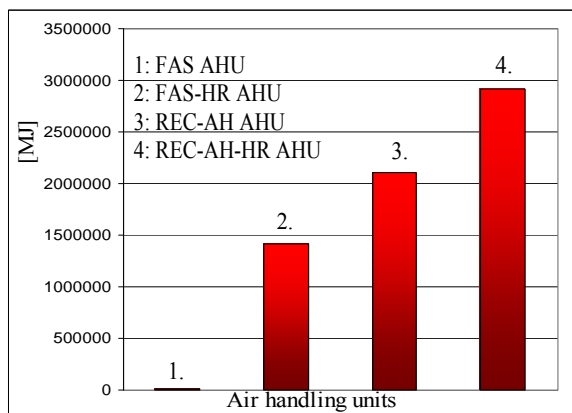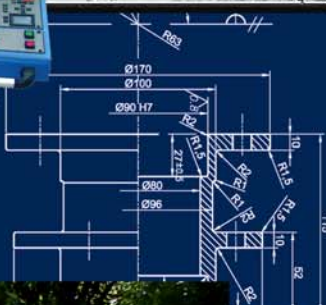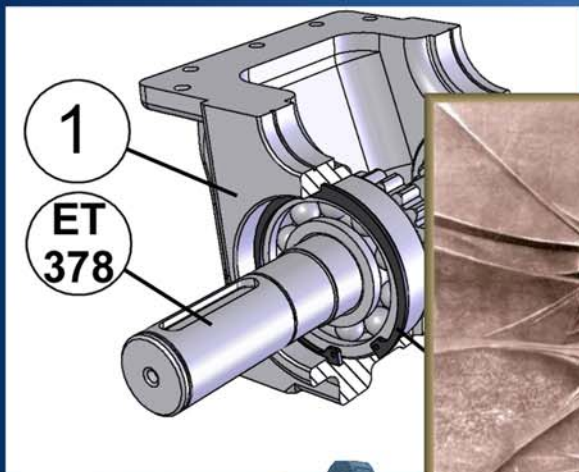| AHU	Energy saving	
	[MJ/year]	[%]
1. FAS AHU	0	0
2. FAS-HR AHU	1 417 239	38
3. REC-AH AHU	2 102 541	57
4. REC-AH-HR AHU	2 916 135	79

Figure 10. Energy savings from October until March (00-24)

On the basis of the new theoretical method it was possible to estimate the energy savings for each air handling units to take into account heat recovery and heat recirculation. Daytime and nightly energy consumptions of the four air handling units have been analyzed by the developed methods from October until March. Results of energetic analysis are presented in Table 4. and on Fig. 10. Results

show that energy savings are significant and applying of air-recirculation and heat recovery energy saving can be 79%.

References

[1] Monostory I.: Valószínűségelmélet és matematikai statisztika, Budapest, 2002.: Műegyetemi Kiadó.

[2] Recknagel, H.; Sprenger; Schramek, E.-R.: Taschenbuch für Heizung und Klimatechnik. 68. Aufl. München: R. Oldenbourg Verlag, 1997. –ISBN 3-486-26214-9.

[3] Max H.: Hinweise zur Ausführung und zum Energieverbrauch von Heiz- und Raumlufttechnischen Anlagen. Ort, Verlag, Jahr: Düsseldorf, VDI-Verl., 1992.

[4] Kajtár L., Vörös Sz.: Influence of Climate Change on Modelling of HVAC Systems. 2007. Portoroz, 2nd IASME / WSEAS International Conference on Energy & Environment. 232-235 p.

[5] Kajtár L., Kassai M.: Levegőkezelő központ energiafelhasználásának elem-zése valószínüségelméleti módszerrel. Budapest, 2007.: Magyar Épületgépé-szet 2007/4. sz. 3-7 p.

[6] Kajtár L.: Klímatechnikai rendszerek energetikai, gazdasági elemzése valószínűség-elméleti alapon. Budapest, 2005: 17. Fűtés- és légtechnikai kon-ferencia CD kiadvány 12p.

[7] Kajtár L., Kassai M.: Evaluation of energy demand of air-conditioning systems based on probability theory. Greece, Rhodos, 2008.: 6th IASME/WSEAS International Conference on Heat transfer, Thermal engineering and Environment.. 266.-300.p. ISBN: 978-960-6766-97-8

[8] Kajtár L., Kassai M.: Analysis of air treatment equipment using the probability theory. 14th Building Services, Mechanical and Building Industry Days. 127.p. Debrecen, 2008.

[9] Kiss R.: Légtechnikai adatok. Budapest, 1980.: Műszaki Kiadó

[10] Hermann R, Klaus F.: Raumklimatechnik, Bald 2: Raumluft-und Raumkühltechnik. Springer, Berlin. SBN 978-3-540-57011-0.

[11] Trogisch A.: Plannungshilfen Lüftungstechnik. C.F. Müller Technik 2009. ISBN 978-3-7880-7833-1

[12] Kajtár L., Kassai M.: Klímatizált épületek energetikai elemzése. Budapest, 2008.: Magyar Épületgépészet 2008.7-8. szám 3-7 p.

[13] Kajtár L.: Klímatechnika – komfort – energetika. Budapest, 2008. Műszaki Kiadványok: Fűtés-, hűtés- és klímatechnika XI. évf. 2008/171. 8-11p. Info-Prod Kiadó és Kereskedő Kft. ISSN:1587-6853, ISSN: 1785-2307